

Particle Formation from Evaporating Microdroplets for Inhaled Drug Delivery

by

James Willard Ivey

A thesis submitted in partial fulfillment of the requirements for the degree of

Doctor of Philosophy

Department of Mechanical Engineering
University of Alberta

© James Willard Ivey, 2018

Abstract

This thesis is concerned with the mechanisms by which evaporating droplets containing dissolved or suspended solids transform into dry particles, and emphasizes applied research in the area of inhaled drug delivery. The main focus is on understanding and quantifying the relationships between the composition of the droplets, the evaporation conditions, and the resulting physical properties of the residual particles.

Chapter 1 briefly introduces the basic principles of inhaled drug delivery, the importance of the drug particle physical properties, and the most commonly used delivery devices. The delivery of drugs using pressurized metered dose inhalers is described in more detail. The spray drying process is introduced at a high level, and some considerations specific to the spray drying of engineered particles for pulmonary drug delivery are presented.

In Chapter 2, models are developed for the prediction of the aerodynamic particle size distribution produced by pressurized metered dose inhalers. Dimensional analysis is employed to analyze a large set of aerodynamic particle size distribution data for solution metered dose inhalers, resulting in a correlation equation for prediction of the mass median aerodynamic diameter. A stochastic model is developed to simulate the spatial distribution of a polydisperse discrete phase amongst a polydisperse spray of droplets, with the intention of evaluating the effect of aggregation on the aerodynamic particle size distribution for suspension pMDIs. A nonlinear curve fit to model results is developed which enables predictions of the aerodynamic particle size distribution for suspension metered dose inhalers as well.

Chapter 3 presents a study of the effects of air relative humidity on the morphology of particles emitted by solution metered dose inhalers containing a common inhaled drug. The work demonstrates that condensed water can have a strong effect on particle morphology, with the extent determined by the formulation variables; in this case highly porous particles were produced when the metered dose inhaler was sprayed in humid air. The possible implications for the efficacy of treatment are discussed.

Chapter 4 describes the design of a custom modular laboratory scale spray dryer; in combination with a novel isokinetic sampling system, its use for the characterization of atomization and collection equipment is demonstrated. Integration of a custom atomizer enables monodisperse spray drying using conventional solvents or superheated liquid propellants.

Parametric particle formation studies are conducted with organic solutes in ethanol and a hydrofluoroalkane propellant which is widely used in pressurized metered dose inhalers. The dependence of particle physical properties on droplet diameter, solution concentration, solvent type, and evaporation rate are evaluated using models of particle formation.

Chapter 5 reiterates the main conclusions arising from the work, and suggests possible areas for future investigations.

Preface

Chapter 1, Section 1.3 consists of a published review article:

Ivey, J. W., Vehring, R. and Finlay, W. H. (2015). Understanding pressurized metered dose inhaler performance. *Expert Opinion on Drug Delivery* 12:901-916.

My coauthors Reinhard Vehring and Warren Finlay assisted with manuscript concept development. I wrote the manuscript myself.

The major portions of Chapter 2 have been published or will be published soon. Section 2.2 has been published as a research article:

Ivey, J. W., Lewis, D., Church, T., Finlay, W. H. and Vehring, R. (2014). A correlation equation for the mass median aerodynamic diameter of the aerosol emitted by solution metered dose inhalers. *International Journal of Pharmaceutics* 465:18-24.

I had no involvement with conducting the cascade impaction testing; the impaction dataset was furnished by my coauthors Dave Lewis and Tanya Church of Chiesi Ltd., Chippenham, UK. I conducted additional analysis on the cascade impaction data set, including dimensional analysis and curve fitting. I wrote the manuscript, save that my coauthor R. Vehring drafted portions of the text in Section 2.2.2.1: Content equivalent diameter. Section 2.3 consists of a poster presentation abstract which has been accepted for presentation and will be published in peer-reviewed conference proceedings:

Ivey, J. W. and Vehring, R. (2018). An *in-silico* investigation of formulation and device effects on the aerodynamic particle size distributions of suspension pressurized metered dose inhalers. in *Respiratory Drug Delivery 2018*, R. N. Dalby, et al., eds., In Press. VCU , Richmond, VA.

It is my original work.

Chapter 3, Section 3.2 consists of a published research article:

Ivey, J. W., Bhambri, P., Church, T. K., Lewis, D. A., McDermott, M. T., Elbayomy, S., Finlay, W. H. and Vehring, R. (2017). Humidity affects the morphology of particles emitted from beclomethasone dipropionate pressurized metered dose inhalers. *International Journal of Pharmaceutics* 520:207-215.

I was responsible for preparation and analysis of samples; my coauthor Pallavi Bhambri assisted with sample analysis. I conducted the analysis of data and wrote the manuscript.

The research spray dryer described in Chapter 4 was primarily designed by myself, with two notable exceptions. The gas cyclone was an existing design which an industrial collaborator generously shared with us. The monodisperse atomizer was designed by fellow graduate students in Prof. Vehring's and Prof. Finlay's research groups. Custom components were fabricated by the Department of Mechanical Engineering machine shop or external vendors. I was responsible for installation and assembly, plumbing, wiring, instrumentation design, and control hardware and software design for the spray dryer. Section 4.4 consists of a poster presentation abstract which has been accepted for presentation and will soon be published as peer-reviewed conference proceedings:

Ivey, J. W., Barona, D., Gomez, M., Kuan, L., McAllister, R., Oberhagemann, L., D'Sa, D., Lechuga-Ballesteros, D., Ajmera, A., Gracin, S. and Vehring, R. (2018). Isokinetic in-line sampling enables rapid characterization of atomizers and cyclones for spray drying process development, in *Respiratory Drug Delivery 2018*, R. N. Dalby, et al., eds., In Press. VCU, Richmond, VA.

My coauthor Reinhard Vehring and I were responsible for the design concept of the isokinetic sampling system, while my coauthor Laurence Kuan developed the detailed design of the custom components of the system under my oversight. I oversaw planning, execution, and data analysis for atomizer and cyclone characterization tests, which were conducted with the assistance of my coauthors Mellissa Gomez and Reagan McAllister. I was responsible for writing the abstract. Section 4.5 consists of the text of a manuscript which at the time of this writing is accepted for publication as a research article:

Ivey, J. W., Bhambri, P., Church, T. K., Lewis, D. A. and Vehring, R. (2018). Experimental investigations of particle formation from propellant and solvent droplets using a monodisperse spray dryer. *Aerosol Sci. Technol.*:In Press.

<https://doi.org/10.1080/02786826.2018.1451818>

I was responsible for design and execution of the experimental program; my coauthor Pallavi Bhambri assisted substantially with the production and physiochemical analysis of monodisperse

beclomethasone dipropionate microparticle samples. I analyzed the experimental results and drafted the manuscript.

This work is dedicated to all of the present and future sufferers of lung disease.

Acknowledgements

First and foremost I must thank my supervisor Prof. Reinhard Vehring, not only for his guidance and support during my graduate studies, but for his excellent mentorship which goes back to the early days of my career. The outstanding work of all the technical personnel in the MecE shop made it possible to put a one-of-a-kind experimental setup in place; I must especially acknowledge Ryan Shoults, Bernie Faulkner, Rick Conrad, and Rick Bubenko. I am indebted to Peng Li, Anqiang He, and Shiau-Yin Wu of the U of A nanoFAB for their patience and support while teaching me the basics of ultramicroscopy. My gratitude goes to Pallavi Bhambri for her contributions to the experimental program. Many thanks are due to Dave Lewis and Tanya Church of Chiesi Ltd. for the opportunity to collaborate on some fascinating science. For the stimulating conversations about inhalers, and the generous invitation to work together on our pMDI review, I must thank Prof. Warren Finlay. To all my fellow graduate students in the particle engineering group, past and present, I offer sincere thanks for sharing experiences, passions, ideas, equipment, insights, and miseries. I am grateful for financial support in the form of a Studentship Award from the Lung Association of Alberta & NWT. Laura, thanks for your endless patience and support while I got this done. Last but not least, a tremendous amount of gratitude is due to my parents. Mom, thanks for showing me how fun it is to learn. Dad, thanks for showing me that sometimes the best way to learn is to do.

Table of Contents

Abstract.....	ii
Preface.....	iv
Acknowledgements.....	viii
Table of Contents.....	ix
Chapter 1 : Introduction.....	1
1.1 Inhaled drug delivery and the importance of particle physical properties.....	1
1.2 Devices for delivering inhaled drugs.....	3
1.3 Understanding pressurized metered dose inhaler performance.....	5
1.3.1 Introduction.....	5
1.3.2 Dose metering.....	8
1.3.3 Atomization in pMDIs.....	14
1.3.4 Aerosol evolution and deposition.....	20
1.3.5 Conclusions.....	26
1.3.6 Expert opinion.....	26
1.4 Introduction to spray drying for inhaled drug delivery.....	28
Chapter 2 : Models for Predicting the Aerodynamic Particle Size Distribution of pMDIs.....	33
2.1 Introduction.....	33
2.2 A correlation equation for the mass median aerodynamic diameter of the aerosol emitted by solution metered dose inhalers.....	34
2.2.1 Introduction.....	34
2.2.2 Materials and methods.....	37
2.2.3 Results and discussion.....	43
2.2.4 Conclusions.....	46
2.2.5 Appendix: Physical properties of propellant-ethanol mixtures.....	46
2.3 An <i>in-silico</i> investigation of formulation and device effects on the aerodynamic particle size distributions of suspension pressurized metered dose inhalers.....	48
2.3.1 Introduction.....	48
2.3.2 Methods.....	48

2.3.3	Results and discussion	50
2.3.4	Conclusions.....	51
Chapter 3	: Environmental Effects on the Aerosols Emitted from pMDIs.....	53
3.1	Introduction	53
3.2	Humidity affects the morphology of particles emitted from beclomethasone dipropionate pressurized metered dose inhalers	54
3.2.1	Introduction.....	54
3.2.2	Materials and methods	58
3.2.3	Results and discussion	61
3.2.4	Conclusions.....	69
Chapter 4	: A Particle Engineering Approach to Spray Drying.....	71
4.1	Introduction	71
4.2	Design of a modular research spray dryer.....	73
4.2.1	User requirements	73
4.2.2	Atomization equipment.....	74
4.2.3	Drying chamber geometry	75
4.2.4	Collection hardware	81
4.2.5	Design summary	81
4.3	Spray drying process modeling	85
4.4	Isokinetic in-line sampling enables rapid characterization of atomizers and cyclones for spray drying process development.....	90
4.4.1	Introduction.....	90
4.4.2	Methods.....	90
4.4.3	Results and discussion	91
4.4.4	Conclusions.....	93
4.5	Experimental investigations of particle formation from propellant and solvent droplets using a monodisperse spray dryer.....	93
4.5.1	Introduction.....	93
4.5.2	Methods.....	96

4.5.3	Results and discussion	103
4.5.4	Conclusions.....	115
4.5.5	Acknowledgements.....	116
4.5.6	Supplementary information	116
Chapter 5 : Conclusions		123
Bibliography		126
Appendices.....		143
A1.	Supplementary materials to Section 2.3.....	143
A1.1.	Methods.....	143
A1.2.	Results and discussion	149
A2.	The influence of environmental factors on pMDI performance	151
A2.1.	Introduction.....	151
A2.2.	Methods.....	151
A2.3.	Results and discussion	152
A2.4.	Conclusions.....	157
A3.	Monodisperse spray drying calculations	158
A3.1.	The dependence of the dry particle diameter on the operating parameters	158
A3.2.	The dependence of the dry mass throughput on the operating parameters.....	159
A3.3.	Propellant jets and the Rayleigh breakup regime	160
A4.	Design documentation for modular laboratory scale research spray dryer and peripheral equipment.....	162
A4.1.	Dryer hardware bill of materials	162
A4.2.	Dryer hardware selected engineering drawings	163
A4.3.	Dryer enclosure bill of materials.....	170
A4.4.	Dryer enclosure assembly graphic	172
A4.5.	Instruments and controls bill of materials.....	173
A4.6.	Instruments and controls wiring diagrams	175
A4.7.	Isokinetic sampling system bill of materials.....	177
A4.8.	Isokinetic sampling system selected engineering drawings.....	179

List of Tables

Table #	Caption	pg.
Table 1.1	Summary of correlations for the mass median content equivalent diameter developed using aerodynamic sizing of residual particles from solution pMDIs. ^a : Symbols used in correlations: Y_e : mass fraction of co-solvent ethanol; d_{ao} : actuator orifice diameter; σ_{pa} : propellant surface tension in air; p_{mc} : metering chamber pressure.	19
Table 2.1	Summary of the ranges of the device and formulation variables in the cascade impaction data set used to develop the correlation.	39
Table 2.2	Summary of the variables in the dimensional analysis, and a brief explanation for the inclusion of each.	40
Table 2.3	Mean, standard deviation, and relative standard deviation of the values of the three dimensionless groups for the cascade impaction data set.	43
Table 2.4	The equations used to approximate physical properties of ethanol and propellants HFA 134a and HFA 227ea.	47
Table 2.5	Parameter ranges evaluated herein; suspended phased density $\rho = 1365 \text{ kg/m}^3$ in all cases.	50
Table 3.1	Summary of the formulation variables for the four tested BDP solution formulations.	58
Table 3.2	Summary of the critical RH for pore formation and the corresponding dew point temperature for each of the tested BDP formulations. The rightmost column indicates whether any particle surface modification was observed below RH_c .	66
Table 4.1	Summary of user requirements for the modular research spray dryer.	73
Table 4.2	Dry particle diameter in μm computed using Equation (4.1) and Equation (1.16) for varying solution concentrations and orifice diameters. It was assumed that the droplets dry into solid spheres with $\rho_p = 1000 \text{ kg/m}^3$	75
Table 4.3	Minimum chamber length calculated using Equation (4.6) for complete drying of a 43 μm droplet at 40 °C, at 1000 L/min drying gas flow rate, for a variety of drying chamber diameters.	78
Table 4.4	Minimum chamber length and chamber Reynolds number for Drying Scenario 2 for three different chamber diameters. Assumes a 100 μm droplet drying at 40 °C, which requires 61 cm to decelerate and subsequently evaporates in 5 s while traveling at a constant velocity with a drying gas flow rate of 200 L/min.	81
Table 4.5	Basic specifications of the custom research spray dryer. ^a : full range achievable using variable number of drying chamber sections.	82
Table 4.6	Summary of process parameter ranges evaluated during heat loss characterization experiments.	89
Table 4.7	Summary of experimental parameters and resulting estimated solids production rate, monodisperse spray drying runs.	103
Table 4.8	Summary of orifice diameter, composition, and drying temperature for BDP particle batches; projected area equivalent diameter distribution statistics; solid phase analysis using Raman spectroscopy. GSD: geometric standard deviation. nd = experiment not conducted, or no data available. S.E.: standard error, nonlinear least squares fitting parameter.	105
Table 4.9	Summary of orifice diameter, composition, drying temperature, Péclet number, and time available for crystal nucleation and growth for caffeine microparticle batches; projected area equivalent diameter distribution statistics. For micrograph image analysis, all particle and crystallite edges were delineated with polygons. GSD: geometric standard deviation. *: standard error of nonlinear least squares fitting parameters was less than the precision error as reported for all fits.	109
Table 4.10	Methods for computing material properties for models.	121
Table A 1	Summary of selected input and output simulation parameters for an extremum case.	149

List of Figures

Figure #	Caption	pg.
Figure 1.1	Cross-section views of a pMDI fitted with a dose retention valve. TOP: pMDI (left) with a detail view of the valve components (right). Gray shaded areas indicate the presence of drug-propellant suspension or solution. 1: Canister. 2: Actuator. 3: Detail view of valve components. 4: Actuator mouthpiece. 5: Crimp. 6: Elastomer seals. 7: Ferrule. 8: Spring. 9: Valve body. 10: Metering chamber. 11: Valve stem orifice. 12: Valve stem. 13: Interior of valve stem; comprises part of the expansion chamber. 14: Actuator orifice. 15: Actuator sump; comprises part of the expansion chamber. 16: Stem receiver block. BOTTOM: Detail views illustrating dose delivery. Left: valve and actuator cross-section, illustrating metered atomization. Center: valve components in the depressed position, after actuation. Right: valve in the released position, illustrating recharging of the metering chamber.	6
Figure 1.2	Theoretical plot of metered dose, normalized by nominal initial metered dose, versus dose number for a canister fired until empty.	10
Figure 1.3	Plot of predicted MMAD of residual aerosol vs. metered dose with varying metering chamber volume for an excipient-free solution pMDI. Given an arbitrary, conservative criterion of MMAD < 5 μm for acceptable performance (denoted by the dashed line), the plot can be used to estimate a maximum attainable dose of roughly 5 mg using a 100 μL metering chamber. Assumptions: initial atomized droplet mass median diameter = 14 μm , initial droplets have the same concentration of nonvolatiles as the bulk formulation.	13
Figure 1.4	Illustration of a hypothesized process by which evaporation of a propellant droplet containing a suspended drug particle is followed by water condensation and secondary evaporation. The formulation and environmental variables expected to affect each step are indicated.	25
Figure 1.5	The major components of a spray drying process.	29
Figure 1.6	An example GEC. The GEC and cut size x_{50} depend on the cyclone geometry and the gas flow rate.	31
Figure 2.1	Simplified cross-sectional views of an MDI valve prior to actuation (left) and during actuation (right). 1: bulk solution; 2: metering chamber; 3: valve stem; 4: seals; 5: expansion chamber, sometimes referred to as the actuator sump; 6: actuator orifice.	34
Figure 2.2	Plot of Π_1 vs. Π_2 and a power-law curve fit to the data.	44
Figure 2.3	Comparison of predicted vs. measured MMAD of experimental data from a variety of literature sources. The data of Meakin (squares, (Meakin et al. 2000)) were generated using an Andersen cascade impactor. The data of Myrdal (circles, (Myrdal et al. 2004)) were generated using a time-of-flight aerodynamic particle sizer (APS) equipped with a USP inlet plus inlet extension. The data of Stein (diamonds, (Stein and Myrdal 2004)) were also generated with an APS, with a USP inlet and no extension. Open symbols: propellant 134a + ethanol; closed symbols: propellant 227ea + ethanol.	45
Figure 2.4	Flow chart describing the function of the stochastic model.	49
Figure 2.5	Left panel: comparison of simulated and selected measured cumulative APSDs for suspension metered dose inhalers containing different concentrations of fluticasone propionate. Right panel: effect of droplet and suspended phase median diameter and suspension concentration on the growth factor Γ for $GSD_0 = 2.1$ and $GSD_{sp} = 1.8$.	51
Figure 2.6	Left panel: dependence of growth factor Γ on the suspended particle to droplet ratio $\frac{N_{sp}}{N_0}$ for varying GSD_0 and GSD_{sp} . Right panel: pMDI MMAD values as predicted using Equation (2.18) vs. stochastic model predictions.	51
Figure 3.1	Schematic of the controlled humidity particle sampling setup used in this work. (1) BDP solution pMDI (2) 9 liter polypropylene evaporation chamber (3) USP induction port (4) Single stage, single nozzle impactor, cut size 0.6 μm at 1.0 SLPM air flow rate (5) Inline HEPA filter (6) Flow control valve (7) Flow meter (8) Shutoff valve.	59

Figure #	Caption	pg.
Figure 3.2	Raman spectra of amorphous and crystalline BDP standards in the low frequency shift region. Spectra are offset vertically.	62
Figure 3.3	Selected FE-SEM micrographs of all four BDP formulations actuated in dry air (leftmost four panels) or humid (RH = $38 \pm 1\%$ for p227ea inhalers or RH = $50 \pm 1\%$ for p134a inhalers) air (rightmost four panels).	62
Figure 3.4	FE-SEM micrographs of BDP particles produced from the 5% w/w ethanol, p134a pMDI. Left panel: air RH $\leq 2\%$. Right panel: RH = $50 \pm 1\%$.	64
Figure 3.5	FIB-HIM micrographs of particles produced by the 5% ethanol, p227ea pMDI. Left panel: air RH $\leq 2\%$. Right panel: air RH = $38 \pm 1\%$.	64
Figure 3.6	Raman spectra of BDP samples in the C-H stretch band. Spectra are offset vertically. Topmost two spectra: crystalline and amorphous standards. Third through tenth spectra from top: spectra from pMDI samples tested at either dry (RH $\leq 2\%$) or humid (RH $38 \pm 1\%$ for p227ea inhalers or RH $50 \pm 1\%$ for p134a inhalers) air. Bottom spectrum: sample obtained from pMDI 134_5 actuated in dry air and stored for three weeks in a desiccator at room temperature.	66
Figure 3.7	FE-SEM micrographs of the particles produced by pMDI 134_5 at varying air relative humidity. In this case a mixed population of porous and non-porous particles was observed at $14 \pm 1\%$ RH, indicating that the critical RH for pore formation RH_c lies in this range.	67
Figure 3.8	FE-SEM micrographs of particles sampled from pMDI 134_18 actuated in dry (left) or $14 \pm 1\%$ RH air.	67
Figure 3.9	A plot of dew point temperature vs RH for air at normal temperature and pressure (NTP, 20 °C and 101.3 kPa), with annotations demonstrating the hypothesized effects of spray plume temperature and air RH on the resulting morphology of the particles produced by BDP solution pMDIs.	69
Figure 4.1	Contour plot of droplet drying time vs. initial droplet diameter and drying temperature as computed using the model presented in Section 4.5.2.5.2: Droplet evaporation rate. Dry air, 101.3 kPa pressure.	78
Figure 4.2	Schematic depicting a configuration of the research spray dryer to enable polydisperse spray drying in a mode similar to conventional laboratory scale spray dryers.	83
Figure 4.3	Assembly drawing showing major drying hardware components as configured for polydisperse spray drying.	84
Figure 4.4	The research spray dryer in its enclosure.	85
Figure 4.5	Control volume diagram for the spray drying process, illustrating the energy transport in the process.	86
Figure 4.6	Left panel: rate of heat loss, \dot{q}_{loss} , vs. dryer outlet temperature, T_{out} , for water-only spray tests; data points are grouped by the drying gas flow rate. Right panel: model prediction vs. observed outlet temperature for subsequent actual spray drying runs conducted using the modular lab scale research dryer.	89
Figure 4.7	Schematic depiction of the isokinetic sampling system, which enabled real-time measurement of the aerodynamic particle size distribution of aerosol in the drying process at varying locations within the drying process.	91
Figure 4.8	Mass median droplet diameter vs. atomization air-liquid ratio for the tested Büchi twin fluid atomizer. An intermediate point was replicated three times to assess measurement variability. The error bar represents one standard deviation.	92
Figure 4.9	Separation efficiency curves for Büchi's high-efficiency cyclone separator at air flow rates of 100, 200, and 300 SLPM. Symbols: measured data using Equation (4.27). Closed lines: curve fits using Equation (4.29). 50% cut size from curve fits: 1.24 μm at 100 SLPM, 0.84 μm at 200 SLPM, 0.35 μm at 300 SLPM.	93
Figure 4.10	Schematic depicting the experimental setup for monodisperse spray drying.	97

Figure #	Caption	pg.
Figure 4.11	Highly uniform microparticles were produced using various orifice diameters, solvents, solutes, and drying conditions. a.) 0.1 mg/mL BDP dissolved in p134a + 20 % w/w ethanol, 23 μ m orifice, dried at 130 ° C inlet temperature. b.) 2.0 mg/mL BDP dissolved in p134a + 20% w/w ethanol, 23 μ m orifice, dried at 130 ° C inlet temperature. c.) 4.0 mg/mL caffeine dissolved in ethanol, 35 μ m orifice, dried at 130 ° C inlet temperature. d.) 4.0 mg/mL caffeine dissolved in ethanol, 10 μ m orifice, dried at 30 °C.	104
Figure 4.12	BDP Raman spectra in the C-H stretch band, offset for display purposes. Bottom two spectra: crystalline and amorphous references. Group A: spectra attained from 3 distinct locations on a single sample collected during production of BDP from 2.0 mg/mL solution in p134a + 5% w/w ethanol, using a 23 μ m orifice, dried at 30 ° C inlet temperature. Group B: spectra attained from 3 distinct locations on a single sample (0.1 mg/mL BDP in p134a + 5% w/w ethanol, 23 μ m orifice, dried at 130 ° C inlet temperature).	107
Figure 4.13	Drying temperature affects the morphology of BDP microparticles.	108
Figure 4.14	FIB-HIM cross-sections of BDP microparticles attained using a 23 μ m orifice. Top: 0.1 mg /mL BDP in 134a + 5% w/w ethanol, dried at an inlet temperature of 130 °C. Bottom: 2.0 mg/mL BDP in 134a + 20 % w/w ethanol, dried at 130 ° C.	108
Figure 4.15	Caffeine microparticles produced using a 35 μ m microorifice. a.) 4.0 mg/mL, ethanol, 30 ° C inlet temperature. b.) 4.0 mg/mL, ethanol, 130 ° C inlet temperature. c.) 0.1 mg/mL, ethanol, 30 ° C inlet temperature. d.) 0.1 mg/mL, ethanol, 130 ° C inlet temperature.	111
Figure 4.16	Caffeine microparticles produced using a 10 μ m microorifice. a.) 4.0 mg/mL, ethanol, 30 ° C inlet temperature. b.) 4.0 mg/mL, ethanol, 130 ° C inlet temperature. c.) 0.1 mg/mL, ethanol, 30 ° C inlet temperature. d.) 0.1 mg/mL, p134a, 130 ° C inlet temperature.	112
Figure 4.17	Dimensions of individual crystallites (black boxes: maximum Feret diameter, red circles: minimum Feret diameter) vs. t_c , the time available for nucleation and crystal growth predicted by the particle formation model presented in Section 4.5.2.5.3. Error bars indicate one standard deviation.	113
Figure 4.18	Caffeine spectra from 1000 to 1600 cm ⁻¹ . Spectra are offset for clarity. Arrows indicate marker peaks for caffeine polymorphic form I. Spray-dried microparticle samples consist predominantly of form II.	114
Figure 4.19	Results of the quasistationary droplet evaporation model. Droplet evaporation rate (left) and equilibrium temperature (right) as a function of the gas temperature far from the droplet.	118
Figure A 1	Graphical illustration of some key steps in the stochastic particle-to-droplet assignment model.	143
Figure A 2	Screenshot of selected output plots from the Excel analysis template for a simulation run employing a high suspension concentration with relatively large suspended particles.	150
Figure A 3	Data of (Shemirani et al. 2013): <i>in vitro</i> lung dose (normalized by mean at 0 % RH) vs. relative humidity for two solution and one suspension pMDI tested at 20 °C. Data points are offset horizontally for visibility.	153
Figure A 4	Data of (Morin et al. 2014): <i>in vitro</i> lung dose (normalized by the mean at 20 °C) vs. temperature for four commercial pMDI products ; for these experiments, inhalers were in thermal equilibrium with ambient during testing. Data points are offset horizontally for visibility.	154
Figure A 5	Data of (Morin et al. 2014): <i>in vitro</i> lung dose (normalized by the mean at 20 °C) vs. gas temperature for four commercial pMDI products. In these experiments, inhalers were equilibrated at 20 °C and tested at varying ambient temperature. Data points are offset horizontally for visibility.	155

Figure #	Caption	pg.
Figure A 6	Data of (Morin et al. 2014): <i>in vitro</i> lung dose (normalized by the mean at 20 °C) vs. inhaler temperature; here inhalers were equilibrated at the nominal temperature and tested at the ambient lab temperature of 20 °C. Data points are offset horizontally for visibility.	155
Figure A 7	Left panel—initial droplet mass median diameter (computed with Equation A.17) vs. propellant temperature for p134a and p227ea. Right panel—results from the quasistationary droplet evaporation model including Stefan flow assuming droplet evaporation at standard pressure: time required for droplet evaporation vs. the initial droplet diameter for p134a at -10 and 20 °C. “Lower bound” was calculated at nominal air temperature, while “upper bound” was calculated at an outlet condition assuming complete evaporation of propellant in an adiabatic process to provide an extremum case.	156
Figure A 8	Contour plot of dry particle size (μm) vs. orifice diameter and solution concentration for $\rho_p = 1000 \text{ kg/m}^3$ and $d_d/d_o = 1.95$.	159
Figure A 9	Contour plots of maximal feasible solids throughput for monodisperse spray drying computed using Equation (A.26) for water (left panel) or p134a (right).	160
Figure A 10	Plot of gas Weber number vs. pressure drop across the orifice for 10 μm (dashed line, transition Weber number 1.30) or 35 μm (closed line, transition Weber number 1.26) liquid jets discharging into air at 101.3 kPa and 20 °C. Propellant liquid properties were computed at 0 °C.	161

Nomenclature

Roman Characters

A	Area
A_{ch}	Drying chamber cross sectional area
ALR	Air-liquid mass ratio
a	Empirical constant
b	Empirical constant
C_c	Cunningham correction factor for noncontinuum effects
C_d	Drag coefficient; discharge coefficient
CMD	Count median diameter
c	Concentration; empirical constant
c_{mc}	Drug concentration in pMDI metering chamber
c_{nv}	Total concentration of nonvolatiles
c_p	Specific heat capacity
c_r	Reference concentration
c_s	Solution or suspension concentration
c_{sp}	Suspension concentration
D	Diffusion coefficient
D_p	Particle diffusion coefficient
D_s	Solute diffusion coefficient
D_v	Vapor diffusion coefficient
d	Diameter
$d_{\text{A,eq}}$	Projected area equivalent diameter
d_0	Initial droplet diameter
$d_{0,50}$	Droplet mass median diameter
d_a	Aerodynamic diameter
$d_{\text{a},50}$	Mass median aerodynamic diameter
d_{ao}	Actuator orifice diameter
d_c	Content equivalent diameter
$d_{\text{c},50}$	Mass median content equivalent diameter
d_d	Droplet diameter
$d_{\text{d},50}$	Droplet mass median diameter
$d_{\text{d},90}$	Droplet 90 th percentile mass diameter
d_j	Jet diameter
d_l	Liquid orifice diameter
d_o	Orifice diameter
d_p	Particle diameter
$d_{\text{p},50}$	Particle mass median diameter
$d_{\text{sp},50}$	Suspended phase mass median diameter
d_v	Volume equivalent diameter
E_{ss}	Steady-state surface enrichment
GSD	Geometric standard deviation
GSD_0	Droplet geometric standard deviation

GSD_{sp}	Suspended phase geometric standard deviation
f	Function; discrete particle size frequency distribution; frequency
g	Acceleration due to gravity
h	Specific enthalpy
k	Thermal conductivity
k_b	Boltzmann's constant
L	Length; flow field characteristic length; specific enthalpy of vaporization
M_g	Gas molar mass
M_v	Vapor molar mass
$MMAD$	Mass median aerodynamic diameter
MMD_0	Initial droplet mass median diameter
m	Mass; grade efficiency curve sharpness parameter
m_e	Propellant mass emitted per dose
m_i	Residual propellant vapor mass per dose
m_p	Particle mass
\dot{m}	Mass flow rate
N_0	Number of droplets
N_{sp}	Number of suspended phase particles
n	Surface enrichment growth parameter
p	Pressure
p_∞	Ambient pressure
p_{ec}	Expansion chamber pressure
p_g	Gas partial pressure
p_{mc}	Metering chamber pressure
p_{out}	Drying chamber outlet pressure
p_{sat}	Saturation pressure
p_v	Vapor partial pressure
Q	Volume flow rate
q_{ec}	Vapor quality in the expansion chamber
\dot{q}	Rate of energy transfer
R^2	Coefficient of determination
R^2_{adj}	Adjusted coefficient of determination
RH	Relative humidity
RH_c	Critical relative humidity for pore formation
S	Particle stopping distance; solute degree of saturation
S_0	Initial degree of solute saturation
T	Temperature
T_∞	Temperature far from the droplet surface
T_0	Initial temperature
T_e	Exit temperature
T_{eq}	Droplet equilibrium temperature
T_{in}	Dryer inlet temperature
T_{out}	Dryer outlet temperature
\bar{T}	Average temperature
t	Time

t_c	Time available for crystal nucleation and growth
t_{res}	Residence time
t_{sat}	Time to reach solute saturation at droplet surface
U_0	Particle initial velocity; characteristic velocity of a flow field
V	Volume
V_0	Droplet volume
V_{ch}	Drying chamber volume
V_{mc}	pMDI metered volume
V_{sp}	Suspended phase particle volume
\dot{V}	Volume flow rate
\dot{V}_{dg}	Drying gas volume flow rate
v	Velocity
v_0	Initial velocity; flow field characteristic velocity
v_d	Droplet velocity
v_{dg}	Drying gas velocity
v_{rel}	Relative velocity
$v_{settling}$	Particle settling velocity
x_{50}	Cyclone cut size
Y	Species mass fraction
Y_∞	Vapor mass fraction far from droplet surface
Y_{drug}	Drug mass fraction
Y_e	Ethanol mass fraction
Y_s	Solids mass fraction; vapor mass fraction at droplet surface

Greek Characters

α_i	Dilution factor due to creaming, pMDIs
β	Binary solution / suspension parameter, pMDIs
Γ	Growth factor due to aggregation (ratio of pMDI MMAD to suspended phase MMAD)
ΔH_v	Specific enthalpy of vaporization
Δm	Change in propellant mass per actuation, pMDIs
Δp	Pressure difference
δ_m	pMDI metered dose
$\eta(x)$	Cyclone fractional efficiency
κ	Evaporation rate
λ	Wavelength
μ	Fluid dynamic viscosity
ξ	Ratio of slip correction factors
Π	Dimensionless group
ρ	Density
ρ^*	Reference density, 1000 kg/m ³
ρ_D	Suspended drug density
ρ_d	Droplet density
ρ_g	Gas density
ρ_{L,T_c}	Propellant liquid density at the canister temperature
ρ_l	Liquid density

ρ_p	Particle density
ρ_t	True density
ρ_v	Vapor phase density
ρ_{v,T_e}	Propellant vapor phase density at the post-actuation temperature, pMDI
σ_{lg}	Liquid surface tension in gas
σ_{pa}	Propellant surface tension in air
τ	Dimensionless drying time
τ_{sat}	Dimensionless time to reach solute saturation at the droplet surface
ϕ	Particle void fraction; relative humidity
φ	General thermophysical property
φ_e	Ethanol thermophysical property
φ_m	Mixture thermophysical property
φ_p	Propellant thermophysical property
χ	Particle dynamic shape factor
ω	Humidity ratio, i.e. mass ratio of solvent vapor to dry air

Dimensionless Numbers

Ja	Jakob number
Le	Lewis number
Oh	Ohnesorge number
Pe	Péclet number
Re	Reynolds number
Re_{ch}	Drying chamber Reynolds number
Re_d	Droplet Reynolds number
Stk	Stokes number
We	Weber number
We_G	Gas Weber number
We_L	Liquid Weber number

Chapter 1 : Introduction

1.1 Inhaled drug delivery and the importance of particle physical properties

The oral inhalation route has been employed for delivering medicines for millennia (Stein and Thiel 2017). The surface area of a typical human lung is about 50—70 m², much of which is highly vascular and offers rapid access to the bloodstream (Cloutier and Thrall 2010). Therefore orally inhaled therapies have been developed with both local and systemic action. Locally acting treatments are designed to treat diseases of the lung itself, such as asthma, COPD, cystic fibrosis, or tuberculosis (Barnes and Pedersen 1993; Høiby 2011; Misra et al. 2011; Siafakas et al. 1995), and may have anti-inflammatory (Keatings et al. 1997), bronchodilatory (Donohue 2004; Gross 2006), or antibacterial action (Hoe et al. 2013; Ryan et al. 2011). Systemic treatments leverage the lung's ready access to the bloodstream to rapidly deliver a drug to a different part of the body (Laube 2005). Diabetes and migraine are two major diseases which orally inhaled drugs have shown promise in treating (Patton et al. 1999; Shrewsbury et al. 2008). Immunomodulation with pulmonary delivery of vaccines has also been demonstrated (Low et al. 2008; Meyer et al. 2015).

An effective orally inhaled treatment requires delivery of the drug substance to the lung tissue; this is most readily accomplished by aerosol administration. Aerosols deposit in human airways by three main mechanisms: sedimentation due to gravity, inertial impaction, and Brownian diffusion (Finlay 2001b). Drug pharmacokinetics may vary with the region of the airways where the deposition occurs (Kleinstreuer et al. 2008); the regional deposition efficiency will depend on the flow field *via* the patient-specific airway geometry and breathing pattern, and the aerosol's particle size distribution (Heyder 2004). Typically, efficient treatment requires a substantial proportion of the drug to pass through the upper airways in the mouth, throat, and trachea to allow deposition in the lower airways, which requires a fairly fine aerosol. If the particles are too fine, however, they may be exhaled without depositing in the lung (Gill et al. 2007). As a general rule of thumb for the human airways, pulmonary delivery is most efficient when the particles fall within the size range of about 0.5—5 μm (Darquenne 2012), subsequently referred to here as the respirable size range.

The likelihood of particle deposition in the lung by sedimentation, impaction, or diffusion depends on the properties of the aerosol particles. For gravitational sedimentation in air of a particle in the respirable size range, deposition probability is related to the particle settling

velocity, v_{settling} (Hinds 1999):

$$v_{\text{settling}} = \frac{C_c \rho_p g d_v^2}{18 \mu \chi} . \quad (1.1)$$

Here d_v is the particle's volume equivalent diameter and ρ_p its density, g is the acceleration due to gravitation, μ is the fluid viscosity, χ is a shape parameter accounting for non-spherical particles, and C_c is a slip correction parameter accounting for non-continuum effects (significant only for submicron particles). Inertial impaction is related to the particle's Stokes number, Stk ; for a particle traveling in a flow field with characteristic velocity v_0 and characteristic dimension L ,

$$Stk = \frac{v_0 C_c \rho_p d_v^2}{18 L \mu \chi} . \quad (1.2)$$

The particle aerodynamic diameter, d_a , is defined as the diameter of a sphere with a reference density of $\rho^* = 1000 \text{ kg/m}^3$ which settles at the same velocity as the particle in question; it is related to the volume equivalent diameter by (Hinds 1999)

$$d_a = \sqrt{\frac{\rho_p \xi}{\rho^* \chi}} d_v , \quad (1.3)$$

where ξ is a ratio of slip correction factors:

$$\xi = \frac{C_c(d_v)}{C_c(d_a)} . \quad (1.4)$$

The aerodynamic diameter is a widely used particle size metric in the inhalation drug delivery field, and is useful for comparing deposition data between aerosols with differing particle density or shape.

The probability of particle deposition by Brownian diffusion in the lung depends in part on the particle's diffusion coefficient D_p (Hinds 1999):

$$D_p = \frac{k_b T C_c}{3 \pi \mu \chi d_v} \quad (1.5)$$

Here k_b is Boltzmann's constant, and T is the absolute temperature of the fluid. Considering the terms in Equations (1.1) through (1.5), it is apparent that the particle size, density, and shape play important roles in the mechanisms of aerosol deposition in the airways.

The human respiratory system has been designed by evolution to protect its user from aerosols, which in nature vary from slight irritants to deadly pathogens. The nose, mouth, and

upper airways provide coarse filtration functionality; particles which deposit there are enveloped in mucus and transported away by cilia to be swallowed and neutralized in the digestive system (Cloutier and Thrall 2010). Particles depositing deeper in the lung, in the bronchiolar airways, are also subject to mucociliary clearance, while those reaching the alveoli are subject to engulfment by the alveolar macrophages (Cloutier and Thrall 2010). The pharmacokinetics of inhaled drugs thus depend on how the drug particles interact with the tissues and clearance mechanisms of the lung following deposition (Ruge et al. 2013). The solid phase of the drug plays a role, since the dissolution rate in mucus of a drug present in an amorphous, disordered form may be much higher than for the same drug in an ordered, crystalline state (Lehto 2010). The effect of solid phase on dissolution rate has been demonstrated for inhaled drugs *in vitro* (Grainger et al. 2012; Haghi et al. 2014); the drug solid phase has also been shown to affect pharmacokinetics and pharmacodynamics for inhaled drugs *in vivo* in animal models (Sakagami et al. 2001; Sakagami et al. 2002). The drug particle morphology may also affect how the particle interacts with lung tissues following deposition. It has been suggested that very low density particles may reach the alveolar airways by virtue of their low aerodynamic diameter, while evading clearance by macrophages due to their large volume equivalent diameter (Tsapis et al. 2002). Also, the surface composition and geometry of a particle have the potential to alter the ability of the mucus to wet a particle (Schürch et al. 1990), with possible implications for the rates of dissolution and mucociliary clearance. So while particle size is a critical factor in deposition, other physical properties may have an influence on pharmacokinetics by affecting the way the particles interact with the lung tissues following deposition.

1.2 Devices for delivering inhaled drugs

The need to deliver an accurate, reproducible dose of drug within the respirable size range places exacting requirements on the devices used to deliver inhaled drugs. For the most part, inhaled drugs are delivered with one of three types of device: nebulizers, dry powder inhalers (DPIs), or pressurized, metered dose inhalers (pMDIs). Given the prominent role of pMDIs in the present work, an extensive review of their use in pulmonary drug delivery is presented in Section 1.3. DPIs are introduced briefly below, with an emphasis on how attributes of the powder formulation affect the performance. This is an important application area for pharmaceutical spray drying.

DPIs deliver aerosolized drug to the patient in a powdered form; inhalers generally consist of the powdered formulation itself, a metering system (usually a capsule or blister pack), and a means of aerosolization and delivery to the patient (i.e. the device). Devices are classified as either passive, where the airflow induced by the patient's inhalation maneuver provides the means of powder aerosolization, or active, where an additional mechanical or electrical energy source is harnessed to disperse the powdered drug (Dunbar et al. 1998). Since the required dose of drug is typically on the order of 100 μg (Hoppentocht et al. 2014)—a very small quantity of powder to efficiently and consistently fill, meter, and deliver—a means of bulking the formulation is usually employed. Therefore a common strategy is to employ a blend of the drug particles with a larger mass of a carrier excipient (Telko and Hickey 2005), most commonly crystalline lactose monohydrate (Singh et al. 2015). Alternatively, spray-dried engineered particles with tailored properties may incorporate drug and excipient into a single particle, and can be filled into DPIs to enable carrier-free formulations (Geller et al. 2011).

The performance of a DPI product depends critically on the physical properties of the drug and the carrier. The drug particles must be in the respirable size range in order to reach the lung. Since DPIs rely on aerodynamic forces to entrain the drug particles and empty the metered dose, and since these forces increase with increasing particle size (Finlay 2001b), the carrier particles are generally larger than the drug particles by approximately an order of magnitude. Assemblies of carrier particles with drug particles adhered to the surface are entrained during emptying of the metered powder dose; the drug particles must then be separated from the carrier particles, either in the device or in the airways, in order to reach the lung. Sufficient adhesion between drug and carrier is required to achieve a uniform blend and maintain uniformity during device filling (Flament et al. 2004), but if drug-carrier adhesion is too strong then the respirable dose will be adversely affected since the drug will remain attached to the carrier and deposit in the upper airways (Malcolmson and Embleton 1998). Thus development of a successful carrier-based dry powder formulation is something of a balancing act, and the adhesive and cohesive forces among the drug and carrier particles are very important to consider (Jones et al. 2008). For constituent particles in dry powder inhalers, the strength of these forces will depend on the size (Chew and Chan 1999), shape (Kaialy et al. 2012), surface composition (Singh et al. 2015), and surface roughness (Tan et al. 2016; Zeng et al. 2001) of the drug and carrier particles. These

are relevant considerations in the development of spray dried engineered particles for use in dry powder inhalers, a topic which is introduced further in Section 1.4.

1.3 Understanding pressurized metered dose inhaler performance¹

1.3.1 Introduction

The pressurized metered dose inhaler (pMDI) is nearing its seventh decade of use (Thiel 1996), and is currently the most commonly utilized device to deliver medicine to the lung (Lechuga-Ballesteros et al. 2011). Given its prevalence and history, it is no surprise that a large body of scientific literature on the topic of pMDI performance exists. The goal of this paper is to present a review of published studies that have informed our current understanding of the fundamental mechanisms driving pMDI performance. This necessitates a brief introduction to the pMDI device and common methods used to quantify its performance.

A center-plane cross section view of a typical pMDI is shown in the top panel of Figure 1.1, including a detail view of the valve hardware. A solution or suspension of drug and possibly excipients in a volatile propellant makes up the formulation, and is contained inside a metal canister which is capped by crimping a metering valve atop it. The metering valve separates a fixed volume of the formulation from the bulk in the canister and retains it in the metering chamber. A dose is administered when the filled valve-canister assembly is placed in a plastic actuator and the canister is depressed. Elastomer seals allow only the metered dose to leave the valve. Due to the pressure of the volatile propellant, the metered volume of formulation is driven through the valve stem orifice and into the expansion chamber, which consists of the interior of the valve stem and the actuator sump. The formulation flashes in the expansion chamber, and is atomized into a fine spray that passes through the actuator orifice. The initial characteristics of the spray and its subsequent evolution are to a great extent determined by the geometry of the valve and actuator and the properties of the formulation. Once released, a spring causes the valve to return to its rest position, where the metering chamber is refilled and the device is ready

¹ This section consists of a published review article:

Ivey, J. W., Vehring, R. and Finlay, W. H. (2015). Understanding pressurized metered dose inhaler performance. *Expert Opinion on Drug Delivery* 12:901-916.

My contributions to the work are summarized in the Preface.

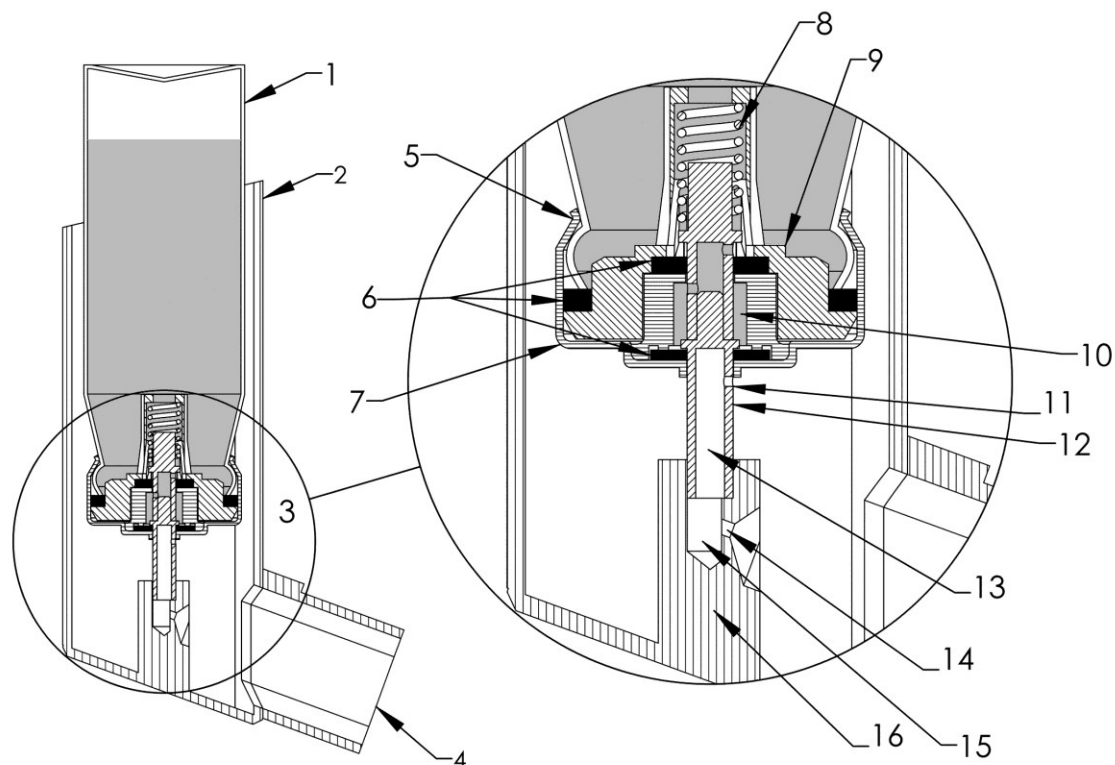


Figure 1.1: Cross-section views of a pMDI fitted with a dose retention valve. TOP: pMDI (left) with a detail view of the valve components (right). Gray shaded areas indicate the presence of drug-propellant suspension or solution. 1: Canister. 2: Actuator. 3: Detail view of valve components. 4: Actuator mouthpiece. 5: Crimp. 6: Elastomer seals. 7: Ferrule. 8: Spring. 9: Valve body. 10: Metering chamber. 11: Valve stem orifice. 12: Valve stem. 13: Interior of valve stem; comprises part of the expansion chamber. 14: Actuator orifice. 15: Actuator sump; comprises part of the expansion chamber. 16: Stem receiver block. BOTTOM: Detail views illustrating dose delivery. Left: valve and actuator cross-section, illustrating metered atomization. Center: valve components in the depressed position, after actuation. Right: valve in the released position, illustrating recharging of the metering chamber.

to deliver another dose. While information on pMDIs is available in recent reviews (Myrdal et al. 2014; Stein et al. 2014), the focus of this review is the factors affecting the performance of the pMDI device.

Since the aerodynamic diameter distribution of the emitted aerosol is critical in determining pulmonary drug deposition (Darquenne 2012), cascade impaction² is the most widely utilized means of quantifying the performance of pMDIs (Mitchell et al. 2007). These measurements are a mainstay of both research and development of pMDIs, providing a great deal of information on how formulation and device variables affect pMDI performance. Cascade impactors fractionate an aerosol by inertial separation (Son et al. 2011), and when coupled with gravimetric or chemometric assays can be used to estimate the aerodynamic diameter distribution of the aerosol emitted from a pMDI. The aerodynamic diameter distribution is generally approximated as log-normal, and can thus be quantified by the mass median aerodynamic diameter (MMAD) and the geometric standard deviation (GSD) (Hinds 1999). For inhaler testing, cascade impactors are normally fitted with an inlet device to simulate particle deposition in the human upper airways (USP 2013). Thus a cascade impaction test can also estimate the delivery efficiency, i.e. the fraction of the aerosol deemed capable of reaching the human lung. This may be quantified by the fine particle fraction (FPF), which as used herein is defined as the mass fraction of the dose emitted from the inhaler which is less than a given aerodynamic diameter (USP 2013). The FPF may be expressed as a percentage, and alternate definitions are common in the literature. At present *in vitro-in vivo* correlations with cascade impactor data remain an active area of research, with recent work focusing on better mouth-throat models (Mitchell et al. 2013). This review is divided into three main sections that follow logically from the way pMDIs deliver a drug: dose metering, atomization, and aerosol evolution and deposition. The emphasis is on research which illuminates the underlying mechanisms driving the performance of pMDI products. Developing a deeper understanding of these fundamentals is worthwhile, as it may lead to improved products with reduced development time as compared to empirically driven efforts. A relevant example was the industry-wide transition from

² Cascade impaction is a technique for separation of a polydisperse aerosol into multiple size classes based on the particles' differing inertia; in combination with gravimetric or chemometric assays the mass of drug in a range of aerodynamic diameter size bins can be measured, enabling determination of the aerodynamic diameter distribution. The interested reader is referred to an aerosol text (Hinds 1999) for further technical details.

chlorofluorocarbon (CFC) to hydrofluoroalkane (HFA) propellants during the 1990s and 2000s, which was necessitated by environmental regulations (Vervaet and Byron 1999). Existing, empirically developed knowledge was often inadequate in predicting the performance of pMDIs with the new HFA propellants. Fundamental research was required, and improved products were the result (Dolovich and Dhand 2011). While it appears that the contribution of medical use of HFA propellants to global warming is quite small relative to major industrial emissions, given their greenhouse potential it is not inconceivable that future environmental regulation might necessitate a similar industry-wide reformulation effort (Stein and Fradley 2010). Should this occur, a deeper understanding of the basic mechanisms at play in pMDIs will be of great benefit.

1.3.2 Dose metering

1.3.2.1 General considerations on dose metering

Since a typical pMDI contains hundreds of doses, accurate dose metering from first to last dose is essential to ensure reproducible drug delivery. This task is accomplished by the metering valve. The valves used in pMDIs function by separating a fixed volume of the drug solution or suspension from the bulk in the canister (Newman 2005). To illustrate the function of a typical pMDI valve, cross section views of a dose retention valve during dosing, after dosing and during recharging are given in the bottom panels of Figure 1.1. In a dose retention valve, the dose is separated from the bulk formulation and held in the metering chamber between doses. The metered dose, δ_m , is defined as the mass of drug contained in the metering chamber, and can be calculated using the relation

$$\delta_m = c_{mc} V_{mc} \quad , \quad (1.6)$$

where c_{mc} is the concentration of drug in the metering chamber of the valve expressed in mass / volume units, and V_{mc} is the metering chamber volume. Thus, the upper and lower limits on the metered dose are constrained by the metering chamber volume and the feasible range for the drug concentration. In the event that excipients are present in the formulation, Equation (1.6) can be modified:

$$\delta_m = Y_{drug} c_{mc,total} V_{mc} \quad . \quad (1.6a)$$

Here Y_{drug} is the mass fraction of drug relative to the total dissolved or suspended solids in the formulation at concentration $c_{mc,total}$. In the following calculations, for simplicity formulations are assumed to contain only drug in propellant and Equation (1.6) applies.

Since a pMDI valve essentially works by pumping solution or suspension out of a closed vessel, liquid-vapor equilibrium in the canister results in a small, gradual increase in the average solution or suspension concentration in the canister through the life of the inhaler (Lewis et al. 2011). Each time a dose is emitted from the valve, the mass of propellant expelled is

$$m_e = \rho_{L,T_c} V_{mc} \left(1 - \beta \frac{c_{mc}}{\rho_D} \right) . \quad (1.7)$$

Here ρ_{L,T_c} is the density of the liquid propellant at the temperature in the canister T_c , β is a parameter correcting for solution or suspension volume effects ($\beta = 1$ for suspensions, $\beta = 0$ for solutions), and ρ_D is the density of the drug present as a dispersed discrete phase. As illustrated in Figure 1.1, after a dose has been emitted from a pMDI some residual propellant vapor will be contained in the metering chamber. When the valve is released to its rest position, this residual gas is transported into the canister as it is displaced by liquid propellant. Its mass is approximately

$$m_i = \rho_{V,T_e} V_{mc} , \quad (1.8)$$

where ρ_{V,T_e} is the density of the vapor phase of the propellant at the local temperature after actuation, T_e . Thus, the reduction in mass of propellant contained in the canister for each dose is

$$\Delta m = m_e - m_i = V_{mc} \left[\rho_{L,T_c} \left(1 - \beta \frac{c_{mc}}{\rho_D} \right) - \rho_{V,T_e} \right] \quad (1.9)$$

This reduction in mass is accompanied by a reduction in the volume of liquid present in the canister and an increase in the vapor volume. The additional vapor is supplied partially by the residual gas in the metering chamber, with the rest coming from evaporation of the bulk formulation. Assuming no drug is retained in the valve metering volume, for each dose the mass of drug in the canister is reduced by an amount equal to the metered dose given in Equation (1.6). Thus Equations (1.6) and (1.9) allow calculation of the mass of propellant and drug present in the canister through the life of the inhaler. Then, given the volume of the canister and knowledge of the liquid and vapor phase densities of the propellant, the balance of mass and balance of volume equations can be solved to yield the drug concentration c_s after any number of doses. Enrichment of drug concentration due to the vapor equilibrium effect in a solution formulation with no co-solvent is illustrated in Figure 1.2, and is most pronounced as the canister approaches empty. If ethanol is included as a co-solvent, the calculations are more involved due to the non-ideality of liquid-vapor equilibrium in the HFA-ethanol system (Vervaeet and Byron 1999), and the ethanol concentration is expected to increase as the canister is emptied as well.

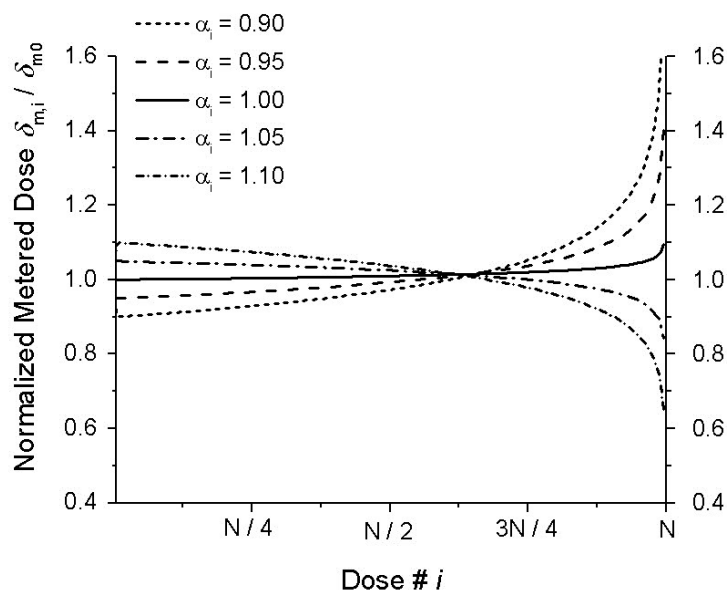


Figure 1.2: Theoretical plot of metered dose, normalized by nominal initial metered dose, versus dose number for a canister fired until empty. The plots were generated using the mass and volume balance calculations discussed in section 2.1. For solution formulations, $\alpha_i = 1.00$. The drug mass balance was modified using Equation (1.11) to model the effects of creaming ($\alpha_i = 0.90, 0.95$) and settling ($\alpha_i = 1.05, 1.10$) suspensions. Assumptions and constants: α_i is constant through life of inhalers, propellant type 227ea, canister volume 14 mL, valve metered volume 50 μL , initial fill volume 10.1 mL, canister temperature 20 $^\circ\text{C}$, residual vapor temperature -10 $^\circ\text{C}$, initial drug concentration $c_s = 0.50$ mg/mL, nominal initial metered dose $\delta_{m0} = 25$ μg , number of doses $N = 200$.

1.3.2.2 The influence of formulation

As seen in Equation (1.6), the drug concentration has a direct impact on the attainable range for the metered dose. For both solution and suspension formulations, the practical upper limit is related to the delivery efficiency—as solution or suspension concentration increases, so does the median particle size of the residual particles after propellant evaporation (Roth and Gebhart 1996). At high drug concentrations, the aerosol may become too coarse to reach the lung in sufficient amounts. An additional constraint for solution formulations is the drug solubility itself; use of a co-solvent (typically ethanol) can increase the solubility of the drug, but at the cost of reduced delivery efficiency (Gupta et al. 2003).

In solution formulations, very low drug concentrations are feasible (Lewis et al. 2005) while appropriate residual particle size can be maintained by addition of a soluble non-volatile excipient such as glycerol (Lewis et al. 2014). For suspension formulations, attaining reproducible dosing at low drug concentrations is challenging due to the inevitable adsorption of

drug particles onto the valve and canister (Dellamary et al. 2000). Several approaches have been proposed to solve this problem, including incorporating amorphous (Dellamary et al. 2000) or microcrystalline (Tarara et al. 2004) drug into engineered particles, addition of engineered particles to form a co-suspension (Noga et al. 2012; Vehring et al. 2012), or addition of nanoparticles as a suspension bulking agent (James et al. 2008).

In the context of dose metering, solution formulations behave differently than suspensions. In a solution formulation, assuming the drug stays dissolved through the life of the inhaler, the drug will remain homogeneously distributed through the volume of the propellant (Lewis et al. 2004). Thus the overall concentration of drug in the propellant, c_s , is the same as that in the metering chamber, c_{mc} . In suspension formulations, buoyant forces may result in sedimentation or creaming of the drug-containing dispersed phase (Tam et al. 2010); thus for suspensions prone to rapid separation, c_{mc} may differ substantially from c_s even shortly after shaking the inhaler (Weers and Tarara 2014). In this scenario, the metered dose may differ from that anticipated based on the bulk concentration c_s . This effect can be modeled by introduction of a parameter α_i that accounts for enrichment or dilution in the metering chamber relative to the overall concentration after the i^{th} actuation of the inhaler:

$$c_{mc,i} = \alpha_i c_{s,i} \quad (1.10)$$

A value of unity for α_i corresponds to solution or ideal suspension behavior; $\alpha_i < 1$ would result from creaming or losses from wall deposition, while $\alpha_i > 1$ would result from sedimentation. The parameter α_i likely depends on formulation variables as well as patient handling, and may vary through the life of the inhaler.

The metered dose introduced in Equation (1.6) may be modified using Equation (1.10) to simulate the effects of creaming or sedimentation:

$$\delta_{m,i} = \alpha_i c_{s,i} V_{mc} \quad (1.11)$$

Since the concentration of drug in the metering chamber differs from the concentration in the bulk reservoir for α_i not equal to 1, a cumulative effect on the bulk concentration c_s emerges through the life of the inhaler. This can be seen by modifying the drug mass balance discussed in Section 1.3.2.1 with Equation (1.11), and assuming constant values of α_i throughout the canister lifetime for simplicity, resulting in the theoretical dose through life plots of Figure 1.2. In the case of solution formulations, a very mild rise through life is expected due to the vapor equilibrium effect discussed in Section 1.3.2.1. Since both the vapor equilibrium effect and local

dilution during dose metering result in enrichment of the bulk in the canister, creaming suspensions are expected to display the most pronounced change in dose through life. Settling suspensions are expected to fare somewhat better since the two mechanisms counteract each other.

Though the model presented above is simple, it does provide some physical insight into factors which can influence the reproducibility of the metered dose through the life of an inhaler. As seen in Figure 1.2, regardless of formulation, the drift in metered dose is most severe as the inhaler approaches empty. This is a major justification for the need to fill an overage of solution or suspension (Smyth 2005) and to provide patients with a means of dose counting to determine when an inhaler needs replacement (Conner and Buck 2013; Dolovich and Dhand 2011). Further, in the case of suspensions, minimizing the rate at which the suspended phase separates is expected to improve the dose reproducibility. Means of doing so are presented in detailed reviews on the topic of colloidal stability in suspension pMDIs by, for example, O'Donnell and Williams III (O'Donnell and Williams III 2013) and Rogueda (Rogueda 2005). A recent numerical investigation of the problem was conducted by Javaheri and Finlay (Javaheri and Finlay 2014), who simulated the flocculation and creaming of polydisperse spheres in liquid propellant under the influence of buoyancy, Brownian motion, and van der Waals forces. Their results indicated that the density difference between the discrete phase and the propellant, the initial mass median diameter, the GSD, and the suspension concentration all had an influence on a characteristic time for phase separation. The complexity of the responses—even under a relatively restrictive set of assumptions—exemplify why colloidal stability in pMDIs remains an active area of research with many questions still to be answered.

Other formulation considerations that can affect the metered dose include chemical stability and drug-container interactions. Solution formulations may be more prone to chemical instability than suspension formulations (Wu et al. 2012), while suspensions can be adversely affected by loss of the dispersed phase onto canister and valve components (Young et al. 2003). Both of these problems can result in a reduction in the metered dose. The use of coatings on canisters (Smith et al. 2010) and valve components (Dohmeier et al. 2009) has been shown to improve both chemical stability and to prevent loss of suspended drug by adsorption to container components.

1.3.2.3 Device-specific effects

In addition to the formulation factors discussed above, the attainable dose range of a pMDI also depends on the viable range for the valve metered volume. As seen in Equation (1.6), the valve metered volume has a direct relationship to the metered dose. pMDI metering chamber volumes range from approximately 25 to 100 μL (Stein et al. 2014). The upper limit is due to loss of dosing efficiency as metered volume increases (Stein et al. 2004). Increasing the metered volume also necessarily increases the duration of the dosing event (Lewis et al. 2006), which introduces an additional constraint since a patient can only inhale for so long. The lower limit is possibly due to a decrease in the spray duration as valve volume is reduced (Lewis et al. 2006), where non-equilibrium events at the beginning and end of the spray may dwarf the fully developed portion of the spray (Versteeg and Hargrave 2002), resulting in poor atomization performance. The relationships between metering chamber volume, metered dose, and MMAD of the residual aerosol for a solution formulation are explored in Figure 1.3, using techniques presented by Vehring and Finlay (Vehring and Finlay 2013). The plot allows order-of-magnitude estimation of the maximum feasible dose from a solution pMDI given the criteria that the MMAD be less than a limiting value of 5 μm ; for a 100 μL metering valve, this maximum dose is approximately 5 mg.

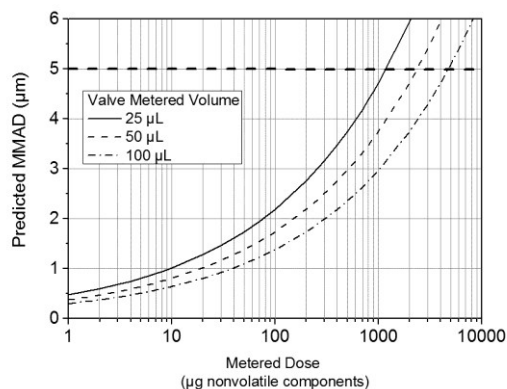


Figure 1.3: Plot of predicted MMAD of residual aerosol vs. metered dose with varying metering chamber volume for an excipient-free solution pMDI. Given an arbitrary, conservative criterion of MMAD < 5 μm for acceptable performance (denoted by the dashed line), the plot can be used to estimate a maximum attainable dose of roughly 5 mg using a 100 μL metering chamber. Assumptions: initial atomized droplet mass median diameter = 14 μm , initial droplets have the same concentration of nonvolatiles as the bulk formulation.

The valve design plays an important role in accurately metering the dose of drug. In dose retention valve designs, such as that depicted in Figure 1.1, the metered dose is sequestered from the bulk drug immediately following the previous dosing event and is retained in the metering chamber until the next dose is delivered (Schultz 1995). Dose retention valves rely on capillary forces (Lewis et al. 2011) and sometimes an additional enclosure around the valve metering chamber (Thiel 1996)—known as a retaining cup—to prevent the metered dose from draining out if the canister is inverted. Such loss-of-prime events can obviously have a negative effect on the metered dose, and a valve-up orientation during storage (Cummings 1999) and large ambient temperature variations (Church et al. 2011) can increase their likelihood. Another failure mode of dose retention valves arises with suspension formulations: over time the suspended material may settle or cream inside the metering chamber and thus adhere to the device surfaces despite agitation. This so-called “Cyr effect” may result in erratic dosing when the time between doses is variable (Cyr et al. 1991). Valve manufacturers have attempted to address some of the issues with dose retention valves by introducing “fast fill, fast drain” valve designs, where the dose is only segregated from the bulk as part of the dosing event (Fradley and Hodson 2008). Though they eliminate loss of prime and the Cyr effect, these valve designs can suffer from inconsistent dosing when drug deposits on dose metering surfaces during the dosing event and is subsequently flushed back into the bulk solution or suspension (Colombani et al. 2010).

1.3.3 Atomization in pMDIs

1.3.3.1 Background

In order for the dose to reach the human lung, a pMDI must produce an aerosol containing an appreciable fraction with an aerodynamic diameter in the respirable range of typically 0.5—5 μm (Pilcer and Amighi 2010). Since the particle size distribution of the aerosol emitted by a pMDI is directly related to the initial droplet diameter distribution, the device must produce a fine spray to meet this requirement. The initial droplet diameter distribution is also fundamentally tied to the maximum feasible emitted dose: as discussed previously, the solution or suspension concentration has an upper limit beyond which an excessively coarse aerosol is produced. This effect can be mitigated by reducing the initial droplet size. The droplet initial velocity distribution is also relevant since the aerosol must navigate the upper airways where inertial impaction of particles is important (Cheng et al. 1999).

In a typical pMDI with a dose retention valve, atomization is achieved as illustrated in the lower left panel of Figure 1.1. As the valve stem is pushed up into the body of the valve, the orifice connecting the metering chamber to the bulk reservoir in the canister is closed off by a seal. Simultaneously the valve stem orifice is introduced into the metering chamber, thus providing the volatile formulation with a means of egress. As the solution or suspension passes through the valve stem orifice, the pressure drops and propellant begins to rapidly evaporate or flash due to its superheated state. The resulting multiphase fluid exits through the actuator orifice, undergoing a further pressure drop that results in additional flash evaporation of propellant, so that a fine spray is produced at the mouthpiece. This spray comprises approximately 10^8 droplets (Stein 2008b) with mass median diameter of roughly 10–20 μm (Clark 1992; Stein 2008a) traveling at an initial velocity of about 50 m/s (Clark 1991); the spray event lasts around 200–400 milliseconds (Hochrainer et al. 2005). Due to evaporation and spray plume deceleration, the diameter and velocity distributions evolve rapidly over short scales of length and time (Crosland et al. 2009; Finlay 2001b). Thus, in order to predict how pMDI sprays will interact with patients' airways, the state of the aerosol entering the mouth from this complex system must be approximated. This state is governed by the atomization process of the pMDI device itself.

1.3.3.2 The mechanisms of primary atomization in pMDIs

Investigations of the primary atomization process have relied on simplified theoretical descriptions coupled with numerical techniques and experimental methods (Finlay 2011). Clark conducted early investigations of both continuous and metered discharge of CFC and HFA propellants through twin-orifice systems representative of pMDI valve geometries (Clark 1991; Clark 1992). He developed a theoretical model of metered discharge to predict propellant mass flow rate, expansion chamber pressure, and expansion chamber vapor mass fraction. This model was compared with experimental measurements of expansion chamber conditions, with good agreement for geometries relevant to pMDIs. Further, he was able to use this model to correlate experimentally measured initial mass median droplet diameter of metered sprays with the peak vapor mass fraction and pressure in the expansion chamber:

$$MMD_0 = \frac{1.82}{d_{ec}^{0.46} \left(\frac{p_{ec} - p_{\infty}}{p_{\infty}} \right)^{0.56}} , \quad (1.12)$$

where MMD_0 is the initial droplet mass median diameter, q_{ec} is the vapor mass fraction in the expansion chamber, and p_{ec} and p_{∞} are the pressure in the expansion chamber and the ambient pressure, respectively. Based on the similarity of the form of Equation (1.12) to correlations developed in non-flashing effervescent atomizers, Clark hypothesized that the aerodynamic forces generated during expansion of the vapor phase external to the actuator orifice are the primary mechanism for atomization in pMDIs.

Dunbar and colleagues (Dunbar 1997; Dunbar and Miller 1997; Dunbar et al. 1997) developed a model similar to Clark's to describe the thermodynamic state of propellants within the valve and expansion chamber during metered discharge. They also numerically modelled the temporal and spatial evolution of droplet diameter and velocity distributions of the spray external to the actuator orifice, and utilized phase Doppler anemometry (PDA) to measure droplet diameter and velocity distributions of pMDI sprays. They obtained good agreement between measured and modelled spray characteristics only when a version of Clark's Equation (1.12) was used to specify the initial droplet diameter distribution in the model. However, based on photographic evidence of the spray issuing from an actuator orifice, Dunbar et al. (Dunbar et al. 1997) concluded that the droplets were fully formed upon exit and thus that flashing and bubble growth must have been the primary mode of atomization. Their visualization work also indicated periodic variation of spray density with frequency of approximately 700 Hz, and an observed downward inclination of the spray was hypothesized to be related to asymmetry of the flow field in the actuator orifice.

More extensive flow visualization work was conducted by Versteeg et al. (Versteeg and Hargrave 2002; Versteeg et al. 2006; Versteeg and Hargrave 2006) using transparent valve stem, expansion chamber, and actuator orifice models discharging HFA propellants with ethanol as co-solvent for the formulation. This body of work explored the multiphase flow inside the expansion chamber and actuator orifice, and provided general descriptions of the flow regimes. A central void composed predominantly of propellant vapor develops in the expansion chamber, and is surrounded by a swirling, bubbly two-phase flow. As the developing void travels through the actuator orifice, the flow appears to consist of a vapor-rich core surrounded by an annular, mostly liquid region near the wall. Photographs taken near the actuator orifice show a fine spray issuing, with some larger droplets generated at the edge of the spray cone, particularly during transients at the beginning and end of the spray event. Periodic variations in spray density and

cone angle of frequencies similar to those observed by Dunbar were also observed; these were postulated to be linked to fluctuations in the internal flow field. The authors concluded that not only is propellant flashing the predominant mechanism of atomization in pMDIs, but that the internal two-phase flow regime had a substantial impact on the characteristics of the external spray.

1.3.3.3 Experimental investigations of pMDI atomization

Phase Doppler anemometry (PDA) has been widely used for investigations of pMDI sprays, since the droplet diameter distribution, velocity distribution, and number concentration can be obtained simultaneously (Bayvel and Orzechowski 1993). When combined with a means of traversing the spray, PDA allows calculation of time and space averaged velocity and diameter distributions. However, the difficulty of obtaining near-orifice measurements, coupled with the rapid variation of droplet size due to evaporation, make determination of a true initial droplet size distribution challenging. Dunbar et al. (Dunbar et al. 1997) used PDA to characterize the temporal and spatial variation of CFC and HFA sprays from a pMDI valve. Of particular interest was the finding that droplet diameter increased toward the edge of the spray cone at a measurement station 25 mm downstream from the actuator orifice, perhaps reinforcing Versteeg's qualitative observation about the near-nozzle spray structure. Wigley et al. (Wigley et al. 2002) conducted PDA measurements at various radial locations closer to the actuator orifice (2.6 mm) on a pMDI containing HFA 227. Their results indicated a fully atomized spray existed at the measured locations. Both diameter and velocity distributions varied with time and radial location within the spray, with the Sauter mean diameter (defined in e.g. (Hinds 1999)) ranging from approximately 5-15 μm and axial velocity ranging from about 30 to 90 m/s. More recently, Liu et al. (Liu et al. 2012b) investigated plume centerline axial velocity and diameter distributions with a PDA technique for nine commercial pMDIs at 3 and 6 cm downstream of the mouthpiece. The velocity and droplet diameter distributions were observed to vary across the tested pMDIs, though no attempt was made to correlate droplet diameter or velocity parameters with formulation or device variables.

Other researchers of pMDI atomization have obtained meaningful results using the relatively simple technique of dissolving a non-volatile component in propellant, and measuring the residual particle size distribution to infer information about the initial droplet size distribution. Since the concentration of non-volatiles at the actuator orifice may be difficult to

specify precisely due to internal flashing in the valve and expansion chamber (Clark 1991), Ivey et al. (Ivey et al. 2014) used the measured residual mass median aerodynamic diameter, $MMAD_r$, to predict the mass median content equivalent diameter, $d_{c,50}$, corresponding to the formulated concentration of non-volatiles c_{nv} :

$$d_{c,50} \cong \sqrt[3]{\frac{\rho^*}{c_{nv}}} \sqrt[6]{\frac{\rho^*}{\rho_p}} MMAD_r \quad (1.13)$$

Here ρ^* is a reference density (1000 kg/m³ by convention) and ρ_p is the particle density. (Ivey et al. 2014) defined the content equivalent diameter as the diameter of a solution droplet, with concentration c_{nv} , that contains a mass of non-volatile components equal to the dry particle mass. They utilized a large set of cascade impaction data and dimensional analysis to relate the content equivalent diameter distribution to properties of the propellant itself. The resulting correlation was valid for either propellant 134a or 227ea, with varying co-solvent content, and provided accurate predictions of published data from the literature. The value of $MMAD_r$ may be determined by cascade impaction, a time of flight instrument, or any other suitable technique, and will of course depend on whether any classification of the aerosol occurs prior to the sizing instrument (a common example being use of a model throat upstream of a cascade impactor). The particle density ρ_p is often not accurately known (DeCarlo et al. 2004), but a reasonable estimate is sufficient due to the sixth-root dependence. Equation (1.13) additionally assumes spherical residual particles and neglects corrections for non-continuum behavior, both of which are justified for the residual particles emitted by pMDIs (Grainger et al. 2012; Hinds 1999; Mitchell et al. 2003a).

Researchers working with solution formulations have utilized the residual particle sizing technique to explore the dependence of the content equivalent diameter distribution on formulation and device variables. Building on earlier studies (Brambilla et al. 1999; Lewis et al. 2004; Meakin et al. 2000), Lewis and colleagues investigated the dependence of the content equivalent diameter distribution on propellant type, actuator orifice diameter and geometry, and valve metered volume using an Andersen cascade impactor equipped with a USP/Ph.Eur. induction port (Lewis 2013). They observed that the content equivalent diameter is fairly insensitive to device variables, and that choice of propellant dominates the other factors. Essentially they concluded that the $d_{c,50}$ is relatively constant for a given propellant. Stein and Myrdal investigated the mass median content equivalent diameter's dependence on propellant

type, co-solvent concentration, valve metered volume, and actuator orifice diameter, and gave correlations for experiments conducted with and without a USP/Ph.Eur. induction port (Stein and Myrdal 2004). They discerned small but statistically significant effects from co-solvent concentration, actuator orifice diameter, and valve metered volume. Their correlations gave accurate predictions of data from the literature. Selected correlations developed using the residual particle sizing technique are summarized in Table 1.1. To fully describe the content equivalent diameter distribution, the observed range of GSD is included as well if reported. It should be noted that while some of the above referenced works aimed to measure the initial droplet diameter distribution, or the initial diameter distribution of the droplets passing through a model throat, Ivey et al. (Ivey et al. 2014) pointed out that the content equivalent diameter calculated at the formulated non-volatile concentration may differ from the initial droplet diameter in pMDIs due to propellant evaporation in the valve expansion chamber and consequent enrichment of non-volatiles prior to droplet formation. In scenarios where the residual aerodynamic diameter distribution is the primary distribution of interest, such as cascade impaction testing, the content equivalent diameter distribution may be more meaningful and readily measurable than the initial droplet diameter distribution.

Table 1.1: Summary of correlations for the mass median content equivalent diameter developed using aerodynamic sizing of residual particles from solution pMDIs. ^a: Symbols used in correlations: Y_e : mass fraction of co-solvent ethanol; d_{ao} : actuator orifice diameter; σ_{pa} : propellant surface tension in air; p_{mc} : metering chamber pressure.

Correlation ^a	Validity; units	Reference
$d_{c,50} = 10.7$	pMDI containing propellant 134a with 2-15% w/w ethanol sized after passing through a USP/Ph.Eur. induction port at 28.3 standard L/min gas flow rate; $d_{c,50}$ in μm	(Lewis 2013)
$d_{c,50} = 14.7$	pMDI containing propellant 227ea with 13-15% w/w ethanol sized after passing through a USP/Ph.Eur. induction port at 28.3 standard L/min gas flow rate; $d_{c,50}$ in μm	(Lewis 2013)
$d_{c,50} = 6.90 + 0.0441V_{mc} + 23.6Y_e - 63.8Y_e^2 + 24.7Y_e d_{ao} - 0.129Y_e V_{mc}$ $1.61 \leq GSD \leq 2.04$	pMDI containing propellant 134a with 0-20 % ethanol sized after passing through a USP/Ph.Eur. induction port at 28.3 standard L/min gas flow rate; $d_{c,50}$ in μm , V_{mc} in μL , d_{ao} in mm	(Stein and Myrdal 2004)

Correlation ^a	Validity; units	Reference
$d_{c,50} = 11.0 - 7.80Y_e - 20.0d_{ao} + 67.6Y_e^2 + 26.5d_{ao}^2 + 39.8Y_e d_{ao}$ $1.54 \leq GSD \leq 1.76$	pMDI containing propellant 134a with 0-20 % ethanol sized after passing through a large-volume evaporation chamber at 28.3 L/min gas flow rate. Actuators were modified to minimize mouthpiece deposition; $d_{c,50}$ in μm , V_{mc} in μL , d_{ao} in mm	(Stein and Myrdal 2004)
$d_{c,50} = \frac{416\sigma_{pa}}{p_{mc}}$ $1.8 \leq GSD \leq 3.1$	pMDI with either propellant 134a or 227ea, 0-15% ethanol, sized after passing through a USP/Ph.Eur. induction port at 28.3 standard L/min gas flow rate; $d_{c,50}$ in m, σ_{pa} in N/m, p_{mc} in Pa.	(Ivey et al. 2014)

1.3.4 Aerosol evolution and deposition

1.3.4.1 Deposition from pMDI aerosols

Deposition in the human lung may occur by diffusion, settling, and inertial impaction, and all of these mechanisms are dependent on particle size (Crosland et al. 2009). The probability of impaction also depends on the velocity of the particle in question, and is related to the particle stopping distance S (Clark 1996; Hinds 1999):

$$S = \frac{\rho_p U_0 d_p^2 C_c}{18\mu} \quad (1.14)$$

where U_0 is the initial particle velocity, ρ_p and d_p are the particle density and volume equivalent diameter, respectively, C_c is the slip correction factor evaluated at d_p , and μ is the dynamic viscosity of the gas phase. pMDIs are distinct from many other pulmonary delivery devices in that they produce an aerosol that initially has a significant velocity relative the surrounding gas phase (Nikander 2010). This peculiarity of delivery from pMDIs must be taken into consideration when evaluating extrathoracic deposition, whereas it may be justifiable to assume that downstream of the throat, the aerosol has decelerated to a velocity close to that of the gas phase (Buchmann et al. 2014). Once past the throat, the extensive body of literature on the topic of aerosol deposition in the human lung pertains—see recent reviews by Cheng (Cheng 2014) and Darquenne (Darquenne 2012)—with the aerodynamic diameter distribution and inspiratory flow rate largely determining deposition.

The rate of droplet evaporation also plays a role in deposition, as it is related to the temporal and spatial evolution of the droplet diameter distribution (Finlay 2001b; Fuchs 1959).

This is of particular importance if a co-solvent such as ethanol is included in the formulation, as the less volatile co-solvent will slow down the evaporation process, which has been observed to affect throat deposition and thus delivery efficiency in *in vitro* tests (Lewis et al. 2004). An additional complication arises if the ambient air is somewhat humid: residual particles from pMDI sprays are expected to be quite cold due to evaporative cooling (Brambilla et al. 2011) and thus could become nuclei for the condensation of water vapor (Martin and Finlay 2005). These pMDI-specific issues, as well as other factors pertinent to deposition, are discussed in greater detail below in the context of formulation, device, and environmental variables.

1.3.4.2 The effect of formulation variables

Since the content equivalent diameter distribution is related to the aerodynamic diameter distribution of the residual particles emitted from a pMDI, formulation variables affecting the initial droplet size will play a role in determining aerosol deposition. Thus, as discussed in Section 1.3.3.3, the vapor pressure, surface tension, and co-solvent concentration are expected to have an effect on deposition by virtue of their effect on the initial droplet diameter distribution. Also, the amount of solids dissolved or suspended in the propellant will play a role in determining the final residual particle size distribution and thus will affect deposition. The relationship between the MMAD and the mass median content equivalent diameter is straightforward for solution formulations, and is obtained by simple rearrangement of Equation (1.13):

$$MMAD_r \cong \sqrt[3]{\frac{c_{nv}}{\rho^*}} \sqrt[6]{\frac{\rho_p}{\rho^*}} d_{c,50} \quad (1.15)$$

Thus, empirical correlations for the median content equivalent diameter such as those discussed earlier (Brambilla et al. 1999; Ivey et al. 2014; Lewis et al. 2004; Lewis 2013; Meakin et al. 2000; Stein and Myrdal 2004) have been used with a good degree of success to predict changes in residual aerodynamic diameter distribution in response to formulation changes (Lewis et al. 2014; Saleem and Smyth 2013). In the case of suspensions, such a straightforward relationship does not exist since suspensions are heterogeneous at the length scale of the propellant droplets. Rather, a single propellant droplet may contain zero, one, or more particles of the dispersed phase, depending on the size distributions of the propellant droplets and the suspended particles

as well as the suspension concentration. While some researchers have had success utilizing stochastic modeling techniques to accurately predict residual aerodynamic diameter distributions from suspension formulations (Callingham 1980; Ivey and Vehring 2010; Sheth et al. 2013; Stein et al. 2012), the MMAD of the residual aerosol depends nonlinearly on the model inputs (initial droplet diameter distribution, suspended phase diameter distribution, and suspension concentration). Sheth et al. used multiple linear regression to fit an empirical model which predicts the residual MMAD for the case of an excipient-free suspension formulation in propellant 134a (Sheth et al. 2015).

The composition of the solution or suspension may influence deposition in other ways. Using *in vitro* testing, Clark found that the inclusion of surfactants resulted in reduced delivery efficiency, and attributed this finding to a reduced evaporation rate of atomized droplets and consequent increased inertial losses in a throat model (Clark 1991). The inclusion of ethanol as a co-solvent not only affects content equivalent diameter distribution, but also decreases the rate of evaporation of droplets. While incorporation of up to 15% w/w ethanol is expected to have only a modest effect on the mass median content equivalent diameter (Stein and Myrdal 2004), several *in vitro* studies, which altogether spanned a range of ethanol concentration from 2 to 40% w/w, reported a substantial increase in throat deposition and a resultant reduction in fine particle fraction as ethanol content is increased (Gupta et al. 2003; Lewis et al. 2004; Sheth et al. 2014; Zhu et al. 2014a; Zhu et al. 2014b). Haynes et al. (Haynes et al. 2004) measured particle size distributions from pMDIs containing 15% w/w ethanol and varying levels of propylene glycol using a USP/Ph.Eur. induction port throat equipped with heated extension sections. They employed a light scattering particle sizing technique immediately downstream of the throat. They found that the mass median particle diameter decreased as longer throat extensions were utilized, and that heating the extensions further reduced the mass median particle diameter. Since the initial droplet size distribution was not varied in these experiments, the implication is that the aerosol was not fully evaporated after traversing the USP/Ph.Eur. induction port and extension. Stein and Myrdal (Stein and Myrdal 2006) utilized a simple single droplet evaporation model to predict that a pure ethanol droplet takes approximately seven times longer to evaporate than an HFA droplet of the same initial diameter. They also demonstrated with *in vitro* tests using a variety of co-solvents that fine particle fraction depended not only on the initial droplet diameter distribution, but the evaporation rate as well. They hypothesized that this

outcome was caused by increased deposition in the actuator and USP/Ph.Eur. induction port in the case of the less volatile aerosols, which were still undergoing evaporation. Thus, it is fair to conclude based on theory and experimental evidence that inclusion of ethanol in a pMDI formulation will significantly reduce the droplet evaporation rate, resulting in increased throat deposition. As discussed in the atomization section, it should be noted that inclusion of a co-solvent will also affect the content equivalent diameter distribution, with the general effect being a coarser spray which will further reduce lung delivery efficiency.

1.3.4.3 The effect of device variables

The actuator orifice diameter and the valve metered volume may influence the aerosol transport from the inhaler and the subsequent deposition profile. The actuator orifice diameter has been shown to be inversely related to fine particle fraction in cascade impaction tests (Lewis et al. 2006), presumably due to the increase in plume momentum as orifice diameters are increased (Clark 1991; Gabrio et al. 1999), resulting in increased inertial impaction in the mouthpiece and throat. However, reduction in actuator orifice diameter has limitations: the probability of clogging is greater (Ganderton et al. 2002). Further, since spray duration increases with smaller actuator orifices (Lewis et al. 2006), at some point a patient may have difficulty coordinating inhalation with actuation or be unable to inhale an entire dose (McFadden 1995). The valve metered volume has been demonstrated to have an effect on fine particle fraction in *in vitro* tests, with increasing metered volume resulting in decreased fine particle fraction (Dunbar and Hickey 1998; Lewis et al. 2004; Stein et al. 2014). It has been suggested that this is due to a dependence of the droplet evaporation rate on the metered volume, with a larger release of propellant requiring more heat from the surrounding air to fully evaporate (Newman et al. 1982). Improved valve designs and the use of add-on devices such as spacers and valved holding chambers may help to mitigate some of these limitations of pMDI devices (Stein et al. 2014).

1.3.4.4 Other factors

The environment in which a pMDI is stored or used may impact drug deposition and delivery efficiency. The vapor pressures of pMDI propellants depend strongly on temperature, and *in vitro* experiments with heated and chilled inhalers have shown that inhaler temperature does indeed have an effect on the delivery efficiency and the aerodynamic diameter distribution of the residual particles (Haynes et al. 2004; Morin et al. 2014; Stein and Cocks 2013; Wilson et

al. 1991), with increasing temperature leading to more efficient delivery and a finer residual particle size for both solution and suspension formulations. These trends are not unexpected in light of the vapor pressure dependence of the content equivalent diameter distribution discussed earlier.

The temperature, relative humidity, and flow rate of the ambient air during pMDI actuation also play a role in deposition. The air temperature is expected to alter the droplet evaporation rate and thus mouth-throat deposition, though to our knowledge this effect has only been studied independently of the inhaler temperature by Morin et al. (Morin et al. 2014). They demonstrated with *in vitro* tests on commercially available pMDIs that the delivery efficiency of some formulations decreased as the dry air temperature was reduced to 0 and -10 °C, while other formulations were relatively unaffected. While a definitive causative mechanism was not conclusively identified, they speculated that the loss of *in vitro* lung dose for certain inhalers was attributable to increased mouthpiece or throat deposition caused by a reduced propellant evaporation rate relative to standard laboratory conditions.

Ambient humidity has been demonstrated to influence deposition and delivery as well. This was systematically explored by Lange and Finlay (Lange and Finlay 2000) in *in vitro* tests of a suspension pMDI used in conjunction with open tube spacer devices and an endotracheal tube to simulate mechanically ventilated patients. They found that the fraction of the aerosol passing through the spacer and endotracheal tube was inversely related to the mole fraction of water vapor in the air, and that this effect was mitigated by incorporation of a large volume evaporation chamber upstream of the endotracheal tube. Further investigations by Martin and co-workers established that humidity does not significantly affect the evaporation rate of droplets of pure HFA 227ea or HFA 227ea – ethanol mixtures (Martin et al. 2005), but rather that condensational growth of residual aerosol from pMDIs increased deposition in a valved holding chamber as well as MMAD as measured with cascade impaction (Martin and Finlay 2005). There was evidence that the condensational growth was followed by evaporation of the condensed water as the aerosol progressed toward equilibrium with the water vapor content of the surrounding air flow. The process hypothesized is illustrated in Figure 1.4, and as reported by Shemirani et al. (Shemirani et al. 2013) is likely to depend on the choice of propellant and formulation (solution or suspension) as well as the temperature, humidity, and flow rate of the gas phase.

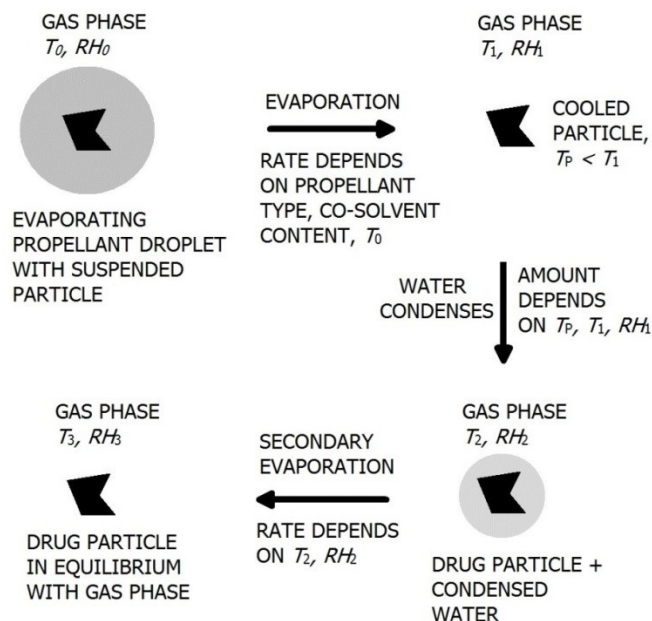


Figure 1.4: Illustration of a hypothesized process by which evaporation of a propellant droplet containing a suspended drug particle is followed by water condensation and secondary evaporation. The formulation and environmental variables expected to affect each step are indicated.

The volumetric flow rate of gas drawn through the inhaler is expected to influence deposition as well. Assuming that the aerosol has decelerated and has the same velocity as the surrounding gas, Equation (1.14) suggests that increasing gas flow rate (and thus particle velocity) should result in an increased stopping distance and thus a greater probability of impaction if the aerosol travels a curved flow path (such as a mouth-throat model). Thus it is somewhat surprising that several studies have shown that increasing the gas flow rate used in *in vitro* tests can result in decreased deposition in mouth-throat models (Hoe et al. 2009; Rahmatalla et al. 2002; Shrubbs 1998; Stein and Gabrio 2000). This suggests that inertial impaction may not be the sole mechanism of deposition in mouth-throat models. Several researchers have pointed out the role of turbulence in deposition (Longest and Hindle 2009; Rahmatalla et al. 2002; Stein and Gabrio 2000), though further investigation in the context of pMDIs is merited. It therefore appears that delivery efficiency may depend on inspiratory flow rate in a complicated way, with implications for lung dose reproducibility in a patient's hands.

1.3.5 Conclusions

In reviewing the relevant literature, it is apparent that solid progress has been made in understanding how pMDIs work. While the development of a new pMDI product will always have unique challenges specific to the target product profile, product developers have access to a broad knowledge base to make the job easier. A variety of formulation strategies and device designs are now available to ensure robust and reproducible dosing, even for challenging formulations. Predictive equations which account for the influence of the formulation and device variables are available for both the initial droplet diameter and residual aerodynamic diameter distributions for solution formulations, and have been used to streamline formulation development and device selection. Progress has been made to extend these methods to suspension formulations, with current results providing a trend-wise understanding of the influence of the formulation and device variables on the residual aerodynamic diameter distribution. In the context of drug deposition, the effects of formulation, device, and environmental variables on delivery efficiency have been studied and quantified.

It is also apparent that some gaps in knowledge still exist. The primary atomization event in pMDIs has been studied, the flow regime has been qualitatively described, and correlations for droplet diameter and velocity exist. Based on the reviewed work, it seems the content equivalent diameter distribution is most strongly affected by propellant composition and valve geometry. Thus to create finer sprays and increase the maximum feasible dose for pMDIs, fundamental modifications to formulations or devices will be necessary. For example, Kelkar and Dalby obtained substantially reduced median droplet diameters by dissolving CO₂ in HFA propellants (Kelkar and Dalby 2014), suggesting that this is an area where further investigation is merited. The high velocity, rapidly evaporating multiphase jet produced by pMDIs has been shown in *in vitro* experiments to interact in complicated ways with the inspiratory gas flow, with implications for drug deposition. A better understanding of these interactions could prove useful in developing pMDIs that are more robust to variations in patient technique and environmental conditions.

1.3.6 Expert opinion

Given the abundance of information available on the topic, scientists working with pMDIs have some excellent tools available to assist in product development. However, barring

some notable exceptions, much of the know-how has been developed empirically, while the underlying physical mechanisms remain poorly understood. As a result, extremely accurate predictions of pMDI performance (for example, prediction of *in vitro* metrics such as MMAD and FPF for a solution formulation) are possible, so long as the formulation and device variables are within the ranges used to develop the predictive equations. This approach works very well for product development that relies on existing device and formulation technology but may break down when circumstances require an outside-the-box solution. It is thus no coincidence that much of the best fundamental research into pMDI performance occurred during the transition from CFC to HFA propellants. If we are to keep pushing the envelope of pMDI performance, it makes sense to invest in additional fundamental investigations.

For example, fundamental research on atomization in pMDIs has the potential to expand the dose range of the device. Currently, the high end of the dose range for pMDIs is on the order of 1 milligram, and is limited to a large extent by the feasible drug concentration: as more drug is dissolved or suspended, the residual particle size increases. At some point the pMDI will have an unacceptably high extrathoracic deposition. However, even a small reduction in the median initial droplet diameter distribution could result in a substantial increase in the maximum deliverable dose. This can be seen in Figure 1.3, where reducing the initial droplet size would also reduce the residual MMAD and effectively shift the curves downward. Therefore, a deeper understanding of the atomization process could lead to finer sprays and an expanded dose range, with the potential to open up new areas of therapy. Also, to enable more robust products, further research is needed into how pMDI aerosols evolve and deposit in the human airways. *In vitro* testing indicates that pMDI performance is strongly tied to the device temperature, and to some extent to ambient temperature, ambient humidity, and inspiratory flow rate. However, these effects and their interactions have yet to be fully explored, and it is currently unclear why some commercial pMDIs maintain adequate performance over a wide range of environmental conditions while others do not. Answering this question should result in more robust future products, but additional experimental and theoretical work is required to do so. As computing power continues to increase, it is likely that computational multiphase fluid dynamics simulations involving coupled heat and mass transfer modeling will play an increasingly prominent role in addressing these questions.

Given its long history, low price, portability, robustness, and versatility, it is likely that the pMDI will continue to play a major role in inhalation therapy in the coming decades. As device and formulation technologies continue to evolve, pMDIs will thus be utilized in a wider range of indications, including systemic delivery and biologics. Research on the use of engineered particles in pMDIs is of particular interest, as it may offer a means of stabilizing labile biological molecules, vaccines, or phages in the presence of HFA propellants. Deepening our understanding of the physical mechanisms involved in drug delivery from pMDIs will prove especially worthwhile as we expand the frontiers of what is possible with this fascinating and useful device.

1.4 Introduction to spray drying for inhaled drug delivery

Spray drying is a widely used process to convert solutions, suspensions, emulsions, slurries, or other complex liquids into dried powders. The basic components of a spray drying process are illustrated in Figure 1.5. A liquid feedstock is converted into a fine spray by an atomizer at one end of a drying chamber, where it is mixed with heated drying gas. The volatile fraction of the feedstock evaporates rapidly due to the large surface area, producing an aerosol of dried powder which is then separated from the gas using a cyclone (as in Figure 1.5) or other means of filtration. Spray drying is a popular drying technique in many industries due to its economy, scalability, the potential for continuous operation, and the ability to fine tune the physical properties of the dry product by manipulating the composition of the feedstock and the process parameters. A brief discussion of spray drying hardware follows, with emphasis on the configurations most commonly used for the production of pharmaceutical powders in the respirable size range.

The choice of the atomization equipment is an important consideration for many applications since the particle size distribution of the dried material is directly related to the size distribution and composition of the atomized spray from which it formed. For the simple case of a solution droplet with diameter d_0 and concentration c_s which dries completely to form a particle with density ρ_p , the dry particle diameter is

$$d_v = \sqrt[3]{\frac{c_s}{\rho_p}} d_0 \quad . \quad (1.16)$$

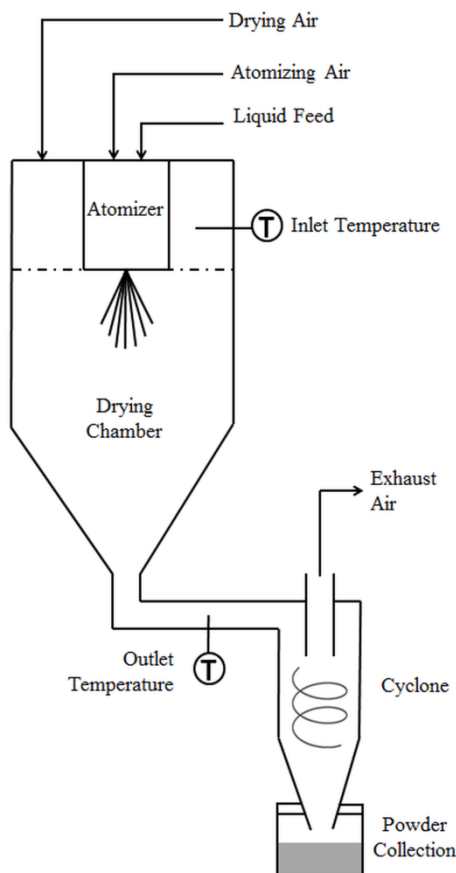


Figure 1.5: The major components of a spray drying process.

Equation (1.16) indicates that for solution feedstocks the primary means of manipulating the dry particle size distribution is altering the atomized droplet diameter distribution, with the solids content and particle density having secondary effects. To produce particles in the respirable size range, atomized droplets in the range of approximately 5–25 μm are required. Twin fluid atomizers are a popular choice for spray drying of respirable particles, since for typical spray solvents they produce a fine spray with the mean droplet diameter adjustable in the required range (Bayvel and Orzechowski 1993). They work by producing a high velocity jet of gas which interacts with the liquid jet, resulting in atomization of the liquid under aerodynamic forces. The droplet diameter distribution produced by a twin fluid atomizer depends on the geometry of the atomizer, the physical properties of the gas and the liquid, the velocity of the gas relative to the liquid, and the air—liquid mass ratio (*ALR*). Droplet size correlations are often developed in

terms of ALR , Weber number, We_g , and Ohnesorge number, Oh , taking the form (Lefebvre 2011)

$$\frac{\bar{d}_0}{d_1} = \left(\frac{a}{We_g^{0.5}} + b \cdot Oh \right) \left(1 + \frac{1}{ALR} \right)^c, \quad (1.17)$$

with

$$We_G = \frac{\rho_g v_{rel}^2 d_1}{\sigma_{lg}} \quad \text{and} \quad Oh = \frac{\mu_l}{\sqrt{\rho_l d_1 \sigma_{lg}}}. \quad (1.18)$$

Here \bar{d}_0 is a median diameter of the droplet distribution, d_1 is the diameter of the liquid orifice, ρ_l and ρ_g are the liquid and gas densities, σ_{lg} and μ_l are the liquid surface tension and dynamic viscosity, v_{rel} is the relative velocity between the gas and the liquid, and a , b , and c are empirically determined constants. Thus for constant atomizer geometry, liquid properties, and gas properties the median diameter is readily adjustable by increasing or decreasing the amount of atomizing gas. For a given atomizer design, manufacturers may provide curves of \bar{d}_0 vs. ALR for common solvents; otherwise these curves can be determined experimentally, allowing estimation of the dry particle size distribution using Equation (1.16).

The drying chamber of a spray dryer must be sufficiently large to allow the atomized droplets to decelerate without hitting the chamber walls, and to provide adequate residence time for the droplets to evaporate prior to separation. Drying processes can be configured in a co-current mode, where the spray and the drying gas are introduced at the same end of the dryer, or in a counter-current mode, where the drying gas enters at one end (usually the top of a vertically oriented drying chamber) and the spray is introduced at the other end. The counter-current configuration allows more residence time, which may be useful for processes requiring large initial droplet diameters. Since relatively fine sprays are used to produce respirable particles, drying processes are usually configured in a co-current mode, and a fairly small drying chamber is often adequate even at pilot or production scale. As droplet and particle settling velocities are quite low in these cases, the drying chamber may be oriented horizontally or vertically as needed depending on facility space requirements.

Gas cyclones are a popular choice for powder separation in pharmaceutical spray drying due to their sanitary design; unlike porous filter elements, they can be operated for prolonged periods without requiring back-pulsing or change-out, and do not pose a risk of contamination by filtration media. Cyclones separate the dispersed phase of an aerosol from the gas by creating a highly swirling flow field which creates a centrifugal force on the particles. Particles with a large enough Stokes number are driven towards the wall of the cyclone, where they are

transported toward a collection vessel; those with smaller Stokes numbers are not separated, and will exit with the exhaust gas in the overhead fraction. Cyclones do not have a perfectly sharp filtration function; rather the separation efficiency for a given cyclone geometry is a function of the aerodynamic diameter and the gas flow rate, and is described by a grade efficiency curve (GEC), an example of which is presented in Figure 1.6 for demonstration purposes. For a given gas flow rate, the cyclone separation performance can thus be quantified by its cut size x_{50} , defined as the particle aerodynamic diameter which is separated with 50% efficiency (Hoffman and Stein 2008). To maximize product yield, the cyclone cut size x_{50} should be substantially smaller than the particles to be collected. For the collection of particles in the respirable size range, cyclones with $x_{50} < 1 \mu\text{m}$ are usually required.

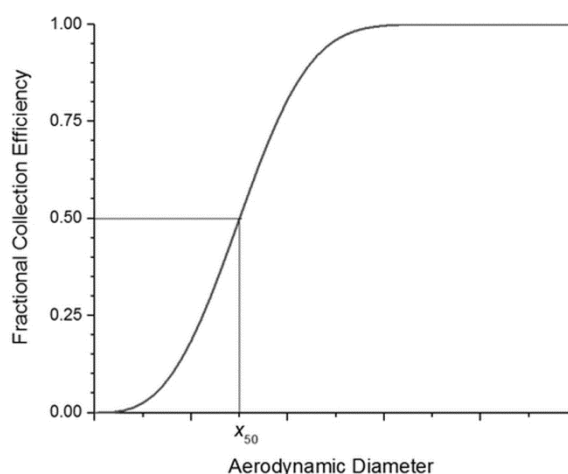


Figure 1.6: An example GEC. The GEC and cut size x_{50} depend on the cyclone geometry and the gas flow rate.

Due to the versatility of the process, spray drying has been used in the pharmaceutical industry in a wide variety of applications. In the production of solid dosage forms for oral administration, spray drying has proven useful in the preparation of powders for direct tablet compression (Gonnissen et al. 2007) and bioavailability enhancement of low solubility drugs (Davis 2018; Paudel et al. 2013), and shows promise as a technique enabling drug encapsulation for stability enhancement (Truong-Le et al. 2015) or modification of the drug release profile (Walz et al. 2017). Spray drying has also been used to successfully dry and stabilize biological macromolecules (Chang et al. 2017; LeClair et al. 2016; Saboo et al. 2016), and as a technique

for preparation of nasally delivered small molecule drugs and biologics (Kulkarni et al. 2016; Scherließ et al. 2015).

Since spray drying offers a great deal of control over the particle size distribution, composition, and morphology of the dried product, it is particularly well suited to the production of powders for pulmonary drug delivery (Chow et al. 2007). Spray dried drug particles and carrier particles with physical properties that are optimized for the application—engineered particles—can provide advantages in performance compared to conventional micronized particles in DPIs (Duddu et al. 2002; Feng et al. 2011; Lechuga-Ballesteros et al. 2008; Littringer et al. 2012) and suspension pMDIs (Tarara et al. 2004; Vehring et al. 2012). However, such approaches come with added complexity, and optimizing the particle properties for the intended application may require substantial formulation and process development. The discipline of particle engineering is helpful in this context, as it offers a methodology for quantifying relationships between the formulation variables, the process parameters, and the physical properties of the spray dried powders. These methods are readily extended to the study of solution pMDIs as well given the similarities of the particle formation processes involved. As inhalation devices and formulations will inevitably become more technically complex, continued theoretical and experimental investigations into the mechanisms of particle formation will prove worthwhile in ensuring that the development of the next generation of inhaled drug products proceeds on a rational basis. I hope the work that follows will contribute to that goal.

Chapter 2 : Models for Predicting the Aerodynamic Particle Size Distribution of pMDIs

2.1 Introduction

Given the importance of the aerodynamic diameter distribution in the context of pulmonary drug delivery, and the large presence of the pMDI in that space, it is no surprise that a substantial amount of research on pMDIs has focused on quantifying the relationships between the formulation, the device, and the properties of the aerosol produced upon actuation. The ability to make accurate predictions of product performance is often invaluable during product development; this is the domain of modeling. Models which incorporate available mechanistic understanding may outperform purely empirical models, particularly during the development of innovative products where the properties of the formulation or the device components may differ radically from those of conventional inhalers. In this chapter, modeling techniques are presented for predicting the aerodynamic particle size distribution from both solution and suspension pMDIs. Where possible, engineering principles and mechanistic understanding have been utilized, and model results have been quantified in terms of easily applied equations to enable utilization by scientists in academia and industry.

Sections 2.2 and 2.3 are presented without alteration of the peer-reviewed texts³, save that manuscript headers, equations, tables, and figures, and the references thereto, have been renumbered for internal consistency within this document. My contributions to these works are explicitly described in the Preface. Section 2.3 is quite brief; this was necessary to comply with submission guidelines. A more detailed description of the methods and some additional results are presented as Appendix A1.

³ Section 2.2 consists of a published research article:

Ivey, J. W., Lewis, D., Church, T., Finlay, W. H. and Vehring, R. (2014). A correlation equation for the mass median aerodynamic diameter of the aerosol emitted by solution metered dose inhalers. *International Journal of Pharmaceutics* 465:18-24.

Section 2.3 consists of peer-reviewed conference proceedings:

Ivey, J. W. and Vehring, R. (2018). An *in-silico* investigation of formulation and device effects on the aerodynamic particle size distributions of suspension pressurized metered dose inhalers. in *Respiratory Drug Delivery*, R. N. Dalby, et al. ed., In Press. VCU Richmond, VA.

2.2 A correlation equation for the mass median aerodynamic diameter of the aerosol emitted by solution metered dose inhalers

2.2.1 Introduction

In spite of its age, the pressurized, metered-dose inhaler (MDI) remains the most popular delivery device for local delivery of drugs to treat respiratory disease. Modern MDI formulations are either suspensions or solutions of drugs and excipients in propellants HFA 134a or 227ea. In cases where the drug has some solubility in the propellant, it is generally preferable to dissolve the drug in the propellant to avoid physical instability (Byron 1990) or colloidal instability (Brindley 1999). However, inclusion of a co-solvent is often required to attain sufficient solubility to meet dose targets; ethanol is the most common choice for this purpose (Bell and Newman 2007; Gupta et al. 2003). General descriptions of the design and principle of operation of the MDI can be found in the literature (da Rocha et al. 2011; Lewis 2007; Newman 2005; Smyth 2003). Figure 2.1 presents simplified cross-sectional views of an MDI valve prior to and during dose actuation; some key features of the valve are labeled.

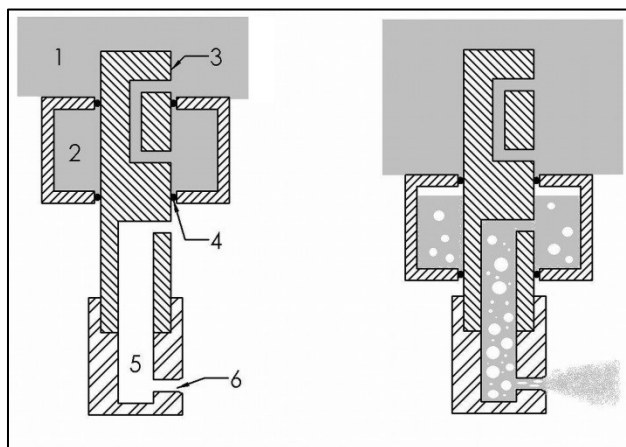


Figure 2.1: Simplified cross-sectional views of an MDI valve prior to actuation (left) and during actuation (right). 1: bulk solution; 2: metering chamber; 3: valve stem; 4: seals; 5: expansion chamber, sometimes referred to as the actuator sump; 6: actuator orifice.

A factor of critical importance to the efficacy of solution MDIs is the aerodynamic diameter distribution of the drug particles emitted from the device, as a sufficiently fine aerosol must be administered to the patient for efficient lung delivery. It is the aerosol's aerodynamic diameter distribution in combination with its momentum distribution which determines the deposition in the lung (Finlay 2001b). Extensive research has been conducted on the effect of

particle size on regional and total deposition in the human lung (Darquenne 2012; Heyder et al. 1986; Stahlhofen et al. 1989); as a result of this research, MDIs are typically formulated such that most of the drug delivered is in the range of 0.5 – 5 μm aerodynamic diameter (Pilcer and Amighi 2010).

The final dry particle aerodynamic diameter distribution produced by an MDI is related to the propellant droplet diameter distribution. Therefore it is helpful to consider the atomization mechanisms responsible for droplet formation. The physics involved in converting the bulk solution or suspension into a fine spray in metered dose inhalers are complex. The flow regime is turbulent, the composition is multiphase, the temporal behavior is unsteady and transient, and the entire process takes place in three spatial dimensions (Finlay 2001). Given the great complexity of the problem, analytical determination of the droplet size distribution in an MDI spray is not currently feasible; therefore, researchers have relied on numerical and empirical methods to study the problem. Clark (Clark 1991; Clark 1992) conducted theoretical and experimental investigations into the atomization process from metered dose inhalers containing CFC (chlorofluorocarbon) and HFA propellants, and developed an empirical correlation for the median atomized droplet diameter produced at the actuator orifice for both continuous and metered valve operation. The droplet size was found to depend on the pressure and the vapor quality of the two-phase mixture in the expansion chamber⁴:

$$d_{d,50} = \frac{1.82}{q_{ec}^{0.46} \left(\frac{p_{ec} - p_{\infty}}{p_{\infty}} \right)^{0.56}} \quad (2.1)$$

where $d_{d,50}$ is the droplet mass median diameter, q_{ec} is the vapor quality (the mass fraction of vapor) of the propellant vapor-liquid mixture in the expansion chamber, p_{ec} is the pressure in the expansion chamber, and p_{∞} is the ambient pressure external to the nozzle. The utility of this correlation is limited because the pressure and quality in the expansion chamber are not typically known *a priori* for a given MDI formulation, though in his thesis Clark suggests that the pressure dependence of this relationship should also hold if the pressure in the metering chamber is used instead of that in the expansion chamber, due to the approximate proportionality between the

⁴ Due to an oversight on my part, and a typographical error in Clark's thesis, an incorrect version of this equation made it into the journal article. I have corrected it here to avoid further confusion, using the version developed by Clark for metered discharges. The correct relationship is also presented in the Introduction as Equation (1.12).

two. Since the pressure in the metering chamber can be determined theoretically based on the choice of propellant and the amount and type of co-solvent, Equation (2.1) predicts a decrease in median droplet diameter as the pressure in the metering chamber is increased. Clark concluded, based on the similarity of his droplet diameter correlation to those developed in study of air-blast atomizers, that the atomization mechanism in MDIs was primarily aerodynamic breakup of the liquid phase by the vapor phase. Dunbar et al. conducted numerical (Dunbar and Miller 1997) and experimental (Dunbar et al. 1997) studies on MDI sprays; Clark's correlation for the droplet size was utilized by Dunbar's numerical model, which gave good agreement with experimental results for droplet size and velocity in the near-nozzle region. However, these researchers concluded, based on flow visualization experiments, that internal flash-boiling, not aerodynamic breakup, was the primary atomization mechanism. A more detailed flow visualization study was performed by Versteeg et al. (Versteeg et al. 2006) utilizing transparent model actuator components, allowing observation of the internal flow in the expansion chamber and nozzle in addition to the external spray. Based on the observations of the internal flow in the model nozzle and the characteristics of the spray issued from the nozzle, they concluded that for the majority of the duration of the metered spray event, flash-boiling was the dominant mechanism of droplet formation.

Despite differing opinions on the underlying mechanism of atomization in MDIs, researchers of solution MDIs have had considerable success employing empirical models to aid in formulation challenges (Lewis et al. 2014). A common technique in some of these studies (Lewis et al. 2004; Stein et al. 2005) is to measure the residual aerodynamic diameter distribution directly and then use this information to infer what has been termed an initial droplet size distribution (Stein and Myrdal 2004) based on mass balance considerations and the definition of the aerodynamic diameter. Since a significant portion of the propellant vaporizes prior to reaching the actuator orifice, neither the initial concentration nor the initial droplet diameter can be determined precisely. In this paper we introduce the concept of the content equivalent diameter to formalize what is being measured by such techniques.

2.2.2 Materials and methods

2.2.2.1 Content equivalent diameter

We define the content equivalent diameter, d_c , as the diameter of a sphere that contains the same mass of nonvolatile components, at a volumetric reference concentration, c_r , as the mass of the particle in question. If the mass, m_p , of the particle is known, the content equivalent diameter follows from a mass balance:

$$d_c = \sqrt[3]{\frac{6m_p}{\pi c_r}} = \sqrt[3]{\frac{\rho_p}{c_r}} d_v \quad (2.2)$$

This concept has been used previously with nebulized aerosols (Roth and Gebhart 1996). In many cases the mass of an individual particle is not available but rather the particle density, ρ_p , and an analytically accessible equivalent diameter describing the size of the particle can be used. For example, the volume equivalent diameter, d_v , may be used, which yields the second version of Equation (2.2) above. The volume equivalent diameter includes all open or closed voids in the primary form of the particle (DeCarlo et al. 2004); therefore, the increased volume of porous particles is also accounted for in the particle density. Alternatively, the particle density can be replaced by the true density of the particle material and the void spaces can be accounted for by incorporating a void fraction into this equation.

Respirable particles are usually characterized by their aerodynamic diameter, which can be assessed by compendial methods. The aerodynamic diameter, d_a , is related to the volume equivalent diameter by (Hinds 1999)

$$d_a = \sqrt{\frac{\rho_p \xi}{\rho^* \chi}} d_v, \text{ with } \xi = \frac{C_c(d_v)}{C_c(d_a)} \quad (2.3)$$

where ρ^* is the reference density (typically 1.00 g / mL), χ is the shape factor accounting for the influence of non-spherical shape on drag force, and ξ captures the effect of non-continuum flow conditions for small particles. The ratio of the Cunningham corrections, C_c , evaluated at the volume equivalent diameter and the aerodynamic diameter, respectively, is very close to 1 and can be neglected if these equivalent diameters are similar. However, for submicron particles with low particle density in air or similar gases under standard conditions, this factor becomes significant and Equation (2.3) must be solved iteratively, using an appropriate correlation for the Cunningham correction (Allen and Raabe 1985). The content equivalent diameter can thus be expressed as

$$d_c = \sqrt{\frac{\chi}{\xi}}^3 \sqrt{\frac{\rho^*}{c_r}}^6 \sqrt{\frac{\rho^*}{\rho_p}} d_a \quad (2.4)$$

The content equivalent diameter is a property of the aerosol particles and as such, can be defined without detailed knowledge of the actual atomization process.

If the concept of the content equivalent diameter is applied to metered dose inhalers, the volumetric concentration of all non-volatile components in the propellant present in the canister, c_s , is a useful selection for the reference concentration c_r . The concentration c_s is accurately set during the fill finish process of the inhaler. Thus, using Equation (2.4) we can relate the aerodynamic diameter of the aerosol from a metered dose inhaler to its content equivalent diameter:

$$d_a = \sqrt{\frac{\xi}{\chi}}^3 \sqrt{\frac{c_s}{\rho^*}}^6 \sqrt{\frac{\rho_p}{\rho^*}} d_c \approx {}^3\sqrt{\frac{c_s}{\rho^*}}^6 \sqrt{\frac{\rho_p}{\rho^*}} d_c \quad (2.5)$$

Because most metered dose inhalers produce aerosols with a mass median aerodynamic diameter larger than 1 μm (Mitchell et al. 2003a) with aspect ratios expected to be close to 1 (Grainger et al. 2012; Lewis et al. 2014), non-continuum and shape effects can usually be neglected. The effect of varying particle density is also quite small for typical pharmaceutical actives or excipients, due to the weak sixth root dependence in Equation (2.5). Hence, an approximate estimate of particle density, if available, may be used.

Utilizing Equation (2.5) in combination with a means of measuring the aerodynamic diameter distribution of the aerosol from MDIs allows us to study the effects of device and formulation variables on the content equivalent diameter distribution. We use this approach to develop a single correlation for the MMAD of solution MDIs as measured by cascade impaction operating at laboratory conditions, accounting both for choice of propellant (134a or 227ea) and for ethanol concentration.

2.2.2.2 Cascade impaction testing of metered dose inhalers

Cascade impaction testing on 170 solution MDIs was performed; the results comprise the data set used to develop the model presented below. MDIs consisted of an active pharmaceutical ingredient dissolved in either propellant HFA 134a or HFA 227ea using ethanol as a co-solvent; in some cases glycerol was added as a non-volatile modulator of aerodynamic size distribution. All MDIs were filled using a two-stage filling process: first, known quantities of drug, ethanol,

and non-volatile additive were added and a valve was crimped onto the canister; then propellant was filled through the valve. Filled MDIs were then paired with an actuator prior to testing. Valves and actuators were supplied by Bepak (Bepak Ltd., King’s Lynn, UK). Formulation and device variable ranges of the tested MDIs appear in Table 2.1.

Aerodynamic diameter distributions were measured with an Andersen cascade impactor (Mark II, Copley Scientific, Nottingham, UK) fitted with a USP (United States Pharmacopeia) induction port (Apparatus 1, USP 35) and comprising eight metal stages plus a final filter. All measurements were performed at laboratory conditions of 20 ± 3 °C at ambient humidity. Air flow rate through the impactor was 28.3 ± 0.5 standard L/min for all tests. Metered dose inhalers were actuated from one to ten times per determination depending on active ingredient and dose. The mass of drug deposited on each impactor plate was determined via high-performance liquid chromatography or ultra-performance liquid chromatography, with method dependent on active ingredient.

All aerodynamic diameter distributions were assumed to be log-normal. The cumulative mass aerodynamic diameter distribution from each cascade impaction measurement was fit using the best-fit log-normal cumulative distribution function (Hinds 1999) with mass median aerodynamic diameter and geometric standard deviation as the fitting parameters in a nonlinear least squares analysis.

Table 2.1: Summary of the ranges of the device and formulation variables in the cascade impaction data set used to develop the correlation.

Variable	Tested range (X – Y) or discrete values (X, Y, ..., Z)
Active pharmaceutical ingredient	b-oestradiol 17-enanthate, beclomethasone dipropionate, budesonide, dex budesonide, diisobutyl apomorphine, flunisolide, formoterol fumarate, ipratropium bromide, oestradiol valerate, tetrahydrocannabinol hemisuccinate
Valve metering volume (µL)	25, 50, 100
Actuator orifice diameter (mm)	0.22, 0.30, 0.42
Propellant type	HFA 134a, HFA 227ea
Drug dose, metered (µg)	6 – 1000
Total solution concentration (mg/mL)	0.4 – 22.0
% Ethanol (w/w)	2.0 – 15.2

2.2.2.3 Dimensional analysis

The method of Buckingham (Buckingham 1914) was used to simplify the analysis of the cascade impaction data. Dimensional analysis is described procedurally elsewhere (Kundu et al. 2012). As the objective of the analysis was to find a correlation for the mass median content equivalent diameter at the formulated solution concentration, $d_{c,50}$, independent formulation and device variables expected to have an effect on $d_{c,50}$ were selected assuming that flash boiling and aerodynamic breakup contribute to the atomization process; they are summarized in Table 2.2.

Since the only variables containing units of temperature were c_p and $(T_0 - T_e)$, they were grouped as a product, $c_p(T_0 - T_e)$, to limit the number of dimensionless groups required. Including $d_{c,50}$ there were then six variables involved in the system, which contains three independent dimensions (mass, length, time); consequently three independent dimensionless groups describe this system.

Table 2.2: Summary of the variables in the dimensional analysis, and a brief explanation for the inclusion of each.

Variable	Symbol	Reasons for inclusion in analysis
Mass median content equivalent diameter	$d_{c,50}$	Dependent variable of interest
Pressure in MDI metering chamber	p_{mc}	Primary source of energy for atomization
Actuator orifice diameter	d_o	Non-dimensionalization of $d_{c,50}$
Surface tension of liquid propellant in air	σ_{pa}	Related to the surface energy of the propellant droplets upon atomization
Specific heat capacity of liquid propellant	c_p	Describes thermal energy in the liquid propellant; relevant to flash atomization
Temperature drop of propellant during atomization	$(T_0 - T_e)$	Describes exchange of sensible heat for latent heat during propellant evaporation; relevant to flash atomization
Specific enthalpy change of vaporization of propellant	ΔH_v	Related to the amount of energy consumed to evaporate propellant; relevant to flash atomization

Using d_o , σ_{pa} , and ΔH_v as repeating variables and forming the dimensionless groups, the following relationship was obtained:

$$\Pi_1 = \frac{d_{c,50}}{d_o} = f(\Pi_2, \Pi_3) \quad (2.6)$$

with

$$\Pi_2 = \frac{p_{mc}d_o}{\sigma_{pa}} \quad (2.7)$$

$$\Pi_3 = \frac{c_p(T_0 - T_e)}{\Delta H_v} \quad (2.8)$$

where f denotes a functional relationship to be determined (i.e. the desired correlation).

Π_2 as defined by Equation (2.7) resembles the Weber number,

$$We_L = \frac{\rho_L v_L^2 d_o}{\sigma_{LG}}$$

where ρ_L refers to the liquid density, v_L to the liquid velocity relative to the surrounding medium, and σ_{LG} is the surface tension of the liquid in the surrounding medium. The Weber number arises in the study of liquid jet stability and atomization (Bayvel and Orzechowski 1993). Assuming a dynamic pressure scaling relationship,

$$p_{mc} \approx \rho v^2,$$

the similarity between Π_2 and the Weber number is apparent. In the context of MDIs, density and velocity are difficult to measure due to the two-phase nature of the flow at the actuator orifice exit. However, as will be seen below, the metering chamber pressure p_{mc} is more readily specified. Thus Π_2 provides an easily calculated surrogate for the Weber number, encompassing the effects of jet inertia and droplet surface energy.

Π_3 as defined by Equation (2.8) is similar to the Jakob number,

$$Ja = \frac{\rho_l c_p (T_0 - T_e)}{\rho_v \Delta H_v}$$

where ρ_l and ρ_v are the liquid and vapor phase densities, respectively. The Jakob number occurs in theoretical and experimental investigations of bubble growth rate in flashing atomization (Kitamura et al. 1986; Sher et al. 2008).

2.2.2.4 Calculation of dimensionless groups

To calculate the mass median content equivalent diameter for each MDI, Equation (2.5) was adapted using some simplifying assumptions. Assuming spherical particles with particle

density equal to the reference density and neglecting non-continuum effects, the mass median content equivalent diameter can be expressed as a function of the measured MMAD:

$$d_{c,50} = \sqrt[3]{\frac{\rho^*}{c_s}} MMAD \quad (2.9)$$

When using Equation (2.9) to analyze a set of impaction data, it is important that conditions which may affect the rates of evaporation or growth (i.e., gas temperature, flow rate, and relative humidity) are held relatively constant across the measurements.

Examining Equations (2.6—2.8), some physical properties of the propellant system must be known in order to calculate values for the dimensionless groups. As all of the tested solution MDIs were dilute, with an initial concentration of non-volatile components of at most 22 mg/mL, they were approximated as pure propellant-ethanol mixtures for the purposes of evaluating physical properties. References for the physical properties and the equations utilized in this model are given in Section 2.2.5.

The metering chamber pressure p_{mc} was equated to the vapor pressure of the HFA-ethanol mixtures. Published data for the vapor pressure of HFA-ethanol mixtures at 20 °C were used; see Section 2.2.5. The data from 0 to 30% ethanol by weight were adequately approximated with a linear fit. This approach was taken since due to the non-ideal behavior of the HFA-ethanol mixtures, use of Raoult's Law for the calculation of vapor pressure results in significant errors (Smyth et al. 2002; Vervaet and Byron 1999).

To calculate the temperature dependent material properties σ_{pa} , c_p , ΔH_v and the temperature drop during atomization ($T_0 - T_e$), it was necessary to estimate the final temperature of the propellant droplets upon complete atomization, T_e . Liquid phase breakup and droplet formation were assumed to occur during flash-boiling of propellant, with atomization ceasing once flash-boiling stops. Therefore the boiling temperature of the propellant-ethanol mixture was chosen instead of the droplet wet bulb temperature as the more relevant temperature to the phenomena being modeled, and T_e was assumed to be the normal boiling point of the propellant only. The relatively small boiling point increase due to the presence of ethanol was neglected.

With an approximate final temperature T_e determined, a reference temperature for the calculation of material properties was defined:

$$\bar{T} = \frac{(T_0 + T_e)}{2} \quad (2.10)$$

Surface tension, specific heat capacity, and specific enthalpy change of vaporization for each MDI were then calculated using the relationship

$$\varphi_m = Y_p \varphi_p(\bar{T}) + Y_e \varphi_e(\bar{T}) \quad (2.11)$$

where φ_m denotes the mass-weighted material property of the mixture, Y_p and Y_e are the mass fractions of propellant and ethanol, respectively, and φ_p and φ_e are the pure component property at \bar{T} for propellant and ethanol, respectively. Equations for calculating the pure component physical properties are presented in Section 2.2.5.

Once all of the variables in Table 2.2 were determined for each observation in the data set, the dimensionless groups of Equations (2.6—2.8) were calculated, and the data were evaluated to find a correlation for the dimensionless mass median content equivalent diameter as a function of the independent dimensionless groups.

2.2.3 Results and discussion

The range of values of the dimensionless groups for the evaluated cascade impaction data are summarized in Table 2.3. Since the dimensionless group Π_3 did not vary much in the data set, it could not be assessed if a correlation with Π_1 existed. Thus for the purposes of the model presented here, Π_1 was considered to be independent of Π_3 . In contrast, a clear relationship between Π_1 and Π_2 can be seen in Figure 2.2. The best fit power function yielded an exponent of -1.01, so for simplicity the data were re-fit with an exponent of -1 with no decrease in coefficient of determination (R^2) value:

$$\Pi_1 = 416 \Pi_2^{-1}, \quad R^2 = 0.75 \quad (2.12)$$

The R^2 value of 0.75 indicates appreciable unexplained variation in the data, which is unsurprising given the simplicity of the model. However, the relatively good fit identifies the primary variables influencing the mass median content equivalent diameter, while some of the unexplained variation is likely attributable to variables that were not considered in this analysis. Inserting the definitions of Π_1 and Π_2 from Equations 2.6 and 2.7 into the fitted function, and solving for the mass median content equivalent diameter yields

$$d_{c,50} = \frac{416 \sigma_{pa}}{p_{mc}}, \quad (2.13)$$

from which we find a dependence of $d_{c,50}$ on propellant surface tension in air and metering chamber pressure only. Actuator orifice diameter d_o has cancelled out, consistent with other

researchers' findings that for solution MDIs, actuator orifice diameter has little effect on content equivalent diameter distribution (Lewis et al. 2006; Stein and Myrdal 2004).

Table 2.3: Mean, standard deviation, and relative standard deviation of the values of the three dimensionless groups for the cascade impaction data set.

Dimensionless group	Mean ± Standard Deviation	Relative Standard Deviation
Π_1	0.0398 ± 0.0079	20%
Π_2	$10,800 \pm 2160$	20%
Π_3	0.118 ± 0.010	8%

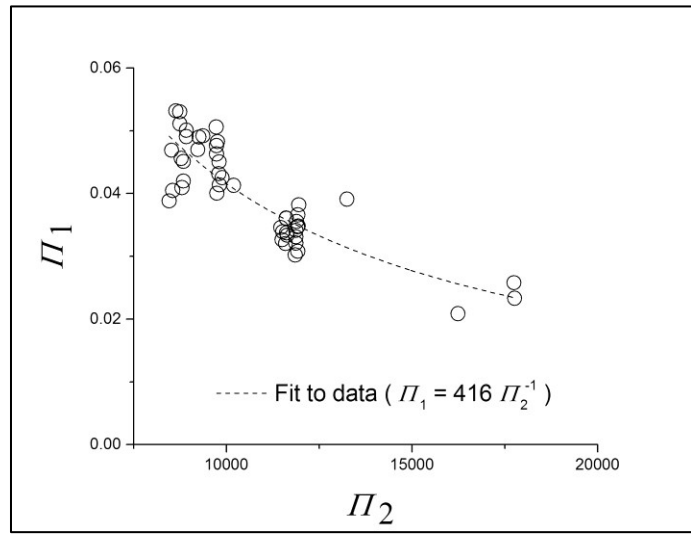


Figure 2.2: Plot of Π_1 vs. Π_2 and a power-law curve fit to the data.

Substituting Equation (2.13) into Equation (2.9) and solving for MMAD yields

$$MMAD = 416 \sqrt[3]{\frac{c_s}{\rho^*} \frac{\sigma_{pa}}{p_{mc}}} \quad (2.14)$$

Equation (2.14) is valid for any consistent set of units, and gives the MMAD in meters if the independent variables are specified in SI units. It is a correlation equation that predicts the mass median aerodynamic diameter of a solution MDI given the formulated concentration of drug plus non-volatile excipient, the surface tension of the propellant in air, and the metering chamber pressure. Since the correlation was developed using the concept of the content equivalent diameter, which is a parameter of the measured aerosol, it is only strictly valid for similarly measured aerosols, i.e., for cascade impaction data generated in a 20 °C laboratory, with air flow

rate of 28.3 standard L/min, and using a USP throat inlet. These are relevant conditions for MDI development. Use of this correlation at other conditions should be considered extrapolation and the results treated with due caution; as other research (Stein and Myrdal 2004) has demonstrated, such correlations are specific to the means of sampling and measuring the aerosol.

To test the accuracy of the correlation of Equation (2.14), it was applied to experimental data in the literature and the predicted MMAD was compared to the experimentally determined values; see Figure 2.3. Meakin et al. (Meakin et al. 2000) tested solution MDIs with both HFA 134a and 227ea as propellant with an Andersen cascade impactor, as was done in this work. Myrdal et al. (Myrdal et al. 2004) and Stein and Myrdal (Stein and Myrdal 2004) measured the aerodynamic diameter distributions of solution MDIs in both propellants, using a time-of-flight aerodynamic particle sizer (APS) equipped with a USP inlet; in Myrdal's work, a 20 cm extension was added downstream of the USP inlet and prior to the sizing equipment.

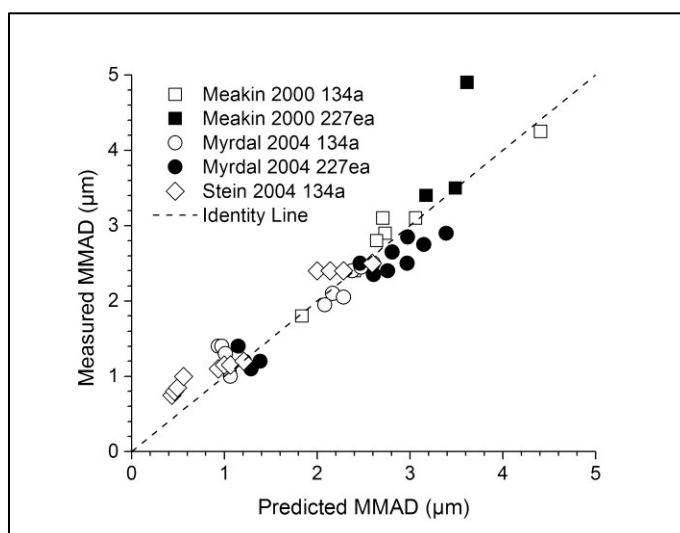


Figure 2.3: Comparison of predicted vs. measured MMAD of experimental data from a variety of literature sources. The data of Meakin (squares, (Meakin et al. 2000)) were generated using an Andersen cascade impactor. The data of Myrdal (circles, (Myrdal et al. 2004)) were generated using a time-of-flight aerodynamic particle sizer (APS) equipped with a USP inlet plus inlet extension. The data of Stein (diamonds, (Stein and Myrdal 2004)) were also generated with an APS, with a USP inlet and no extension. Open symbols: propellant 134a + ethanol; closed symbols: propellant 227ea + ethanol.

Our correlation predicts the data of Meakin et al. quite well, save for one outlier. It also predicts the data measured with the APS with reasonable accuracy, showing that some extrapolation is possible. Overall Equation (2.14) predicts this sample of literature data adequately given the different techniques employed by each source. While prior research has yielded similar

correlation equations (Lewis et al. 2004; Stein and Myrdal 2004), these have been propellant-specific, requiring a separate equation for each propellant.

The calculated GSDs of the measured aerodynamic diameter distributions of the entire dataset ranged from 1.8 to 3.1, with an overall average value of 2.1. As no correlations with the dimensionless groups or independent variables were found, use of the overall average value of 2.1 for the GSD is recommended for predictive purposes.

2.2.4 Conclusions

The content equivalent diameter distribution, as defined here, is a property of the measured residual aerosol. For MDIs, use of the content equivalent diameter distribution allows experimental investigation of the effects of formulation and device variables on the residual aerosol size distribution without necessitating a detailed description of the droplet diameter or momentum distribution of the propellant spray.

Dimensional analysis was utilized to identify dimensionless groups describing the mass median content equivalent diameter of the portion of the spray sized in a standard cascade impaction testing apparatus. Dimensionless mass median content equivalent diameter was found to be correlated with one dimensionless group; using this result, a correlation for the MMAD of the resulting aerosol was developed, depending on propellant vapor pressure in the metering chamber, surface tension of the liquid propellant in air, and the formulated concentration of non-volatiles in the HFA solution. Unlike propellant-specific correlations previously presented in the literature, the correlation developed here links the observed behavior to physical properties of the system, offering the potential to describe novel or unconventional propellant-co-solvent combinations. The equation is simple and provides the formulator of solution MDIs with a tool to easily select an appropriate level of non-volatile additives to achieve a target MMAD for a given drug formulation. It is valid for cascade impaction testing of solution metered dose inhalers provided that the testing parameters are within the ranges described in section 2.2.2.2.

2.2.5 Appendix: Physical properties of propellant-ethanol mixtures

Metering chamber pressure p_{mc} was equated to the vapor pressure of the HFA-ethanol mixture at 20 °C. Linear fits to vapor pressure data from a propellant supplier (Solvay Fluor GmbH 2007) in the range of 0 – 30 % by weight ethanol were used. The fitting equations are

$$p_{134a+EtOH} = 5.72 \times 10^5 - 2.8 \times 10^5 X_{EtOH}$$

$$p_{227\text{ea}+\text{EtOH}} = 3.90 \times 10^5 - 2.7 \times 10^5 X_{\text{EtOH}},$$

where $p_{134\text{a}+\text{EtOH}}$ and $p_{227\text{ea}+\text{EtOH}}$ are the absolute vapor pressure of HFA 134a or HFA 227ea mixed with ethanol in Pa, and X_{EtOH} is the mass fraction of ethanol present in the mixture.

Surface tension in air, specific heat capacity, and specific enthalpy of vaporization for propellant-ethanol mixtures were evaluated using mass weighting per Equation (2.11), with pure component properties evaluated at the mean temperature defined in Equation (2.10). The equations used to approximate the pure component properties are summarized in Table 4.

Table 2.4: The equations used to approximate physical properties of ethanol and propellants HFA 134a and HFA 227ea.

Property	Equation	Reference
Surface tension in air in N/m; T in K	$\sigma_{134\text{a}} = 0.06021747 \left(1 - \frac{T}{374.2}\right)^{1.26}$	(Mexichem UK Limited 2010a)
	$\sigma_{227\text{ea}} = 0.05047773 \left(1 - \frac{T}{376.0}\right)^{1.26}$	(Mexichem UK Limited 2010b)
	$\sigma_{\text{EtOH}} = 0.05 \left(1 - \frac{T}{513.9}\right)^{0.952}$	(Mulero et al. 2012)
Specific heat capacity at constant pressure in J/kg K; T in K	$c_{p,134\text{a}} = -132,323 + 1,000.153 T - 2.8 T^2 + 2.79 \times 10^{-3} T^3 + \frac{9.396558 \times 10^8}{T^2}$	(Mexichem UK Limited 2010a)
	$c_{p,227\text{ea}} = -139,133 + 1,001.004 T - 2.68 T^2 + 2.55 \times 10^{-3} T^3 + \frac{1.088237 \times 10^9}{T^2}$	(Mexichem UK Limited 2010b)
	$c_{p,\text{EtOH}} = 2770 - 14.91 T + 0.09132 T^2 - 2.574 \times 10^{-4} T^3 + 3.564 \times 10^{-7} T^4$	(Brown Jr and Ziegler 1979)
Enthalpy change of vaporization in J/kg; T in K	$\Delta H_{v,134\text{a}} = 163,731.3 x + 534,468.4 x^2 - 510,952 x^3 + 219,188.6 x^4$ with $x = \sqrt[3]{1 - \left(\frac{T}{T_c}\right)}$ and $T_c = 374.2$ K	(Mexichem UK Limited 2010a)
	$\Delta H_{v,227\text{ea}} = 39,210.01 x + 850,109 x^2 - 1,725,330 x^3 + 1,188,758 x^4$ with $x = \sqrt[3]{1 - \left(\frac{T}{T_c}\right)}$ and $T_c = 376.0$ K	(Mexichem UK Limited 2010b)
	$\frac{\Delta H_{v,\text{EtOH}}}{T} = 1,094,677 \exp(0.4775 T_r)(1 - T_r)^{0.4989}$ with $T_r = \frac{T}{513.9 \text{ K}}$	(NIST Chemistry Webbook 2015a)

2.3 An *in-silico* investigation of formulation and device effects on the aerodynamic particle size distributions of suspension pressurized metered dose inhalers

2.3.1 Introduction

To provide effective treatment, pressurized metered dose inhalers (pMDIs) must produce drug particles with a small aerodynamic particle size distribution (APSD). The equilibrium APSD produced by solution pMDIs can be controlled by manipulating the concentration of nonvolatile solutes (Lewis et al. 2005). With suspension formulations, the matter is somewhat more complex: atomized propellant droplets may contain zero, one, or multiple particles (multiplets) of the suspended phase. Multiplets result in coarsening of the APSD, and their frequency depends on the concentration and size distribution of the suspended particles in the metering chamber and the size distribution of the atomized droplets. This effect is of particular importance for high dose suspension pMDIs, which may require relatively high concentrations of suspended drug in the propellant. Since the problem of sorting polydisperse suspended particles into polydisperse droplets has not been solved analytically, researchers have relied on stochastic modeling techniques to explore the effects of drug size distribution and concentration on the APSD of the aerosol following evaporation of the volatile phase (Clark 2008; Gonda 1985; Ivey and Vehring 2010; Sheth et al. 2015; Stein et al. 2010; Stein et al. 2012; Stein et al. 2015). In this work, a stochastic model was utilized to further explore these effects, and an analytical equation was derived for general use.

2.3.2 Methods

A stochastic model was developed to simulate sorting of suspended particles into atomized droplets and assess the particle size distribution present after evaporation of the volatile phase; the basic functionality is depicted in Figure 2.4. The model was implemented in C++. The spray of droplets and the suspended phase were assumed to be made up of spheres with known lognormal size distributions. After generating a sorted array of $N_0 = 10^6 - 10^7$ droplets, the number of suspended particles to simulate, N_{sp} , was calculated (please see Table 2.5 for variable definitions) using the Hatch-Choate conversion equations (Hinds 1999):

$$\frac{N_{sp}}{N_0} = \frac{c_{sp}}{\rho} \left[\frac{d_{0,50} \exp\left(-\frac{3}{2} \ln^2 GSD_0\right)}{d_{sp,50} \exp\left(-\frac{3}{2} \ln^2 GSD_{sp}\right)} \right]^3 \quad (2.15)$$

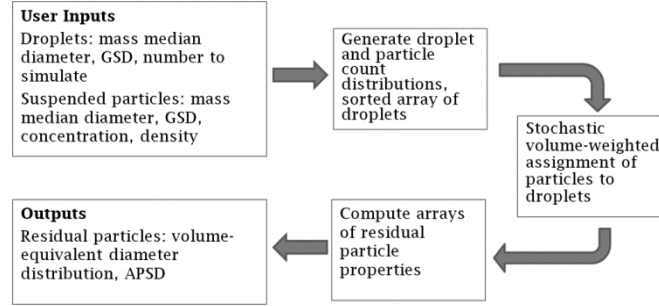


Figure 2.4: Flow chart describing the function of the stochastic model.

Then particles of suspended phase were assigned to droplets using a volume-weighted random assignment scheme, with the total volume of suspended phase contained in each droplet tracked throughout. In rare cases where the volume of suspended particle(s) assigned to a droplet, V_{sp_i} , exceeded the droplet volume, V_{0_i} , the droplet volume was increased:

$$V_{0_{i,new}} = V_{0_i} + V_{sp_i} \quad (2.16)$$

In the case of multiplets, packing effects⁵ were neglected by coalescing the constituent particles into a single larger sphere. Droplets were then “evaporated” and the residual particle volume equivalent and aerodynamic diameters (d_{v_i} , d_{a_i} , respectively) were computed:

$$d_{v_i} = \frac{6}{\pi} \sqrt[3]{V_{sp_i}} \quad , \quad d_{a_i} = \sqrt{\frac{\rho}{\rho^*}} d_{v_i} \quad (2.17)$$

Here shape effects⁵ have been neglected for simplicity, which for irregular particles will tend to result in some systematic overestimation of the aerodynamic diameter. Finally, mass-weighted frequency distributions were computed and output; data analysis was conducted using Excel 2010 (Microsoft, Redmond, WA, USA) and Origin 2018 (OriginLab, Northampton, MA, USA). Model results were compared to experimentally determined APSDs of suspension pMDIs containing varying concentrations of micronized fluticasone propionate (pMDI droplet $d_{0,50}$ $9.6 \pm 0.7 \mu\text{m}$, GSD_0 1.5, suspended material c_{sp} 0.9 – 11.8 mg/mL, $d_{sp,50}$ $1.2 \pm 0.1 \mu\text{m}$, GSD_{sp} 1.7). APSDs of these pMDIs were determined by actuating inhalers into a 30 L evaporation chamber and prolonged sampling using a time of flight aerodynamic particle sizer (Model 3321, TSI Inc.,

⁵ The implications of these assumptions about shape and packing effects are treated in more detail in Appendix A1.

Shoreview, MN, USA). A total of 90 sets of conditions were simulated using the model; evaluated parameter ranges are summarized in Table 2.5.

Table 2.5: Parameter ranges evaluated herein; suspended phased density $\rho = 1365 \text{ kg/m}^3$ in all cases.

Input Parameter	Range Evaluated
Droplet mass median diameter $d_{0,50}$	9 - 36 μm
Droplet geometric standard deviation GSD_0	1.5 – 2.1
Suspended phase concentration c_{sp}	0.06 - 256 mg/mL
Suspended phase mass median diameter $d_{sp,50}$	1.0 – 5.0 μm
Suspended phase geometric standard deviation GSD_{sp}	1.5 – 2.1

2.3.3 Results and discussion

As illustrated in the left panel of Figure 2.5, model results were in reasonable agreement with experimentally determined APSDs, indicating that the set of model assumptions is suitable to describe the problem. As previously reported by researchers utilizing similar models (Sheth et al. 2015; Stein et al. 2012) and as illustrated in the right panel of Figure 2.5, the model predicts that for constant GSD_0 and GSD_{sp} the ratio of the MMAD of the aerosol emitted by the pMDI to the MMAD of the micronized suspended particles, Γ , increases for increasing suspension concentration. The rate of increase is dependent on the ratio of the median droplet diameter to the median suspended particle diameter, $d_{0,50}/d_{sp,50}$. As shown in the left panel of Figure 2.6, for constant GSD_0 and GSD_{sp} the growth factor Γ collapses to a single curve when plotted against the suspended particle to droplet number ratio, $\frac{N_{sp}}{N_0}$. Further, the rate of increase of Γ for increasing $\frac{N_{sp}}{N_0}$ depends quite strongly on the ratio of GSD_0 to GSD_{sp} . To enable utilization of these results for researchers without access to the stochastic model itself, Γ values from a subset of simulation data covering a wide range of all input parameters was fit as a training set using nonlinear least squares regression:

$$\Gamma = \left[0.939 \ln \left(\frac{N_{sp}}{N_0} + 3.42 \right) \right]^{1.03GSD_0/GSD_{sp}}, \quad R_{adj}^2 = 0.96 \quad (2.18)$$

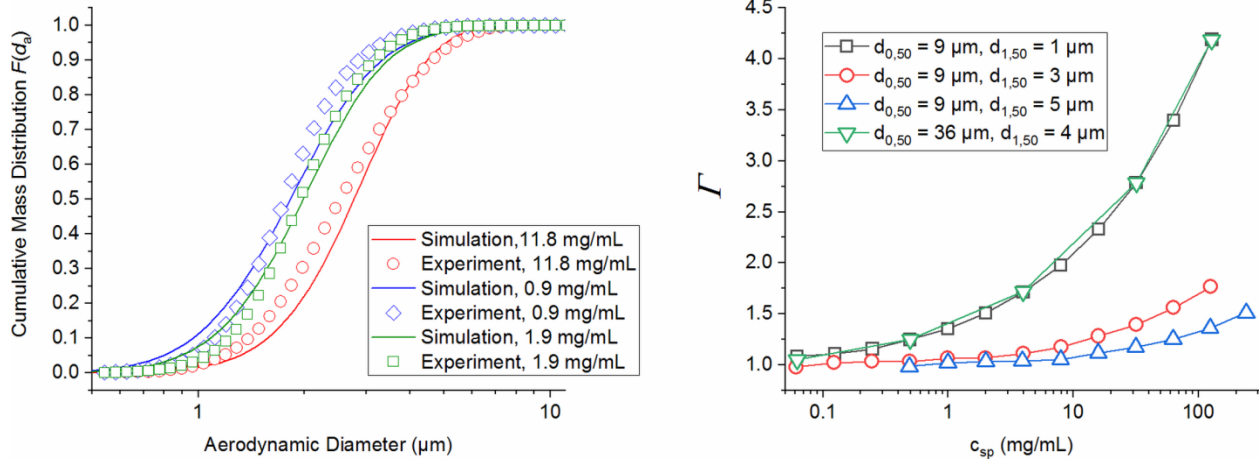


Figure 2.5: Left panel: comparison of simulated and selected measured cumulative APSDs for suspension metered dose inhalers containing different concentrations of fluticasone propionate. Right panel: effect of droplet and suspended phase median diameter and suspension concentration on the growth factor Γ for $GSD_0 = 2.1$ and $GSD_{sp} = 1.8$.

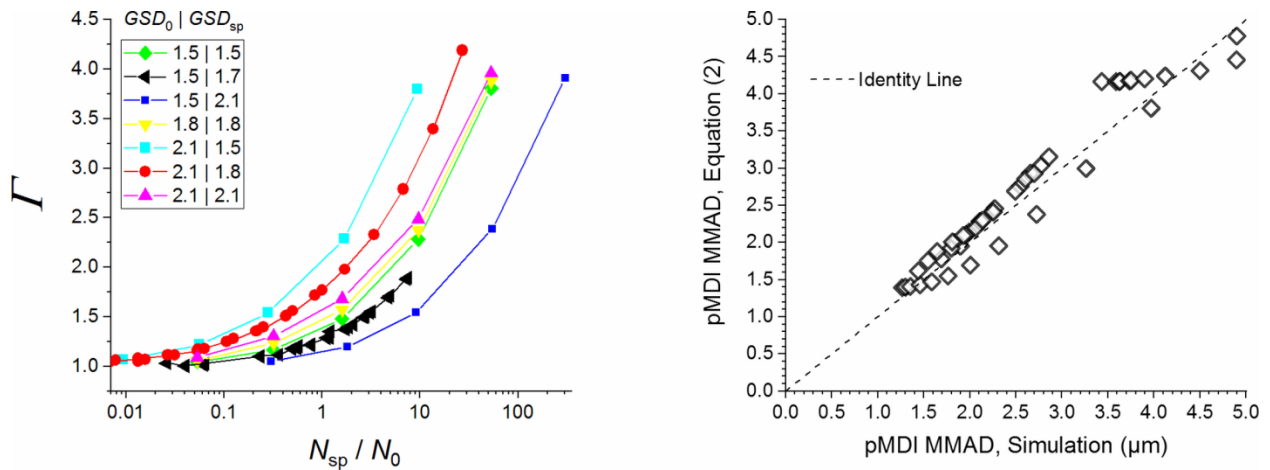


Figure 2.6: Left panel: dependence of growth factor Γ on the suspended particle to droplet ratio $\frac{N_{sp}}{N_0}$ for varying GSD_0 and GSD_{sp} . Right panel: pMDI MMAD values as predicted using Equation (2.18) vs. stochastic model predictions.

Equation 2.18 was then used to estimate the MMAD for the remaining simulated conditions; as shown in the right panel of Figure 2.6, Equation (2.18) provides estimates in reasonable agreement with the actual simulation results.

2.3.4 Conclusions

The stochastic modeling technique used here accurately predicts the APSD of suspension pMDIs and enables *in-silico* explorations of the input parameter space. While the effects of suspension concentration, atomized droplet diameter, and suspended particle size on the APSD

of solution pMDIs are well-documented, this work indicates that the breadth of the droplet size distribution and the breadth of the suspended phase size distribution may also have a strong effect on the APSD for high suspension concentrations or for fine suspended material. By utilizing the curve fit of Equation (2.18) the results can be applied by practitioners in industry without the need to develop complicated models. These findings suggest that repeatable drug delivery from a suspension pMDI—whether through the life of a single inhaler or the life cycle of a product—requires a robust device capable of producing consistent spray characteristics coupled with a well-controlled, stable suspension formulation.

Chapter 3 : Environmental Effects on the Aerosols Emitted from pMDIs

3.1 Introduction

The environment in which a pMDI is utilized has the potential to impact the efficacy of treatment by influencing the atomization event and the subsequent dynamics of the evaporating aerosol. The literature surveyed in Section 1.3.4.4 indicates that the inhaler temperature, the ambient temperature, and the ambient humidity can have just as large of an effect on *in vitro* performance metrics as the device and formulation variables. These considerations are especially relevant to patients living in locations with extremes of temperature or humidity. Unfortunately for such patients, the impact of environmental factors on inhalation product performance is not widely appreciated or studied within the pharmaceutical industry and the regulatory agencies. It is therefore up to researchers in academia to advance understanding and awareness of these issues with experimental and theoretical work. This chapter summarizes my own contributions to this effort.

Section 3.2 consists of a published research article⁶; in this work I investigated a mystery related to the origin of porosity in the residual drug particles produced from solution pMDIs. It is presented as published save that the headings, figures, tables, and equations, and all references thereto, have been renumbered for consistency within this thesis.

Additionally, in collaboration with my colleagues here at the University of Alberta, I made contributions to investigations of the effects of environmental factors on pMDI performance *in vitro*. This work was presented as posters at two conferences, and is summarized in Appendix A2.

⁶ Section 3.2 consists of the as-published text of a research article:

Ivey, J. W., Bhambri, P., Church, T. K., Lewis, D. A., McDermott, M. T., Elbayomy, S., Finlay, W. H. and Vehring, R. (2017). Humidity affects the morphology of particles emitted from beclomethasone dipropionate pressurized metered dose inhalers. *International Journal of Pharmaceutics* 520:207-215

3.2 Humidity affects the morphology of particles emitted from beclomethasone dipropionate pressurized metered dose inhalers

3.2.1 Introduction

Inhaled corticosteroids are widely prescribed for prophylactic asthma therapy (Busse 2002), and may also benefit patients with moderate to severe chronic obstructive pulmonary disease (Gartlehner et al. 2006). A large proportion of inhaled corticosteroid doses are delivered using pressurized metered dose inhalers (pMDIs) (Lechuga-Ballesteros et al. 2011; Roche and Dekhuijzen 2016). In modern pMDIs, the drug is either suspended or dissolved in a volatile hydrofluoroalkane (HFA) propellant, with the choice dependent on the solubility of the drug in the propellant (Myrdal et al. 2014); the inhaled corticosteroid beclomethasone dipropionate (BDP) has generally been formulated as a solution (Spahn 2016) utilizing ethanol as a co-solvent (Gupta et al. 2003). The resulting formulation is contained in a pressurized canister equipped with a metering valve and paired with an actuator (Stein et al. 2014). When a patient administers a dose from a pMDI, the volatile formulation exits the valve via the actuator and is atomized into a fine, rapidly evaporating spray which is inhaled into the patient's lungs (Finlay 2001a).

The aerodynamic particle size distribution of a therapeutic aerosol has a large effect on the efficacy of treatment in pulmonary delivery because of its prominent role in the physical mechanisms of particle deposition in the human airways (Darquenne 2012). Consequently, a substantial amount of research on pMDIs has focused on measurement and prediction of the drug particle size distribution for solution and suspension formulations. The matter is complicated by the highly dynamic nature of the aerosol generated by pMDIs: as the spray of propellant droplets interacts with the surrounding gas phase, heat, mass, and momentum are transferred (Xu and Hickey 2014), and thus the velocity, size, and concentration of droplets vary in time and space (Dunbar et al. 1997). Available theory (Finlay 2001a) suggests that the formulation (propellant physical properties, inclusion of co-solvent) and usage environment (air temperature, relative humidity) have the potential to alter these spray dynamics and therefore the deposition in human airways. Indeed, *in vitro* studies summarized in our recent review (Ivey et al. 2015) have demonstrated all of these effects.

As the interaction of pMDI-generated aerosols with humidity is of particular relevance to the present study, a brief survey of research on this topic is merited. Evaporative cooling in pMDI spray plumes can produce temperatures well below 0 °C (Brambilla et al. 2011), and the

plume may contain as many as hundreds of millions of microparticles (Stein 2008b). If the air entrained into the pMDI spray plume is sufficiently humid, these conditions might produce supersaturation of water vapor and subsequent nucleated condensation of water (Hinds 1999). An early evaluation of the effect of humidity on the aerodynamic particle size distribution of nine commercial chlorofluorocarbon pMDIs was conducted by Kim et al. (Kim et al. 1985). Testing was conducted with air conditioned to 22-23 °C and either < 1% or 90% relative humidity (RH). A 20 liter evaporation chamber was employed upstream of an Andersen cascade impactor to measure the aerodynamic particle size distribution of the fully evaporated aerosols. No significant effect of RH on the aerodynamic particle size distribution for eight of the nine tested inhaler types was observed when the RH was increased from near zero to 90%, and thus it was concluded that for the tested pMDIs humidity did not alter the particle size distribution of the aerosol reaching the impactor. In a later study, Lange and Finlay administered doses from an HFA-propelled suspension pMDI to a model ventilation circuit equipped with a pediatric endotracheal tube coupled to an Andersen cascade impactor (Lange and Finlay 2000). Ventilation air was supplied at 4.8 L/min with a square wave profile. Ventilation air temperature was varied from 25 °C to 37 °C, and was either unhumidified (RH 8-15%) or humidified to near saturation (RH \approx 100%). The *in vitro* inhaled dose was observed to depend heavily on the amount of water vapor present in the ventilation air (i.e. the absolute humidity), with the inhaled dose decreasing as the water vapor mole fraction increased. Importantly, Lange and Finlay observed that the aerodynamic particle size distribution of the aerosol passing the endotracheal tube was unaffected by changes in air humidity and that the deleterious effect of humidity on the *in vitro* inhaled dose was mitigated when a spacing device was added to the ventilation circuit prior to the endotracheal tube and impactor. This data suggests that humidity could affect particle sizes in the spacer immediately after droplet production. In a subsequent study designed to further examine the effect of humidity, Martin et al. examined the evaporation rate of millimeter size pendant propellant-ethanol droplets in air with varying humidity levels (Martin et al. 2005). They found no effect of air humidity on droplet evaporation rates.

Evidence that humidity can alter the aerodynamic particle size distribution from pMDIs was published by Mitchell and colleagues, who utilized an Andersen cascade impactor with an endotracheal tube fixed to the inlet to evaluate the effect of air humidity on the aerodynamic particle size distribution of BDP solution pMDIs paired with valved holding chambers (Mitchell

et al. 2003b). They found that increasing the absolute humidity of the testing air resulted in a large increase in the mass median aerodynamic diameter (MMAD) for an HFA BDP pMDI and concluded that the effect was due to growth by condensation of the aerosol particles generated by the inhaler. Martin and Finlay sized salbutamol sulfate suspension pMDIs actuated into valved holding chambers in 37 °C air using an Andersen cascade impactor; to evaluate any effects related to aerosol maturation, they varied the distance between the holding chamber and the impactor by using different lengths of connecting tubing (Martin and Finlay 2005). They found that increasing the RH from 8% to near 100% resulted in significant increases in holding chamber deposition and MMAD for a conventional formulation containing ethanol and surfactant as well as for an excipient-free formulation. Furthermore, in humidified air the MMAD was observed to decrease significantly as the spacing tubing length was increased. Martin and Finlay's results suggest that significant condensational growth of pMDI drug particles occurs at high air relative humidity, and that this growth is followed by secondary evaporation of the condensed water. This idea is consistent with the prior results: if the aerosol is given sufficient time to mature (as with the large volume evaporation chamber of Kim et al. or the low sampling flow rate employed by Lange and Finlay), any transient size increases will be undetectable by typical particle sizing techniques, as secondary evaporation will have taken place prior to sizing. On the other hand, if the sizing occurs while condensational size changes are still underway (as with the studies of Mitchell et al. and Martin and Finlay), the measured aerodynamic particle size distribution will depend on how far along the aerosol maturation process has progressed. Thus, although condensational growth and secondary evaporation of pMDI-generated aerosols have not been observed directly, the available research provides indirect evidence that these phenomena do indeed occur.

Recently, researchers studying solution pMDIs have focused attention on particle properties other than the aerodynamic particle size distribution. Notably, the solid phase and the particle morphology become important after particle deposition in the airways (de Souza Carvalho et al. 2014), as they may affect particle wettability, dissolution rate, and susceptibility to the lungs' particle clearance mechanisms (Ruge et al. 2013). The solid phase of inhaled drugs has been shown to affect pharmacokinetics and pharmacodynamics in animal models (Sakagami et al. 2001; Sakagami et al. 2002). This is a relevant consideration since unlike in suspension formulations, the drug in a solution pMDI undergoes a rapid transition from a solute to a solid

during dosing, with the resultant solid phase potentially dependent on the formulation and usage environment. Therefore, some recent research has evaluated the effects of formulation variables (ethanol content, presence of excipients) on the solid phase and the resultant dissolution and transport characteristics of the drug particles. Grainger and colleagues evaluated two commercially available BDP pMDIs, distinguished by ethanol content and use of the excipient glycerol (Grainger et al. 2012). They found that the glycerol-containing formulation differed significantly from the glycerol-free formulation in its extent of crystallinity, dissolution rate, and *in vitro* transcellular absorption. Similar findings were reported in work by Lewis, Haghi, and colleagues (Haghi et al. 2014; Lewis et al. 2014). Further studies with BDP solution pMDIs (Buttini et al. 2014) and with model propellant systems (Bouhroum et al. 2010; Ooi et al. 2014) indicate that BDP may form solvates or clathrates with ethanol or propellants during drug particle formation.

The morphology of a drug particle may alter its fate after deposition in the lungs as well. Specifically, particle density (Tsapis et al. 2002) and wettability (Schürch et al. 1990) have the potential to affect the rate of particle dissolution or clearance in the airways. Zhu et al. investigated the effect of ethanol content on the morphology of particles generated from budesonide solution pMDIs (Zhu et al. 2013). Utilizing field emission scanning electron microscopy (FE-SEM) and focused ion beam milling-scanning electron microscopy (FIB-SEM), they found that ethanol content had a large effect on the particle morphology. Particles produced from pMDIs with a low ethanol content tended to have an irregular envelope shape and a porous morphology, while those produced from pMDIs with more ethanol were generally smooth, solid, and spheroidal. In a subsequent study, similar morphological transitions related to ethanol content were observed for both BDP and fluticasone propionate solution pMDIs (Zhu et al. 2014a). Porous BDP particles have also been observed by other researchers (Buttini et al. 2014; Grainger et al. 2012; Lewis et al. 2014). In the present study, we build on these findings by investigating the effect of propellant type and air humidity on the morphology and solid phase of the particles produced by BDP solution pMDIs.

3.2.2 Materials and methods

3.2.2.1 pMDI filling and particle sampling

BDP solution pMDIs were prepared by first weighing out and dissolving beclomethasone dipropionate (Chiesi Farmaceutici, Parma, Italy) in anhydrous reagent grade ethanol. The resulting concentrated solutions were added to 19 mL aluminum aerosol canisters with a fluoropolymer internal coating (Presspart Ltd, Blackburn, UK). Canisters were capped with 50 μ L metering valves (BK357, Bepak Ltd, Kings Lynn, UK) and then crimped and filled with a metered volume of propellant using a lab-scale aerosol container crimper-filler (Lab Plant, Pamasol AG, Pfäffikon, Switzerland). Each inhaler was filled to a target solution volume of 10 mL with a target BDP concentration of 2 mg/mL and paired with a polymer actuator with a nominal actuator orifice diameter of 0.30 mm (Presspart Ltd, Blackburn, UK). Both HFA propellants p134a (Linde, Mississauga, Canada) and p227ea (Mexichem Fluor, Runcorn, UK) were assessed. Formulations are summarized in Table 3.1.

Table 3.1: Summary of the formulation variables for the four tested BDP solution formulations.

Formulation Identifier	Propellant type	Ethanol Content (% w/w)	BDP Metered Dose (μg)
134_5	134a	5	100
134_18	134a	18	90
227_5	227ea	5	100
227_18	227ea	18	100

The experimental setup for pMDI particle sampling at controlled humidity conditions is shown schematically in Figure 3.1. Humidity control was achieved by situating the test apparatus inside an enclosed environment and conducting testing therein. For humidified conditions ($RH \geq 8\%$), an environmental chamber (Lunaire, White Deer, PA, USA) maintained the temperature at 20.0 ± 0.5 $^{\circ}$ C, and the RH to within ± 1 % of set point (95% confidence interval). For tests at very dry conditions, a glove box with dry gas purge (Terra Universal, Fullerton, CA, USA) was better able to maintain the dry environment; dry tests were conducted at 22.0 ± 1.0 $^{\circ}$ C, with $RH \leq 2\%$ in all cases. A translucent polypropylene box with a volume of

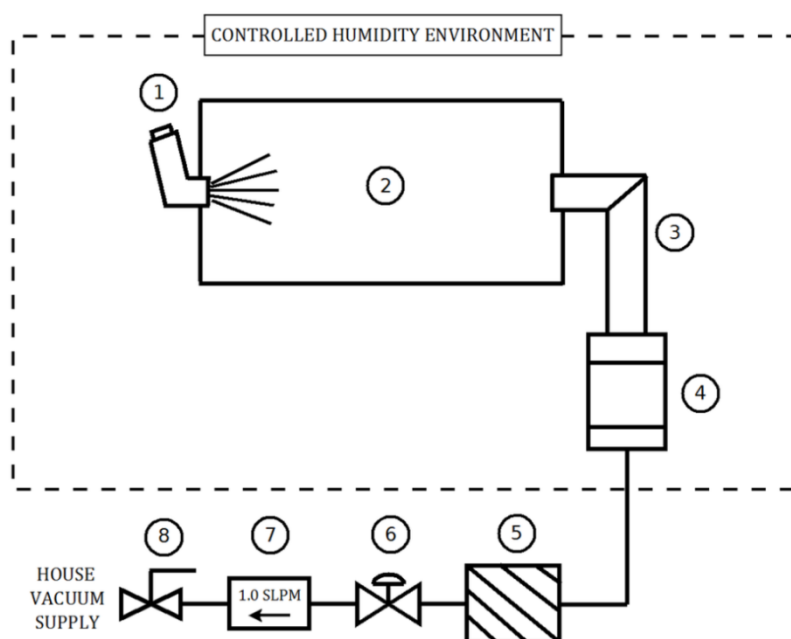


Figure 3.1: Schematic of the controlled humidity particle sampling setup used in this work. (1) BDP solution pMDI (2) 9 liter polypropylene evaporation chamber (3) USP induction port (4) Single stage, single nozzle impactor, cut size $0.6\ \mu\text{m}$ at 1.0 SLPM air flow rate (5) Inline HEPA filter (6) Flow control valve (7) Flow meter (8) Shutoff valve.

9 liters served as an evaporation chamber; it was modified to allow a pMDI mouthpiece adapter to be ported at one end. A USP induction port (USP 2013) was fitted at the other end. The downstream end of the USP induction port was coupled to a custom, single nozzle, single stage impactor (Wang 2015) configured with a nozzle diameter of 0.6 mm, a nozzle-to-collection-plate distance of 2.5 mm, and a calculated cut size of $0.6\ \mu\text{m}$ at a nominal flow rate of 1.0 SLPM. The impactor utilized standard 12.7 mm diameter ultramicroscopy pin mounts (Ted Pella, Redding, CA, USA) as removable collection plates. Samples for ultramicroscopy were collected onto double-sided adhesive conductive carbon tabs (Ted Pella, Redding, CA, USA) affixed to pin mounts; samples for spectroscopy were collected onto bare aluminum pin mounts that had been cleaned by double washes in reagent grade acetone and methanol. The sampling flow rate was set by means of a needle valve and monitored with a gas mass flow meter (Model 4043, TSI, Shoreview, MN, USA); it was maintained at 1.00 ± 0.05 SLPM for all tests. For each sample collection, a single priming shot was fired into a waste flask and then 5-10 shots from the pMDI were administered into the evaporation chamber, with a pause of approximately one second

between each shot. Then a 10 ± 1 second holding period to allow aerosol maturation was followed by 5 minutes of aerosol sampling. Given the multitude of actuations, the length of the sampling period, and the cut size of the impactor, the sampled fraction was expected to be adequately representative of the entire aerosol. After the sampling period, the impactor was disassembled and particle-laden pin mounts were transferred to a specimen box with a desiccant sachet to await analysis. The USP induction port and the impactor components were cleaned with ethanol and lint-free wipes between every measurement.

3.2.2.2 BDP particle morphology by FE-SEM, FIB-HIM

Samples were coated in gold by sputter deposition (Desk II, Denton Vacuum, Moorestown, NJ, USA) for 120 seconds at 15-20 mA current, resulting in a coating thickness of approximately 20 nm. Samples were imaged using FE-SEM (Sigma FE-SEM, Zeiss, Jena, Germany) with an accelerating voltage of 3-5 kV and a 30 μm lens aperture. Secondary electrons were detected with the out-of-lens detector. Selected samples were also analyzed using focused gallium ion beam milling and helium ion microscopy (Ga-FIB-HIM) (Orion NanoFab, Zeiss, Jena, Germany). Particles were sectioned with a gallium ion beam (30 kV accelerating voltage, 50 pA beam current, 40 μm aperture) and then imaged by helium beam (30 kV accelerating voltage, 1 pA beam current). Analysis of Ga-FIB-HIM micrographs was conducted with image analysis software (ImageJ, NIH, Bethesda, MD, USA).

3.2.2.3 BDP solid phase by Raman microscopy

Due to the small sample mass contained in each dose, Raman microscopy was selected to assess the solid phase of BDP pMDI samples. This allowed preparation of samples with adequate Raman signal while consuming only 5-10 shots from each inhaler. Samples were analyzed by placing particle-laden pin mounts directly onto the stage of a Raman microscope (inVia, Renishaw, Prospect Scientific, Ontario, Canada). An argon ion laser with a 514.5 nm wavelength was operated at 5 mW and focused through a 20x objective lens to a spot size of roughly 5 μm . The Raman spectrum from 2100-3600 cm^{-1} was acquired with a spectral resolution of approximately 1.5 cm^{-1} . A moderate fluorescence background was present in many spectra; this was subtracted using software (Origin 2015, OriginLab, Northampton, MA, USA). Since the low-frequency shift region of the spectrum was inaccessible due to the configuration of the instrument optics, the degree of crystallinity was assessed qualitatively by comparison to the

spectra of crystalline and amorphous standards in the C-H stretch band around 3000 cm^{-1} (top two spectra in Figure 3.6). The spectrum of the anhydrous microcrystalline BDP raw material was used as the crystalline standard. An amorphous BDP standard was generated by spray drying monodisperse droplets of BDP dissolved in HFA 134a-ethanol at a very low liquid flow rate at near room temperature to produce a dried powder sample; the powder production method is described in detail elsewhere (Azhdarzadeh et al. 2016). Low frequency shift Raman spectroscopy was utilized as a complementary technique to verify the solid phase of the standard materials; this technique has been shown to be extremely sensitive to the level of intramolecular order and thus degree of crystallinity (Hédoux et al. 2011b). A spectral comparison of the dried powder and crystalline samples was conducted using techniques and equipment similar to those described in previous work (Wang et al. 2014). Briefly, analysis of the BDP standards was conducted on a custom macro Raman system. A comparison of the low frequency shift band of the spectra is presented in Figure 3.2. The dried powder sample displayed an absence of the peaks corresponding to crystalline lattice vibrations present in the crystalline standard. This comparison suggested that the dried powder sample was highly amorphous, and it was thus selected as the spectral standard for amorphous BDP.

3.2.3 Results and discussion

The aim of the first round of inhaler testing was to qualitatively assess the impact of formulation and air humidity on the morphology and solid phase of the BDP particles. Selected FE-SEM micrographs of all four pMDI formulations actuated in very dry ($\text{RH} \leq 2\%$) or humid ($\text{RH} = 38 \pm 1\%$ for p227ea inhalers or $\text{RH} = 50 \pm 1\%$ for p134a inhalers) air are presented in Figure 3.3. BDP particles generated from pMDIs actuated in dry air (leftmost four panels in Figure 3.3) were generally spheroidal, with numerous submicron surface concavities. Some particles displayed a single larger concavity as well. Overall, little effect of propellant type or ethanol content on the particle morphology was observed.

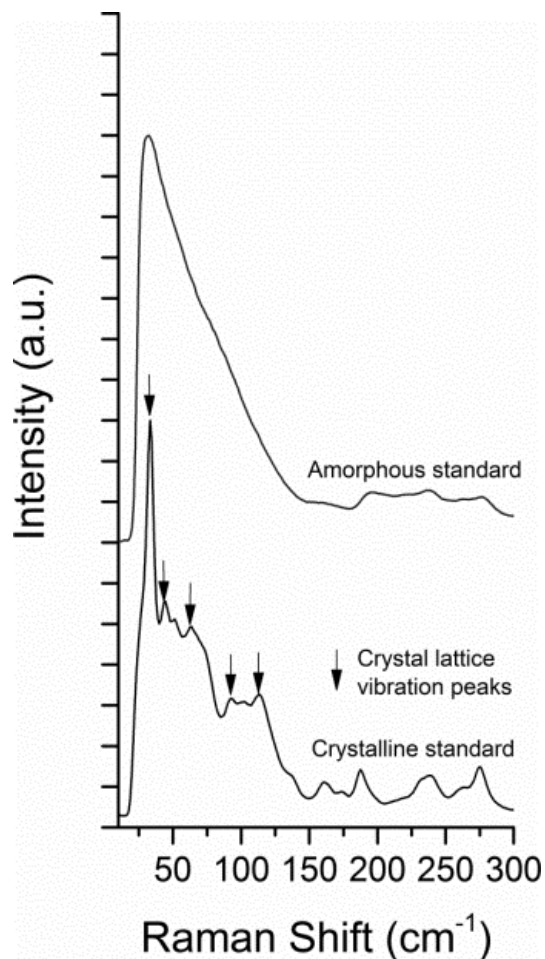


Figure 3.2: Raman spectra of amorphous and crystalline BDP standards in the low frequency shift region. Spectra are offset vertically.

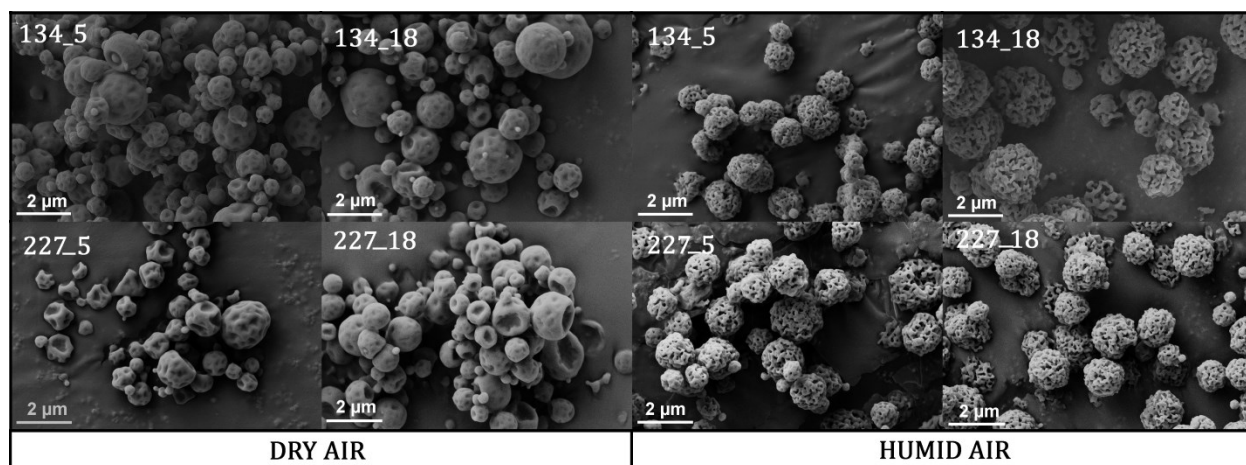


Figure 3.3: Selected FE-SEM micrographs of all four BDP formulations actuated in dry air (leftmost four panels) or humid ($RH = 38 \pm 1\%$ for p227ea inhalers or $RH = 50 \pm 1\%$ for p134a inhalers) air (rightmost four panels).

For all tested pMDI formulations, the presence of humidity in the air substantially altered the morphology of the BDP particles. While the size and envelope shape of the particles appeared similar regardless of humidity, extensive pores with characteristic dimension on the order of 100 nm were present in the particles produced in humid air. Figure 3.4 offers a closer view of particles produced by pMDI 134_5 in dry (left) or humid (right) conditions. Micrographs of single particles produced by pMDI 227_5 after cross-sectioning using FIB-HIM are shown in Figure 3.5. Unlike the almost entirely solid particle produced in dry air, the BDP particle produced in humid air (right panel) contains pores throughout the entire cross section. These results indicate that a minimal level of water vapor in the air is required to produce pores in the BDP microparticles, and that the pore former must be condensed water or ice. Further, the abundance of pores throughout the particle cross-section observed in Figure 3.5 suggests that pore formation occurs while particle drying and surface recession are still underway; otherwise we would expect pores to be confined to the near-surface region of the particles. The pores make up an appreciable fraction of the particle volume. The area occupied by pore space and the total cross section of the porous particle in the right hand panel of Figure 3.5 were estimated using image analysis software. Taking the ratio of these two quantities yielded a rough estimate for the particle void fraction of 0.2. This allows estimation of the effect of humidity-induced pore formation on the MMAD of the aerosol. For a solution pMDI, the MMAD of the residual aerosol after the liquid phase is fully evaporated is related to the mass median diameter of the spray of droplets from which it formed, MMD_d , by

$$MMAD \cong \sqrt[3]{\frac{c}{\rho^*}} \sqrt[6]{\frac{\rho_p}{\rho^*}} MMD_d, \quad (3.1)$$

where c is the concentration of solids in the droplet, ρ_p is the particle density, and ρ^* is a reference density of 1000 kg/m^3 (Ivey et al., 2014). For a porous particle, the particle density is related to the void fraction ϕ by

$$\rho_p = (1 - \phi)\rho_t \quad (3.2)$$

where ρ_t is the bulk or true density of the matrix material (Dullien 1992). Taking the ratio of the MMAD of an aerosol comprising porous particles where the condensed pore former has fully evaporated to that of an aerosol produced by the same spray and consisting of solid particles with $\rho_p = \rho_t$ then gives

$$\frac{MMAD_{\text{porous}}}{MMAD_{\text{solid}}} \cong \sqrt[6]{1 - \phi}. \quad (3.3)$$

This result indicates that very extensive porosity is required to substantially alter the MMAD of solution pMDI aerosols due to the weak sixth-root dependence on void fraction. The level of porosity seen in the right panel of Figure 3.5, and generally in particles produced under humid conditions in this study, is unlikely to meaningfully alter the MMAD of the aerosol relative to the nonporous particles produced under dry conditions. As discussed in the introduction, pMDI aerosols may undergo condensational growth and secondary evaporation depending on environmental conditions, and these processes may still be underway as particles deposit in sizing equipment or human airways. Thus the effects of environmental conditions on *in vitro* deposition observed by other researchers are more likely attributable to the extent to which aerosol maturation has progressed than to humidity-related alterations to particle morphology.

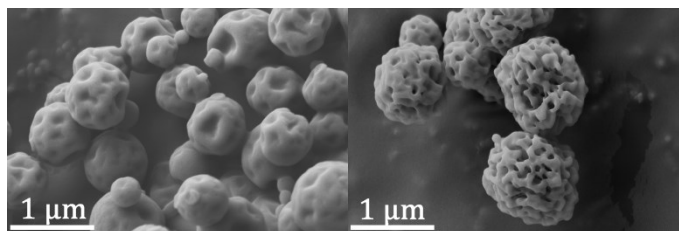


Figure 3.4: FE-SEM micrographs of BDP particles produced from the 5% w/w ethanol, p134a pMDI. Left panel: air RH \leq 2%. Right panel: RH = $50 \pm 1\%$.

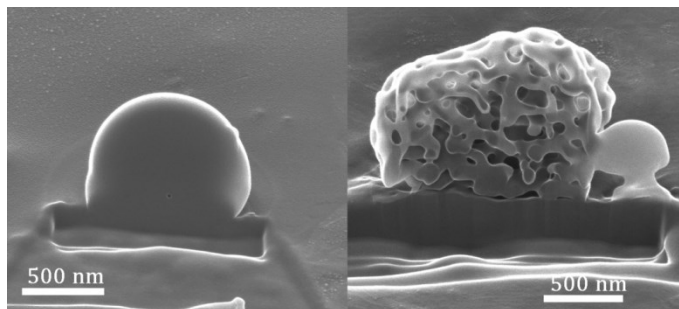


Figure 3.5: FIB-HIM micrographs of particles produced by the 5% ethanol, p227ea pMDI. Left panel: air RH \leq 2%. Right panel: air RH = $38 \pm 1\%$.

The micro-Raman spectra of all four formulations tested in dry and humidified air are presented in Figure 3.6, along with the spectra of the crystalline and amorphous standards. The spectra of the pMDI-produced powders are very similar to the amorphous standard regardless of formulation or level of humidity in the air, indicating that BDP pMDIs produce predominantly amorphous particles; this is consistent with the results of other researchers (Lewis et al. 2014;

Zhu et al. 2014a). In a sample that had been stored in a desiccator for three weeks prior to analysis (bottom spectrum in Figure 3.6), a characteristic peak at 2996 cm^{-1} , which is prevalent in the crystalline standard, appeared, suggesting that some crystallization had occurred during storage. This finding is somewhat surprising: since the unplasticized glass transition temperature of amorphous BDP has been reported as approximately $65\text{ }^{\circ}\text{C}$ (Abdel-Halim et al. 2011), available theory suggests the amorphous phase should be fairly stable at room temperature (Hancock et al. 1995). Other research demonstrates that ethanol may alter the solid phase of BDP produced by solution pMDIs (Buttini et al. 2014). It is possible that the solid phase change observed during storage is related to residual ethanol content or the presence of a crystalline fraction in the form of nanocrystalline nuclei. Regardless of the source of the instability, given the similarity of the solid phase of the porous and the non-porous particle samples, it appears unlikely that crystallization of BDP is responsible for pore formation.

Additional experiments were conducted to identify the critical air relative humidity required for pore formation, RH_c . In these experiments, for a given pMDI formulation the RH of the air in the environmental chamber was increased in discrete steps and the resulting particle morphologies were assessed via SEM until a mixed population of porous and pore-free particles was observed in a single sample. An example of this approach is provided in Figure 3.7, where pMDI 134_5 first yielded both porous and non-porous particles when tested at an air RH of $14 \pm 1\%$ RH. Hence for that formulation, we concluded that $RH_c = 14 \pm 1\%$. The values of RH_c thus determined for each formulation are summarized in Table 3.2, along with the corresponding dew point temperatures. These results show that the critical RH for pore formation depends on the ethanol content in the pMDI. Any effect of propellant type is within the error of the RH measurement. For three of the four tested formulations, a more subtle morphological transition was observed when air humidity increased from the dry ($\leq 2\%$ RH) condition to a level slightly below RH_c . For example in Figure 3.8, the numerous submicron surface concavities present in particles from pMDI 134_18 sampled from very dry air were no longer present when the same pMDI was actuated in air humidified to $14 \pm 1\%$ RH. The rightmost column of Table 3.2 indicates for which formulations this phenomenon was observed. This finding suggests that in addition to forming pores, condensed water (liquid or solid) may alter the surface roughness of BDP particles.

Table 3.2: Summary of the critical RH for pore formation and the corresponding dew point temperature for each of the tested BDP formulations. The rightmost column indicates whether any particle surface modification was observed below RH_c .

Formulation Identifier	Propellant type	Ethanol Content (% w/w)	RH_c (± 1 % at 95% confidence interval)	Dew point temperature corresponding to RH_c ($^{\circ}\text{C}$)	Particle surface smoothing for $2\% < RH < RH_c$?
134_5	134a	5	14	-7 ± 1	Yes
134_18	134a	18	16	-6 ± 1	Yes
227_5	227ea	5	14	-7 ± 1	No
227_18	227ea	18	17	-5 ± 1	Yes

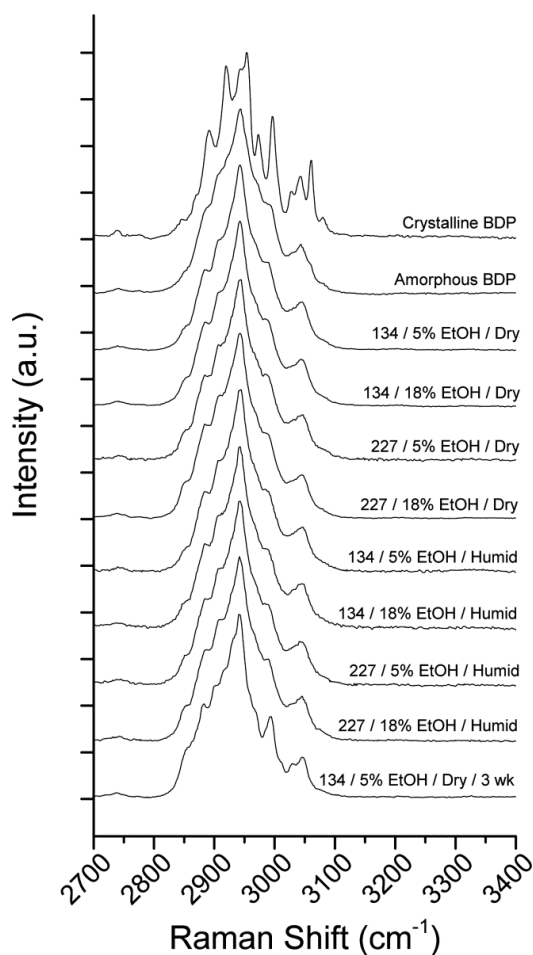


Figure 3.6: Raman spectra of BDP samples in the C-H stretch band. Spectra are offset vertically. Topmost two spectra: crystalline and amorphous standards. Third through tenth spectra from top: spectra from pMDI samples tested at either dry ($RH \leq 2\%$) or humid ($RH 38 \pm 1\%$ for p227ea inhalers or $RH 50 \pm 1\%$ for p134a inhalers) air. Bottom spectrum: sample obtained from pMDI 134_5 actuated in dry air and stored for three weeks in a desiccator at room temperature.

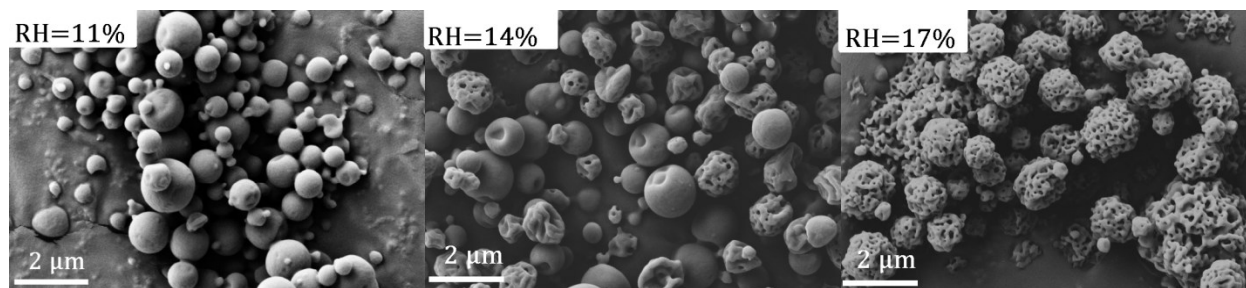


Figure 3.7: FE-SEM micrographs of the particles produced by pMDI 134_5 at varying air relative humidity. In this case a mixed population of porous and non-porous particles was observed at $14 \pm 1\%$ RH, indicating that the critical RH for pore formation RH_c lies in this range.

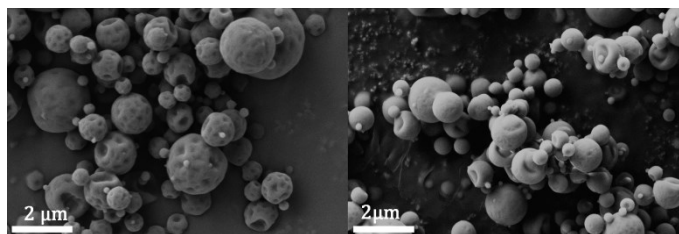


Figure 3.8: FE-SEM micrographs of particles sampled from pMDI 134_18 actuated in dry (left) or $14 \pm 1\%$ RH air.

It is interesting to place the current findings in the context of previous research by Zhu and colleagues, who separated a fraction of pMDI-produced aerosols for analysis using cascade impaction (Zhu et al. 2014a). They reported a transition from porous to nonporous particle morphology with solution formulations of BDP and fluticasone propionate as pMDI ethanol content was increased. The employed particle sampling technique allowed less time for aerosol maturation prior to deposition than in this work, which may account for qualitative differences in particle morphology compared to the present study. The proposed pore formation mechanism of Zhu et al. did not include any interaction with condensed water from the surrounding air, whereas the present study conclusively demonstrates that absent sufficient air humidity, no pores are formed in particles from BDP solution pMDIs regardless of formulation variables. In this study, we demonstrate that sufficiently humid air is a necessary condition for pore formation. The effect of ethanol content reported by Zhu et al. is likely due to ethanol's effect on RH_c as demonstrated in this work. Increasing ethanol content has been shown to slow propellant evaporation (Stein and Myrdal 2006), which will tend to reduce evaporative cooling and generally increase the temperature of the pMDI spray plume. Therefore the degree of water vapor saturation achieved as parcels of entrained air are cooled will decrease as spray plume

temperature increases. Thus the temperature and humidity of the air entrained into the pMDI spray plume and the temperature field within the spray plume itself largely determine whether water vapor saturation and subsequent morphology modification might occur.

These effects are illustrated conceptually in Figure 3.9. The dew point temperature—that is, the temperature at which the water vapor in air reaches saturation when cooled at constant pressure (Van Wylen and Sonntag 1965)—of air at 20 °C and 101.3 kPa absolute pressure is plotted against the air relative humidity using a simple model (Buck 1981). As an illustrative example, the value of RH_c determined for pMDI 134_18 ($16 \pm 1\%$) defines the center of a transition RH range wherein particle formation may occur either above or below the dew point temperature and thus below or above water vapor saturation. A transition range is expected rather than an abrupt transition because the temperature of pMDI spray plumes vary in time and space (Oliveira et al. 2013); this likely explains the observation of a mixed population of particle morphologies at RH_c . The intersection of this RH range with the dew point curve corresponds to a range of spray plume temperatures. Since pMDI spray plume temperatures are affected by formulation and device variables (Brambilla et al. 2011), the position and breadth of the transition RH region and the spray plume transition temperature region may respond to changes in formulation or device. Increasing ethanol content is expected to increase the spray plume temperature, which can be visualized on Figure 3.9 as an upward shift in the transition temperature range. This is expected to shift the transition RH region to the right and increase RH_c , as was observed in this study.

The dew point temperatures corresponding to the observed values of RH_c in Table 3.2 are all less than 0 °C. At these temperatures, the degree of saturation with respect to the ice phase is greater than with respect to the water phase (Hobbs 1974). It is therefore impossible to say whether the pore formers are liquid water droplets or ice crystals without additional experimental work. Either scenario is possible given the low aqueous solubility of BDP (Sakagami et al. 2002) and the complexities of nucleated water condensation or ice deposition from the vapor phase (Hoose and Möhler 2012). Regardless of the exact mechanism of pore formation, porosity in inhaled BDP microparticles alters both the particle density (Edwards et al. 1997) and the wettability via contact angle modification (Israelachvili 2011). Therefore the fate of a porous drug particle might differ from that of a smooth, solid particle after deposition in the airways, with potential implications on pharmacokinetics.

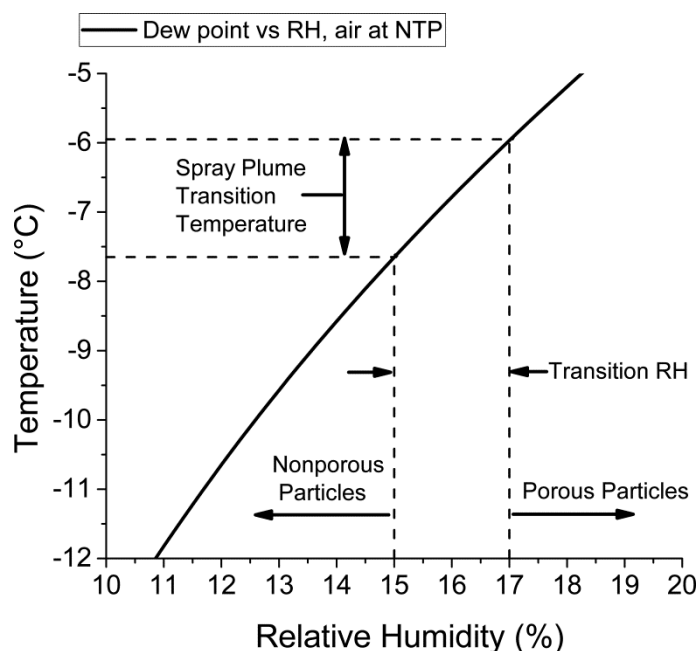


Figure 3.9: A plot of dew point temperature vs RH for air at normal temperature and pressure (NTP, 20 °C and 101.3 kPa), with annotations demonstrating the hypothesized effects of spray plume temperature and air RH on the resulting morphology of the particles produced by BDP solution pMDIs.

3.2.4 Conclusions

In this work, we demonstrate that air humidity can strongly affect the morphology of microparticles produced by solution pMDIs. Our results indicate that under the right environmental conditions, water in a condensed phase is capable of acting as a templating agent during particle formation from propellant solution droplets. This occurs at room temperature at levels of humidity that are very likely to be encountered during typical patient usage or in the clinic, and results in highly porous particles for the inhaled corticosteroid beclomethasone dipropionate. The resulting modifications to surface and internal morphology may affect particle density and wettability, with the potential to alter the way these porous drug particles interact with the human airways. While no humidity induced changes to the solid phase of BDP particles were observed in this work, this may not hold true for a more hydrophilic drug. Therefore, solution pMDI researchers and clinicians should strongly consider controlling or measuring the air humidity during experiments or trials.

These results may be of interest to researchers in the field of particle engineering for pulmonary drug delivery as well: highly porous particles have been shown to have advantageous aerodynamic properties (Tsapis et al. 2002), low cohesive forces (Tarara et al. 2000), and excellent colloidal stability in suspension (Tarara et al. 2004). However, producing such particles typically requires complicated formulation or processing techniques. Here, we produced porous microparticles with a relatively straightforward formulation and spray evaporation process, albeit at a very small scale.

Chapter 4 : A Particle Engineering Approach to Spray Drying

4.1 Introduction

In the particle engineering research group at the University of Alberta, much of the experimental work is related to the production and characterization of spray dried materials. Experiments employing model systems, such as monodisperse chains of evaporating microdroplets, enable fundamental investigations into the mechanisms of particle formation during spray drying. In combination with theoretical work, such experiments help illuminate the relationships between the formulation and process parameters and the physical properties of the resulting dried particles. In collaboration with industrial partners, University of Alberta particle engineers apply the knowledge gained from such theoretical and experimental investigations to efficiently develop robust formulations and spray drying processes at the laboratory scale. The work presented in this chapter represents my contributions to these efforts⁷.

In Section 4.2, the design approach and resulting design of a modular research spray dryer are presented. The flexible design allows the dryer to serve in a variety of capacities. Monodisperse spray drying is made possible by incorporating a monodisperse droplet generator, enabling systematic studies of particle formation as well as production of uniform test particles for additional experimentation or analysis. The dryer can also be configured for moderate throughput production of polydisperse respirable powders, with batch sizes on the order of 10 g. In this mode the attainable range of process parameters, the degree of instrumentation, the data

⁷ Some of the work presented in Chapter 4 is accepted for publication at the time of writing. My contributions to each of these works are described in the Preface.

Section 4.4 consists of peer-reviewed conference proceedings:

Ivey, J. W., Barona, D., Gomez, M., Kuan, L., McAllister, R., Oberhagemann, L., D'Sa, D., Lechuga-Ballesteros, D., Ajmera, A., Gracin, S. and Vehring, R. (2018). Isokinetic in-line sampling enables rapid characterization of atomizers and cyclones for spray drying process development, in *Respiratory Drug Delivery*, R. N. Dalby, et al., ed., VCU, Richmond, VA.

Section 4.5 consists of the “as-accepted” text of a manuscript which was in press at the time of writing:

Ivey, J. W., Bhambri, P., Church, T. K., Lewis, D. A. and Vehring, R. (2018). Experimental investigations of particle formation from propellant and solvent droplets using a monodisperse spray dryer. *Aerosol Sci. Technol.*:In Press. <https://doi.org/10.1080/02786826.2018.1451818>

logging capabilities, and the flexibility of the configuration all compare very favorably with commercially available laboratory spray drying equipment of similar cost. This dryer was utilized in subsequent work presented in this chapter.

In Section 4.3, a spray drying process model is described which is capable of accurately predicting powder physical properties based on the formulation and process parameters. A thermodynamic model is used to predict the temperature and relative humidity at the outlet or collection point of a spray dryer. For amorphous spray dried powders, this model can be used in conjunction with material characterization data—specifically, the moisture uptake isotherm and the plasticization curve—to predict the glass transition temperature and residual moisture content of the powder during and after processing. These techniques can greatly expedite the development and scale up of complex amorphous spray dried formulations: by placing physically based constraints on formulation and process parameters, model users can limit experimental work to explorations of a rationally defined parameter space.

Section 4.4 summarizes the development of an in-line isokinetic sampling system and its application to the characterization of spray dryer atomizers and cyclones. The text is presented unmodified from the peer-reviewed version save for re-numbering of headings, figures, tables, and equations to integrate with this thesis. It presents a method for rapid and cost effective characterization of spray drying process equipment. Once the atomizer and cyclone performance are quantified, the response of the dry powder particle size distribution to changes in the formulation or process parameters can be accurately modeled. This methodology is especially relevant to spray drying for pulmonary drug delivery, where the particle size distribution is of primary importance.

Experimental work studying the formation of amorphous and crystalline particles from monodisperse evaporating solution droplets with dissolved organic solutes is presented in Section 4.5; at the time of writing, the text of this section is currently submitted for publication as a research article. Monodisperse particles were generated from droplets of the HFA propellant p134, ethanol, or mixtures of the two. Comprehensive parametric studies evaluating the effects of solvent type, solution concentration, droplet diameter, and drying rate on the size, morphology, and solid phase of the dried particles were conducted for two solutes: the agricultural caffeine or the corticosteroid beclomethasone dipropionate. Powder physical properties were correlated with droplet composition and drying rate with the aid of a particle

formation model. The results demonstrate the capabilities and limitations of such models, and suggest there is a need for additional experimental and theoretical investigations of particle evolution following shell formation or crystal nucleation. The work demonstrates that monodisperse spray drying is a powerful technique for conducting fundamental studies on particle formation from solution droplets, particularly where measuring properties of interest requires collection of mg quantities of powdered sample.

4.2 Design of a modular research spray dryer

4.2.1 User requirements

Table 4.1: Summary of user requirements for the modular research spray dryer. ^a: The transition Reynolds number for fully developed flow in a cylindrical pipe was utilized as a first approximation, even though in the dryer the flow field is expected to be developing.

Attribute	User Requirement(s)
Dry particle mass median diameter range	<1 μm to 20 μm for monodisperse spray drying 1 – 5 μm for typical lab scale drying operations
Breadth of dry particle size distribution	GSD < 1.2 for monodisperse spray drying GSD < 2 for typical lab scale drying operations
Inlet temperature range	< 0 °C to 200 °C
Drying chamber Reynolds number	< 2300 for monodisperse spray drying ^a
Typical batch size	~ 10 g for typical lab scale drying operations
Solvent compatibility	Compatible with: water, ethanol, HFA propellants
Instrumentation	Required process measurements: inlet temperature, outlet temperature, drying gas flow rate, atomizing gas pressure, chamber gauge pressure Additional instrumentation requirements: near-nozzle region to be optically accessible; ports to enable particle sampling throughout the process

The particle engineering research group at the University of Alberta is concerned with developing and applying knowledge about spray drying processes. An experimental tool was required to advance this work: namely a laboratory scale spray dryer suitable for employment in a wide variety of capacities, ranging from fundamental experimental investigations of particle formation from monodisperse droplets (monodisperse spray drying), to conventional laboratory scale production of polydisperse powders. Thus the main requirement was a need for substantial versatility in the configuration and operating parameters. Specific user requirements developed

during discussions with the particle engineering group are summarized in Table 4.1. It was apparent from discussions within the group that commercially available laboratory spray drying equipment was unable to satisfy these requirements, it was therefore decided to undertake the design of a custom spray dryer.

4.2.2 Atomization equipment

Per Equation (1.16) the dry particle diameter produced from an evaporating solution droplet with concentration c_s can be estimated provided the initial diameter of the droplet, d_d , is known:

$$d_p = \sqrt[3]{\frac{c_s}{\rho_p}} d_d \quad (1.16)$$

The user requirements for dry particle size in Table 4.1 thus inform the choice of the atomization equipment. A custom twin fluid atomizer with mass median droplet diameter adjustable from around 7 to 20 μm for aqueous sprays, and a typical GSD of the spray of 1.7 – 1.8, was selected for use during moderate throughput, polydisperse powder production runs. Assuming feedstock concentration ranges from about 1 to 200 mg/mL, and that the spray of droplets dries into solid spheres with $\rho_p = 1000 \text{ kg/m}^3$, the resulting range of dry particle mass median diameter computed using Equation (1.16) is 1 to 12 μm , which satisfies the user requirement for dry particle size for a typical polydisperse lab scale spray drying process.

For monodisperse spray drying, a custom designed atomizer was selected; the design and operation of this atomizer is described in some detail in Section 4.5.2.1, and extensively in a research article (Azhdarzadeh et al. 2016). Briefly, the atomizer creates a monodisperse chain of droplets by producing longitudinal surface waves at a single wavelength on a laminar jet using a piezoceramic transducer; the jet subsequently undergoes regular breakup into droplets. The droplet chain is then disrupted and mixed with drying gas in the drying chamber of a spray dryer with a concentric jet of dispersing gas. The diameter of the produced droplets, d_d , is around twice the diameter of the microorifice, d_o , and may be manipulated further by adjusting the excitation frequency or the injection pressure (Berglund and Liu 1973). Taking as a first estimate

$$d_d \approx 2d_o \quad (4.1)$$

the dry particle size for various solution concentrations and orifice diameters were computed using Equation (1.16) assuming the droplets dry into solid spheres with $\rho_p = 1000 \text{ kg/m}^3$. The results⁸ are summarized in Table 4.2, and indicate that the required dry particle size range is covered using orifice diameters ranging from 5 to 80 μm . Notably, this atomizer was designed to have the same basic outer housing dimensions as the twin fluid atomizer, which made integrating the two atomization options with the spray dryer fairly straightforward.

Table 4.2: Dry particle diameter in μm computed using Equation (4.1) and Equation (1.16) for varying solution concentrations and orifice diameters. It was assumed that the droplets dry into solid spheres with $\rho_p = 1000 \text{ kg/m}^3$.

Orifice Diameter (μm)	Solution Concentration (mg/mL)			
	0.1	1	10	100
5	0.5	1.0	2.2	4.6
10	0.9	2.0	4.3	9.3
20	1.9	4.0	8.6	18.6
40	3.7	8.0	17.2	37.1
80	7.4	16.0	34.5	74.3

4.2.3 Drying chamber geometry

In spray drying processes, the mean residence time of a drying particle in the chamber must exceed the time required for the droplet to fully evaporate. Otherwise, the particle may still contain an appreciable amount of solvent when it exits the drying chamber, making it difficult or impossible to separate and collect the aerosol while maintaining desired powder physical properties. An additional consideration in the sizing of the drying chamber is related to the momentum distribution of the spray of atomized droplets. The drying chamber must be large enough to allow the droplets to decelerate and reach dynamic equilibrium with the drying gas, otherwise excessive wall deposition of droplets will negatively impact the product yield.

Given the user requirements summarized in Section 4.2.1 and the chosen atomization equipment described in Section 4.2.2, two extremum scenarios requiring large drying chamber volumes were examined assuming co-current operation:

⁸ More detailed calculations which account for the effects of the injection pressure and the transducer actuation frequency are presented in Appendix A3.

Drying Scenario 1. Polydisperse aqueous spray drying using the twin fluid atomizer and a large drying gas flow rate⁹ of 1000 L/min. Process requirements: drying temperature 40 °C, mass median droplet diameter $d_{d,50}$ 20 μm , atomized droplet diameter distribution GSD_d 1.8

Drying Scenario 2. Monodisperse aqueous spray drying using the monodisperse atomizer. Process requirements: initial droplet diameter 100 μm , drying temperature 40 °C, drying chamber Reynolds number < 2300.

The residence time, t_{res} , for the drying gas in a drying chamber with volume V_{ch} and drying gas volume flow rate \dot{V}_{dg} is

$$t_{\text{res}} = \frac{V_{\text{ch}}}{\dot{V}_{\text{dg}}} . \quad (4.2)$$

The residence time for drying droplets and particles will differ from this value somewhat due to initial droplet motion relative to the gas phase, gravitational settling, and turbulence effects; in drying processes with a polydisperse spray and turbulence or eddies in the flow field, the droplet or particle residence time is best described using a distribution rather than a single value (Huang et al. 2003). For purposes of drying chamber sizing calculations, turbulence effects on the residence time were neglected, and simple models and observations were employed to account for settling and initial droplet velocity relative to the drying gas.

For the polydisperse spray drying process of Drying Scenario 1, visual observations of the spray plume of the twin fluid atomizer were conducted in the lab, and indicated a fairly narrow plume angle of roughly 20 ° with a typical plume length L_{plume} of around 30 cm. To estimate a suitable chamber size for Drying Scenario 1, we consider the 90th mass percentile droplet, which for $d_{d,50} = 20 \mu\text{m}$ and $GSD_d = 1.8$ has diameter $d_{d,90} = 43 \mu\text{m}$. Assuming this droplet travels in one dimension an axial distance L_{plume} down a vertically oriented drying chamber before reaching dynamic equilibrium with the drying gas, and neglecting size changes

⁹ This about twice the drying gas flow rate employed in the most popular commercially available laboratory scale spray dryer, the Büchi B-290. A high drying gas flow rate is desirable for applications requiring very low collection relative humidity and low residual moisture content in the powder. However, increasing the drying gas flow rate for a given drying chamber geometry will reduce the residence time, so a relatively large drying gas flow rate was assumed to provide an extremum scenario for calculating the drying chamber volume.

due to evaporation to provide a conservative sizing estimate, the droplet will then travel down the drying chamber with velocity

$$v_d = v_{dg} + v_{\text{settling}} , \quad (4.3)$$

where v_{dg} is the velocity of the drying gas and v_{settling} is the terminal settling velocity of the droplet. The drying gas velocity depends on the cross-sectional area of the drying chamber, A_{ch} , and the drying gas volume flow rate \dot{V}_{dg} , and is approximately

$$v_{dg} = \frac{\dot{V}_{dg}}{A_{ch}} . \quad (4.4)$$

The droplet's diameter indicates that it settles in the Stokes drag regime, and thus for droplet density ρ_d the settling velocity in a gas with viscosity μ under gravitational acceleration g is (Hinds 1999)

$$v_{\text{settling}} = \frac{\rho_d g d_{d,90}^2}{18\mu} . \quad (4.5)$$

The time required for a droplet to evaporate depends on its diameter and the gas phase temperature and water vapor content; the droplet evaporation model presented in Section 4.5.2.5.2: Droplet evaporation rate was utilized to estimate droplet drying times for chamber sizing calculations. A contour plot of droplet drying time vs. droplet diameter and gas temperature for water droplets evaporating in dry air at 101.3 kPa ambient pressure is presented in Figure 4.1. This plot gives a drying time $t_1 \cong 1$ s for $d_{d,90} = 43$ μm at 40 °C. Then to accommodate scenario 1 we have as a criterion for the required drying chamber length

$$L_{ch1} \geq L_{\text{plume}} + v_d t_1 , \quad (4.6)$$

the value of which depends on the chamber diameter d_{ch} by way of the drying gas velocity dependence in Equation (4.4). This is explored in Table 4.3, in which minimum chamber length is computed using Equation (4.6) for three possible chamber diameters. This exercise indicates that scenario 1 can be accommodated with a drying chamber of less than 1 m in length provided the inner diameter is greater than around 20 cm.

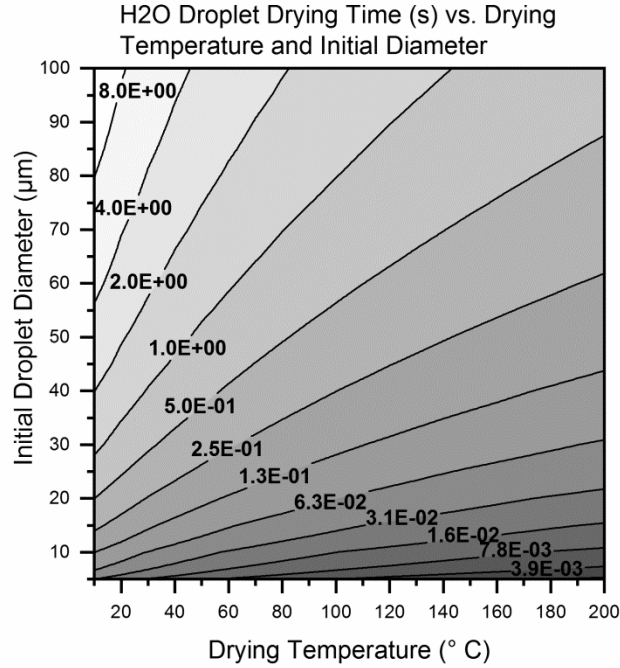


Figure 4.1: Contour plot of droplet drying time vs. initial droplet diameter and drying temperature as computed using the model presented in Section 4.5.2.5.2: Droplet evaporation rate. Dry air, 101.3 kPa pressure.

Table 4.3: Minimum chamber length calculated using Equation (4.6) for complete drying of a 43 µm droplet at 40 °C, at 1000 L/min drying gas flow rate, for a variety of drying chamber diameters.

Chamber diameter d_{ch} (cm)	Minimum chamber length L_{ch1} (m) per Equation (4.6)
10	2.5
20	0.9
30	0.6

For Drying Scenario 2, in which 100 µm droplets are produced using the monodisperse atomizer and dried at 40 °C, some assumptions about the atomizer operating parameters must be made to estimate the distance required for the droplets to reach dynamic equilibrium with the surrounding drying gas. To produce 100 µm droplets, an orifice diameter d_o of about 50 µm is required per Equation (4.1). For a cylindrical jet of a Newtonian liquid with diameter $d_j \cong d_o$, velocity v_j , density ρ_l , and surface tension in the gas σ_{lg} issuing into a gaseous medium with

density ρ_g , monodisperse breakup may occur provided the operation is in the Rayleigh breakup regime (Dumouchel 2008). This places constraints on the liquid and gas Weber numbers, We_L and We_G :

$$We_L = \frac{\rho_l v_j^2 d_o}{\sigma_{lg}} > 8 \quad (\text{Ranz 1959}) \quad (4.7)$$

and

$$We_G = \frac{\rho_g v_j^2 d_o}{\sigma_{lg}} < 0.4 \quad (\text{Ranz 1959}) \quad (4.8)$$

or

$$We_G < 1.2 + 3.41 Oh^{0.9}, \text{ with } Oh = \frac{\mu_l}{\sqrt{\rho_l d_o \sigma_{lg}}} \quad (\text{Sterling and Sleicher 1975}) \quad (4.9)$$

The criterion of Equation (4.7) describes a transition from dripping flow to a continuous jet, while those of Equation (4.8) and (4.9) describe a transition from breakup which is dominated by interfacial forces to breakup in which the aerodynamic forces exerted on the jet by the surrounding gas also play a role. For a 50 μm water jet in air at standard temperature and pressure, all three criteria are satisfied for $4 \text{ m/s} \leq v_j \leq 20 \text{ m/s}$; this provides an upper estimate of the initial droplet velocity for use in the drying chamber sizing calculation.

The cylindrical jet will travel a distance L_{bu} prior to breaking up into droplets, which can be neglected for purposes of this calculation: Leroux et al. (Leroux et al. 1996) found $\frac{L_{bu}}{d_o} \approx 50$ in the Rayleigh breakup regime in experiments on the stability of millimeter scale jets issuing from capillaries. We thus proceed by assuming the droplet enters the top of the vertically oriented drying chamber with initial velocity $v_0 \approx 20 \text{ m/s}$ and travels in one dimension, with the motion influenced by gravity and aerodynamic drag. The settling of a 100 μm spherical droplet occurs in the transition drag regime (Hinds 1999), with

$$v_{\text{settling}} = \left[\frac{4\rho_d d_d g}{3\rho_g C_d} \right]^{\frac{1}{2}} ; \quad (4.10)$$

the drag coefficient C_d can be computed based on the droplet Reynolds number Re_d using the empirical correlation (Crowe et al. 2011)

$$C_d = \frac{24}{Re_d} (1 + 0.15 Re_d^{0.687}) . \quad (4.11)$$

Plugging Equation (4.11) into Equation (4.10) and solving iteratively gives $v_{\text{settling}} = 0.25$ m/s. The droplet will travel some distance before decelerating to dynamic equilibrium, and this deceleration also occurs in the transition drag regime; to keep the calculations simple the distance traveled by the droplet during deceleration, $L_{\text{deceleration}}$, was approximated as the Stokes-regime stopping distance S (Equation (1.14) with $C_c \approx 1$):

$$L_{\text{deceleration}} \cong S = \frac{\rho_d v_{\text{rel},0} d_d^2}{18\mu} . \quad (4.12)$$

It should be noted that employing this formula will overestimate the stopping distance since the drag coefficient is underestimated; this is acceptable given the ‘worst case’ nature of this calculation. Then for $\rho_d = 1000$ kg/m³, $d_d = 100$ μm , and assuming $v_{\text{rel},0} \cong v_0 = 20$ m/s, Equation (4.12) gives $L_{\text{deceleration}} = 61$ cm.

Again consulting Figure 4.1 to estimate the required drying time for a 100 μm droplet drying at 40 °C gives $t_2 \cong 5$ s. The criterion for the required drying chamber length is then

$$L_{\text{ch},2} \geq L_{\text{deceleration}} + v_d t_2 . \quad (4.13)$$

The droplet velocity v_d in Equation (4.13) depends on the drying gas flow rate, \dot{V}_{dg} , and the chamber diameter, d_{ch} ; to compute a suitable value for drying gas flow rate, the process model presented in Section 4.3 was utilized. A sufficient quantity of drying gas is required to enable complete evaporation of the liquid in the process. The liquid flow rate was computed based on the known jet velocity v_j and the orifice diameter d_o . An adiabatic process in which the water was fully evaporated was assumed, and the drying gas flow rate resulting in a post-evaporation relative humidity of 50 % was computed to be about 200 L/min. With this estimate in hand, Equation (4.13) was used to explore the minimum drying chamber length for different chamber diameters; the results are presented in Table 4.4. A comparison with Table 4.3 indicates that Drying Scenario 2 is the more demanding in terms of the required size of the drying chamber. A fairly tall chamber is required to accommodate this extremum scenario. The drying chamber Reynolds number requirement is satisfied for the 20 or 30 cm chamber diameters.

Based on these calculations, 8 inch nominal stainless steel tubing was selected as the material for the main body of the drying chamber (actual inner diameter 200 mm). For ease of operation and to enable flexibility in the chamber configuration, the chamber design consisted of multiple sections 470 mm in length connected by flanged joints with sealing gaskets (tri-clamp).

The chamber length and thus the particle residence time can be adjusted by adding or removing chamber sections.

Table 4.4: Minimum chamber length and chamber Reynolds number for Drying Scenario 2 for three different chamber diameters. Assumes a 100 μm droplet drying at 40 $^{\circ}\text{C}$, which requires 61 cm to decelerate and subsequently evaporates in 5 s while traveling at a constant velocity with a drying gas flow rate of 200 L/min.

Chamber diameter d_{ch} (cm)	Minimum chamber length $L_{\text{ch},2}$ (m) per Equation (4.13)	Drying chamber Reynolds number
10	4.0	2800
20	2.4	1400
30	2.1	940

4.2.4 Collection hardware

A gas cyclone was chosen as the primary device for powder separation and collection; design specifications were kindly shared with the particle engineering group by an industrial partner. The specifics of the geometry shall remain unpublished at the request of the partner, but the design has a proven track record of collecting respirable sized particles with high efficiency for gas flow rates in the range of 300—600 L/min.

For collection of submicron particles, or for delicate engineered particles which might be damaged by wall impacts in a cyclone, the electrostatic precipitator furnished with the particle engineering group’s Büchi B-90 spray dryer was integrated with the custom spray dryer.

4.2.5 Design summary

Basic specifications of the as-built custom lab scale dryer are summarized in Table 4.5. A dryer configuration enabling production of polydisperse powder at a relatively high throughput is shown schematically in Figure 4.2, and an assembly drawing showing key drying hardware components in this configuration is shown in Figure 4.3. A single pass configuration with drying gas supplied by in house compressed dry air and nitrogen supply systems was employed to enable low humidity processing even at fairly low process temperatures. Drying gas can be heated using an electrical process gas heater, and chilled using a shell and tube heat exchanger with the shell side connected to a high capacity circulating chiller. An inlet temperature control

scheme was chosen for temperature control. The drying gas flow rate is controlled using a gas mass flow controller. The heated drying gas enters the top of the chamber through a port perpendicular to the long axis of the chamber, and then passes through a flow shaping element made up of a section of honeycomb material situated near the top of the chamber. The atomizer is installed at the centerline and clamped in place, and the near-nozzle region is optically accessible through four 40 mm sight glasses spaced at 90 ° around the chamber perimeter. The drying chamber is made up of the head assembly, one or two cylindrical chamber spools, and a large concentric reducer. Downstream of the drying chamber, a u-bend, a riser section, an elbow, an instrumentation manifold, and a series of reducers precedes the collection point. Sanitary tri-clamp fittings are used throughout. A HEPA filter is used to remove remaining fines from the exhaust gas, which is ducted to vent into a fume hood. Drying and collection hardware is mounted in an enclosure with glove ports to enable containment during drying of toxic or biohazardous materials. A photograph of the dryer at work in its enclosure is presented in Figure 4.4.

Table 4.5: Basic specifications of the custom research spray dryer. ^a: full range achievable using variable number of drying chamber sections.

Process configuration:	Co-current
Gas source:	Compressed N ₂ or air
Drying gas flow rate:	100—1000 L/min
Drying gas temperature:	-10 – 200 °C
Drying chamber volume:	13 – 43 L ^a
Gas residence time:	0.8 – 26 s ^a
Atomization hardware:	Twin fluid atomizer; continuous jet monodisperse atomizer
Collection hardware:	Gas cyclone, electrostatic precipitator
Instrumentation ports:	40 mm optical ports (4), 19 mm process ports (14)

Mechanical safety interlocks were employed to prevent dangerous operating conditions; please see Appendix A4.6 for wiring diagrams. Two normally closed temperature switches were wired in series with two normally open flow switches arranged in parallel in the control loop of a normally open solid state relay controlling the heater power circuit. The temperature switches

interrupt the heater power in the event of excessively high heater coil temperature or process gas temperature, while the flow switches ensure that the heater only receives power when gas is flowing through the system. A normally closed pressure switch with an adjustable set point was wired into the power supply circuit of the gas mass flow controller; in the event that the pressure exceeds the set point, power to the normally closed gas mass flow controller is interrupted, resulting in a shutdown of the drying gas and thus preventing overpressure events in the heater or drying chamber.

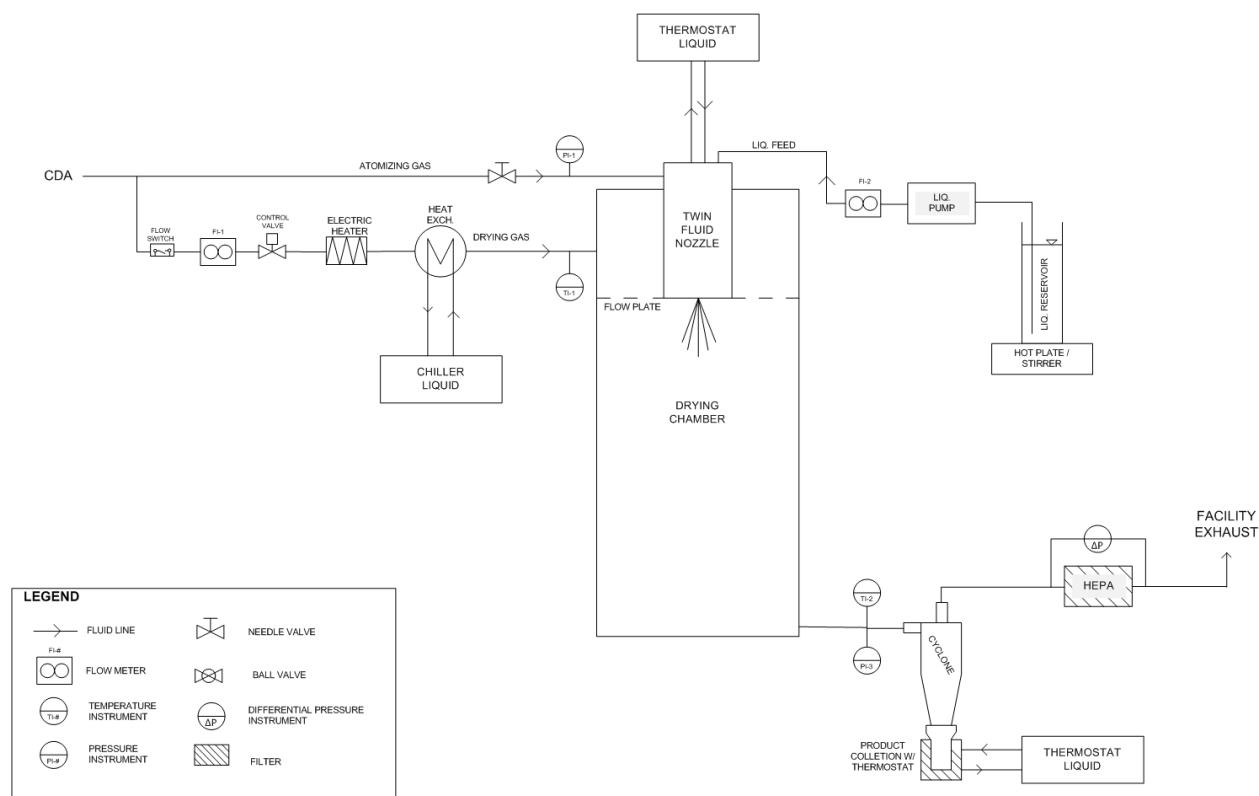


Figure 4.2: Schematic depicting a configuration of the research spray dryer to enable polydisperse spray drying in a mode similar to conventional laboratory scale spray dryers.

A modular I/O hardware platform (cDAQ 9178, National Instruments, Austin, TX, USA) was used for data acquisition and process control. Software was developed in LabView 2011 (National Instruments, Austin, TX, USA). The drying gas flow rate and the dryer inlet temperature set points were specified by the user. The drying gas flow rate was controlled with a 4–20 mA control signal to the gas mass flow controller. The inlet temperature was controlled by sending a 0.1 Hz digital square wave with a variable duty cycle to a solid state relay on the

heater power circuit; for each cycle of the square wave, the duty cycle was computed using a PID algorithm. Process data were sampled at 1 Hz, plotted real time, and logged for subsequent analysis.

Additional design documentation, including selected engineering drawings for drying hardware and wiring diagrams for controls components, are included in Appendix A4.

Item #	Part #	Description	Qty
1	N/A	ATOMIZER	1
2	LD044 r.00	HEAD CAP WELDMENT	1
3	ALFA-LAVAL 40-MOF-8-X	8" TRI-CLAMP GASKET, SILICONE	4
4	LD019 r.01	HEAD WELDMENT	1
5	MCMASSTER 942IT210	SHAFT COLLAR, 1.25" OD	1
6	LD024 r.00	STRAIGHTENER ASSEMBLY	1
7	ALFA-LAVAL 40MP-3-X	3" TRI-CLAMP GASKET, SILICONE	7
8	N/A	3" SANITARY SIGHT GLASS	4
9	LD028 r.00	SIGHT GLASS WELDMENT	1
10	LD011 r.00	DRYING CHAMBER SPOOL WELDMENT	2
11	LD014 r.01	8 X 3 CONCENTRIC REDUCER WELDMENT	1
12	ALFA-LAVAL B2CMP-3-316L-7	3" TRI-CLAMP ELBOW, 316L SS	1
13	ALFA-LAVAL B31-14MP-3x2-316-7	3" X 2" TRI-CLAMP CONCENTRIC REDUCER	1
14	ALFA-LAVAL 40MP-2-X	2" TRI-CLAMP GASKET, SILICONE	1
15	LD037 r.00	2 x 1 OUTLET REDUCER WELDMENT	1
16	ALFA-LAVAL 40MP-1-X	1" TRI-CLAMP GASKET, SILICONE	1
17	LD006 r.01	CYCLONE WELDMENT	1
18	LD008 r.00	VORTEX FINDER WELDMENT	1

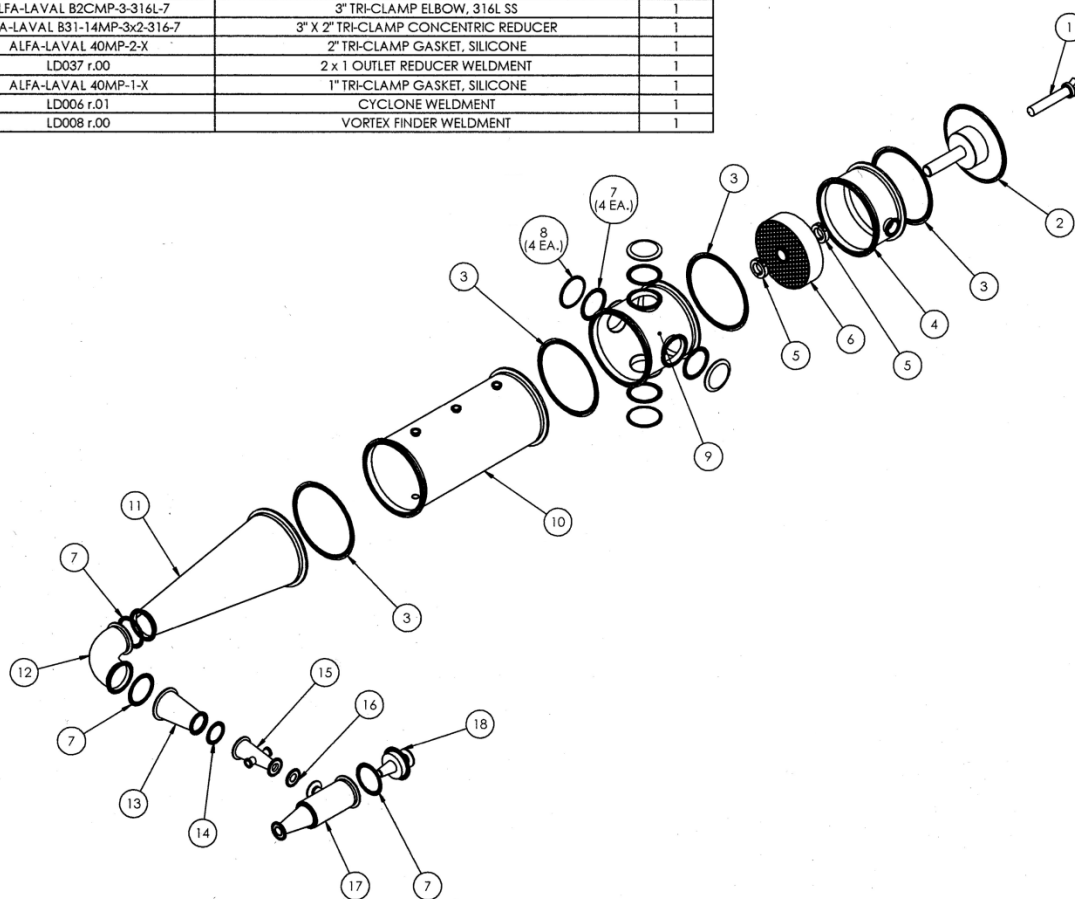


Figure 4.3: Assembly drawing showing major drying hardware components as configured for polydisperse spray drying.

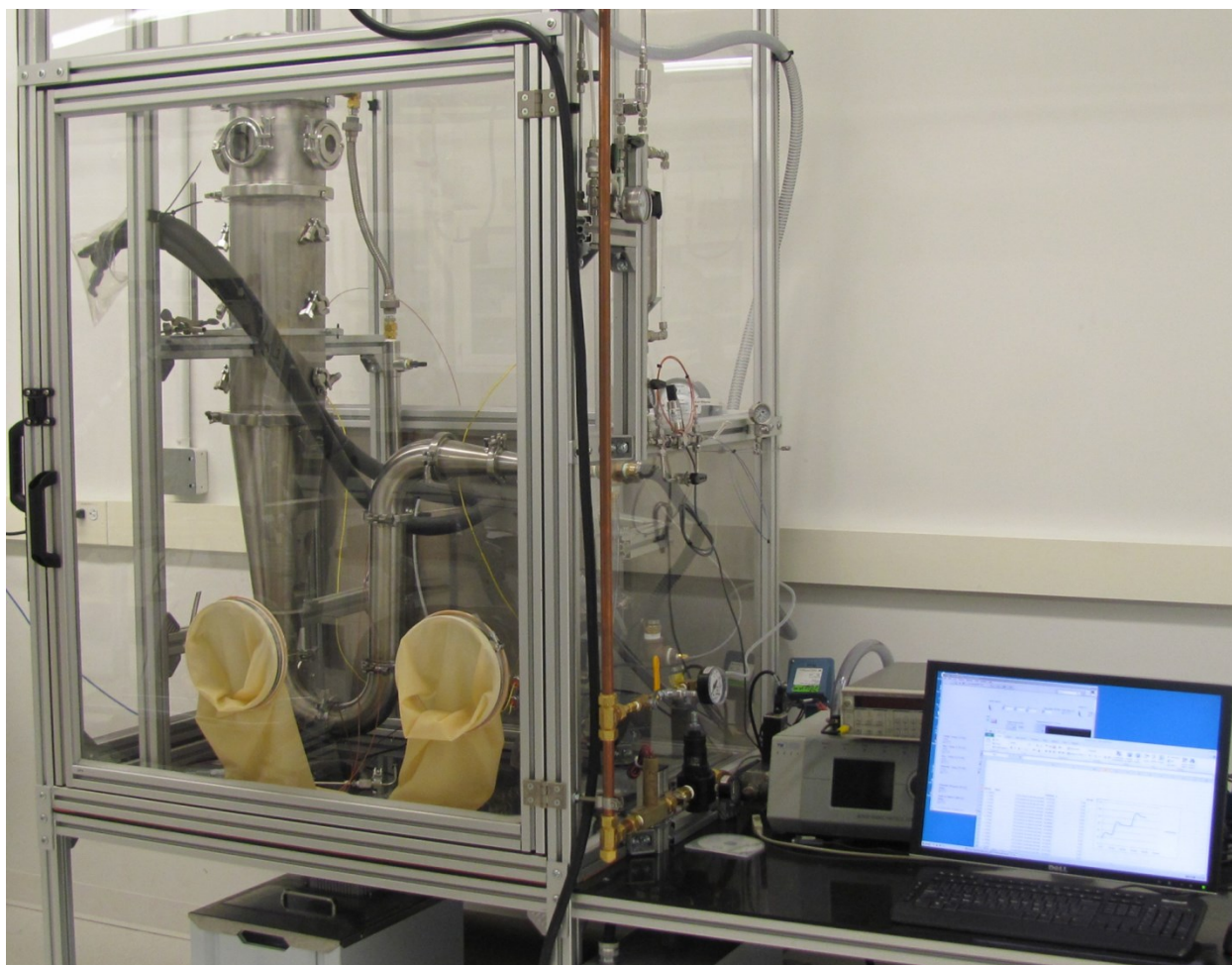


Figure 4.4: The research spray dryer in its enclosure.

4.3 Spray drying process modeling

The potency, physical stability, and chemical stability of spray dried powders are often strongly influenced by the temperature and amount of solvent vapor in the process. As discussed in Chapter 1, the conditions at the point where the powder is separated and collected (i.e. the outlet conditions) are especially important for amorphous materials. Fortunately for appropriately characterized process equipment the outlet conditions can be calculated using the principles of thermodynamics; this approach has been used with good success to aid in process development for spray dried pharmaceutical products (Dobry et al. 2009; Grasmeijer et al. 2013; Ivey and Vehring 2010). A similar process model was developed for the modular laboratory scale research spray dryer (Ivey and Vehring 2016), and it is described briefly here.

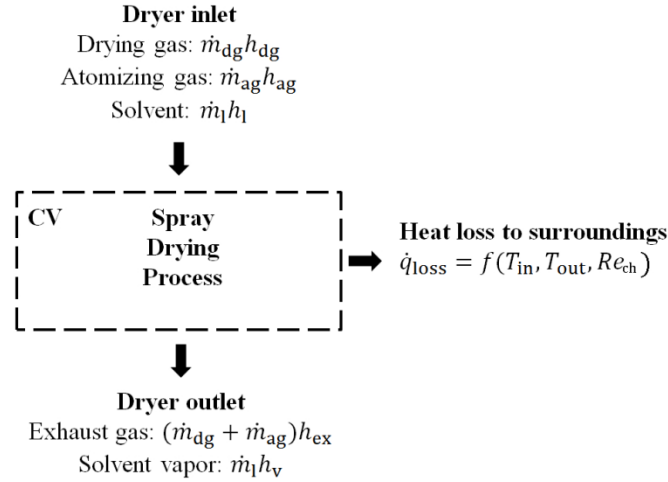


Figure 4.5: Control volume diagram for the spray drying process, illustrating the energy transport in the process. \dot{m} : mass flow rate; h : specific enthalpy.

In Figure 4.5, a control volume is placed around a spray drying process with twin fluid atomization, and the energy transfer terms are enumerated; the energy transport terms associated with the solids in the process are neglected, and it is assumed that the solvent is entirely evaporated prior to exiting at the outlet. A balance of energy statement for the drying process is

$$\dot{m}_{dg} h_{dg} + \dot{m}_{ag} h_{ag} + \dot{m}_l h_l = \dot{q}_{loss} + (\dot{m}_{dg} + \dot{m}_{ag}) h_{ex} + \dot{m}_l h_v . \quad (4.14)$$

The gas mass flow rates are known, and the mass flow rate of solvent can be calculated from the known mass flow rate, \dot{m}_{feed} , and mass fraction of solids, Y_s , for the feed solution:

$$\dot{m}_l = (1 - Y_s) \dot{m}_{feed} . \quad (4.15)$$

For the gas transport terms, a constant specific heat assumption is reasonable given the anticipated range of the process gas temperatures; assuming the process utilizes an ideal gas with specific heat $c_{p,g}$ the gas specific enthalpy changes can be related to temperature changes. For the drying gas, which enters the process at temperature T_{in} and exits at the outlet temperature T_{out} we have:

$$h_{ex} - h_{dg} = c_{p,g} (T_{out} - T_{in}) . \quad (4.16)$$

For atomizing gas entering at lab temperature T_{lab} and undergoing an isenthalpic decompression through the atomizer,

$$h_{ex} - h_{ag} = c_{p,g} (T_{out} - T_{lab}) . \quad (4.17)$$

The solvent enters the process as a liquid at a known temperature (in this case assumed at T_{lab}), is atomized, and evaporates at T_{evap} ¹⁰; the solvent then exits as vapor at T_{out} . Assuming as constants the solvent specific enthalpy of vaporization, ΔH_{vap} , liquid phase specific heat, $c_{p,l}$, and vapor phase specific heat, $c_{p,v}$, the specific enthalpy change of the solvent in the process is then

$$h_v - h_l = c_{p,v}(T_{out} - T_{evap}) + \Delta H_{vap} + c_{p,l}(T_{evap} - T_{lab}). \quad (4.18)$$

The rate of heat transfer to the surroundings, \dot{q}_{loss} , will in general depend on the process temperatures T_{in} and T_{out} , the Reynolds number in the drying chamber Re_{ch} , and the temperature and flow field of the air external to the drying chamber (Jiji 2006). For an enclosed installation in an air-conditioned laboratory, we assume the internal flow and temperature fields drive the heat transfer, and we have

$$\dot{q}_{loss} = f(T_{in}, T_{out}, Re_{ch}), \quad (4.19)$$

with f a functional dependence which can be determined experimentally. Once this is done, Equations (4.15) through (4.19) can be used to replace specific enthalpy terms with temperature terms in Equation (4.14); this results in an equation which can be solved to yield the outlet temperature T_{out} .

With T_{out} determined, the relative humidity (or degree of solvent vapor saturation) at the outlet can be computed as well. The relative humidity ϕ is defined as the ratio of the solvent vapor partial pressure, p_v , to its saturation pressure, p_{sat} :

$$\phi = \frac{p_v}{p_{sat}}. \quad (4.20)$$

The temperature dependence of p_{sat} can be accurately modeled using an Antoine equation with basic form

$$\log(p_{sat}) = a - \frac{b}{c + T_{out}}, \quad (4.21)$$

and the values of coefficients a , b , and c are readily available in the literature for common spray drying solvents. Thus the problem of determining the relative humidity ϕ is reduced to finding

¹⁰ This temperature is generally unknown, but fortunately for typical lab scale spray drying processes with common solvents the ΔH_{vap} term dominates the other two in the right hand side of Equation (4.18). Thus a reasonable guess for T_{evap} is more than adequate; the wet bulb temperature of the solvent at a typical drying gas inlet condition was used in this work.

an expression for p_v in terms of the known properties of the solvent—gas mixture at the outlet. This can be done using the ideal gas law.

Defining ω as the mass ratio of solvent vapor to dry gas, and assuming the solvent evaporates completely to form an ideal gas—solvent vapor mixture, we have

$$\omega = \frac{\dot{m}_l}{\dot{m}_{dg} + \dot{m}_{ag}} = \frac{M_v p_v}{M_g p_g}, \quad (4.22)$$

where M_v and M_g are the solvent and gas molar masses, and p_g is the partial pressure of the gas. The vapor and gas partial pressures are related to the total pressure at the dryer outlet, p_{out} , by Dalton's law of partial pressures:

$$p_g = p_{out} - p_v. \quad (4.23)$$

Plugging this expression for p_g into Equation (4.22) and solving for the vapor pressure gives

$$p_v = \frac{p_{out}}{1 + \frac{M_v}{\omega M_g}}. \quad (4.24)$$

The relative humidity ϕ can now be determined using Equations (4.20) through (4.24).

For spray drying of amorphous materials, knowledge of the relative humidity at the outlet or the collection point is very useful: if information on the solvent uptake behavior of the material is available, the residual solvent content in the powder at the dryer outlet or in the collector can be predicted. Further, if the plasticization curve is available, the glass transition temperature of the powder can be predicted as well. The combination of this thermodynamic process model with basic material characterization data for the formulation components is thus an extremely effective tool for defining the feasible operating space, which can greatly expedite formulation and process development in the laboratory.

To apply this model to the new modular research spray dryer, an experiment was conducted to determine the dependence of the rate of heat loss, \dot{q}_{loss} , on the drying process parameters. A series of 16 spray tests spanning the parameter ranges in Table 4.6 was conducted with pure water as the spray solvent. The dryer was operated with in-house compressed air as the source of drying and atomizing gas and with the enclosure doors closed to eliminate any variability related to air currents in the laboratory. At each condition, the dryer was allowed to thermally equilibrate until the outlet temperature stabilized within ± 0.2 °C for 10 min or more. Then process parameters were recorded and the system of Equations (4.14) through (4.18) was solved to determine the value of \dot{q}_{loss} for each tested condition; the values are plotted against the

outlet temperature, T_{out} , in the left panel of Figure 4.6. The rate of heat loss depends linearly ($R^2 = 0.98$) on the outlet temperature for the tested range of conditions:

$$\dot{q}_{\text{loss}} = 0.00661 \frac{\text{kW}}{^\circ\text{C}} T_{\text{out}} - 0.147 \text{ kW} . \quad (4.25)$$

Incorporating this result into the thermodynamic model of Equations (4.14) through (4.18) enabled accurate predictions of the dryer outlet temperature. As shown in the right panel of Figure 4.6, predicted values have been within 2 °C of observed values for subsequent spray drying runs spanning a wide variety of experimental conditions.

Table 4.6: Summary of process parameter ranges evaluated during heat loss characterization experiments.

Process parameter	Range evaluated
Drying gas flow rate	250—750 standard L/min
Atomizing gas flow rate	11—33 standard L/min
Liquid flow rate	2.5—7.5 mL/min
Inlet temperature	50—130 °C
Outlet temperature	30—80 °C
Enclosure temperature	24—32 °C

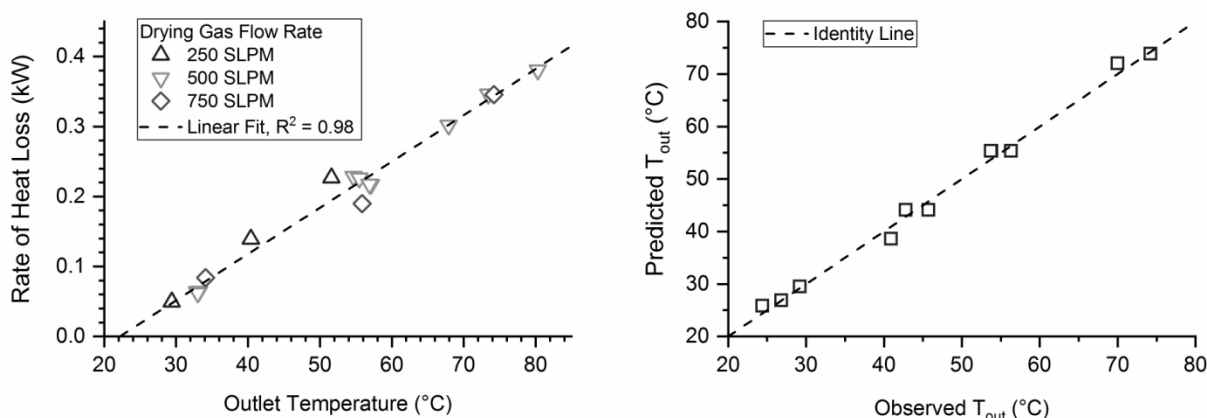


Figure 4.6: Left panel: rate of heat loss, \dot{q}_{loss} , vs. dryer outlet temperature, T_{out} , for water-only spray tests; data points are grouped by the drying gas flow rate. Right panel: model prediction vs. observed outlet temperature for subsequent actual spray drying runs conducted using the modular lab scale research dryer.

4.4 Isokinetic in-line sampling enables rapid characterization of atomizers and cyclones for spray drying process development

4.4.1 Introduction

In the competitive inhalation space, researchers developing the next generation of DPI and pMDI products have focused attention on tailoring the properties of the drug or carrier particles to maximize the efficiency and repeatability of drug delivery (Kaialy and Nokhodchi 2015; Vehring et al. 2012; Weers and Tarara 2014). Spray drying is an attractive process for producing such engineered particles since critical physical properties such as size, particle density, dispersibility, or flowability can be manipulated by modifying the formulation and process parameters (Hoe et al. 2014). Achieving such control requires knowledge about the process equipment itself: the size distribution of the collected dried particles depends strongly on the atomized droplet diameter distribution (Boraey and Vehring 2014), and may be influenced by the means of collection as well (Haig et al. 2014). Therefore, attaining reliable performance specifications for atomization and collection equipment is valuable in enabling the development of quantitative relationships between the formulation and process parameters and the critical quality attributes of the powder. To this end, an isokinetic aerosol sampling system was developed. The system was used to characterize the performance of an atomizer and cyclone supplied with a popular pharmaceutical lab scale spray dryer (B-290, Büchi, Flawil, Switzerland).

4.4.2 Methods

Real-time measurements of the aerodynamic particle size distribution of aerosols at various sampling locations within the drying process were attained using a variable flow rate isokinetic sampling system. The system is depicted schematically in Figure 4.7; it incorporates a time-of-flight aerodynamic particle sizer (Model 3321, TSI, Shoreview, MN, USA), and was integrated into a custom laboratory-scale spray dryer. Atomized droplet mass median diameter ($d_{0,50}$) and geometric standard deviation (GSD_0) were measured indirectly by atomizing and drying disaccharide solutions of known concentration (c_s). Dried aerosols were sampled and measured upstream of the cyclone separator. Assuming spherical particles of known particle density (ρ_p), droplet size distribution parameters were computed based on the measured mass

median diameter ($d_{a,50}$) and breadth (GSD_a) of the aerodynamic diameter distribution of the dried aerosol ($\rho^* = 1000 \text{ kg/m}^3$):

$$d_{0,50} = \sqrt[3]{\frac{\rho^*}{c_s}} \sqrt[6]{\frac{\rho^*}{\rho_p}} d_{a,50} \text{ with } GSD_0 = GSD_a . \quad (4.26)$$

Cyclone separation efficiency curves were determined by measuring the aerodynamic diameter distributions of the feed (inlet) and the overhead (outlet) fractions: for the i -th diameter bin (x_i) the fractional efficiency ($\eta(x_i)$) was computed based on the discrete count distributions of the feed and the overhead fractions ($f_F(x_i)$ and $f_O(x_i)$), respectively):

$$\eta(x_i) = 1 - \frac{f_O(x_i)}{f_F(x_i)} . \quad (4.27)$$

Atomization and collection equipment supplied with the Büchi B-290 was characterized with the sampling system. Atomized droplet diameter distributions were measured for a twin fluid atomizer with a 0.7 mm liquid nozzle diameter and a 1.5 mm diameter gas cap. Cyclone separation efficiency was determined at three gas flow rates for Büchi’s “high efficiency” cyclone design.

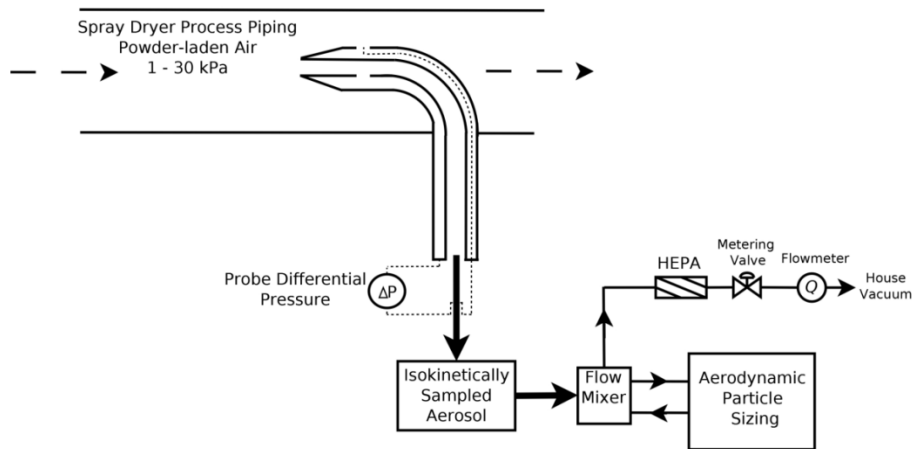


Figure 4.7: Schematic depiction of the isokinetic sampling system, which enabled real-time measurement of the aerodynamic particle size distribution of aerosol in the drying process at varying locations within the drying process.

4.4.3 Results and discussion

The response of the atomized droplet mass median diameter as measured using Equation (4.26) to changes in the atomizing air-liquid mass ratio is presented in Figure 4.8 for water sprays at 2, 5, or 8 mL/min and for ethanol at 5 mL/min. Measured geometric standard deviation

varied from 1.4 to 1.7 with a mean of 1.6 across all sprays, and was not obviously correlated with any parameter. A substantial degree of control on the atomized droplet diameter can be attained by manipulating the air-liquid ratio: for a given flow rate, this is achieved by modifying the atomizing air pressure. With this data, the mass median diameter $d_{p,50}$ for powders produced from solutions can be estimated provided an estimate is available for ρ_p :

$$d_{p,50} = \sqrt[3]{\frac{c_s}{\rho_p}} d_{0,50} . \quad (4.28)$$

Cyclone separation efficiency curves for the high-efficiency cyclone operating at 100, 200, and 300 SLPM gas flow rate are presented in Figure 4.9. Due to measurement range limitations of the aerodynamic particle size measurement system, extrapolation was required to estimate the 50% cut size of the cyclone operating at the highest tested flow rate. This was done using nonlinear curve fitting, with functional form

$$\eta(x) = 1 - \exp \left[\ln \left(\frac{1}{2} \right) \left(\frac{x}{x_{50}} \right)^m \right] . \quad (4.29)$$

Noting that the typical operating flow rate for a 100% aspirator setting is roughly 300 SLPM, this cyclone is expected to offer very high efficiency collection of typical powders for inhalation.

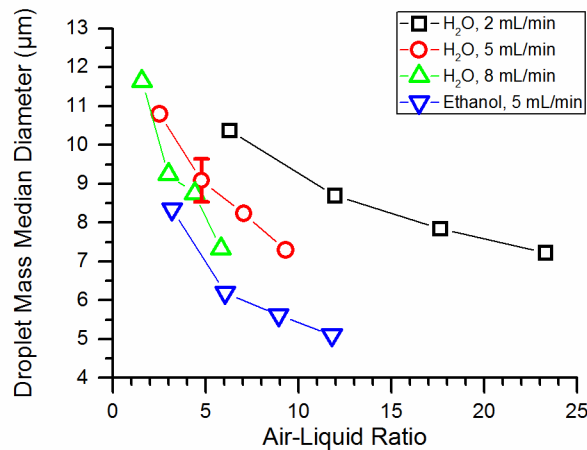


Figure 4.8: Mass median droplet diameter vs. atomization air-liquid ratio for the tested Büchi twin fluid atomizer. An intermediate point was replicated three times to assess measurement variability. The error bar represents one standard deviation.

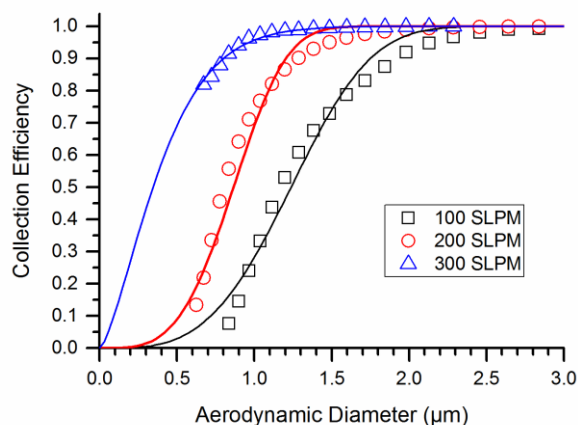


Figure 4.9: Separation efficiency curves for Büchi's high-efficiency cyclone separator at air flow rates of 100, 200, and 300 SLPM. Symbols: measured data using Equation (4.27). Closed lines: curve fits using Equation (4.29). 50% cut size from curve fits: 1.24 μm at 100 SLPM, 0.84 μm at 200 SLPM, 0.35 μm at 300 SLPM.

4.4.4 Conclusions

The new isokinetic sampling system allows real-time measurement of the aerodynamic particle size distribution in spray drying processes. The utility of the technique is demonstrated by rapidly characterizing the atomizer and cyclone of a commercially available lab scale spray dryer. Indirect measurements of atomized droplet diameter distributions enable estimation of the dry particle size distribution for solution-based drying processes. Measured cyclone collection efficiency curves indicate that the tested cyclone is capable of collecting even sub-micron particles with high efficiency. These equipment performance data are required for process models which quantify the relationships between the formulation and drying process parameters and the physical properties of the dried powders. Such mechanistic models can reveal critical process parameters and streamline process development, resulting in substantial savings in both time and capital.

4.5 Experimental investigations of particle formation from propellant and solvent droplets using a monodisperse spray dryer

4.5.1 Introduction

The formation of solid particles from evaporating solution droplets is a phenomenon of some interest in the field of aerosol science, with particular importance in pharmaceutical spray drying (Paudel et al. 2013; Singh and Van den Mooter 2016) and inhaled drug delivery (Sheth et

al. 2017; Zhu et al. 2015). The initial size and composition of the droplet and the conditions under which it evaporates determine the kinetics of the transition from droplet to residual particle, with consequences for the morphology and degree of molecular order of the dried particle (Hoe et al. 2014). Developing an understanding of these relationships is within the purview of particle engineering, a discipline that has proven useful in applications where precise control over particle properties is required. Examples in pharmaceutical spray drying include bioavailability enhancement of orally administered drugs (Davis 2018), glass stabilization of biologics (LeClair et al. 2016), and drug encapsulation for stabilization or modified release (Walz et al. 2017). In inhaled drug delivery, particle engineering principles have been applied to optimize powder physical properties for delivery with dry powder inhalers (Kaialy and Nokhodchi 2015; Weers and Tarara 2014) and to manipulate the size (Zhu et al. 2015) and physical properties (Haghi et al. 2014) of particles produced from pressurized metered dose inhalers.

Since the time required for a droplet to evaporate scales as the square of the droplet diameter (Fuchs 1959), the drying kinetics and thus the particle properties are very sensitive to the initial diameter of the droplet. For this reason, fundamental experimental investigations of particle formation from solution droplets have typically relied on the study of single evaporating droplets or chains of monodisperse droplets since these techniques offer precise control of the initial droplet diameter. Single droplet techniques allow measurements through the entire drying event, and excel where the quantities of interest can be measured by *in-situ* microscopic or spectroscopic observations (Fu et al. 2012; Kalume et al. 2017; Reid and Mitchem 2006), but are incapable of producing samples of dried powder in useful quantities. Chains of monodisperse droplets can be created using droplet-on-demand devices (also known as inkjet nozzles), where droplets are ejected singly from the nozzle by acoustic waves (Bogy and Talke 1984), or continuous jet devices (often called vibrating orifice aerosol generators), where a jet issues from the nozzle and is perturbed with regular longitudinal surface waves prior to breaking up into a chain of droplets (Berglund and Liu 1973). Droplet-on-demand generators may be better suited than continuous jet devices for applications requiring precise control or measurement of droplet evaporation rate due to the larger spacing between droplets in the chain (Baldelli et al. 2015). In terms of liquid throughput, production frequencies for continuous jet devices depend on orifice diameter, and range from approximately 10^4 to 10^6 Hz for droplets in the 10 to 100 μm range

(Berglund and Liu 1973). For droplet-on-demand devices, the production frequency is limited by the time required for each droplet to separate from the nozzle (Bogy and Talke 1984), with a practical maximum of several thousand Hz (Shah and Hayes 2002). Thus for applications requiring significant quantities of dried monodisperse powders, continuous jet devices are preferred based on feasible production rates (Liu et al. 2015). Continuous jet devices produce droplets which are roughly twice the diameter of the orifice, while for droplet-on-demand devices the droplet diameter is approximately the same size as the orifice (Patel and Chen 2007).

Integrating monodisperse droplet generators into lab scale spray dryers enables investigations of the relationships between droplet composition, drying rate, and dry particle properties (Leong 1981; Wu et al. 2007). Monodisperse spray drying has a proven track record as a useful technique for studies with moderately volatile solvent systems: changing the drying temperature has been shown to modify particle physical properties for dried milk particles (Rogers et al. 2012; Wu et al. 2014), amino acid particles (Lin et al. 2015), and for silica-lactose composite particles (Liu et al. 2012a). For solutions with multiple crystallizing solutes, modification of solute ratios may alter the overall morphology and the size of individual crystallites (Lin et al. 2017). Choice of solvent has been shown to affect the polymorphic composition and particle morphology for crystalline monodisperse particles formed from solution (Carver and Snyder 2012). In a series of studies on structured monodisperse microparticles, researchers have utilized monodisperse spray drying of complex feedstocks to demonstrate an ability to alter the release rate of model drugs by modifying excipient ratios (Liu et al. 2011; 2013) and pH (Liu et al. 2012a).

In the present study, we build on prior experimental work by utilizing a monodisperse spray dryer to systematically investigate particle formation from solution droplets. Parametric studies are conducted to explore the effects of solution composition, droplet size, and drying rate for two organic solutes: beclomethasone dipropionate (BDP) and caffeine. Using a novel nozzle design, solvent systems including volatile hydrofluoroalkane propellants are evaluated. Where applicable, particle formation models are utilized to interpret results.

4.5.2 Methods

4.5.2.1 Generation of monodisperse droplets

Monodisperse droplets were generated using a custom, continuous-jet droplet generator. The design and capabilities of this droplet generator are described in detail elsewhere (Azhdarzadeh et al. 2016); the device is capable of operating at pressure of up to 2 MPa, with the liquid supply temperature controllable in the range of -10 to 50 °C, enabling experiments with superheated liquid propellants as well as less volatile solvents. Solutions were supplied from a 300 mL pressure vessel, with the supply pressure controllable by means of a pressure regulator. To monitor the flow rate during monodisperse droplet production, the liquid flowed through a calibrated laminar flow element (LFE) consisting of a coil of capillary tubing; the pressure drop through this element was monitored using a differential pressure transducer (Model PX419, Omega, Laval, QC, Canada). The droplet generator utilized laser-drilled pinhole orifice plates with diameters ranging from 5 to 35 μm (Edmund Optics, Barrington, NJ, USA). Orifice diameters were verified using scanning electron microscopy (EVO M10, Zeiss, Jena, Germany) prior to use. Orifice discharge coefficients were measured experimentally by gravimetric determination of mass discharge rate. Liquid jets were perturbed by a lead zirconate titanate (PZ26) piezoceramic transducer driven by a function generator (Model DS340, Stanford Research Systems, Sunnyvale, CA, USA) supplying square waveforms with peak-to-peak voltage of 10 V and set frequencies ranging from 30 kHz to 1.1 MHz. For each particle drying experiment, monodisperse operation was achieved by sweeping the frequency until monodisperse jet breakup was achieved; this was verified by measuring the width of the size distribution of dried aerosol particles with an aerodynamic particle sizer (Model 3321, TSI, Shoreview, MN, USA) and visually using a laminar cross flow jet deflection technique (Ström 1969).

4.5.2.2 Monodisperse spray drying

The experimental setup for monodisperse spray drying is depicted schematically in Figure 4.10. The droplet generator was integrated with a custom laboratory scale spray dryer with modular stainless steel construction. The drying chamber consisted of a main cylindrical section 200 mm in diameter by 620 mm in length plus a 200 mm x 75 mm conical reducer section 500 mm in length, for an effective chamber volume of roughly 30 L. Drying air was

supplied at 100 standard L/min using a mass flow controller, and heated to the set inlet temperature using a gas heater and a PID controller. Gas temperatures were monitored near the bottom of the cylindrical section of the chamber and at the dryer outlet as indicated in the schematic. The monodisperse droplet chain was disrupted and mixed with the drying gas using a small amount of dispersing air. Dried aerosol particles were sampled by withdrawing a portion of the process gas through a 90 ° sampling probe using a vacuum pump, and separated using either track-etched polycarbonate membrane filters (IsoPore 0.2 μm , Millipore, Billerica, MA, USA) or using a custom single-nozzle, single stage inertial impactor with a stage cut size of approximately 0.8 μm (Wang et al. 2017).

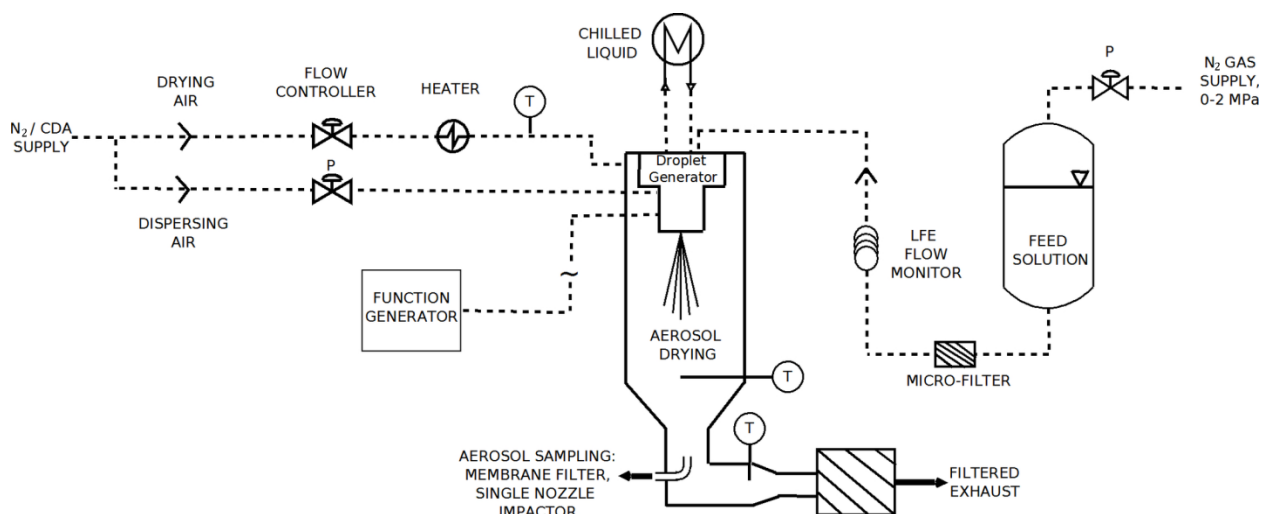


Figure 4.10: Schematic depicting the experimental setup for monodisperse spray drying.

Solutes BDP (kindly supplied by Chiesi Ltd., Chippenham, UK) and anhydrous caffeine (Sigma-Aldrich, Saint Louis, MO, USA) were dissolved in anhydrous ethanol (Commercial Alcohols, Toronto, ON, Canada), the hydrofluoroalkane propellant 134a (p134a) (Linde, Mississauga, ON, Canada), or combinations thereof. A diaphragm pump (Model X2008, Pamasol AG, Pfäffikon, Switzerland) was used to pressure fill the feed solution vessel for solutions utilizing p134a. Complete dissolution was verified visually. Solutions containing p134a were supplied to the orifice at ≥ 700 kPa absolute pressure to prevent flashing in the supply lines, and the droplet generator was cooled to ≤ 5 °C to suppress flash-boiling in the jet prior to droplet breakup (Shemirani et al. 2015).

4.5.2.3 Particle morphology assessment with ultramicroscopy

Collected particle samples were examined using field emission scanning electron microscopy (FE-SEM). Samples were first coated in gold by sputter deposition (Desk II, Denton Vacuum, Moorestown, NJ, USA) for 120 s at 15-20 mA then imaged using FE-SEM (Sigma FE-SEM, Zeiss, Jena, Germany). A 30 μm aperture was employed, and accelerating voltage was 2 – 5 kV. Imaging was achieved by detection of secondary electrons using the out-of-lens detector. Selected samples were analyzed by sectioning particles with a focused beam of gallium ions (30 kV accelerating voltage, 50 pA beam current, 40 μm aperture) followed by imaging with a beam of helium ions (30 kV accelerating voltage, 1 pA beam current) (Orion NanoFab, Zeiss, Jena, Germany). Selected micrographs were analyzed to evaluate particle size distributions. Particle edges were delineated using circles for spheroidal particles (MATLAB R2014a, Mathworks, Natick, MA, USA). The edges of collapsed spheroidal particles and irregular crystalline particles were delineated with freehand tracing and polygons, respectively (ImageJ, NIH, Bethesda, MD, USA). For each particle, a projected area equivalent diameter (Hinds 1999) $d_{A,\text{eq}}$ was then computed based on the area enclosed by the bounding shape A :

$$d_{A,\text{eq}} = \sqrt{\frac{4A}{\pi}} . \quad (4.30)$$

For particles composed of discernible primary crystallites, maximum and minimum Feret diameters (Hinds 1999) of individual crystallites were determined for each particle batch.

4.5.2.4 Solid phase analysis by Raman spectroscopy

Selected BDP microparticle samples were assessed for crystallinity using Raman microscopy, employing a method which is described in detail elsewhere (Ivey et al. 2017). Briefly, BDP samples were separated using the single stage, single nozzle impactor and analyzed directly on the aluminum collection plates using a Raman microscope (inVia, Renishaw, Prospect Scientific, ON, Canada). The excitation source was an Argon-ion laser operating at a wavelength of 514.5 nm and a power of 5 mW, focused through a 20x objective lens, resulting in a spot size of roughly 5 μm . Spectra were acquired with a resolution of approximately 1.5 cm^{-1} ; the C-H stretch band around 3000 cm^{-1} was used to assess the degree of crystallinity present in the BDP samples by comparison with amorphous and crystalline reference standards.

Caffeine polymorphism was investigated using macro-Raman spectroscopy using a custom dispersive Raman instrument. Selected caffeine samples were collected onto membrane filters then transferred into an aluminum sample holder with a small cavity. A 671 nm solid state laser (Ventus 671, Laser Quantum, Stockport, Cheshire, UK) operating at 50-200 mW was focused onto the samples to a spot size of approximately 50 μm with a convex lens. Scattered light was collimated and filtered to remove the laser line, then separated into its spectrum using a Czerny-Turner spectrograph (SpectraPro-500i, Acton Research Corp., Acton, MA, USA). The sensor was a CCD detector (LN/CCD-400EHR-G1, Princeton Instruments, Trenton, NJ, USA). The spectral resolution of the system was approximately 1.2 cm^{-1} . The spectra from $100 - 1600\text{ cm}^{-1}$ were collected then processed and analyzed using software (Origin 2015, OriginLab, Northampton, MA, USA).

Reference samples of the two caffeine polymorphs were prepared using techniques described in the literature (Descamps et al. 2005). Caffeine II was prepared by annealing the as-received material for 18 hours at $90-100\text{ }^\circ\text{C}$ to allow conversion of any trace caffeine I. Caffeine I was prepared by heating the as-received material to $155-160\text{ }^\circ\text{C}$ for 30 minutes, then quenching in liquid nitrogen immediately prior to analysis.

4.5.2.5 Modeling

4.5.2.5.1 Solids production rate, initial droplet diameter

Since the drying kinetics of evaporating droplets with dissolved solids depend strongly on the initial droplet diameter, the experimentalist requires a means of control over the droplet diameter. In the present work, this was achieved by manipulating the orifice diameter, the injection pressure, and the excitation frequency. The effects of these independent variables on the initial droplet diameter and the resulting solids production rate were estimated as follows. The diameters of the droplets produced by a continuous jet droplet generator depend on the liquid flow rate and the frequency at which the jet breakup occurs. For an incompressible liquid jet issuing from a circular orifice of diameter d_o , the liquid volume flow rate Q is related to the pressure difference across the orifice Δp by

$$Q = C_d \frac{\pi d_o^2}{4} \sqrt{\frac{2\Delta p}{\rho_l}} \quad , \quad (4.31)$$

where C_d is the discharge coefficient and ρ_l is the liquid density (Bayvel and Orzechowski 1993).

For a given solution concentration, c_s , Equation (4.31) can be used to estimate the rate of dry solids production, \dot{m}_s , during monodisperse spray drying runs:

$$\dot{m}_s = c_s Q = c_s C_d \frac{\pi d_0^2}{4} \sqrt{\frac{2\Delta p}{\rho_l}} . \quad (4.32)$$

Assuming the liquid jet undergoes monodisperse breakup, with droplets of diameter d_d produced at frequency f , the volume flow rate of liquid Q may also be written as (Berglund and Liu 1973)

$$Q = \frac{\pi d_d^3}{6} f . \quad (4.33)$$

Using this expression to eliminate Q from Equation (4.31) and solving for the droplet diameter d_d gives

$$d_d = \left[\frac{3c_s d_0^2}{2f} \left(\frac{2\Delta p}{\rho_l} \right)^{\frac{1}{2}} \right]^{\frac{1}{3}} . \quad (4.34)$$

For a given injection pressure, production frequency, and orifice diameter, Equation (4.34) allows estimation of the initial droplet diameter produced from a continuous-jet droplet generator operating in monodisperse breakup mode.

4.5.2.5.2 Droplet evaporation rate

The solvent evaporation rate exerts a strong influence on the drying kinetics, and will vary as drying temperature or droplet composition are altered. Estimating the evaporation rate for monodisperse drying experiments enables utilization of particle formation models such as the one presented in Section 4.5.2.5.3, which can facilitate particle design or analysis of experimental results. Therefore, evaporation rates were computed for the pure solvents using an established analytical model.

The rate of evaporation of a spherical droplet in a uniform, quiescent, continuous medium under the quasistationary assumption—that is, that the droplet surface recession during evaporation has a negligible effect on the evaporation rate—can be determined analytically (Fuchs 1959). In the case of evaporating propellant droplets, the Stefan flow will increase the rate of evaporation (Finlay 2001a). An expression for the evaporation rate κ including the effect of the Stefan flow is (Vehring et al. 2007):

$$\kappa = 8D_v \frac{\rho_g}{\rho_l} \ln \left(\frac{1-Y_\infty}{1-Y_s(T_{eq})} \right) . \quad (4.35)$$

Here D_v is the mass diffusivity of the vapor species in the gas, ρ_g is the density of the gas phase, and Y_s and Y_∞ are the mass fractions of vapor present at the droplet surface and far from the droplet, respectively. The vapor mass fraction at the droplet surface depends on the droplet temperature. Assuming the gas phase at the droplet surface is saturated with vapor, this dependence, $Y_s(T_{eq})$, can be represented using an Antoine equation. Therefore, to solve Equation (4.35), the equilibrium droplet temperature T_{eq} must be known. This was determined by finding the root of the equation

$$\frac{L}{c_p} - \frac{(1-Y_s(T_{eq}))^{\frac{1}{Le}} (T_\infty - T_{eq})}{(1-Y_\infty)^{\frac{1}{Le}} - (1-Y_s(T_{eq}))^{\frac{1}{Le}}} = 0, \text{ with } Le = \frac{k}{c_p \rho_g D_v}, \quad (4.36)$$

where L is the latent heat of vaporization of the solvent, c_p is the specific heat of the solvent vapor, T_∞ is the temperature of the gas phase far from the droplet surface, and k is the gas phase thermal conductivity.

This model provides a useful first estimate for the evaporation rate during monodisperse spray drying runs. Therefore Equations (4.35) and (4.36) were used to estimate evaporation rates for pure solvents ethanol and p134a. The model was verified by comparison with published experimental data for water droplets (Vehring et al. 2007). Additional assumptions and methods for determining thermophysical properties of air and solvents, and model results, are presented in Section 4.5.6: Supplementary information.

4.5.2.5.3 Particle formation model

The physical properties of the dry particles resulting from the evaporation of solution droplets are largely determined by the composition and the drying kinetics. In particular, the dry particle size, density, and morphology depend on the size and composition of the droplet at characteristic times: the time at which a surface shell forms for amorphous systems, and the time at which crystal nucleation commences for crystalline systems (Vehring 2008). Under the assumption of a constant droplet evaporation rate, particle formation models can be applied to compute closely related characteristic times: the time to reach solute true density at the surface for amorphous particles, and the time to reach solute saturation at the droplet surface for crystalline particles. These modeling techniques may complement experimental investigations by revealing the mechanisms underlying the relationships between the droplet composition, the

evaporation rate, and the dry particle physical properties. To this end, a hybrid analytical-numerical model describing the temporal evolution of the radial solute concentration profile in a spherical droplet drying at a uniform evaporation rate was employed (Boraey and Vehring 2014). The temporal dependence of the solute concentration profiles is quantified in terms of the dimensionless drying time τ :

$$\tau = \frac{\kappa t}{d_0^2} , \quad (4.37)$$

where d_0 is the initial droplet diameter. Numerical results were classified into several regimes based on the Péclet number, which in this application quantifies the ratio of the evaporation rate to the speed of solute diffusion:

$$Pe = \frac{\kappa}{8D_s} . \quad (4.38)$$

Here D_s is the mass diffusivity of the solute in the solvent. Using a curve fit for model results for $0.5 < Pe < 25$ (Boraey and Vehring 2014), an equation for the dimensionless time to reach saturation at the surface, τ_{sat} , was derived (full derivation in Section 4.5.6: Supplementary information):

$$S_0 \left(\frac{E_{ss} - e^{-n}}{1 - e^{-n}} - \frac{E_{ss} - 1}{1 - e^{-n}} e^{-n\tau_{\text{sat}}} \right) (1 - \tau_{\text{sat}})^{-\frac{3}{2}} - 1 = 0 , \quad (4.39)$$

where S_0 is the initial degree of saturation of the solute, the growth parameter $n = 15Pe^{0.7}$, and the steady state enrichment E_{ss} is given by

$$E_{ss} = 1 + \frac{Pe}{5} + \frac{Pe^2}{100} - \frac{Pe^3}{4000} . \quad (4.40)$$

After iteratively solving Equation (4.39) for τ_{sat} , the time to reach saturation t_{sat} and the time available for crystal nucleation and growth t_c were computed:

$$t_{\text{sat}} = \frac{\tau_{\text{sat}} d_0^2}{\kappa} . \quad (4.41)$$

and

$$t_c = (1 - \tau_{\text{sat}}) \frac{d_0^2}{\kappa} . \quad (4.42)$$

Methods for determining solute solubility and mass diffusivity are presented in Section 4.5.6: Supplementary information.

4.5.2.6 Experimental design for monodisperse spray drying runs

The motivation of the experimental program was to thoroughly explore the effects of droplet composition, droplet initial diameter, and evaporation rate on the resulting morphology

and solid phase composition of the dried BDP and caffeine particles. The evaluated ranges of experimental parameters are summarized in Table 4.7. Solute concentration ranges were selected based on the solute, with the high level chosen to stay below the solubility limit. Droplet initial diameter was manipulated primarily by changing the orifice diameter, which ranged from 5 to 35 μm . The corresponding range of initial droplet diameters per Equation (4.34) was 10 – 100 μm . The effects of changing droplet evaporation rate were evaluated by varying the drying inlet temperature from 30 ° C to 130 ° C.

Table 4.7: Summary of experimental parameters and resulting estimated solids production rate, monodisperse spray drying runs.

Solute (concentration, mg/mL)	Solvent	Co-solvent (%w/w)	Orifice Diameter (μm)	Inlet Temperature(s) (° C)	Solids Production Rate, Equation (4.32) (mg/min)
BDP (0.1)	p134a	ethanol (5)	23	30, 130	0.07
BDP (0.1)	p134a	ethanol (20)	23	30, 130	0.07
BDP (2.0)	p134a	ethanol (5)	5	30	0.07
BDP (2.0)	p134a	ethanol (5)	23	30, 130	1
BDP (2.0)	p134a	ethanol (20)	23	30, 130	1
BDP (2.0)	p134a	ethanol (20)	35	30, 130	3
caffeine (0.1)	ethanol	-	10	30, 130	0.008
caffeine (0.1)	ethanol	-	35	30, 80, 130	0.08
caffeine (0.1)	p134a	-	10	30, 130	0.008
caffeine (1.0)	p134a	ethanol (5)	35	30, 130	1
caffeine (4.0)	ethanol	-	10	30, 80, 130	0.3
caffeine (4.0)	ethanol	-	35	30, 130	3

4.5.3 Results and discussion

Highly uniform microparticles were produced from both solutes dissolved in the solvents ethanol, p134a, and mixtures thereof; selected representative micrographs demonstrating the observed variety of particle sizes and shapes are presented in Figure 4.11. Particle size data and Raman spectroscopy results are summarized in Table 4.8 and Table 4.9. For selected particle batches the projected area equivalent diameters were fit using a cumulative lognormal distribution function using nonlinear regression; for all fits the adjusted coefficient of determination R^2 was ≥ 0.92 . The geometric standard deviations (GSDs) for these fits ranged

from 1.1 to 1.3 across all experiments, indicating a high degree of uniformity in particle size. A notable feature observed in many samples was the presence of some proportion of particles larger than the main population, manifesting as a second mode in the projected area equivalent diameter distributions. The diameter of this second mode was typically around 25% greater than the median particle diameter, indicating that these particles were formed from droplets with twice the mass of the median droplet. Thus these larger droplets likely resulted from the coalescence of two median-sized droplets. Some samples contained a fraction of fines comprising 10 % or less of all particles by count; these are likely the result of the formation of satellite droplets by the droplet generator (Anders et al. 1992), which subsequently dry into particles substantially smaller than the main population. Despite the presence of satellites and doublets, the degree of uniformity achieved was adequate to enable evaluation of the effects of droplet size, composition, and evaporation rate on the dry particle properties for BDP and caffeine.

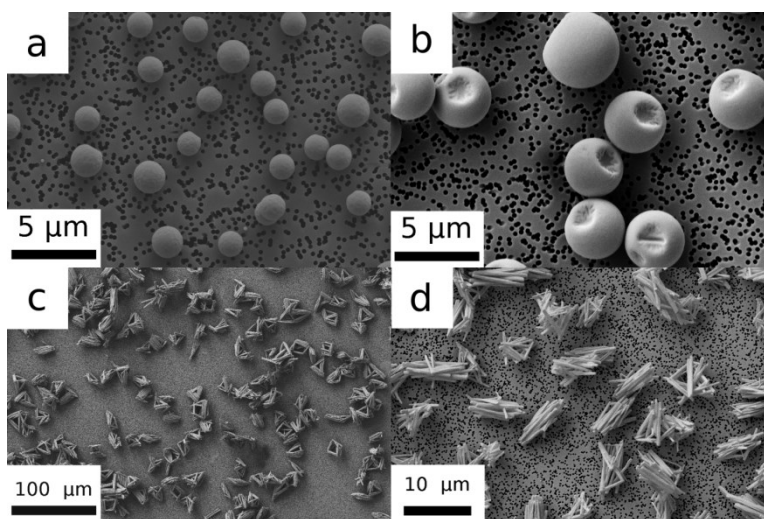


Figure 4.11: Highly uniform microparticles were produced using various orifice diameters, solvents, solutes, and drying conditions. a). 0.1 mg/mL BDP dissolved in p134a + 20 % w/w ethanol, 23 μm orifice, dried at 130 $^{\circ}\text{C}$ inlet temperature. b). 2.0 mg/mL BDP dissolved in p134a + 20% w/w ethanol, 23 μm orifice, dried at 130 $^{\circ}\text{C}$ inlet temperature. c). 4.0 mg/mL caffeine dissolved in ethanol, 35 μm orifice, dried at 130 $^{\circ}\text{C}$ inlet temperature. d). 4.0 mg/mL caffeine dissolved in ethanol, 10 μm orifice, dried at 30 $^{\circ}\text{C}$.

Particle Formation from Evaporating Microdroplets for Inhaled Drug Delivery

Table 4.8: Summary of orifice diameter, composition, and drying temperature for BDP particle batches; projected area equivalent diameter distribution statistics; solid phase analysis using Raman spectroscopy. GSD: geometric standard deviation. nd = experiment not conducted, or no data available. S.E.: standard error, nonlinear least squares fitting parameter.

Orifice diameter (μm)	Solution conc. (mg/mL)	Solvent mass fraction p134a	Solvent mass fraction ethanol	Inlet Temp. (° C)	Particle edge delineation	# of particles for size analysis	Median projected area equivalent diameter ± S.E. (μm)	GSD ± S.E.	Solid phase via Raman
5	2	0.80	0.20	30	Circle	60	0.70 ± 0.01	1.13 ± 0.02	nd
23	0.1	0.80	0.20	30	Circle	145	1.51 ± 0.01	1.06 ± 0.01	Partially crystalline
23	0.1	0.80	0.20	130	Circle	89	1.54 ± 0.02	1.08 ± 0.01	Partially crystalline
23	0.1	0.95	0.05	30	Circle	92	1.39 ± 0.01	1.19 ± 0.01	Partially crystalline
23	0.1	0.95	0.05	130	Circle	58	1.47 ± 0.01	1.05 ± 0.01	Partially crystalline
23	2	0.80	0.20	30	Freehand	140	3.94 ± 0.01	1.10 ± 0.01	nd
23	2	0.80	0.20	130	Circle	771	3.32 ± 0.02	1.14 ± 0.02	nd
23	2	0.95	0.05	30	n/a	nd	nd	nd	Amorphous
23	2	0.95	0.05	130	Circle	58	3.22 ± 0.04	1.16 ± 0.02	Amorphous
35	2	0.80	0.20	30	Freehand	217	6.68 ± 0.01	1.13 ± 0.01	Amorphous

As seen in Table 4.8, solid phase analysis of BDP microparticle samples using Raman microscopy indicated that the degree of crystallinity in collected samples was correlated with the particle size. Particles produced from 2.0 mg/mL solution using a 23 or 35 μm orifice were relatively large; the assessed batches were found to be entirely amorphous across all replicate samples (3 unique Raman samples were attained during each particle production experiment) and at all locations within individual samples. A typical set of spectra from 3 different locations on

a single particle sample (23 μm orifice, 2.0 mg/mL BDP in p134a + 5% w/w ethanol, dried at 30 $^{\circ}\text{C}$ inlet temperature) is presented as group A in Figure 4.12. Samples produced from 0.1 mg/mL solution with the 23 μm orifice were made up of comparatively smaller particles, and Raman samples collected from these batches show evidence of a mixture of amorphous and crystalline phases of BDP. An example is presented in group B of Figure 4.12, which are spectra from 3 distinct locations on a single sample (23 μm orifice, 0.1 mg/mL BDP in p134a + 5% w/w ethanol, dried at 130 $^{\circ}\text{C}$ inlet temperature). Two spectra show no evidence of crystallinity, while the third displays peaks indicating a substantial crystalline fraction. To interpret these results, it is useful to consider the factors which can result in crystallization during particle formation from evaporating solution droplets. For crystallization to occur, the solute must reach a critical level of supersaturation (He et al. 2006). At this point the remaining lifetime of the droplet must be sufficient for crystal nucleation and growth to occur; otherwise the molecules making up the dried particle will be in an amorphous, disordered state. Thus for a given droplet diameter, increasing the initial solute concentration or decreasing the evaporation rate will theoretically tend to increase the time available for crystallization, resulting in an increased chance for production of crystalline dried particles (Baldelli et al. 2016). The present results with BDP show an opposite trend: high initial concentration and low drying temperature led to entirely amorphous samples (group A, Figure 4.12), while decreasing the concentration and increasing the drying temperature resulted in some evidence of crystallinity (group B, Figure 4.12). It is therefore likely that the crystalline fraction of BDP observed in some samples formed following evaporation of the volatile solvent phase, perhaps during sampling, sample handling, or storage, with the finer particles potentially more prone to solid phase conversion by virtue of their greater specific surface area.

The effects of solute initial concentration, drying temperature, and cosolvent level on the morphology of BDP particles produced from p134a solution droplets are illustrated in the micrographs of Figure 4.13. Drying inlet temperature had a strong influence on the particle morphology, with spheroidal to ellipsoidal particles with rugose surfaces produced at 30 $^{\circ}\text{C}$, and increasingly spherical and smooth-surfaced particles resulting for all compositions as the drying temperature was increased to 130 $^{\circ}\text{C}$. Increasing the initial solute concentration resulted in larger particles with more prevalent concave surface irregularities, particularly at the lower drying temperature. Cosolvent content had a relatively minor influence on particle morphology,

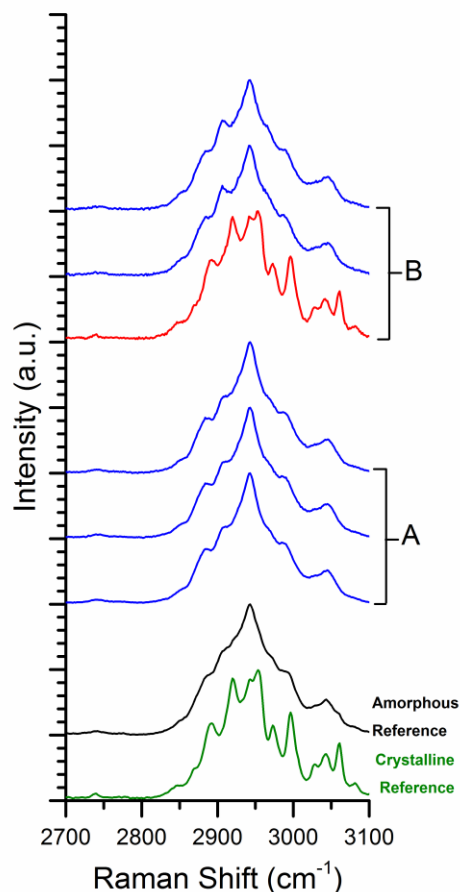


Figure 4.12: BDP Raman spectra in the C-H stretch band, offset for display purposes. Bottom two spectra: crystalline and amorphous references. Group A: spectra attained from 3 distinct locations on a single sample collected during production of BDP from 2.0 mg/mL solution in p134a + 5% w/w ethanol, using a 23 μm orifice, dried at 30 $^{\circ}\text{C}$ inlet temperature. Group B: spectra attained from 3 distinct locations on a single sample (0.1 mg/mL BDP in p134a + 5% w/w ethanol, 23 μm orifice, dried at 130 $^{\circ}\text{C}$ inlet temperature).

with an increase in the extent of surface concavities observed with increasing ethanol fraction at the higher initial solute concentration. FIB-HIM analysis on two particle batches produced at higher drying gas temperature indicate that these particles were solid and free of internal voids—see Figure 4.14.

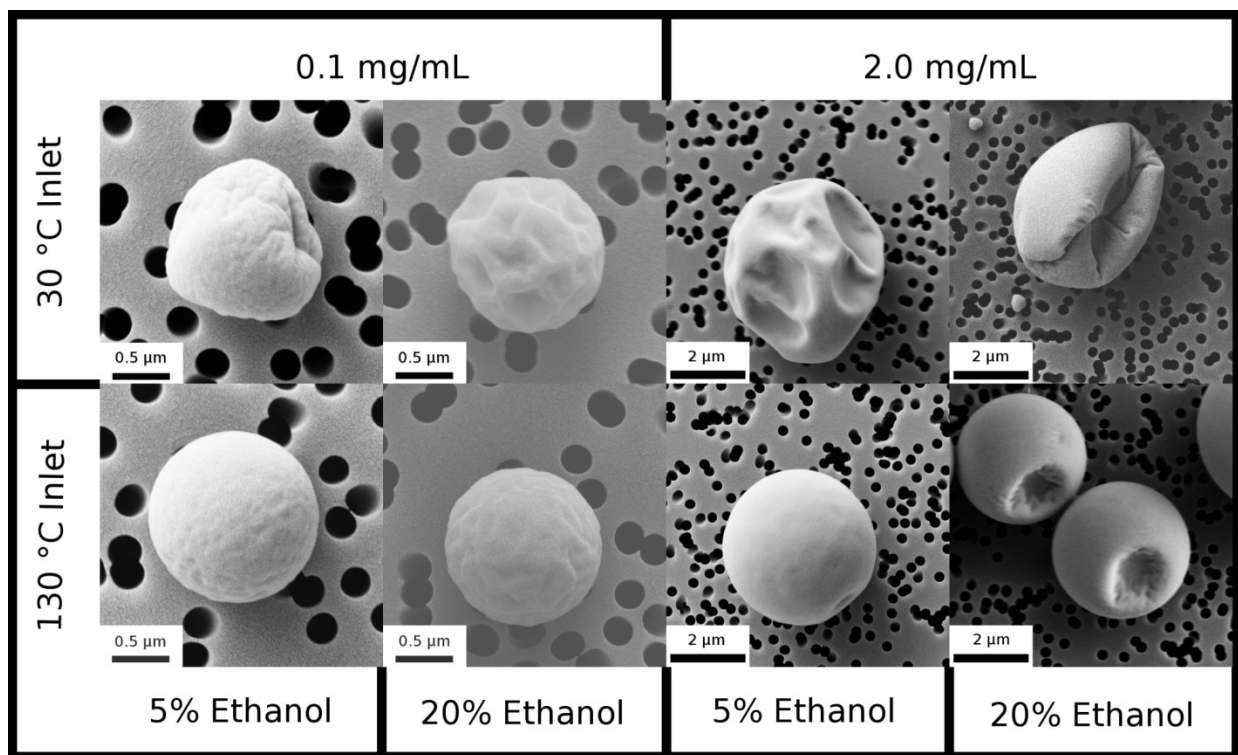


Figure 4.13: Drying temperature affects the morphology of BDP microparticles.

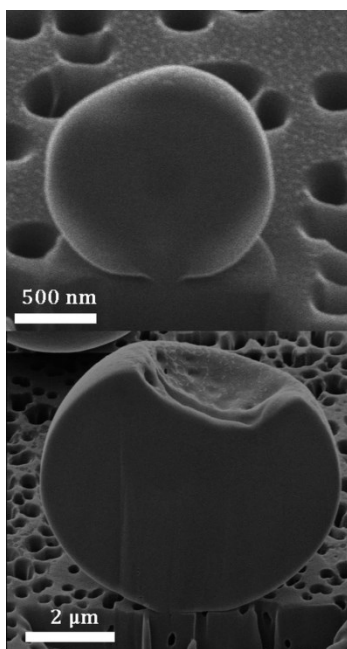


Figure 4.14: FIB-HIM cross-sections of BDP microparticles attained using a 23 μm orifice. Top: 0.1 mg/mL BDP in 134a + 5% w/w ethanol, dried at an inlet temperature of 130 °C. Bottom: 2.0 mg/mL BDP in 134a + 20 % w/w ethanol, dried at 130 °C.

In the case of BDP experiments, use of the p134a-ethanol cosolvent system precluded use of the particle formation modeling techniques of Sections 4.5.2.5.2 and 4.5.2.5.3 due to the variable evaporation rate associated with cosolvent systems (Newbold and Amundson 1973). Nevertheless, theory on the formation of amorphous particles from evaporating solution droplets can be utilized for qualitative interpretation of the observed morphological transitions with changing drying temperature. Increasing the drying temperature will increase the evaporation rate and thus the solute enrichment at the droplet surface. This will promote earlier formation of an amorphous solute shell and an increased likelihood for hollow particles or buckled-shell particle morphologies (Vehring et al. 2007). According to this particle formation model, increasing the drying temperature should result in decreased dry particle density or increased levels of surface irregularities related to shell buckling, phenomena which have been observed in experiments (Vehring 2008). For the BDP microparticles in the present study, drying temperature had no effect on particle density, and higher drying temperatures led to smoother, more spherical particles; very similar trends have also been reported elsewhere (Liu et al. 2012a). Since the thickness (Baldelli et al. 2015) and material properties of the amorphous shell (Baird and Taylor 2012) and the surface tension of the remaining liquid phase (Israelachvili 2011) depend on the drying temperature, and since these factors are all expected to influence the deformation of the shell under interfacial forces (Tsapis et al. 2005), it is possible that the observed effect of drying temperature on the morphology of the BDP particles is related to the mechanisms of shell deformation as drying proceeds following shell formation. The experiments with BDP in the present study thus highlight the importance of the processes occurring after shell formation. These processes are not adequately described by currently available models of particle formation such as that presented in Section 4.5.2.5.3, which can only describe the evolution of the drying droplet up to the point of precipitation or shell formation. In many cases such models are useful in correlating particle physical properties with process parameters, but in the present study the BDP particle morphology seems to be dominated by the evolution of the particle shape following shell formation. This finding highlights the importance of experimental investigations using droplet chains or single droplets in furthering our understanding of particle formation mechanisms.

Particle Formation from Evaporating Microdroplets for Inhaled Drug Delivery

Table 4.9: Summary of orifice diameter, composition, drying temperature, Péclet number, and time available for crystal nucleation and growth for caffeine microparticle batches; projected area equivalent diameter distribution statistics. For micrograph image analysis, all particle and crystallite edges were delineated with polygons. GSD: geometric standard deviation. *: standard error of nonlinear least squares fitting parameters was less than the precision error as reported for all fits.

Orifice diameter (μm)	Solution conc. (mg/mL)	Solvent	Inlet Temp. (° C) / Péclet #	# of particles for size analysis	Time Available for Crystal Nucleation and Growth (ms)	Median projected area equivalent diameter (μm) / GSD *	# of crystallites for size analysis	Crystallite max. Feret diameter: mean ± std. dev. (μm)	Crystallite min. Feret diameter: mean ± std. dev. (μm)
10	0.1	ethanol	30 / 2	243	9	1.6 / 1.11	160	1.12 ± 0.32	0.25 ± 0.09
10	0.1	ethanol	130 / 4	78	3	1.9 / 1.20	158	1.12 ± 0.37	0.21 ± 0.08
10	0.1	p134a	30 / 6	251	2	1.3 / 1.31	65	1.14 ± 0.40	0.20 ± 0.06
10	0.1	p134a	130 / 9	203	1	1.4 / 1.29	44	1.20 ± 0.50	0.23 ± 0.07
10	4	ethanol	30 / 2	105	100	5.0 / 1.20	66	5.81 ± 1.48	0.54 ± 0.16
10	4	ethanol	80 / 3	544	45	4.8 / 1.13	54	4.69 ± 1.29	0.61 ± 0.17
10	4	ethanol	130 / 4	228	27	4.4 / 1.21	99	4.92 ± 1.32	0.54 ± 0.15
35	0.1	ethanol	30 / 2	151	102	5.1 / 1.08	38	4.53 ± 1.79	0.38 ± 0.12
35	0.1	ethanol	80 / 3	94	44	4.8 / 1.08	36	2.70 ± 1.18	0.34 ± 0.19
35	0.1	ethanol	130 / 4	318	30	4.6 / 1.11	76	2.73 ± 1.22	0.33 ± 0.13
35	4	ethanol	30 / 2	22	894	16.2 / 1.13	15	22.26 ± 5.81	2.56 ± 0.74
35	4	ethanol	130 / 4	77	236	15.9 / 1.11	34	18.57 ± 6.78	2.63 ± 0.96

The effects of initial droplet size, solute concentration, solvent type, and drying temperature on the properties of caffeine microparticles were evaluated, resulting in a range of particle size and morphology. Micrographs from selected batches produced using the 35 μm microorifice are presented in Figure 4.15, and particles produced using the 10 μm orifice are shown in Figure 4.16. In all cases the particles appeared crystalline, and were made up of multiple crystallites with lengths of the same order as the overall particle size. Crystallites in the particles produced using a high initial solution concentration and the larger orifice diameter (panels a and b of Figure 4.15) were elongated, with those dried at a low temperature displaying a hollow, tube-like structure toward the ends. Microparticles of intermediate size (panels b and c of Figure 4.15, and a and b of Figure 4.16) were made up a somewhat larger number of crystallites than the other batches; these were acicular crystallites. The smallest particles (e.g. panels c and d of Figure 4.16) contained crystallites with somewhat rounded edges; some dendritic crystallites were observed. Particle size, crystallite size, and solid phase data are summarized for caffeine microparticle batches in Table 4.9.

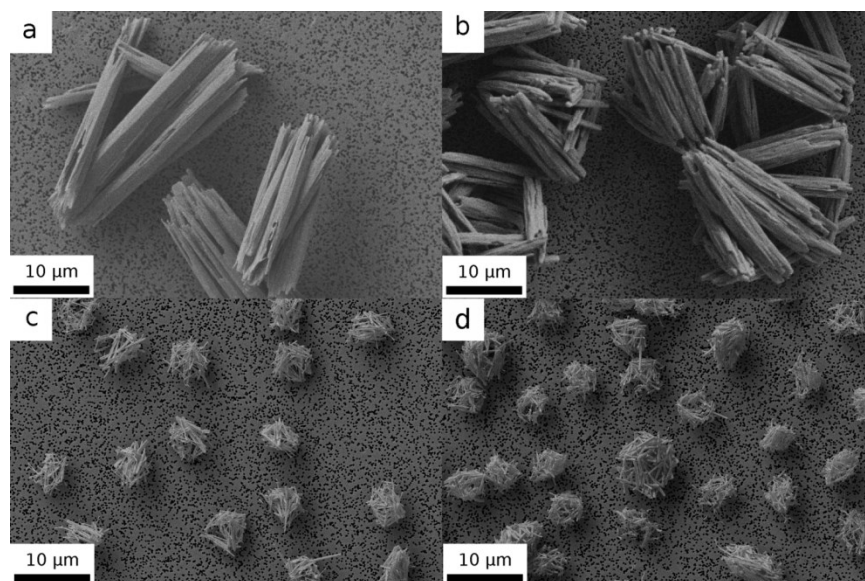


Figure 4.15: Caffeine microparticles produced using a 35 μm microorifice. a.) 4.0 mg/mL, ethanol, 30 $^{\circ}\text{C}$ inlet temperature. b.) 4.0 mg/mL, ethanol, 130 $^{\circ}\text{C}$ inlet temperature. c.) 0.1 mg/mL, ethanol, 30 $^{\circ}\text{C}$ inlet temperature. d.) 0.1 mg/mL, ethanol, 130 $^{\circ}\text{C}$ inlet temperature.

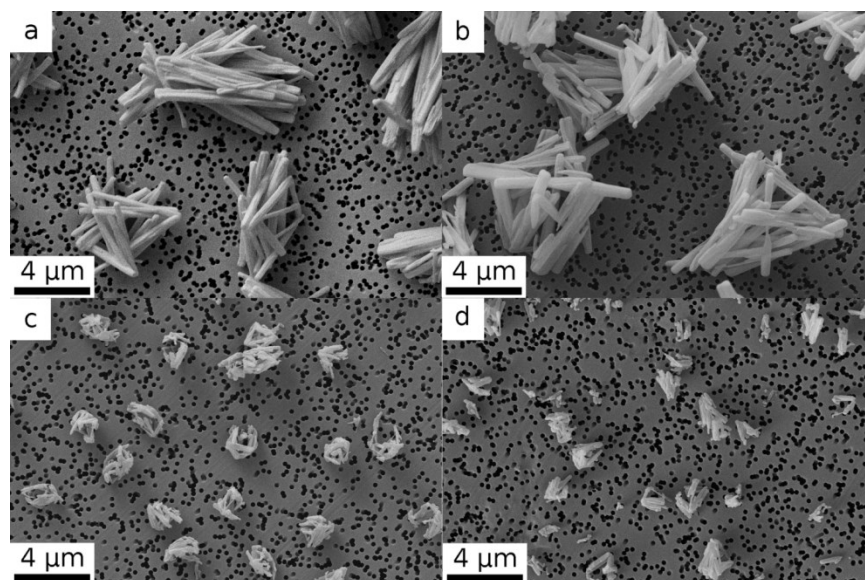


Figure 4.16: Caffeine microparticles produced using a 10 μm microorifice. a.) 4.0 mg/mL, ethanol, 30 $^{\circ}\text{C}$ inlet temperature. b.) 4.0 mg/mL, ethanol, 130 $^{\circ}\text{C}$ inlet temperature. c.) 0.1 mg/mL, ethanol, 30 $^{\circ}\text{C}$ inlet temperature. d.) 0.1 mg/mL, p134a, 130 $^{\circ}\text{C}$ inlet temperature.

Analyzing data across caffeine microparticle samples, the median projected area equivalent diameter $\bar{d}_{A,eq}$ was found to be highly correlated (adjusted $R^2 = 0.96$ for linear regression) with the mean length (Feret's maximum diameter) of individual crystallites. This is consistent with the probable particle formation process: surface nucleation and rapid constrained growth of a few to tens of crystallites, which are then gathered together by the receding droplet surface during the latter portion of the drying event. In Table 4.9 there is some indication that the maximum and minimum Feret diameters of crystallites trend downward as the drying temperature increases for fixed solution concentration, solvent type, and orifice diameter. This finding was further investigated using the modeling techniques presented in Section 4.5.2.5. The Péclet number was computed at a drying temperature defined as the average of the inlet temperature and the centerline gas temperature at the bottom of the cylindrical section of the drying chamber (location shown schematically in Figure 4.10). Initial droplet diameters were estimated using Equation (4.34). Then Equations (4.39) and (4.42) were solved to compute t_c , the time available for crystal nucleation and growth. The computed Péclet number and t_c for each run can be found in Table 4.9. Crystallite maximum and minimum Feret diameter are plotted against t_c in Figure 4.17. Crystallite length and breadth trend upward with increasing t_c for a wide range of t_c . For experiments with t_c between 1 and 10 milliseconds, the crystallite

dimensions are practically constant, possibly as a result of a change in the crystallization mechanism for very rapid drying processes. The general trend is however quite clear: increasing time available for crystal nucleation and growth results in increased length and breadth of crystallites. For the case of crystalline caffeine particles, the chosen particle formation model cannot make specific predictions of particle physical properties due to its inability to describe processes occurring after crystal nucleation. However, it does aid in understanding the relationships between droplet concentration, diameter, drying rate, and dry particle properties, and therefore provides a useful framework for interpreting the data. This highlights the utility of combining experiments and models to gain a mechanistic understanding of the drying process, which may facilitate rational particle design. The present findings with caffeine demonstrate a means of controlling crystallite size, with potential implications for the cohesiveness or dissolution rate of crystalline particles in the context of drug delivery.

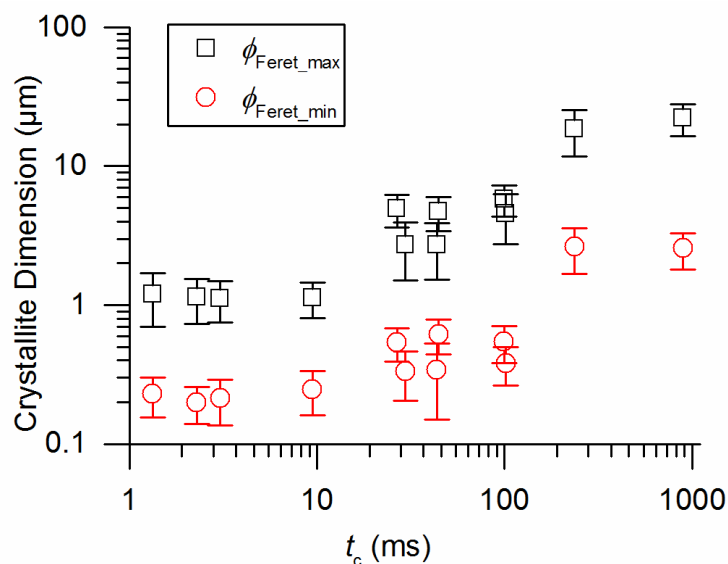


Figure 4.17: Dimensions of individual crystallites (black boxes: maximum Feret diameter, red circles: minimum Feret diameter) vs. t_c , the time available for nucleation and crystal growth predicted by the particle formation model presented in Section 4.5.2.5.3. Error bars indicate one standard deviation.

Unlike experimental techniques relying on the observation of a single drying droplet, monodisperse spray drying is capable of producing sufficient quantities of material (tens to hundreds of mg depending on process conditions, see Table 4.7) to enable post-processing analysis of powder samples. In this work, Raman spectra were attained for caffeine

microparticle samples produced using the 35 μm orifice from ethanol or p134a-ethanol solutions; the spectra from 1000—1600 cm^{-1} are plotted along with those of the caffeine polymorphic forms I and II in Figure 4.18. Subtle spectral differences between forms I and II were observed in this band by other researchers (Hédoux et al. 2011a) and in the present study: form I exhibits splitting of the peak near 1070 cm^{-1} , and sharpening of the peak around 1410 cm^{-1} , relative to form II. These differences are indicated with arrows in Figure 4.18, and enable qualitative assessment of the polymorphic form of the processed samples. There is no evidence of either of these form I markers in the spectra of the prepared microparticle samples, indicating that these samples were predominantly form II. This finding demonstrates the capability of the monodisperse spray drying process to produce sufficient powder to conduct solid phase analyses, enabling evaluation of extent of crystallinity, identification of crystalline polymorph, or other solid phase properties of interest.

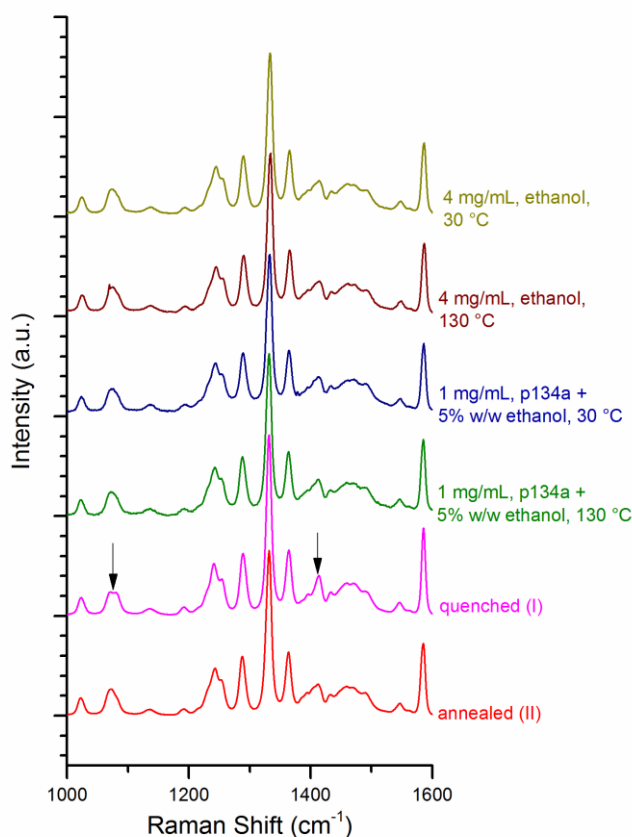


Figure 4.18: Caffeine spectra from 1000 to 1600 cm^{-1} . Spectra are offset for clarity. Arrows indicate marker peaks for caffeine polymorphic form I. Spray-dried microparticle samples consist predominantly of form II.

4.5.4 Conclusions

Incorporating a custom continuous jet droplet generator into a lab scale spray dryer enables systematic experimental studies of particle formation from monodisperse solution droplets. The novel droplet generator is designed to work with pressurized liquid propellants, allowing fundamental investigations in the context of drug particle design for inhalation delivery with solution pressurized metered dose inhalers. The experimental setup can produce particles in a wide size range, from submicron to tens of microns; production quantities range from tens to hundreds of milligrams of dried material, sufficient for a variety of powder characterization techniques. For the amorphous particles produced from propellant droplets containing the corticosteroid BDP, changes in particle morphology with drying temperature were observed which could not be readily explained using available particle formation models, indicating the importance of experimental work. For crystalline particles produced from caffeine solution droplets, a hybrid analytical-numerical particle formation model was employed to relate observed dry particle properties to solution droplet composition and drying rate. Results of particle formation studies with BDP and caffeine highlight the importance of the physical processes which occur following amorphous shell formation or crystal nucleation in determining the dry particle properties. Currently, models for particle formation from solution droplets do not account for these processes. Thus to advance our understanding of particle formation from solution droplets, further theoretical and experimental research is required in the areas of amorphous shell formation, shell buckling, crystal nucleation, and crystal growth.

The work presented herein demonstrates the suitability of monodisperse spray drying as a technique to investigate the underlying mechanisms of particle formation. The combination of experimental work in an idealized monodisperse system and modeling can provide a physically based understanding of the drying process by revealing the relationships between the dry particle properties and the composition, diameter, and drying rate of solution droplets. The knowledge gained from such an approach can be applied to conventional polydisperse spray drying processes, with potential applications to process scale-up, formulation and process development for poorly soluble drugs, and optimization of particle properties for delivery by dry powder inhalers.

4.5.5 Acknowledgements

This work was partially funded by Chiesi Limited UK, enabling development of the experimental setup and execution of experiments with beclomethasone dipropionate. The authors would like to thank Professor Mark McDermott and his research group in the Chemistry Department at the University of Alberta for training and instrument time on the Raman microscope.

4.5.6 Supplementary information

4.5.6.1 Nomenclature

Latin

$c_m(\tau)$	Mean solute concentration at dimensionless drying time τ
c_0	Initial solute concentration
c_p	Specific heat capacity of solvent vapor
$c_s(\tau)$	Solute concentration at the droplet surface at dimensionless drying time τ
c_{sol}	Solute solubility limit
d_0	Droplet initial diameter
$D_{s,s}$	Mass diffusivity of the solute in the solvent
D_v	Mass diffusivity of solvent vapor in the gas phase
$E(\tau)$	Transient solute surface enrichment at dimensionless drying time τ
E_{ss}	Steady-state solute surface enrichment
k	Thermal conductivity, air-solvent vapor mixture
k_{air}	Thermal conductivity of air
k_b	Boltzmann's constant
k_v	Thermal conductivity of solvent vapor
L	Solvent latent heat of vaporization
Le	Lewis number
M_{air}	Molar mass, air
M_v	Molar mass, solvent
n	Fitting parameter, particle formation model of Boraey and Vehring 2014
p_∞	Ambient absolute pressure
$p_{v,s}$	Solvent vapor partial pressure at the droplet surface
Pe	Péclet number
r_m	Solute effective molecular radius
S_0	Solute initial degree of saturation
t	Time

t_c	Time available for solute nucleation and crystal growth
T	Temperature
$T_{1/3}$	“One third” temperature for calculation of gas phase transport properties
T_{eq}	Droplet equilibrium temperature
T_∞	Temperature of gas phase far from the droplet
$Y_{1/3}$	“One third” vapor mass fraction for calculation of gas phase transport properties
$Y_s(T_{eq})$	Mass fraction of solvent vapor at the surface of the droplet
Y_∞	Mass fraction of solvent vapor far from the droplet

Greek

κ	Droplet evaporation rate
μ	Solvent dynamic viscosity
ρ_g	Gas phase density
ρ_l	Solvent liquid density
τ	Dimensionless droplet drying time
τ_{sat}	Dimensionless time to solute surface saturation
$\chi_m(\tau)$	Dimensionless mean solute concentration at dimensionless drying time τ
ϕ	Correction factor in Stokes-Einstein diffusivity estimate

4.5.6.2 Quasistationary droplet evaporation model: determination of thermophysical properties; model results

Droplet evaporation rates were computed for pure droplets of ethanol and p134a. This was achieved by first iteratively solving Equation (4.36) for the droplet equilibrium temperature T_{eq} :

$$\frac{L}{c_p} - \frac{(1 - Y_s(T_{eq}))^{\frac{1}{Le}} (T_\infty - T_{eq})}{(1 - Y_\infty)^{\frac{1}{Le}} - (1 - Y_s(T_{eq}))^{\frac{1}{Le}}} = 0, \text{ with } Le = \frac{\kappa}{c_p \rho_g D_v} . \quad (4.36)$$

Gas phase transport properties were evaluated at “one-third” conditions, i.e. at temperature and solvent vapor mass fraction

$$T_{1/3} = T_{eq} + \frac{(T_\infty - T_{eq})}{3}, \quad Y_{1/3} = Y_s(T_{eq}) - \frac{(Y_s(T_{eq}) - Y_\infty)}{3} . \quad (4.43)$$

Gas phase density ρ_g was computed assuming an ideal mixture of air and solvent vapor assuming an ambient absolute pressure p_∞ of 101.3 kPa. Solvent vapor partial pressure at the droplet surface, $p_{v,s}$, was computed at the droplet equilibrium temperature T_{eq} by assuming

saturation at the droplet surface utilizing Antoine equations. Vapor mass fraction at the surface was determined using the relation

$$Y_s(T_{eq}) = \frac{M_v p_{v,s}}{M_v p_{v,s} + M_{air}(p_{\infty} - p_{v,s})} , \quad (4.44)$$

where M_v and M_{air} are the molar masses of solvent and air.

The effect of solvent vapor on gas phase thermal conductivity was estimated using mass weighting:

$$k = (1 - Y_{1/3})k_{air} + Y_{1/3}k_v . \quad (4.45)$$

Then Equation (4.35) was solved to yield the evaporation rate:

$$\kappa = 8D_v \frac{\rho_g}{\rho_l} \ln \left(\frac{1 - Y_{\infty}}{1 - Y_s(T_{eq})} \right) . \quad (4.35)$$

Methods for computing the thermophysical properties are summarized in Table 4.10.

The model results for rate of evaporation and droplet equilibrium temperature for the case of $Y_{\infty} = 0$ (i.e. air far from the droplet is free of solvent vapor) are presented graphically in Figure 4.19. The model results were verified by comparison to experimentally determined evaporation rates for water droplets, with good agreement; the model results for water are included in the plots.

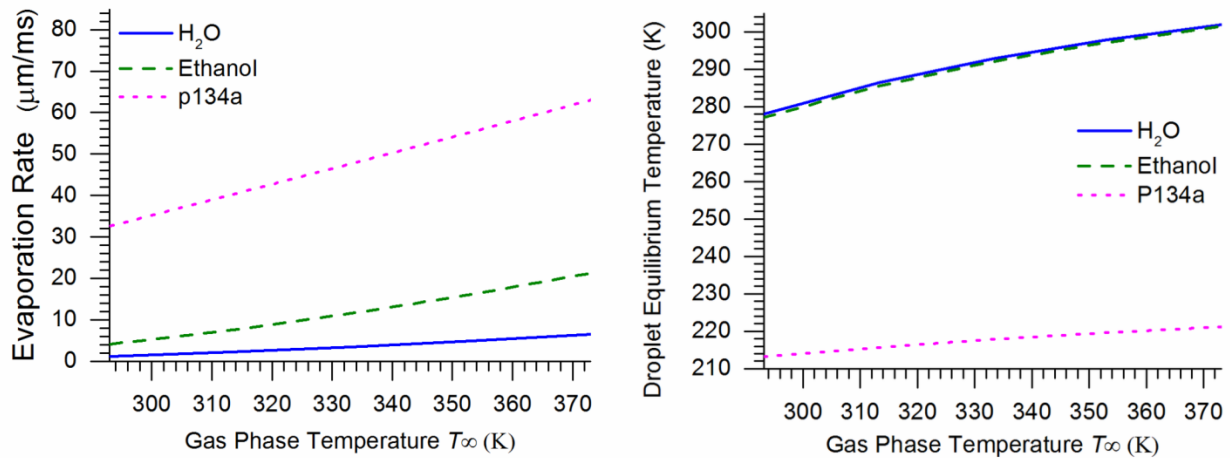


Figure 4.19: Results of the quasistationary droplet evaporation model. Droplet evaporation rate (left) and equilibrium temperature (right) as a function of the gas temperature far from the droplet.

4.5.6.3 Particle formation model of Boraey and Vehring 2014

When the Péclet number is substantially greater than unity, the steady-state VFL model (Vehring et al. 2007) may underpredict the time required for a solute to reach saturation at the droplet surface. In these cases more accurate results can be obtained by taking into account the transient portion of the evolving solute concentration profile, which was done by (Boraey and Vehring 2014). Utilizing a dimensionless drying time τ expressed in terms of the time t , the evaporation rate κ and the initial droplet diameter d_0 ,

$$\tau = \frac{\kappa t}{d_0^2}, \quad (4.37)$$

the transient surface enrichment $E(\tau)$ is then defined as the ratio between the solute concentration at the droplet surface, $c_s(\tau)$, and the average concentration of the solute in the droplet, $c_m(\tau)$:

$$E(\tau) = \frac{c_s(\tau)}{c_m(\tau)}. \quad (4.46)$$

For $0.5 < Pe < 25$, Boraey and Vehring provide a fit to numerical results for the transient surface enrichment:

$$E(\tau) = \frac{E_{ss} - e^{-n}}{1 - e^{-n}} - \frac{E_{ss} - 1}{1 - e^{-n}} e^{-n\tau}, \quad (4.47)$$

where the fitting parameter $n = 15Pe^{0.7}$ and E_{ss} is the steady-state surface enrichment of the VFL model:

$$E_{ss} = 1 + \frac{Pe}{5} + \frac{Pe^2}{100} - \frac{Pe^3}{4000}. \quad (4.40)$$

The time to reach surface saturation is the moment when the solute reaches its solubility limit, c_{sol} , at the droplet surface. This occurs when

$$E(\tau_{sat})c_m(\tau_{sat}) = c_{sol}. \quad (4.48)$$

Equation (4.48) can be nondimensionalized by introducing the dimensionless mean solute concentration, χ_m , and the initial droplet saturation, S_0 , using the initial solute concentration c_0 :

$$\chi_m(\tau) = \frac{c_m(\tau)}{c_0} = (1 - \tau)^{-\frac{3}{2}} \quad (4.49)$$

$$S_0 = \frac{c_0}{c_{sol}} \quad (4.50)$$

Now the surface enrichment at saturation can be expressed as

$$E(\tau_{\text{sat}}) = \frac{(1-\tau_{\text{sat}})^{\frac{3}{2}}}{S_0} . \quad (4.51)$$

Evaluating Equation (4.47) at τ_{sat} and using Equation (4.51) to eliminate $E(\tau_{\text{sat}})$ yields an equation which can be iteratively solved to determine τ_{sat} :

$$S_0 \left(\frac{E_{\text{ss}} - e^{-n}}{1 - e^{-n}} - \frac{E_{\text{ss}} - 1}{1 - e^{-n}} e^{-n\tau_{\text{sat}}} \right) (1 - \tau_{\text{sat}})^{-\frac{3}{2}} - 1 = 0 . \quad (4.39)$$

With τ_{sat} determined, the time available for crystal nucleation and growth, t_c , can be calculated:

$$t_c = (1 - \tau_{\text{sat}}) \frac{d_0^2}{\kappa} . \quad (4.42)$$

To use this model, the mass diffusivity of the solute in the solvent must be known or estimated in order to compute the Péclet number. For caffeine in ethanol and p134a, the Stokes-Einstein equation was used to provide an estimate (Edward 1970):

$$D_{s,s} = \frac{k_b T}{6\pi\mu r_m \phi} . \quad (4.52)$$

Here k_b is Boltzmann's constant, T the absolute temperature, μ the dynamic viscosity of the solvent, r_m a solute molecular radius, and ϕ a parameter correcting for molecule shape effects and interactions with solvent molecules. The product $r_m\phi$ was estimated using the published diffusivity of caffeine in water (McCabe 1972), which neglects any potential dependence on the solvent species. Using the viscosity correlations (see Table 4.10) then allowed the use of Equation (4.52) to estimate caffeine diffusivity at the droplet equilibrium temperature, T_{eq} , determined by the quasistationary droplet evaporation model. A notable assumption in this approach is that the solute is very dilute. Given the relatively low solubility of caffeine in ethanol and p134a, the approach is adequate to provide estimates for the purposes of this model. Due to a lack of available data in the literature on the temperature dependence of caffeine solubility in the chosen solvents, isothermal solubility values were used to compute the initial degree of saturation S_0 . These are summarized in Table 4.10.

Table 4.10: Methods for computing material properties for models. T refers to the temperature in Kelvin.

Property	Material	Expression	Reference, Comments
L , solvent latent heat of vaporization (J/kg)	p134a	$\frac{L}{1000} = 163.7313x + 460.3925x^2 - 510.952x^3 + 219.1886x^4$ with $x = \left(1 - \frac{T}{374.15 \text{ K}}\right)^{\frac{1}{3}}$	(Mexichem UK Limited 2010a)
	ethanol	$L = 1.0947 \times 10^6 \exp(0.4475x) + (1-x)^{0.4989}$ with $x = \frac{T}{513.9 \text{ K}}$	(NIST Chemistry Webbook 2015a)
k , gas / vapor thermal conductivity (W/m·K)	air	$k = -3.3065 \times 10^{-8} T^2 + 9.7116 \times 10^{-5} T - 1.9006 \times 10^{-4}$	Fit to data of (Mason and Monchick 1965), 193-573 K
	p134a	$k = 8.8347 \times 10^{-3} \ln(x) - 8.0757 \times 10^{-4}$	Fit to data of (NIST Chemistry Webbook 2015b), 170-371 K
	ethanol	$k = 0.001 * (-2.09575 + 19.9045x - 53.964 x^2 + 82.1223 x^3 - 1.98864 x^4 - 0.495513 x^5) / (0.17223 - 0.078273 x + x^2)$ with $x = \frac{T}{514.71 \text{ K}}$	(Assael et al. 2013)
c_p , solvent vapor specific heat capacity (J/kg)	p134a	$c_p/1000 = 0.1345064 + 0.003258432T - 4.2343E - 06T^2 + 3.8408E - 09T^3 - \frac{1.370898}{T^2}$	(Mexichem UK Limited 2010a)
	ethanol	$c_p = -2.376 \times 10^{-6} T^3 + 2.933 \times 10^{-3} T^2 + 1.823 T + 689.4$	Fit to data of (NIST Chemistry Webbook 2015a), 50-1000 K
D_v , solvent vapor mass diffusivity (m ² /s)	p134a	$D_v = -5.725646 \times 10^{-6} + 5.265307 \times 10^{-8} T$	(Finlay 2001b)
	ethanol	$D_v = 1.1 \times 10^{-5} \left(\frac{T}{300}\right)^{\frac{3}{2}}$	Datum at 300 K (Martínez 2015) with assumed temperature dependence per (Cussler 2009)

Particle Formation from Evaporating Microdroplets for Inhaled Drug Delivery

Property	Material	Expression	Reference, Comments
$p_{v,s}$, vapor partial pressure at the droplet surface (Pa)	p134a	$p_{v,s} = 1.0E05 \exp(102.5338784 - \frac{5238.8786}{T} + 0.02398227T - 15.8343842\ln(T))$	(Mexichem UK Limited 2010a)
	ethanol	$\log(p_{v,s}) = 10.37229 - \frac{1670.409}{T - 40.191}$	(NIST Chemistry Webbook 2015a)
μ , solvent dynamic viscosity (Pa-s)	ethanol	$\log \mu = -6.90519 + \frac{1922.5}{T + 189.7}$	(Gutmann and Simmons 1952)
	p134a	$\mu = 0.001 * \exp \left[-9.707292 + \frac{1140.7291}{T} + 0.0282451T - 0.00004672T^2 \right]$	(Mexichem UK Limited 2010a)
c_{sol} , caffeine solubility at 20 °C (mg/mL)	ethanol	5.6	(Shurtleff and Shurtleff 2015)
	p134a	1.6	(Hoye and Myrdal 2008)

Chapter 5 : Conclusions

In Chapter 2, useful models for the prediction of the mass median aerodynamic diameter of aerosols emitted by solution and suspension pMDIs were developed:

$$MMAD = 416 \sqrt[3]{\frac{c_s}{\rho^*} \frac{\sigma_{pa}}{p_{mc}}} , \quad (2.14)$$

and

$$\Gamma = \left[0.939 \ln \left(\frac{N_{sp}}{N_0} + 3.42 \right) \right]^{1.03GSD_0/GSD_{sp}} . \quad (2.18)$$

While other researchers have presented models capable of equally accurate predictions of solution pMDI particle size distributions, they have been specific to the propellant system. The use of dimensional analysis to correlate the MMAD to physical properties of the propellant means that unlike previously developed empirical relationships, Equation (2.14) has a chance at predicting the particle size distribution for pMDIs utilizing novel propellant systems. This is relevant in light of environmental concerns related to the greenhouse gas potential of the HFA propellants, as there is some early indication of an emerging market for more environmentally friendly pMDI propellants (Corr 2018).

For suspension pMDIs, Equation (2.18) provides an easy-to-use equation which can be applied by researchers without the need to invest in the development of modeling techniques. It reveals that the aerodynamic particle size distribution depends quite strongly on the breadth of the size distributions of the suspended material and the droplets; this effect had yet to be explored by other researchers using similar modeling techniques. Since aggregation is most pronounced for high suspension concentrations or very fine suspended material, this finding is relevant for the development of high-dose suspension pMDIs or nanoparticle formulations. In these cases, Equation (2.18) suggests that altering the breadth of the droplet diameter distribution or the suspended particle size distribution may offer a means of modulating the extent of aggregation in the aerosol. An interesting potential area of future work is to use the developed stochastic model to explore the dependence of the breadth of the residual aerosol's aerodynamic particle size distribution on the input variables. The model may also be applicable to simulating suspension spray drying or nebulized suspension formulations

In Chapter 3, the morphology of amorphous particles produced by solution pMDIs containing the corticosteroid beclomethasone dipropionate is shown to be humidity dependent,

with high porosity particles produced in humid air and nonporous particles produced in dry air. The air relative humidity at which the morphological transition occurs depends on the amount of co-solvent ethanol used in the formulation. These results suggest that condensed water is responsible for the observed porosity. In samples collected in humid conditions, the porosity extends throughout the entire particle, indicating that condensation occurs while particle formation is still underway. The implications *in vivo* are unclear, but given the high levels of humidity in the human airways this is an area which merits further investigation. Possible areas for future experimental work include investigating the effects of device variables on condensation-induced porosity, determining if the pore formers are liquid water or solid ice, or evaluating the influence of the particle solid phase and composition on the interactions with condensed water. Given the interesting properties of porous microparticles in the context of inhaled drug delivery, the findings suggest spray drying processes using propellant-based feedstocks and humidified drying air might offer a relatively simple means of producing porous particles for use in DPIs or suspension pMDIs.

In Chapter 4, equipment and methods for the production of engineered particles by spray drying are developed and applied. The design approach and functionality of a novel custom modular lab scale research spray dryer is described. The flexible design enables routine lab scale spray drying of polydisperse powders, or monodisperse spray drying using solvents or superheated liquid propellants. An isokinetic sampling system is designed and integrated with the dryer and used to measure in-process particle size distributions in real time, allowing rapid characterization of atomizer and cyclone performance. Lab scale spray drying equipment performance data in combination with modeling techniques enable predictions of powder particle size distribution and process yield, as well as residual moisture content and glass transition temperature for amorphous solids. These approaches exemplify the particle engineering approach to spray dried formulation and process development

The research dryer is configured for monodisperse spray drying and used to conduct thorough parametric studies on the formation of amorphous and crystalline particles from solution droplets with solvents ethanol and propellant p134a. Amorphous particles of beclomethasone dipropionate produced from p134a—ethanol droplets display temperature-dependent particle morphology, with surface smoothing observed as drying temperature increases. Crystalline caffeine particles produced from p134a and ethanol are made up of

assemblies of several to tens of individual crystallites, the dimensions of which are correlated with a characteristic time—the time available for crystal nucleation and growth—computed using a particle formation model. These findings indicate that for both types of particle, the morphology is dominated by the mechanisms which occur after crystal nucleation or amorphous shell formation; thus additional theoretical and experimental work is required to advance particle engineering modeling capabilities. The results demonstrate that monodisperse spray drying is a valuable technique that offers insight into the mechanisms of particle formation while producing adequate quantities of dried powder sample for a variety of analytical techniques. The incorporation of an atomizer capable of handling superheated liquid propellants is of special interest for pulmonary drug delivery, since it enables fundamental and applied investigations of the mechanisms of particle formation from pMDIs.

Bibliography

Abdel-Halim, H., Traini, D., Hibbs, D., Gaisford, S. and Young, P. (2011). Modelling of molecular phase transitions in pharmaceutical inhalation compounds: An *in silico* approach. *European Journal of Pharmaceutics and Biopharmaceutics* 78:83-89.

Allen, M. D. and Raabe, O. G. (1985). Slip correction measurements of spherical solid aerosol particles in an improved Millikan apparatus. *Aerosol Science and Technology* 4:269-286.

Anders, K., Roth, N. and Frohn, A. (1992). Operation characteristics of vibrating-orifice generators: The coherence length. *Particle and Particle Systems Characterization* 9:40 - 43.

Assael, M., Sykioti, E., Huber, M. and Perkins, R. (2013). Reference correlation of the thermal conductivity of ethanol from the triple point to 600 K and up to 245 MPa. *Journal of Physical and Chemical Reference Data* 42:023102.

Azhdarzadeh, M., Shemirani, F. M., Ruzycski, C. A., Baldelli, A., Ivey, J. W., Barona, D., Church, T., Lewis, D. and Olfert, J. S. (2016). An atomizer to generate monodisperse droplets from high vapor pressure liquids. *Atomization and Sprays* 26:121-134.

Baird, J. A. and Taylor, L. S. (2012). Evaluation of amorphous solid dispersion properties using thermal analysis techniques. *Advanced Drug Delivery Reviews* 64:396-421.

Baldelli, A., Boraey, M. A., Nobes, D. S. and Vehring, R. (2015). Analysis of the particle formation process of structured microparticles. *Molecular Pharmaceutics* 12:2562-2573.

Baldelli, A., Power, R. M., Miles, R. E., Reid, J. P. and Vehring, R. (2016). Effect of crystallization kinetics on the properties of spray dried microparticles. *Aerosol Science and Technology* 50:693-704.

Barnes, P. J. and Pedersen, S. (1993). Efficacy and safety of inhaled corticosteroids in asthma. *American Review of Respiratory Disease* 148:S1-S26.

Bayvel, L. and Orzechowski, Z. (1993). *Liquid Atomization*. Taylor & Francis, London.

Bell, J. and Newman, S. (2007). The rejuvenated pressurised metered dose inhaler. *Expert Opinion on Drug Delivery* 4:215-234.

Berglund, R. N. and Liu, B. Y. H. (1973). Generation of monodisperse aerosol standards. *Environmental Science and Technology* 7:147-153.

Bogy, D. B. and Talke, F. (1984). Experimental and theoretical study of wave propagation phenomena in drop-on-demand ink jet devices. *IBM Journal of Research and Development* 28:314-321.

Boraey, M. A. and Vehring, R. (2014). Diffusion controlled formation of microparticles. *Journal of Aerosol Science* 67:131-143.

Bouhroum, A., Burley, J. C., Champness, N. R., Toon, R. C., Jinks, P. A., Williams, P. M. and Roberts, C. J. (2010). An assessment of beclomethasone dipropionate clathrate formation in a model suspension metered dose inhaler. *International Journal of Pharmaceutics* 391:98-106.

Brambilla, G., Ganderton, D., Garzia, R., Lewis, D., Meakin, B. and Ventura, P. (1999). Modulation of aerosol clouds produced by pressurised inhalation aerosols. *International Journal of Pharmaceutics* 186:53-61.

Brambilla, G., Church, T., Lewis, D. and Meakin, B. (2011). Plume temperature emitted from metered dose inhalers. *International Journal of Pharmaceutics* 405:9-15.

- Brindley, A. (1999). The chlorofluorocarbon to hydrofluoroalkane transition: the effect on pressurized metered dose inhaler suspension stability. *Journal of Allergy and Clinical Immunology* 104:s221-s226.
- Brown Jr, G. N. and Ziegler, W. T. (1979). Temperature dependence of excess thermodynamic properties of ethanol+ n-heptane and 2-propanol+ n-heptane solutions. *Journal of Chemical and Engineering Data* 24:319-330.
- Buchmann, N. A., Duke, D. J., Shakiba, S. A., Mitchell, D. M., Stewart, P. J., Traini, D., Young, P. M., Lewis, D. A., Soria, J. and Honnery, D. (2014). A novel high-speed imaging technique to predict the macroscopic spray characteristics of solution based pressurised metered dose inhalers. *Pharmaceutical Research* 31:2963-2974.
- Buck, A. L. (1981). New equations for computing vapor pressure and enhancement factor. *Journal of Applied Meteorology* 20:1527-1532.
- Buckingham, E. (1914). On physically similar systems; illustrations of the use of dimensional equations. *Physical Review* 4:345-376.
- Busse, W. (2002). How inhaled corticosteroids changed asthma therapy, in *Inhaled Steroids in Asthma*, R. P. Schleimer, P. M. O'Byrne, S. J. Szefler and R. Brattsand, eds., Marcel Dekker, New York.
- Buttini, F., Miozzi, M., Balducci, A. G., Royall, P. G., Brambilla, G., Colombo, P., Bettini, R. and Forbes, B. (2014). Differences in physical chemistry and dissolution rate of solid particle aerosols from solution pressurised inhalers. *International Journal of Pharmaceutics* 465:42-51.
- Byron, P. R. (1990). Aerosol formulation, generation, and delivery using metered systems, in *Respiratory Drug Delivery I*, P. R. Byron, ed., CRC Press, Boca Raton, FL, 167-206.
- Callingham, M. (1980). A statistical model for predicting the particle distribution of an atomised powder in liquid mixture. *International Journal of Cosmetic Science* 2:107-126.
- Carver, K. M. and Snyder, R. C. (2012). Unexpected polymorphism and unique particle morphologies from monodisperse droplet evaporation. *Industrial and Engineering Chemistry Research* 51:15720-15728.
- Chang, R. Y., Wong, J., Mathai, A., Morales, S., Kutter, E., Britton, W., Li, J. and Chan, H.-K. (2017). Production of highly stable spray dried phage formulations for treatment of *Pseudomonas aeruginosa* lung infection. *European Journal of Pharmaceutics and Biopharmaceutics* 121:1-13.
- Cheng, Y.-S., Zhou, Y. and Chen, B. T. (1999). Particle deposition in a cast of human oral airways. *Aerosol Science & Technology* 31:286-300.
- Cheng, Y. S. (2014). Mechanisms of pharmaceutical aerosol deposition in the respiratory tract. *AAPS PharmSciTech* 15:630-640.
- Chew, N. Y. K. and Chan, H.-K. (1999). Influence of particle size, air flow, and inhaler device on the dispersion of mannitol powders as aerosols. *Pharmaceutical Research* 16:1098-1103.
- Chow, A. H. L., Tong, H. H. Y., Chattopadhyay, P. and Shekunov, B. Y. (2007). Particle engineering for pulmonary drug delivery. *Pharmaceutical Research* 24:411-437.
- Church, T., Hargrave, G., Johnson, R., Lewis, D. A., O'Shea, H. and Versteeg, H. K. (2011). Visualising dose retention: effects of temperature fluctuation on a pMDI capillary retention model, in *RDD Europe 2011*, R. N. Dalby, P. R. Byron, J. Peart, J. D. Suman and P. M. Young, eds. Virginia Commonwealth University, Richmond, VA, 317-320.
- Clark, A. R., (1991). *Metered atomisation for respiratory drug delivery*. PhD Thesis, Loughborough University of Technology

- Clark, A. R. (1992). The physics of aerosol formation by MDIs: limitations of the current approach. *Journal of Biopharmaceutical Science* 3:69-76.
- Clark, A. R. (1996). MDIs: physics of aerosol formation. *Journal of Aerosol Medicine* 9:S19-S26.
- Clark, A. R. (2008). Optimizing high dose pMDI performance - challenging and improving existing therapy, in *Respiratory Drug Delivery 2008*, R. N. Dalby, P. R. Byron, J. Peart, J. D. Suman, S. J. Farr and P. M. Young, eds., 291-298.
- Cloutier, M. and Thrall, R. (2010). Structure and function of the respiratory system, in *Berne & Levy Physiology*, R. M. Berne, B. M. Koeppen and B. A. Stanton, eds., Mosby Philadelphia.
- Colombani, A., Chambers, F., Lee, K., Jansen, R. and Hodson, D. (2010). Understanding the cause of increasing dose through life from a pressurised metered dose inhaler (pMDI), in *UK PharmSci Conference*, Journal of Pharmacy and Pharmacology, Nottingham, UK, 1314-1315.
- Conner, J. B. and Buck, P. O. (2013). Improving asthma management: the case for mandatory inclusion of dose counters on all rescue bronchodilators. *Journal of Asthma* 50:658-663.
- Corr, S. (2018). Compatibility of p152a with pressurized metered dose inhaler device materials, in *Respiratory Drug Delivery*, R. N. Dalby, ed. VCU, Richmond, VA, In press.
- Crosland, B. M., Johnson, M. R. and Matida, E. A. (2009). Characterization of the spray velocities from a pressurized metered-dose inhaler. *Journal of Aerosol Medicine and Pulmonary Drug Delivery* 22:85-98.
- Crowe, C. T., Schwarzkopf, J. D., Sommerfeld, M. and Tsuji, Y. (2011). *Multiphase flows with droplets and particles*. CRC press, Boca Raton.
- Cummings, R. H. (1999). Pressurized metered dose inhalers: Chlorofluorocarbon to hydrofluoroalkane transition—Valve performance. *Journal of Allergy and Clinical Immunology* 104:s230-s235.
- Cussler, E. L. (2009). *Diffusion: mass transfer in fluid systems*. Cambridge University Press.
- Cyr, T. D., Graham, S. J., Li, K. R. and Levering, E. G. (1991). Low first-spray drug content in albuterol metered-dose inhalers. *Pharmaceutical Research* 8:658-660.
- da Rocha, S. R. P., Bharatwaj, B. and Saiprasad, S. (2011). Science and technology of pressurized metered-dose inhalers, in *Controlled Pulmonary Drug Delivery*, H. D. C. Smyth and A. J. Hickey, eds., Springer, 165-201.
- Darquenne, C. (2012). Aerosol deposition in health and disease. *Journal of Aerosol Medicine and Pulmonary Drug Delivery* 25:140-147.
- Davis, M. (2018). Recent strategies in spray drying for the enhanced bioavailability of poorly water-soluble drugs. *Journal of Controlled Release* 269:110-127.
- de Souza Carvalho, C., Daum, N. and Lehr, C.-M. (2014). Carrier interactions with the biological barriers of the lung: Advanced *in vitro* models and challenges for pulmonary drug delivery. *Advanced Drug Delivery Reviews* 75:129-140.
- DeCarlo, P. F., Slowik, J. G., Worsnop, D. R., Davidovits, P. and Jimenez, J. L. (2004). Particle morphology and density characterization by combined mobility and aerodynamic diameter measurements. Part 1: Theory. *Aerosol Science and Technology* 38:1185-1205.
- Dellamary, L. A., Tarara, T. E., Smith, D. J., Woelk, C. H., Adractas, A., Costello, M. L., Gill, H. and Weers, J. G. (2000). Hollow porous particles in metered dose inhalers *Pharmaceutical Research* 17:168-174.

- Descamps, M., Correia, N. T., Derollez, P., Danede, F. and Capet, F. (2005). Plastic and glassy crystal states of caffeine. *Journal of Physical Chemistry B* 109:16092-16098.
- Desmond, K. W. and Weeks, E. R. (2014). Influence of particle size distribution on random close packing of spheres. *Physical Review E* 90:022204 1-6.
- Dobry, D., Settell, D., Baumann, J., Ray, R., Graham, L. and Beyerinck, R. (2009). A model-based methodology for spray-drying process development. *Journal of pharmaceutical innovation* 4:133-142.
- Dohmeier, D., Heyworth, D. and Wilde, T. (2009). The application of a new high performance dual-layer coating to pressurized metered dose inhaler hardware, in *RDD Europe 2009*, R. Dalby, P. Byron, J. Peart, J. Suman and P. Young, eds. Virginia Commonwealth University, Richmond, VA, 209-212.
- Dolovich, M. B. and Dhand, R. (2011). Aerosol drug delivery: developments in device design and clinical use. *The Lancet* 377:1032-1045.
- Donohue, J. F. (2004). Therapeutic responses in asthma and COPD: bronchodilators. *Chest* 126:125S-137S.
- Duddu, S. P., Sisk, S. A., Walter, Y. H., Tarara, T. E., Trimble, K. R., Clark, A. R., Eldon, M. A., Elton, R. C., Pickford, M. and Hirst, P. H. (2002). Improved lung delivery from a passive dry powder inhaler using an engineered PulmoSphere® powder. *Pharmaceutical Research* 19:689-695.
- Dullien, F. A. L. (1992). Pore structure, in *Porous Media*, Academic Press, San Diego, 5-115.
- Dumouchel, C. (2008). On the experimental investigation on primary atomization of liquid streams. *Experiments in Fluids* 45:371-422.
- Dunbar, C. (1997). Atomization mechanisms of the pressurized metered dose inhaler. *Particulate Science and Technology* 15:253-271.
- Dunbar, C. and Miller, J. (1997). Theoretical investigation of the spray from a pressurized metered-dose inhaler. *Atomization and Sprays* 7:417-436.
- Dunbar, C., Watkins, A. and Miller, J. (1997). An experimental investigation of the spray issued from a pMDI using laser diagnostic techniques. *Journal of Aerosol Medicine* 10:351-368.
- Dunbar, C. A. and Hickey, A. J. (1998). pMDI optimization using an actuator flow model, in *Respiratory Drug Delivery VI*, R. N. Dalby, P. R. Byron and S. J. Farr, eds. Interpharm Press, Buffalo Grove, IL, 319-322.
- Dunbar, C. A., Hickey, A. J. and Holzner, P. (1998). Dispersion and characterization of pharmaceutical dry powder aerosols. *KONA* 16:7-44.
- Edward, J. T. (1970). Molecular volumes and the Stokes-Einstein equation. *Journal of Chemical Education* 47:261-270.
- Edwards, D. A., Hanes, J., Caponetti, G., Hrkach, J., Ben-Jebria, A., Eskew, M. L., Mintzes, J., Deaver, D., Lotan, N. and Langer, R. (1997). Large porous particles for pulmonary drug delivery. *Science* 276:1868 -1871.
- Feng, A., Boraey, M., Gwin, M., Finlay, P., Kuehl, P. and Vehring, R. (2011). Mechanistic models facilitate efficient development of leucine containing microparticles for pulmonary drug delivery. *International Journal of Pharmaceutics*.
- Finlay, W. (2011). Pharmaceutical aerosol sprays for drug delivery to the lungs, in *Handbook of Atomization and Sprays: Theory and Applications*, N. Ashgriz, ed., Springer, 899-907.

- Finlay, W. H. (2001a). Metered Dose Propellant Inhalers, in *The Mechanics of Inhaled Pharmaceutical Aerosols*, Academic Press, San Diego, 277-293.
- Finlay, W. H. (2001b). *The Mechanics of Inhaled Pharmaceutical Aerosols*. Academic Press, San Diego.
- Flament, M.-P., Leterme, P. and Gayot, A. (2004). The influence of carrier roughness on adhesion, content uniformity and the *in vitro* deposition of terbutaline sulphate from dry powder inhalers. *International Journal of Pharmaceutics* 275:201-209.
- Fradley, G. and Hodson, D. (2008). Optimization of fluid flow in pMDI valves, in *Respiratory Drug Delivery 2008*, R. N. Dalby, P. R. Byron, J. Peart, J. D. Suman, S. J. Farr and P. M. Young, eds., Virginia Commonwealth University, Richmond, VA, 329-332.
- Fu, N., Woo, M. W. and Chen, X. D. (2012). Single droplet drying technique to study drying kinetics measurement and particle functionality: A review. *Drying Technology* 30:1771-1785.
- Fuchs, N. A. (1959). *Evaporation and Droplet Growth in Gaseous Media*. Pergamon Press, London.
- Gabrio, B. J., Stein, S. W. and Velasquez, D. J. (1999). A new Method to evaluate plume characteristics of hydrofluoroalkane and chlorofluorocarbon metered dose inhalers. *International Journal of Pharmaceutics* 186:3-12.
- Ganderton, D., Lewis, D., Davies, R., Meakin, B., Brambilla, G. and Church, T. (2002). Modulite®: a means of designing the aerosols generated by pressurized metered dose inhalers. *Respiratory Medicine* 96:S3-S8.
- Gartlehner, G., Hansen, R. A., Carson, S. S. and Lohr, K. N. (2006). Efficacy and safety of inhaled corticosteroids in patients with COPD: a systematic review and meta-analysis of health outcomes. *The Annals of Family Medicine* 4:253-262.
- Geller, D. E., Weers, J. and Heurding, S. (2011). Development of an inhaled dry-powder formulation of tobramycin using PulmoSphere™ technology. *Journal of Aerosol Medicine and Pulmonary Drug Delivery* 24:175-182.
- Gill, S., Löbenberg, R., Ku, T., Azarmi, S., Roa, W. and Prenner, E. J. (2007). Nanoparticles: characteristics, mechanisms of action, and toxicity in pulmonary drug delivery—a review. *Journal of Biomedical Nanotechnology* 3:107-119.
- Gonda, I. (1985). Development of a systematic theory of suspension inhalation aerosols. I. A framework to study the effects of aggregation on the aerodynamic behaviour of drug particles. *International Journal of Pharmaceutics* 27:99-116.
- Gonnissen, Y., Remon, J. P. and Vervaet, C. (2007). Development of directly compressible powders via co-spray drying. *European Journal of Pharmaceutics and Biopharmaceutics* 67:220-226.
- Grainger, C., Saunders, M., Buttini, F., Telford, R., Merolla, L., Martin, G., Jones, S. and Forbes, B. (2012). Critical characteristics for corticosteroid solution metered dose inhaler bioequivalence. *Molecular Pharmaceutics* 9:563-569.
- Grasmeijer, N., de Waard, H., Hinrichs, W. L. and Frijlink, H. W. (2013). A user-friendly model for spray drying to aid pharmaceutical product development. *PLoS ONE* 8:1-11.
- Gross, N. J. (2006). Anticholinergic agents in asthma and COPD. *European Journal of Pharmacology* 533:36-39.
- Gupta, A., Stein, S. W. and Myrdal, P. B. (2003). Balancing ethanol cosolvent concentration with product performance in 134a-based pressurized metered dose inhalers. *Journal of Aerosol Medicine* 16:167-174.
- Gutmann, F. and Simmons, L. (1952). The temperature dependence of the viscosity of liquids. *Journal of Applied Physics* 23:977-978.

- Haghi, M., Bebawy, M., Colombo, P., Forbes, B., Lewis, D. A., Salama, R., Traini, D. and Young, P. M. (2014). Towards the bioequivalence of pressurised metered dose inhalers 2. Aerodynamically equivalent particles (with and without glycerol) exhibit different biopharmaceutical profiles *in vitro*. *European Journal of Pharmaceutics and Biopharmaceutics* 86:38-45.
- Haig, C. W., Hursthouse, A., McIlwain, S. and Sykes, D. (2014). The effect of particle agglomeration and attrition on the separation efficiency of a Stairmand cyclone. *Powder Technology* 258:110-124.
- Hancock, B. C., Shamblin, S. L. and Zografi, G. (1995). Molecular mobility of amorphous pharmaceutical solids below their glass transition temperatures. *Pharmaceutical Research* 12:799-806.
- Haynes, A., Shaik, M. S., Krarup, H. and Singh, M. (2004). Evaluation of the Malvern Spraytec® with inhalation cell for the measurement of particle size distribution from metered dose inhalers. *Journal of Pharmaceutical Sciences* 93:349-363.
- He, G., Bhamidi, V., Tan, R. B., Kenis, P. J. and Zukoski, C. F. (2006). Determination of critical supersaturation from microdroplet evaporation experiments. *Crystal Growth and Design* 6:1175-1180.
- Hédoux, A., Decroix, A.-A., Guinet, Y., Paccou, L., Derollez, P. and Descamps, M. (2011a). Low-and high-frequency Raman investigations on caffeine: polymorphism, disorder and phase transformation. *Journal of Physical Chemistry B* 115:5746-5753.
- Hédoux, A., Guinet, Y. and Descamps, M. (2011b). The contribution of Raman spectroscopy to the analysis of phase transformations in pharmaceutical compounds. *International Journal of Pharmaceutics* 417:17-31.
- Heyder, J., Gebhart, J., Rudolf, G., Schiller, C. F. and Stahlhofen, W. (1986). Deposition of particles in the human respiratory tract in the size range 0.005–15 µm. *Journal of Aerosol Science* 17:811-825.
- Heyder, J. (2004). Deposition of inhaled particles in the human respiratory tract and consequences for regional targeting in respiratory drug delivery. *Proceedings of the American Thoracic Society* 1:315-320.
- Hinds, W. C. (1999). *Aerosol Technology: Properties, Behavior, and Measurement of Airborne Particles*. Wiley, Hoboken, NJ.
- Hobbs, P. V. (1974). *Ice Physics*. Oxford New York.
- Hochrainer, D., Hölz, H., Kreher, C., Scaffidi, L., Spallek, M. and Wachtel, H. (2005). Comparison of the aerosol velocity and spray duration of Respimat® Soft Mist™ inhaler and pressurized metered dose inhalers. *Journal of Aerosol Medicine* 18:273-282.
- Hoe, S., Traini, D., Chan, H.-K. and Young, P. M. (2009). The influence of flow rate on the aerosol deposition profile and electrostatic charge of single and combination metered dose inhalers. *Pharmaceutical Research* 26:2639-2646.
- Hoe, S., Semler, D. D., Goudie, A. D., Lynch, K. H., Matinkhoo, S., Finlay, W. H., Dennis, J. J. and Vehring, R. (2013). Respirable bacteriophages for the treatment of bacterial lung infections. *Journal of Aerosol Medicine and Pulmonary Drug Delivery* 26:317-335.
- Hoe, S., Ivey, J. W., Boraey, M. A., Shamsaddini-Shahrbabak, A., Javaheri, E., Matinkhoo, S., Finlay, W. H. and Vehring, R. (2014). Use of a fundamental approach to spray-drying formulation design to facilitate the development of multi-component dry powder aerosols for respiratory drug delivery. *Pharmaceutical Research* 31:449-465.
- Hoffman, A. C. and Stein, L. E. (2008). *Gas Cyclones and Swirl Tubes: Principles, Design, and Operation*. Springer, Berlin.

- Høiby, N. (2011). Recent advances in the treatment of *Pseudomonas aeruginosa* infections in cystic fibrosis. *BMC medicine* 9:32.
- Hoose, C. and Möhler, O. (2012). Heterogeneous ice nucleation on atmospheric aerosols: a review of results from laboratory experiments. *Atmospheric Chemistry and Physics* 12:9817-9854.
- Hoppentocht, M., Hagedoorn, P., Frijlink, H. W. and de Boer, A. H. (2014). Technological and practical challenges of dry powder inhalers and formulations. *Advanced Drug Delivery Reviews* 75:18-31.
- Hoye, J. A. and Myrdal, P. B. (2008). Measurement and correlation of solute solubility in HFA-134a/ethanol systems. *International Journal of Pharmaceutics* 362:184-188.
- Huang, L., Kumar, K. and Mujumdar, A. S. (2003). Use of computational fluid dynamics to evaluate alternative spray dryer chamber configurations. *Drying Technology* 21:385-412.
- Israelachvili, J. N. (2011). Adhesion and wetting phenomena, in *Intermolecular and Surface Forces*, Academic Press, Burlington, MA.
- Ivey, J. and Vehring, R. (2010). The use of modeling in spray drying of emulsions and suspensions accelerates formulation and process development. *Computers & Chemical Engineering* 34:1030-1035.
- Ivey, J. W., Lewis, D., Church, T., Finlay, W. H. and Vehring, R. (2014). A correlation equation for the mass median aerodynamic diameter of the aerosol emitted by solution metered dose inhalers. *International Journal of Pharmaceutics* 465:18-24.
- Ivey, J. W., Vehring, R. and Finlay, W. H. (2015). Understanding pressurized metered dose inhaler performance. *Expert Opinion on Drug Delivery* 12:901-916.
- Ivey, J. W. and Vehring, R. (2016). A methodology for efficient pharmaceutical spray drying process development, in *AAPS Annual Meeting*, Denver, CO.
- Ivey, J. W., Bhambri, P., Church, T. K., Lewis, D. A., McDermott, M. T., Elbayomy, S., Finlay, W. H. and Vehring, R. (2017). Humidity affects the morphology of particles emitted from beclomethasone dipropionate pressurized metered dose inhalers. *International Journal of Pharmaceutics* 520:207-215.
- James, J., Crean, B., Davies, M., Toon, R., Jinks, P. and Roberts, C. J. (2008). The surface characterisation and comparison of two potential sub-micron, sugar bulking excipients for use in low-dose, suspension formulations in metered dose inhalers *International Journal of Pharmaceutics* 361:209-221.
- Javaheri, E. and Finlay, W. H. (2014). Numerical simulation of flocculation and transport of suspended particles: Application to metered-dose inhalers. *International Journal of Multiphase Flow* 64:28-34.
- Jiji, L. M. (2006). *Heat Convection*. Springer, Berlin.
- Jones, M. D., Harris, H., Hooton, J. C., Shur, J., King, G. S., Mathoulin, C. A., Nichol, K., Smith, T. L., Dawson, M. L., Ferrie, A. R. and Price, R. (2008). An investigation into the relationship between carrier-based dry powder inhalation performance and formulation cohesive–adhesive force balances. *European Journal of Pharmaceutics and Biopharmaceutics* 69:496-507.
- Kaialy, W., Larhrib, H., Ticehurst, M. and Nokhodchi, A. (2012). Influence of batch cooling crystallization on mannitol physical properties and drug dispersion from dry powder inhalers. *Crystal Growth & Design* 12:3006-3017.
- Kaialy, W. and Nokhodchi, A. (2015). Particle engineering for improved pulmonary drug delivery through dry powder inhalers, in *Pulmonary Drug Delivery: Advances and Challenges*, A. Nokhodchi and G. P. Martin, eds., John Wiley & Sons, 171-198.

- Kalume, A., Beresnev, L. A., Santarpia, J. and Pan, Y.-L. (2017). Detection and characterization of chemical aerosol using laser-trapping single-particle Raman spectroscopy. *Applied Optics* 56:6577-6582.
- Keatings, V. M., Jatakanon, A., Worsdell, Y. M. and Barnes, P. J. (1997). Effects of inhaled and oral glucocorticoids on inflammatory indices in asthma and COPD. *American Journal of Respiratory and Critical Care Medicine* 155:542-548.
- Kelkar, M. S. and Dalby, R. N. (2014). Effervescent aerosols: a novel formulation technology for pressurized metered dose inhalers, in *Respiratory Drug Delivery*, R. N. Dalby, P. R. Byron, J. Peart, J. D. Suman, S. J. Farr, P. M. Young and D. Traini, eds. VCU, 669-672.
- Kim, C. S., Trujillo, D. and Sackner, M. (1985). Size aspects of metered-dose inhaler aerosols. *American Review of Respiratory Disease* 132:137-142.
- Kitamura, Y., Morimitsu, H. and Takahashi, T. (1986). Critical superheat for flashing of superheated liquid jets. *Industrial and Engineering Chemistry Fundamentals* 25:206-211.
- Kleinstreuer, C., Zhang, Z. and Donohue, J. (2008). Targeted drug-aerosol delivery in the human respiratory system. *Annual Review of Biomedical Engineering* 10:195-220.
- Kulkarni, A. D., Bari, D. B., Surana, S. J. and Pardeshi, C. V. (2016). *In vitro*, *ex vivo* and *in vivo* performance of chitosan-based spray-dried nasal mucoadhesive microspheres of diltiazem hydrochloride. *Journal of Drug Delivery Science and Technology* 31:108-117.
- Kundu, P. K., Cohen, I. M. and Dowling, D. R. (2012). *Fluid Mechanics*. Academic Press, Waltham, MA.
- Lange, C. F. and Finlay, W. H. (2000). Overcoming the adverse effect of humidity in aerosol delivery via pressurized metered-dose inhalers during mechanical ventilation. *American Journal of Respiratory and Critical Care Medicine* 161:1614-1618.
- Laube, B. L. (2005). The expanding role of aerosols in systemic drug delivery, gene therapy, and vaccination. *Respiratory Care* 50:1161-1176.
- Lechuga-Ballesteros, D., Charan, C., Stults, C., Stevenson, C. L., Miller, D. P., Vehring, R., Tep, V. and Kuo, M.-C. (2008). Trileucine improves dispersibility, aerosol performance and stability of spray-dried powders for inhalation. *Journal of Pharmaceutical Sciences* 97:287-302.
- Lechuga-Ballesteros, D., Noga, B., Vehring, R., Cummings, R. H. and Dwivedi, S. K. (2011). Novel cosuspension metered-dose inhalers for the combination therapy of chronic obstructive pulmonary disease and asthma. *Future Medicinal Chemistry* 3:1703-1718.
- LeClair, D. A., Cranston, E. D., Xing, Z. and Thompson, M. R. (2016). Optimization of spray drying conditions for yield, particle size and biological activity of thermally stable viral vectors. *Pharmaceutical Research* 33:2763-2776.
- Lefebvre, A. H., Atomization, <http://www.thermopedia.com/content/573/>, Accessed 02/11/2018, 2018
- Lehto, P., (2010). *Mechanistic studies of drug dissolution testing*. Ph.D. Thesis, University of Helsinki
- Leong, K. (1981). Morphology of aerosol particles generated from the evaporation of solution drops. *Journal of Aerosol Science* 12:417-435.
- Leroux, S., Dumouchel, C. and Ledoux, M. (1996). The stability curve of Newtonian liquid jets. *Atomization and Sprays* 6:623-647.

- Lewis, D. A., Ganderton, D., Meakin, B. J. and Brambilla, G. (2004). Theory and practice with solution systems, in *Respiratory Drug Delivery IX*, R. N. Dalby, P. R. Byron, J. Peart, J. D. Suman and S. J. Farr, eds. Davis Healthcare International, 109-115.
- Lewis, D. A., Ganderton, D., Meakin, B. J. and Brambilla, G. (2005). Modulite® : A simple solution to a difficult problem. *Respiration* 72 3-5.
- Lewis, D. A., Meakin, B. J. and Brambilla, G. (2006). New actuators versus old: reasons and results for actuator modifications for HFA solution MDIs, in *Respiratory Drug Delivery 2006*, R. N. Dalby, P. R. Byron, J. Peart, J. D. Suman and S. Farr, eds. Virginia Commonwealth University, 101-110.
- Lewis, D. A. (2007). Metered-dose inhalers: actuators old and new. *Expert Opinion on Drug Delivery* 4:235-245.
- Lewis, D. A., O'Shea, H., Johnson, R. and Church, T. (2011). Predicting HFA-MDI dose retention properties: Engineering the marriage between canisters, valves and formulations, in *RDD Europe 2011*, R. N. Dalby, P. R. Byron, J. Peart, J. D. Suman and P. M. Young, eds. Virginia Commonwealth University, Richmond, VA, 89-100.
- Lewis, D. A. (2013). Intrinsic particle size distribution: A new metric to guide the design of HFA solution pMDIs, in *RDD Europe 2013*, R. N. Dalby, P. R. Byron, J. Peart, J. D. Suman, P. M. Young and D. Traini, eds. Virginia Commonwealth University, 175-184.
- Lewis, D. A., Young, P. M., Buttini, F., Church, T., Colombo, P., Forbes, B., Haghi, M., Johnson, R., O'Shea, H. and Salama, R. (2014). Towards the bioequivalence of pressurised metered dose inhalers 1: Design and characterisation of aerodynamically equivalent beclomethasone dipropionate inhalers with and without glycerol as a non-volatile excipient. *European Journal of Pharmaceutics and Biopharmaceutics* 86:31-37.
- Lin, R., Liu, W., Woo, M. W., Chen, X. D. and Selomulya, C. (2015). On the formation of “coral-like” spherical α -glycine crystalline particles. *Powder Technology* 279:310-316.
- Lin, R., Woo, M. W., Wu, Z., Liu, W., Ma, J., Chen, X. D. and Selomulya, C. (2017). Spray drying of mixed amino acids: The effect of crystallization inhibition and humidity treatment on the particle formation. *Chemical Engineering Science* 167:161-171.
- Littringer, E. M., Mescher, A., Schroettner, H., Achelis, L., Walzel, P. and Urbanetz, N. A. (2012). Spray dried mannitol carrier particles with tailored surface properties – The influence of carrier surface roughness and shape. *European Journal of Pharmaceutics and Biopharmaceutics* 82:194-204.
- Liu, W., Wu, W. D., Selomulya, C. and Chen, X. D. (2011). Facile spray-drying assembly of uniform microencapsulates with tunable core-shell structures and controlled release properties. *Langmuir* 27:12910-12915.
- Liu, W., Duo Wu, W., Selomulya, C. and Chen, X. D. (2012a). Spray drying of monodispersed microencapsulates: implications of formulation and process parameters on microstructural properties and controlled release functionality. *Journal of Microencapsulation* 29:677-684.
- Liu, W., Wu, W. D., Selomulya, C. and Chen, X. D. (2013). On designing particulate carriers for encapsulation and controlled release applications. *Powder Technology* 236:188-196.
- Liu, W., Chen, X. and Selomulya, C. (2015). On the spray drying of uniform functional microparticles. *Particuology* 22:1-12.
- Liu, X., Doub, W. H. and Guo, C. (2012b). Evaluation of metered dose inhaler spray velocities using phase doppler anemometry (PDA). *International Journal of Pharmaceutics* 423:235-239.
- Longest, P. W. and Hindle, M. (2009). Quantitative analysis and design of a spray aerosol inhaler. Part 1: effects of dilution air inlets and flow paths. *Journal of Aerosol Medicine and Pulmonary Drug Delivery* 22:271-283.

- Low, N., Kraemer, S., Schneider, M. and Restrepo, A. M. H. (2008). Immunogenicity and safety of aerosolized measles vaccine: systematic review and meta-analysis. *Vaccine* 26:383-398.
- Malcolmson, R. J. and Embleton, J. K. (1998). Dry powder formulations for pulmonary delivery. *Pharmaceutical Science & Technology Today* 1:394-398.
- Martin, A. R. and Finlay, W. H. (2005). The effect of humidity on the size of particles delivered from metered-dose inhalers. *Aerosol Science and Technology* 39:283-289.
- Martin, A. R., Kwok, D. Y. and Finlay, W. H. (2005). Investigating the evaporation of metered-dose inhaler formulations in humid air: single droplet experiments. *Journal of Aerosol Medicine* 18:218-224.
- Martínez, I., Mass diffusivity data, <http://webserver.dmt.upm.es/~isidoro/dat1/Mass%20diffusivity%20data.pdf>, Accessed 21 May, 2015
- Mason, E. and Monchick, L. (1965). Survey of the equation of state and transport properties of moist gases, in *International Symposium on Humidity and Moisture: Fundamentals and Standards*, Reinhold, New York, 257-272.
- McCabe, M. (1972). The diffusion coefficient of caffeine through agar gels containing a hyaluronic acid-protein complex. A model system for the study of the permeability of connective tissues. *Biochemical Journal* 127:249-253.
- McFadden, E. (1995). Improper patient techniques with metered dose inhalers: clinical consequences and solutions to misuse. *Journal of Allergy and Clinical Immunology* 96:278-283.
- Meakin, B., Lewis, D., Ganderton, D. and Brambilla, G. (2000). Countering challenges posed by mimicry of CFC performance using HFA systems, in *Respiratory Drug Delivery VII*, R. N. Dalby, P. R. Byron, S. J. Farr and J. Peart, eds., Serentec, Raleigh, NC, 99-108.
- Mexichem UK Limited (2010a). ZEPHEX® 134a: Physical Property Data Sheet SI Units, Runcorn, UK.
- Mexichem UK Limited (2010b). ZEPHEX® 227ea: Physical Property Data Sheet SI Units, Runcorn, UK.
- Meyer, M., Garron, T., Lubaki, N. M., Mire, C. E., Fenton, K. A., Klages, C., Olinger, G. G., Geisbert, T. W., Collins, P. L. and Bukreyev, A. (2015). Aerosolized Ebola vaccine protects primates and elicits lung-resident T cell responses. *The Journal of Clinical Investigation* 125:3241-3255.
- Misra, A., Hickey, A. J., Rossi, C., Borchard, G., Terada, H., Makino, K., Fourie, P. B. and Colombo, P. (2011). Inhaled drug therapy for treatment of tuberculosis. *Tuberculosis* 91:71-81.
- Mitchell, J. P., Nagel, M. W., Wiersema, K. J. and Doyle, C. C. (2003a). Aerodynamic particle size analysis of aerosols from pressurized metered-dose inhalers: comparison of Andersen 8-stage cascade impactor, next generation pharmaceutical impactor, and model 3321 aerodynamic particle sizer aerosol spectrometer. *AAPS PharmSciTech* 4:425-433.
- Mitchell, J. P., Nagel, M. W., Wiersema, K. J., Doyle, C. C. and Migunov, V. A. (2003b). The effect of humidification on the size distribution of aerosols delivered to the mechanically ventilated patient, in *14th International Society for Aerosols in Medicine Congress Journal of Aerosol Medicine*, 187-227.
- Mitchell, J. P., Newman, S. and Chan, H.-K. (2007). *In vitro* and *in vivo* aspects of cascade impactor tests and inhaler performance: A review. *AAPS PharmSciTech* 8:237-248.
- Mitchell, J. P., Copley, M. and Solomon, D. (2013). Applying the AIM Concept in Support of Developing Improved In Vitro-In Vivo Relationships for OIPs, in *Good Cascade Impactor Practices, AIM and EDA for Orally Inhaled Products* T. P. Tougas, J. P. Mitchell and S. A. Lyapustina, eds., Spring Science & Business Media, New York, 375-400.

- Morin, C. M. D., Ivey, J. W., Titosky, J. T. F., Suderman, J. D., Olfert, J. S., Vehring, R. and Finlay, W. H. (2014). Performance of pressurized metered dose inhalers at extreme temperature conditions. *Pharmaceutical Research* 103:3553-3559.
- Mulero, A., Cachadiña, I. and Parra, M. (2012). Recommended correlations for the surface tension of common fluids. *Journal of Physical and Chemical Reference Data* 41:0431051-13.
- Mulhem, B., Schulte, G. and Fritsching, U. (2006). Solid-liquid separation in suspension atomization. *Chemical Engineering Science* 61:2582-2589.
- Myrdal, P. B., Karlage, K. L., Stein, S. W., Brown, B. A. and Haynes, A. (2004). Optimized dose delivery of the peptide cyclosporine using hydrofluoroalkane based metered dose inhalers. *Journal of Pharmaceutical Sciences* 93:1054-1061.
- Myrdal, P. B., Sheth, P. and Stein, S. W. (2014). Advances in metered dose inhaler technology: Formulation development. *AAPS PharmSciTech* 15:434-455.
- Newbold, F. R. and Amundson, N. R. (1973). A model for evaporation of a multicomponent droplet. *AIChE Journal* 19:22-30.
- Newman, S., Moren, F., Pavia, D., Corrado, O. and Clarke, S. (1982). The effects of changes in metered volume and propellant vapour pressure on the deposition of pressurized inhalation aerosols. *International Journal of Pharmaceutics* 11:337-344.
- Newman, S. P. (2005). Principles of Metered-Dose Inhaler Design. *Respiratory Care* 50:1177-1190.
- Nikander, K. (2010). Challenges and opportunities in respiratory drug delivery devices. *Expert Opinion on Drug Delivery* 7:1235-1238.
- NIST Chemistry Webbook, Ethanol,
<http://webbook.nist.gov/cgi/cbook.cgi?Name=ethanol&Units=SI&cTG=on&cTC=on&cTP=on#ref-34>, Accessed 14 May, 2015
- NIST Chemistry Webbook, Saturation properties for ethane, 1,1,1,2-tetrafluoro- (R134a) — Temperature increments,
http://webbook.nist.gov/cgi/fluid.cgi?ID=C811972&TUnit=K&PUnit=MPa&DUnit=kg%2Fm3&HUnit=kJ%2Fkg&WUnit=m%2Fs&VisUnit=Pa*s&STUnit=N%2Fm&Type=SatP&RefState=DEF&Action=Page//, Accessed 14 May, 2015
- Noga, B., Cummings, R. H., Joshi, V., Lechuga-Ballesteros, D., Schultz, R., Speck, J. H. and Dwivedi, S. (2012). Product performance, stability and dose proportionality of glycopyrrolate metered dose inhaler with sub-microgram doses using cosuspension technology, in *Respiratory Drug Delivery 2012*, R. N. Dalby, P. R. Byron, J. Peart, J. D. Suman and P. M. Young, eds. Davis Healthcare International Publishing, River Grove, IL, 645-648.
- O'Donnell, K. P. and Williams III, R. O. (2013). Pulmonary dispersion formulations: The impact of dispersed powder properties on pressurized metered dose inhaler stability. *Drug Development and Industrial Pharmacy* 39:413-424.
- Oliveira, R. F., Ferreira, A. C., Teixeira, S. F., Teixeira, J. C. and Marques, H. C. (2013). pMDI Spray Plume Analysis: A CFD Study, in *Proceedings of the World Congress on Engineering* International Association of Engineers, London.
- Ooi, J., Gaisford, S., Boyd, B. J., Young, P. M. and Traini, D. (2014). Isothermal calorimetry: A predictive tool to model drug-propellant interactions in pressurized metered dose systems. *International Journal of Pharmaceutics* 461:301-309.

- Patel, K. C. and Chen, X. D. (2007). Production of spherical and uniform-sized particles using a laboratory ink-jet spray dryer. *Asia-Pacific Journal of Chemical Engineering* 2:415-430.
- Patton, J. S., Bukar, J. and Nagarajan, S. (1999). Inhaled insulin. *Advanced Drug Delivery Reviews* 35:235-247.
- Paudel, A., Worku, Z. A., Meeus, J., Guns, S. and Van den Mooter, G. (2013). Manufacturing of solid dispersions of poorly water soluble drugs by spray drying: Formulation and process considerations. *International Journal of Pharmaceutics* 453:253-284.
- Pilcer, G. and Amighi, K. (2010). Formulation strategy and use of excipients in pulmonary drug delivery. *International Journal of Pharmaceutics* 392:1-19.
- Rahmatalla, M. F., Zuberbuhler, P. C., Lange, C. F. and Finlay, W. H. (2002). In vitro effect of a holding chamber on the mouth-throat deposition of QVAR®(hydrofluoroalkane-beclomethasone dipropionate). *Journal of Aerosol Medicine* 15:379-385.
- Ranz, W. E. (1959). On sprays and spraying, in *Department of Engineering Research Bulletin No. 65*, Penn State University.
- Rayleigh, J. W. (1878). On the instability of jets. *Proceedings of the London Mathematical Society* 10:4-13.
- Reid, J. P. and Mitchem, L. (2006). Laser probing of single-aerosol droplet dynamics. *Annual Review of Physical Chemistry* 57:245-271.
- Roche, N. and Dekhuijzen, P. R. (2016). The evolution of pressurized metered-dose inhalers from early to modern devices. *Journal of Aerosol Medicine and Pulmonary Drug Delivery* 29:311-327.
- Rogers, S., Wu, W. D., Lin, S. X. Q. and Chen, X. D. (2012). Particle shrinkage and morphology of milk powder made with a monodisperse spray dryer. *Biochemical Engineering Journal* 62:92-100.
- Rogueda, P. (2005). Novel hydrofluoroalkane suspension formulations for respiratory drug delivery *Expert Opinion on Drug Delivery* 2:625-638.
- Roth, C. and Gebhart, J. (1996). Aqueous droplet sizing by inertial classification. *Particle and Particle Systems Characterization* 13:192-195.
- Ruge, C. A., Kirch, J. and Lehr, C.-M. (2013). Pulmonary drug delivery: from generating aerosols to overcoming biological barriers—therapeutic possibilities and technological challenges. *The Lancet Respiratory Medicine* 1:402-413.
- Ryan, G., Singh, M. and Dwan, K. (2011). Inhaled antibiotics for long term therapy in cystic fibrosis. *Cochrane Database of Systematic Reviews*:Art. No.: CD001021.
- Saboo, S., Tumban, E., Peabody, J., Wafula, D., Peabody, D. S., Chackerian, B. and Muttill, P. (2016). Optimized formulation of a thermostable spray-dried virus-like particle vaccine against human papillomavirus. *Molecular Pharmaceutics* 13:1646-1655.
- Sakagami, M., Sakon, K., Kinoshita, W. and Makino, Y. (2001). Enhanced pulmonary absorption following aerosol administration of mucoadhesive powder microspheres. *Journal of Controlled Release* 77:117-129.
- Sakagami, M., Kinoshita, W., Sakon, K., Sato, J.-I. and Makino, Y. (2002). Mucoadhesive beclomethasone microspheres for powder inhalation: Their pharmacokinetics and pharmacodynamics evaluation. *Journal of Controlled Release* 80:207-218.
- Saleem, I. Y. and Smyth, H. D. (2013). Tuning aerosol particle size distribution of metered dose inhalers using cosolvents and surfactants. *BioMed Research International* 2013.

- Scherließ, R., Mönckedieck, M., Young, K., Trows, S., Buske, S. and Hook, S. (2015). First *in vivo* evaluation of particulate nasal dry powder vaccine formulations containing ovalbumin in mice. *International Journal of Pharmaceutics* 479:408-415.
- Schneider, J. and Hendricks, C. (1964). Source of uniform-sized liquid droplets. *Review of Scientific Instruments* 35:1349-1350.
- Schultz, R. K. (1995). Drug delivery characteristics of metered-dose inhalers. *Journal of Allergy and Clinical Immunology* 96:284-287.
- Schürch, S., Gehr, P., Im Hof, V., Geiser, M. and Green, F. (1990). Surfactant displaces particles toward the epithelium in airways and alveoli. *Respiration Physiology* 80:17-32.
- Shah, V. G. and Hayes, D. J. (2002). Fabrication of passive elements using ink-jet technology, in *IMAPS Advanced Technology Workshop on Passive Integration*, Ogunquit, ME, 32-38.
- Shemirani, F. M., Hoe, S., Lewis, D., Church, T., Vehring, R. and Finlay, W. H. (2013). *In vitro* investigation of the effect of ambient humidity on regional delivered dose with solution and suspension MDIs. *Journal of Aerosol Medicine and Pulmonary Drug Delivery* 26:215-222.
- Shemirani, F. M., Church, T. K., Lewis, D. A., Finlay, W. H. and Vehring, R. (2015). Onset of flash atomization in a propellant microjet. *Journal of Fluids Engineering* 137:091101 1-9.
- Sher, E., Bar-Kohany, T. and Rashkovan, A. (2008). Flash-boiling atomization. *Progress in Energy and Combustion Science* 34:417-439.
- Sheth, P., Stein, S. W. and Myrdal, P. B. (2013). The influence of initial atomized droplet size on residual particle size from pressurized metered dose inhalers. *International Journal of Pharmaceutics* 455:57-65.
- Sheth, P., Fazel, M., Stein, S. W. and Myrdal, P. B. (2014). Formulation effects on differential throat deposition for pMDIs with USP inlet and Alberta idealized throat, in *Respiratory Drug Delivery 2014*, R. Dalby, P. Byron, J. Peart, J. Suman, S. Farr, P. Young and D. Traini, eds., VCU, Fajardo, Puerto Rico, 631-636.
- Sheth, P., Stein, S. W. and Myrdal, P. B. (2015). Factors influencing aerodynamic particle size distribution of suspension pressurized metered dose inhalers. *AAPS PharmSciTech* 16:192-201.
- Sheth, P., Sandell, D., Conti, D. S., Holt, J. T., Hickey, A. J. and Saluja, B. (2017). Influence of formulation factors on the aerosol performance of suspension and solution metered dose inhalers: A systematic approach. *AAPS Journal* 19:1396-1410.
- Shrewsbury, S. B., Cook, R. O., Taylor, G., Edwards, C. and Ramadan, N. M. (2008). Safety and pharmacokinetics of dihydroergotamine mesylate administered via a novel (Tempo™) inhaler. *Headache: The Journal of Head and Face Pain* 48:355-367.
- Shrubb, I. (1998). Influence of throat coating and flow rate on USP throat deposition, in *Respiratory Drug Delivery VI*, R. N. Dalby, P. R. Byron and S. J. Farr, eds. Interpharm Press, Buffalo Grove, IL, 413-416.
- Shurtleff, J. K. and Shurtleff, J. M., Method and devices for manufacturing and delivering of aerosolized formulations, US Patent US20160151275 A1, June 16, 2015
- Siafakas, N., Vermeire, P., Pride, N. a., Paoletti, P., Gibson, J., Howard, P., Yernault, J., Decramer, M., Higenbottam, T. and Postma, D. (1995). Optimal assessment and management of chronic obstructive pulmonary disease (COPD). *European Respiratory Journal* 8:1398-1420.

- Singh, A. and Van den Mooter, G. (2016). Spray drying formulation of amorphous solid dispersions. *Advanced Drug Delivery Reviews* 100:27-50.
- Singh, D. J., Jain, R. R., Soni, P., Abdul, S., Darshana, H., Gaikwad, R. V. and Menon, M. D. (2015). Preparation and evaluation of surface modified lactose particles for improved performance of fluticasone propionate dry powder inhaler. *Journal of Aerosol Medicine and Pulmonary Drug Delivery* 28:254-267.
- Smith, I. J., Bell, J., Bowman, N., Everard, M., Stein, S. and Weers, J. G. (2010). Inhaler devices: what remains to be done? *Journal of Aerosol Medicine and Pulmonary Drug Delivery* 23:S25-S37.
- Smyth, H. D., Mejia-Millan, E. A. and Hickey, A. J. (2002). The effect of ethanol on solvency, vapor pressure, and emitted droplet size of solution metered dose inhalers containing HFA 134a, in *Respiratory Drug Delivery VIII* R. N. Dalby, P. R. Byron, J. Peart and S. J. Farr, eds., VCU, Richmond, VA, 735-738.
- Smyth, H. D. (2003). The influence of formulation variables on the performance of alternative propellant-driven metered dose inhalers. *Advanced Drug Delivery Reviews* 55:807-828.
- Smyth, H. D. (2005). Propellant-driven metered-dose inhalers for pulmonary drug delivery. *Expert Opinion on Drug Delivery* 2:53-74.
- Solvay Fluor GmbH, Solkane® 227 pharma and Solkane® 134a pharma: HFA propellants for medical use, www.solvaychemicals.com//Chemicals%20Literature%20Documents/Fluor/solkane_propellants/Solkane_Pharma_Brochure.pdf. Accessed August 13, 2013
- Son, Y.-J., Mitchell, J. P. and McConville, J. T. (2011). *In vitro* performance testing for pulmonary drug delivery, in *Controlled Pulmonary Drug Delivery*, H. D. C. Smyth and A. J. Hickey, eds., Springer, New York, 383-415.
- Spahn, J. D. (2016). Glucocorticoids, in *Allergy and Asthma: Practical Diagnosis and Management*, M. Mahmoudi, ed., Springer International Publishing, Basel, 599-622.
- Stahlhofen, W., Rudolf, G. and James, A. C. (1989). Intercomparison of experimental regional aerosol deposition data *Journal of Aerosol Medicine* 2:285-308.
- Stein, S. W. and Gabrio, B. J. (2000). Understanding throat deposition during cascade impaction testing, in *Respiratory Drug Delivery VII*, R. N. Dalby, P. R. Byron, S. J. Farr and J. Peart, eds. Serentec Press, Raleigh, NC, 287-290.
- Stein, S. W., Forsyth, B. R., Stefely, J. S., Christensen, J. D., Alband, T. D. and Jinks, P. A. (2004). Expanding the dosing range of metered dose inhalers through formulation and hardware optimization, in *Respiratory Drug Delivery IX*, R. N. Dalby, P. R. Byron, J. Peart, J. D. Suman and S. J. Farr, eds. VCU, Richmond, VA, 125-134.
- Stein, S. W. and Myrdal, P. B. (2004). A theoretical and experimental analysis of formulation and device parameters affecting solution MDI size distributions. *Journal of Pharmaceutical Sciences* 93:2158-2175.
- Stein, S. W., Gabrio, B. J. and Myrdal, P. B. (2005). The influence of vapor pressure on the size of atomized MDI droplets, in *RDD Europe 2005*, R. N. Dalby, P. R. Byron, J. Peart and J. D. Suman, eds., Virginia Commonwealth University, Richmond, VA, 151-156.
- Stein, S. W. and Myrdal, P. B. (2006). The relative influence of atomization and evaporation on metered dose inhaler drug delivery efficiency. *Aerosol Science and Technology* 40:335-347.
- Stein, S. W. (2008a). Aiming for a moving target: challenges with impactor measurements of MDI aerosols. *International Journal of Pharmaceutics* 355:53-61.
- Stein, S. W. (2008b). Estimating the number of droplets and drug particles emitted from MDIs. *AAPS PharmSciTech* 9:112-115.

- Stein, S. W. and Fradley, G. (2010). What is the future of MDIs? , in *Respiratory Drug Delivery 2010*, R. Dalby, P. Byron, J. Peart, J. Suman, S. Farr and P. Young, eds. VCU, Richmond, VA, 373-376.
- Stein, S. W., Sheth, P., Karayiannis, C., Chiou, H. and Myrdal, P. B. (2010). Modeling MDI delivery: *A priori* predictions, empirical models and experiments, in *Respir Drug Delivery*, R. N. Dalby, P. B. byron, J. Peart, J. D. Suman, S. J. Farr and P. Young, eds. VCU, Richmond, VA, 353-64.
- Stein, S. W., Sheth, P. and Myrdal, P. B. (2012). A model for predicting size distributions delivered from pMDIs with suspended drug. *International Journal of Pharmaceutics* 422:101-115.
- Stein, S. W. and Cocks, P. (2013). Size distribution measurements from metered dose inhalers at low temperatures, in *RDD Europe*, R. N. Dalby, P. B. Byron, J. Peart, J. D. Suman, P. M. Young and D. Traini, eds. VCU, Richmond, VA.
- Stein, S. W., Sheth, P., Hodson, P. D. and Myrdal, P. B. (2014). Advances in metered dose inhaler technology: Hardware development. *AAPS PharmSciTech* 15:326-338.
- Stein, S. W., Sheth, P., Younis, U. S., Mogalian, E. and Myrdal, P. B. (2015). Modeling and understanding combination pMDI formulations with both dissolved and suspended drugs. *Molecular Pharmaceutics* 12:3455-3467.
- Stein, S. W. and Thiel, C. G. (2017). The History of therapeutic aerosols: A chronological review. *Journal of Aerosol Medicine and Pulmonary Drug Delivery* 30:20-41.
- Sterling, A. M. and Sleicher, C. (1975). The instability of capillary jets. *Journal of Fluid Mechanics* 68:477-495.
- Ström, L. (1969). The generation of monodisperse aerosols by means of a disintegrated jet of liquid. *Review of Scientific Instruments* 40:778-782.
- Tam, J. M., Engstrom, J. D., Ferrer, D., Williams, R. O. and Johnston, K. P. (2010). Templated open flocs of anisotropic particles for pulmonary delivery with pressurized metered dose inhalers. *Journal of Pharmaceutical Sciences* 99:3150-3165.
- Tan, B. M. J., Chan, L. W. and Heng, P. W. S. (2016). Improving dry powder inhaler performance by surface roughening of lactose carrier particles. *Pharmaceutical Research* 33:1923-1935.
- Tarara, T., Weers, J. and Dellamary, L. (2000). Engineered powders for inhalation, in *Respiratory Drug Delivery VII* Serentec Press, Raleigh, NC, 413-416.
- Tarara, T. E., Hartman, M. S., Gill, H., Kennedy, A. A. and Weers, J. G. (2004). Characterization of suspension-based metered dose Inhaler formulations composed of spray-dried budesonide microcrystals dispersed in HFA-134a. *Pharmaceutical Research* 21:1607-1614.
- Telko, M. J. and Hickey, A. J. (2005). Dry powder inhaler formulation. *Respiratory Care* 50:1209-1227.
- Thiel, C. G. (1996). From susie's question to CFC free: An inventor's perspective on forty years of MDI development and regulation, in *Respiratory Drug Delivery V*, R. N. Dalby, P. R. Byron and S. J. Farr, eds. Interpharm Press, Buffalo Grove, IL, 115-124.
- Titosky, J. T., Morin, C., Suderman, J. D., Olfert, J. S., Finlay, W. H. and Vehring, R. (2014). The effect of altitude on inhaler performance. *Journal of Pharmaceutical Sciences* 103:2116-2124.
- Truong-Le, V., Lovalenti, P. M. and Abdul-Fattah, A. M. (2015). Stabilization challenges and formulation strategies associated with oral biologic drug delivery systems. *Advanced Drug Delivery Reviews* 93:95-108.

Tsapis, N., Bennett, D., Jackson, B., Weitz, D. A. and Edwards, D. A. (2002). Trojan particles: Large porous carriers of nanoparticles for drug delivery. *Proceedings of the National Academy of Sciences of the United States of America* 99:12001 - 12005.

Tsapis, N., Dufresne, E. R., Sinha, S. S., Riera, C. S., Hutchinson, J. W., Mahadevan, L. and Weitz, D. A. (2005). Onset of buckling in drying droplets of colloidal suspensions. *Physical Review Letters* 94:018302 1-4.

USP (2013). Chapter <601> Aerosols, nasal sprays, metered-dose inhalers, and dry powder inhalers, in *USP 36 - NF 31*, United Book Press, Baltimore, MD.

Van Wylen, G. and Sonntag, R. (1965). *Fundamentals of Classical Thermodynamics*. Wiley, New York.

Vehring, R., Foss, W. R. and Lechuga-Ballesteros, D. (2007). Particle formation in spray drying. *Journal of Aerosol Science* 38:728-746.

Vehring, R. (2008). Pharmaceutical particle engineering via spray drying. *Pharmaceutical Research* 25:999-1022.

Vehring, R., Lechuga-Ballesteros, D., Joshi, V., Noga, B. and Dwivedi, S. (2012). Cosuspensions of microcrystals and engineered microparticles for uniform and efficient delivery of respiratory therapeutics from pressurized metered dose inhalers. *Langmuir* 28:15015-15023.

Vehring, R. and Finlay, W. (2013). State of the field: manufacturing and device options for the delivery of biotherapeutics. *Journal of Aerosol Medicine and Pulmonary Drug Delivery* 26:A9.

Versteeg, H. and Hargrave, G. (2002). Near-orifice spray and valve flow regime of a pharmaceutical pressurised metered dose inhaler, in *ILASS 2002 ILASS*, Naples, 167-171.

Versteeg, H., Hargrave, G. and Kirby, M. (2006). Internal flow and near-orifice spray visualisations of a model pharmaceutical pressurised metered dose inhaler, in *Journal of Physics: Conference Series* IOP Publishing, 207.

Versteeg, H. K. and Hargrave, G. (2006). Fundamentals and resilience of the original MDI actuator design, in *Respiratory Drug Delivery*, R. N. Dalby, P. R. Byron, J. Peart, J. D. Suman and S. J. Farr, eds. VCU, Richmond, VA, 91-100.

Vervaet, C. and Byron, P. B. (1999). Drug-surfactant-propellant interactions in HFA formulations. *International Journal of Pharmaceutics* 186:13-30.

Walz, M., Hirth, T. and Weber, A. (2017). Investigation of chemically modified inulin as encapsulation material for pharmaceutical substances by spray-drying. *Colloids and Surfaces A: Physicochemical and Engineering Aspects* 536:47-52.

Wang, H., Boraey, M. A., Williams, L., Lechuga-Ballesteros, D. and Vehring, R. (2014). Low-frequency shift dispersive Raman spectroscopy for the analysis of respirable dosage forms. *International Journal of Pharmaceutics* 469:197-205.

Wang, H., (2015). *Low-frequency and macro-Raman analysis of respirable dosage forms and their sampling with a low flow rate single-nozzle cascade impactor*. M.Sc. Thesis, University of Alberta

Wang, H., Bhamri, P., Ivey, J. and Vehring, R. (2017). Design and pharmaceutical applications of a low-flow-rate single-nozzle impactor. *International Journal of Pharmaceutics* 533:14-25.

Weers, J. and Tarara, T. (2014). The PulmoSphere™ platform for pulmonary drug delivery. *Therapeutic Delivery* 5:277-295.

Wigley, G., Versteeg, H. and Hodson, D. (2002). Near-orifice PDA measurements and atomisation mechanism of a pharmaceutical pressurised metered dose inhaler, in *ILASS 2002 ILASS*, Naples.

Wilson, A. F., Mukai, D. S. and Ahdout, J. J. (1991). Effect of canister temperature on performance of metered-dose inhalers. *American Review of Respiratory Disease* 143:1034-1037.

Wu, W. D., Patel, K. C., Rogers, S. and Chen, X. D. (2007). Monodisperse droplet generators as potential atomizers for spray drying technology. *Drying Technology* 25:1907-1916.

Wu, W. D., Liu, W., Gengenbach, T., Woo, M. W., Selomulya, C., Chen, X. D. and Weeks, M. (2014). Towards spray drying of high solids dairy liquid: Effects of feed solid content on particle structure and functionality. *Journal of Food Engineering* 123:130-135.

Wu, Z., Thatcher, M. L., Lundberg, J. K., Ogawa, M. K., Jacoby, C. B., Battiste, J. L. and Ledoux, K. A. (2012). Forced degradation studies of corticosteroids with an alumina–steroid–ethanol model for predicting chemical stability and degradation products of pressurized metered-dose inhaler formulations. *Journal of Pharmaceutical Sciences* 101:2109-2122.

Xu, Z. and Hickey, A. J. (2014). The physics of aerosol droplet and particle generation from inhalers, in *Controlled Pulmonary Drug Delivery*, H. D. C. Smyth and A. J. Hickey, eds., Springer, New York, 75-100.

Young, P. M., Price, R., Lewis, D., Edge, S. and Traini, D. (2003). Under pressure: predicting pressurized metered dose inhaler interactions using the atomic force microscope. *Journal of Colloid and Interface Science* 262:298-302.

Zeng, X. M., Martin, G. P., Marriott, C. and Pritchard, J. (2001). Lactose as a carrier in dry powder formulations: the influence of surface characteristics on drug delivery. *Journal of Pharmaceutical Sciences* 90:1424-1434.

Zhu, B., Traini, D., Chan, H.-K. and Young, P. M. (2013). The effect of ethanol on the formation and physico-chemical properties of particles generated from budesonide solution-based pressurized metered-dose inhalers. *Drug Development and Industrial Pharmacy* 39:1625-1637.

Zhu, B., Traini, D., Lewis, D. A. and Young, P. (2014a). The solid-state and morphological characteristics of particles generated from solution-based metered dose inhalers: Influence of ethanol concentration and intrinsic drug properties. *Colloids and Surfaces A: Physicochemical and Engineering Aspects* 443:345-355.

Zhu, B., Xu, N., Traini, D. and Young, P. M. (2014b). The effect of temperature on particles delivered by metered dose inhalers, in *Respiratory Drug Delivery*, R. Dalby, Byron, PR, Peart, J, Suman, JD, Farr, SJ, Young, PM and Traini, D, R. N. Dalby, P. R. Byron, J. Peart, J. D. Suman, S. J. Farr, P. M. Young and D. Traini, eds. VCU, Richmond, VA, 793-796.

Zhu, B., Xu, N., Traini, D., Lewis, D. and Young, P. M. (2015). The formation of aerosol particles from solution-based pressurized metered dose inhalers and implications of incomplete droplet drying: Theoretical and experimental comparison. *Aerosol Science and Technology* 49:1090-1099.

Appendices

A1. Supplementary materials to Section 2.3

A1.1. Methods

A1.1.1. Stochastic particle-to-droplet assignment model

A graphic depiction of some of the key steps carried out in the model is presented in Figure A 1.

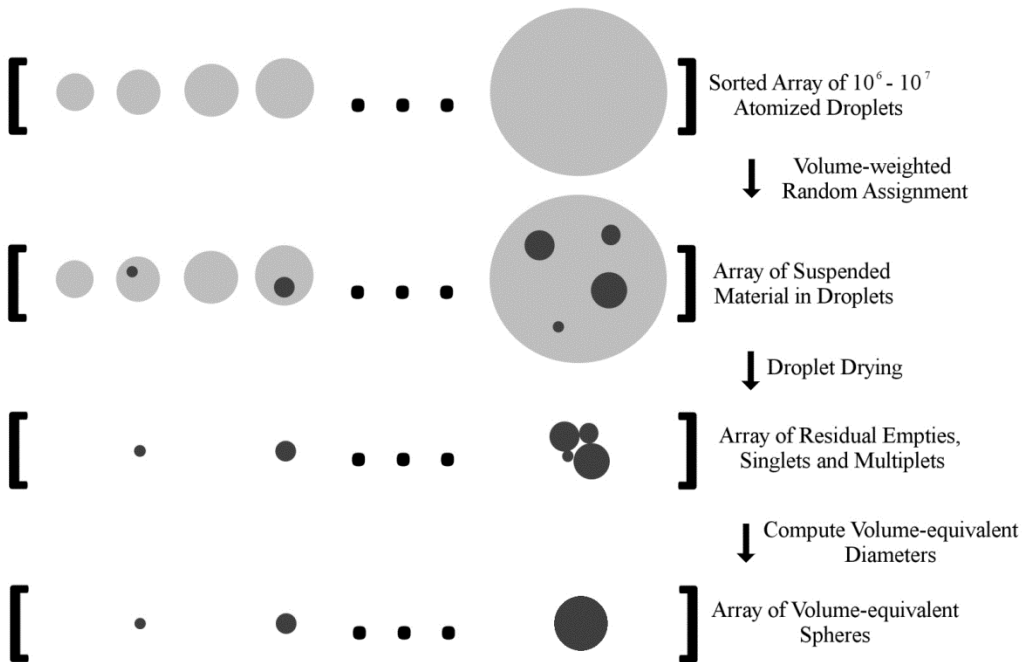


Figure A 1: Graphical illustration of some key steps in the stochastic particle-to-droplet assignment model.

The model was coded in C++ in using an integrated development environment (Visual Studio 2017; Microsoft, Redmond, WA, USA). The main assumptions employed in the model are as follows:

1. The spray of droplets is made up of polydisperse spheres with a lognormal diameter distribution.
2. The suspended phase consists of polydisperse spheres with a lognormal diameter distribution.

3. The presence of a suspended phase does not alter the atomized droplet diameter distribution save as in assumption 4 below.
4. In instances where the volume of suspended material assigned to an atomized droplet, V_{sp_i} , exceeds the volume of that droplet, V_{0_i} , the droplet volume is increased to $V_{0_{i,new}}$ by summing per Equation A.1:

$$V_{0_{i,new}} = V_{0_i} + V_{sp_i} \quad (\text{A.1})$$

5. For multiplets, the shape and packing effects are neglected, and the volume equivalent diameter is computed using Equation A.2:

$$d_{v_i} = \left(\frac{6V_{sp_i}}{\pi} \right)^{\frac{1}{3}} \quad (\text{A.2})$$

The first assumption has been widely adopted by researchers studying pMDI sprays because the lognormal distribution is easy to work with, and it generally describes droplet diameter distributions adequately (Stein and Myrdal 2004). As for the second assumption, the lognormal distribution has been found to provide a satisfactory description of the particle size distribution for micronized drugs as well (Kim et al. 1985). The assumption of spherical suspended phase particles is made due to lack of reliable data on shape factors for micronized drugs. This will result in some uncertainty in the relationship between the volume equivalent diameter distribution and the aerodynamic diameter distribution for micronized drug materials. The third and fourth assumptions seem reasonable in light of the work of Mulhem et al. (Mulhem et al. 2006), who showed in experiments with twin fluid atomization of suspensions with high solids load (~ 50 % by weight) that significant alteration of the atomized droplet diameter distribution only occurs when the median size of the suspended material approaches or exceeds the median atomized droplet diameter. Modifying droplet diameters per Equation A.1 results in effectively diluting the simulated suspension by introducing additional volume of continuous phase into the simulation; this ‘numerical dilution’ effect was tracked for each simulation, as was the effect on the atomized droplet diameter distribution; both effects were found to be negligible for ranges of input variables relevant to suspension pMDIs. The fifth assumption was adopted for simplicity: dynamic shape factors are not generally known for micronized drug material, making the impact of shape on packing difficult to quantify. Further, the aerodynamic diameter of a multiplet made up of many spherical particles can be shown to be relatively insensitive to the degree of packing.

Assuming the shape factor χ and the slip correction ratio ξ are both equal to 1, the aerodynamic diameter of such a multiplet with void fraction ϕ is, using Equation 1.3,

$$d_{a,multiplet} = \sqrt{\frac{(1-\phi)\rho_t}{\rho^*\chi}} d_{v,multiplet} \quad (A.3)$$

The volume equivalent diameter of the multiplet is

$$d_{v,multiplet} = \left(\frac{6V_{multiplet}}{\pi}\right)^{\frac{1}{3}} = \left(\frac{6m_{multiplet}}{\pi\rho_t(1-\phi)}\right)^{\frac{1}{3}}, \quad (A.4)$$

and therefore

$$d_{a,multiplet} \propto (1-\phi)^{\frac{1}{6}}. \quad (A.5)$$

Thus the assumption $\phi = 0$ embodied in Equation A.2 is not likely to result in much of an error in the aerodynamic diameter. For example, assuming a void fraction $\phi \approx 0.35$ for polydisperse spheres (Desmond and Weeks 2014) results in a calculated aerodynamic diameter which is only 7% smaller than that calculated using the approach herein.

For each simulation, the user-defined inputs summarized in Table 2.5 were set to desired levels, and the following computational tasks were executed sequentially:

1. Count median diameters (CMDs) and diameters of average volume were calculated based on the user-defined droplet and suspended particle mass median diameter ($d_{0,50}$, $d_{sp,50}$) and GSD (GSD_0 , GSD_{sp}) using the Hatch-Choate conversion equations (Hinds 1999).

Droplet CMD:

$$CMD_0 = d_{0,50} \exp(-3 \ln^2 GSD_0) \quad (A.6)$$

Droplet diameter of average volume:

$$d_{0\bar{v}} = d_{0,50} \exp\left(-\frac{3}{2} \ln^2 GSD_0\right) \quad (A.7)$$

Suspended material CMD:

$$CMD_{sp} = d_{sp,50} \exp(-3 \ln^2 GSD_{sp}) \quad (A.8)$$

Suspended material diameter of average volume:

$$d_{sp\bar{v}} = d_{sp,50} \exp\left(-\frac{3}{2} \ln^2 GSD_{sp}\right) \quad (A.9)$$

2. The number of suspended particles to simulate was computed based on the suspension concentration and the size distribution parameters:

$$\frac{N_{sp}}{N_0} = \frac{c_{sp}}{\rho_t} \left[\frac{d_{0\bar{v}}}{d_{sp\bar{v}}} \right]^3 \quad (\text{A.10})$$

3. Arrays comprising logarithmically spaced diameter bins were generated for droplets (x_0) and suspended particles (x_{sp}). Each diameter bin array was centered about the corresponding CMD. The number of bins and the spacing constant were user defined, and chosen such that the arrays spanned a broader range of diameters than the count distributions, even for the largest values of GSD_{sp} and GSD_0 .
4. The discrete count distributions for the droplets and the suspended particles were generated using a lognormal frequency distribution function (Hinds 1999). For the i -th droplet diameter bin with upper diameter x_{0i} , lower diameter x_{0i-1} , and centroid $x_{0\bar{t}} = \sqrt{x_{0i} x_{0i-1}}$, the corresponding i -th element of the droplet count distribution, n_{0i} , was computed:

$$n_{0i} = \frac{N_0}{\sqrt{2\pi} x_{0\bar{t}} \ln GSD_0} \exp \left[-\frac{(\ln x_{0\bar{t}} - \ln CMD_0)^2}{2(\ln GSD_0)^2} \right] (x_{0i} - x_{0i-1}) \quad (\text{A.11})$$

For the first element n_{0_0} , the centroid $x_{0\bar{t}} = \frac{x_{0_0}}{2}$, and the bin width (i.e. the difference in parenthesis at the right of Equation (A.11)) was x_{0_0} . The same approach was used to generate the suspended particle count distributions.

5. A sorted array containing the diameter of each of the N_0 droplets in the simulation, X_0 , was generated using the droplet count distribution, n_0 , and the centroids of the diameter bins, $x_{0\bar{t}}$.
6. The total volume of the droplets in the simulation, V_0 , was computed, and an N_0 -element array containing the cumulative distribution of droplet volume, F_0 , was generated.

First element:

$$F_{0_0} = \frac{\pi X_{0_0}^3}{6V_0} \quad (\text{A.12})$$

Subsequent elements:

$$F_{0_i} = F_{0_{i-1}} + \frac{\pi X_{0_i}^3}{6V_0} \quad (\text{A.13})$$

7. Every suspended particle in the simulation was assigned to a droplet as follows¹¹. For the i -th suspended particle with diameter x_{sp_i} , a random floating point number on $[0, 1)$, z_i , was generated and used to determine to which droplet the suspended particle was to be assigned. Using a binary search algorithm, the array index j on $[0, N_0 - 1]$ was determined such that

$$F_{0_{j-1}} \leq z_i < F_{0_j} . \quad (\text{A.14})$$

Then the corresponding elements of N_0 -element arrays containing the total volume of suspended material per droplet, V_{sp_j} , and the number of suspended particles per droplet, p_{sp_j} , were incremented:

$$V_{sp_{j,new}} = V_{sp_j} + \frac{\pi x_{sp_i}^3}{6} \quad (\text{A.15})$$

$$p_{sp_{j,new}} = p_{sp_j} + 1 \quad (\text{A.16})$$

8. Droplet diameter modification per Equation A.1 was conducted if needed.
9. Residual particle volume equivalent and aerodynamic diameters were computed as in Equations (2.17):

$$d_{v_i} = \frac{6}{\pi} \sqrt[3]{V_{sp_i}} , \quad d_{a_i} = \sqrt{\frac{\rho}{\rho^*}} d_{v_i} \quad (\text{2.17})$$

10. Finally, the volume-weighted distributions of diameter and aerodynamic diameter were calculated. Additionally, the ‘‘multiplicity’’ distribution was computed (the fraction, by number, of empty droplets, singlets, doublets, etc.). These outputs were written to a file

¹¹ An alternative technique employed by other researchers (Sheth et al. 2015; Stein et al. 2015; Stein et al. 2012) involves utilizing the Poisson distribution in combination with a pseudorandom number generator to determine the number of suspended particles in each droplet. The equivalency of the technique utilized herein was demonstrated by conducting simulations with monodisperse droplets; in these cases the multiplet distribution was observed to coincide with that predicted by the Poisson distribution.

for additional processing and analysis using Excel 2010 (Microsoft, Redmond, WA, USA) and Origin 2018 (OriginLab, Northampton, MA, USA).

A1.1.2. Experimental determination of suspension pMDI aPSDs

Micronized fluticasone propionate (FP) was recovered from commercially available pMDIs (Flixotide™ Evohaler™ 250 µg, Allen & Hanburys, Middlesex, UK) using the canister freeze-cut-thaw technique described by (Wang et al. 2017). The recovered material was filled into pMDIs with varying suspension concentration; first, FP was weighed into 20 mL aluminum aerosol canisters (Presspart, Blackburn, UK) using an analytical balance with 0.1 mg resolution (ME204E, Mettler-Toledo, Greifensee, Switzerland). Canisters were capped with retention valves with 63 µL nominal metered volume (DF316/63 RCU, Valois S.A.S., Le Neubourg, France), then crimped and pressure filled using a lab scale aerosol canister filling station (Lab Plant, Pamasol Willi Mäder AG, Pfäffikon, Switzerland). A single actuator with a 0.30 mm spray orifice diameter (Nemo, Presspart, Blackburn, UK) was used for all inhaler tests. Inhalers were tested within one week of filling.

For each aPSD determination, 1-3 actuations were sprayed into the drying chamber of the custom lab scale spray dryer described in section 4.1. The drying chamber was open to the ambient atmosphere (21 ± 1 °C, 30 – 60 % RH), and in this case essentially served as an evaporation chamber with a volume of approximately 30 L; the outlet of the dryer was ported directly to the inlet of a time-of-flight aerodynamic particle sizing instrument (Model 3321, TSI, Shoreview, MN, USA). Inhalers were sonicated for 5 seconds prior to testing; a single actuation was fired to waste before each test. Inhalers were shaken vigorously by hand for 5 – 10 seconds between waste shot and test shot(s). The particle sizing instrument was configured for continuous sampling with discrete samples with a duration of 20 s. Typically, the measured aerosol concentration and aPSD remained relatively constant for 3-5 minutes; only samples during this period were considered in the subsequent analysis. 2 – 3 replicate tests were conducted for each inhaler to assess shot-to-shot variability; additionally, two inhalers were filled at the lowest concentration to assess inter-canister variability.

The atomized droplet diameter distribution produced by the tested pMDI device configuration was estimated by filling three different solution pMDIs, determining their aPSD after actuation into the large volume chamber configuration described above, and utilizing the methods presented in section 2.2.2.1 to determine the content equivalent diameter distribution. The three tested solution formulations were 4 mg/mL PVP + 10 % w/w ethanol, 4 mg/mL caffeine + 10 % w/w ethanol, and 2 mg/mL caffeine + 5% w/w ethanol. Pooled analysis of these tests gave an average value for the mass median content equivalent diameter of 9.6 μm , with a standard deviation of 0.7 μm . The average value for the GSD was 1.52, with a standard deviation of 0.03.

A1.2. Results and discussion

To explore the implications of the model assumption implemented by Equation A.1 (i.e. that in cases where the volume of suspended material assigned to a droplet exceeds the volume of the droplet, the droplet volume is increased) on the atomized droplet diameter distribution, results from a specific simulation run are examined here. Since the likelihood that droplet volume modification is required increases as c_{sp} and the ratio $d_{\text{sp},50}/d_{0,50}$ increase, selected input and output parameters for an extremum case are summarized in Table A 1. Selected output plots are included in Figure A 2.

Table A 1: Summary of selected input and output simulation parameters for an extremum case.

Parameter	Value
Number of droplets in simulation N_0	1×10^7
Nominal droplet mass median diameter $d_{0,50}$	9 μm
Droplet geometric standard deviation GSD_0	2.1
Nominal suspended phase concentration c_{sp}	256 mg/mL
Suspended phase density ρ_{sp}	1365 kg/m ³
Suspended phase mass median diameter $d_{\text{sp},50}$	5 μm
Suspended phase geometric standard deviation GSD_{sp}	1.8
Number of droplets requiring modification per Equation A.1	1.9×10^5
Droplet mass median diameter following modification per Equation A.1	9.08 μm
Suspension concentration computed after droplet modification	241 mg/mL

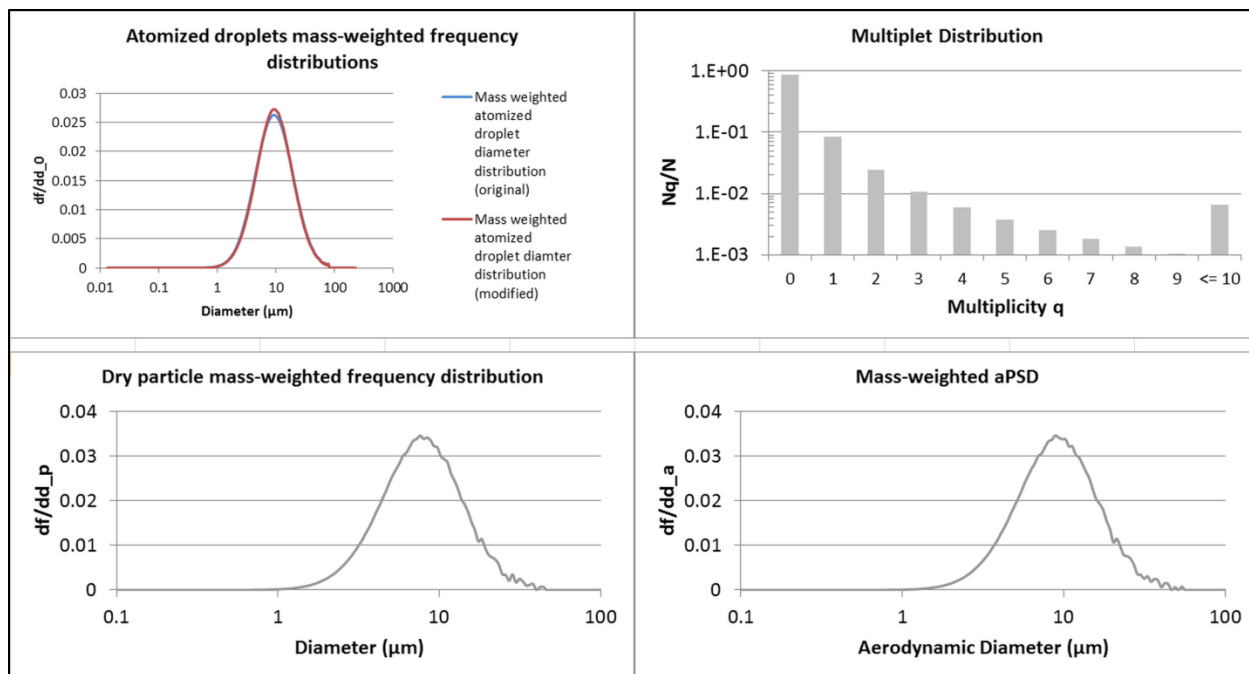


Figure A 2: Screenshot of selected output plots from the Excel analysis template for a simulation run employing a high suspension concentration with relatively large suspended particles.

This example employs a suspension concentration which is at least an order of magnitude higher than is feasible for suspension pMDI delivery, and suspended particles which are fairly coarse relative to typical suspension pMDI formulations. However, the effects on the simulated suspension concentration and atomized droplet diameter distribution are minor, and were far less for other simulation runs. Thus for the simulations presented here, the actual droplet diameter and suspension concentration were very close the nominal values input by the user.

A2. The influence of environmental factors on pMDI performance¹²

A2.1. Introduction

While performance testing of pressurized metered dose inhalers (pMDIs) is typically conducted at controlled laboratory conditions, patients may utilize their inhalers at locations with substantial variations in temperature, humidity, or atmospheric pressure (e.g. at altitude). Since effective drug delivery from pMDIs relies on adequate atomization and sufficiently rapid evaporation of droplets, *in vitro* evaluations were conducted while varying device and ambient temperature (Morin et al. 2014), humidity (Shemirani et al. 2013), and altitude (Titosky et al. 2014) to assess the influence of these factors on the *in vitro* lung dose. Additionally, mechanistic models were used to aid in interpretation of the results.

A2.2. Methods

A2.2.1. *In vitro* lung dose testing

The Alberta Idealized Mouth-Throat Model with a downstream filter classified MDI aerosols into respirable and non-respirable fractions. Filter deposition was assayed gravimetrically or chemometrically to determine *in vitro* lung dose; all experiments were conducted at 28.3 standard L/min air flow rate. A custom environmental chamber allowed manipulation of inhaler or air temperature (Morin et al. 2014) and relative humidity (RH) (Shemirani et al. 2013). A mobile test station was used to conduct high-altitude tests on Mt. Evans, Colorado (Titosky et al. 2014). Save for high-altitude tests and experiments where RH was deliberately varied, all testing was conducted with $RH \lesssim 1\%$.

¹² Appendix A2 consists of material presented in two poster presentations, with some additional text as needed to clarify and elaborate:

Ivey, J. W., Morin, C., Shemirani, F., Suderman, J., Titosky, J., Hoe, S., Finlay, W. and Vehring, R. (2015). The influence of environmental factors on pressurized metered dose inhaler performance, *20th ISAM Congress*, Munich, Germany.

Ivey, J. W., Morin, C., Shemirani, F., Suderman, J., Titosky, J., Hoe, S., Finlay, W. H. and Vehring, R. (2015). Temperature and humidity effects on pressurized metered dose inhaler sprays, *AAAR 34th Annual Conference*, Minneapolis, MN.

A2.2.2. Mechanistic models

A model was developed to assess the influence of pMDI temperature on droplet size. The temperature and formulation dependent mass median initial droplet diameter $d_{0,50}$ was estimated using Equation 2.13, assuming the mass median content equivalent diameter provides a reasonable approximation for the initial mass median diameter:

$$d_{0,50} \approx d_{c,50} = 416 \frac{\sigma_{pa}}{p_{mc}} . \quad A.17$$

The temperature dependence of the propellant vapor pressure in the metering chamber, p_{mc} , and the surface tension in air, σ_{pa} , were modeled using correlations in published datasheets (Mexichem UK Limited 2010a; b).

The quasistationary single droplet evaporation model described in Section 4.5.6.2 was utilized to evaluate the effect of gas temperature and vapor partial pressure on the evaporation rate of propellant droplets.

A2.3. Results and discussion

Varying ambient pressure in the range 61—94 kPa had no statistically significant effect on the *in vitro* lung dose for any of the tested pMDIs (Titosky et al. 2014). This finding may be attributable to the fact that the flow through the actuator orifice is likely choked for a large portion of the metered spray event (Clark 1991), and thus the atomization is insensitive to the pressure downstream of the orifice.

The effect of humidity on the *in vitro* lung dose for three different pMDI formulations tested in a 20 °C laboratory is presented in Figure A 3 (Shemirani et al. 2013). Varying the relative humidity had no significant effect on the *in vitro* lung dose for the tested solution pMDIs. For the suspension pMDI Flixotide 250, a statistically significant reduction ($p < 0.05$) in *in vitro* lung dose was observed at 80 % RH relative to the tests in dry air. Shemirani et al. (Shemirani et al. 2013) propose that condensation of water vapor on drug particles is responsible for the reduction of *in vitro* lung dose at elevated RH for Flixotide 250, and discuss several possible contributing factors which may explain these observations. The formulation and device variables influence the spray plume temperature (Brambilla et al. 2011), and thus may affect the degree of saturation of water vapor and the amount of condensation on the drug aerosol as

ambient air is entrained into the cool spray plume. In this specific case, the inclusion of ethanol in the two solution formulations is notable as it will tend to increase the spray plume temperature relative to propellant-only formulations. As seen in Chapter 3, varying the ethanol content may alter the extent of condensation occurring on particles produced from pMDIs. Another relevant consideration relates to a major difference between suspension and solution formulations: suspension pMDIs typically produce at least an order of magnitude fewer dry residual particles than solution pMDIs (Stein 2008b). Since the amount of condensation on each particle is likely related to the aerosol number concentration, suspension formulations may differ from solution formulations in the extent of transient condensational growth occurring on each particle, with consequent differences in the temporal evolution of the particle size distributions.

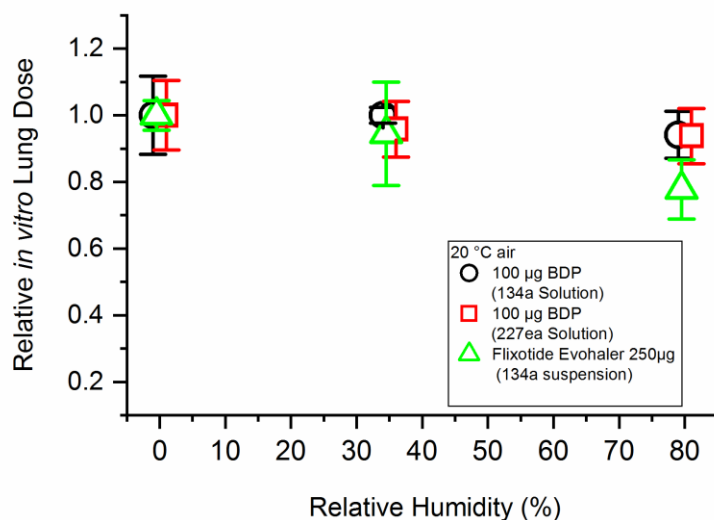


Figure A 3: Data of (Shemirani et al. 2013): *in vitro* lung dose (normalized by mean at 0 % RH) vs. relative humidity for two solution and one suspension pMDI tested at 20 °C. Data points are offset horizontally for visibility.

The data of Morin et al. (Morin et al. 2014) shown in Figure A 4 indicate that temperature has a strong effect on *in vitro* lung dose for inhalers in thermal equilibrium with the testing environment; the strength of the effect varied across the tested inhalers. The data presented in Figure A 5 and Figure A 6 demonstrate that changing the inhaler temperature and the ambient temperature have independent effects, suggesting that more than one mechanism is responsible for the changes in deposition in the throat model. Decreasing the ambient air temperature will slow the rate of propellant evaporation; since evaporation may still be underway

in the throat model (Haynes et al. 2004), this will result in a coarser aerosol that is more prone to deposition by inertial impaction, with a consequent reduction in *in vitro* lung dose. Reducing the temperature of the inhaler will reduce the vapor pressure and the degree of superheat of the propellant in the canister; as discussed in Section 2.2, this will coarsen the droplet size distribution produced by the pMDI and the resulting aerosol, thus increasing deposition in the throat model.

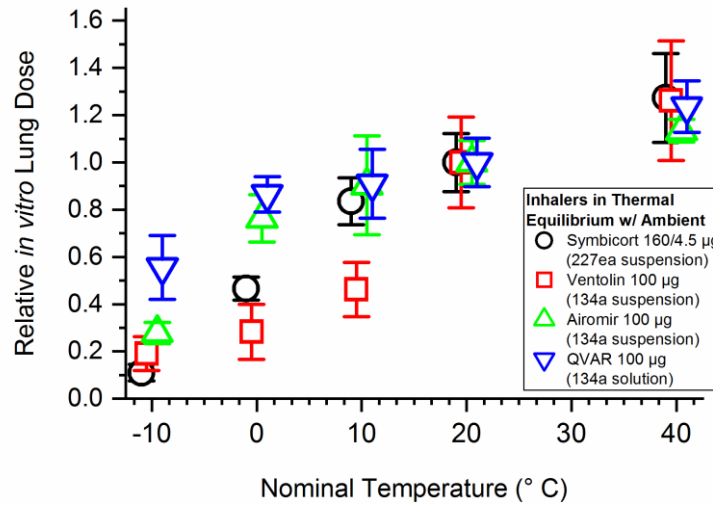


Figure A 4: Data of (Morin et al. 2014): *in vitro* lung dose (normalized by the mean at 20 °C) vs. temperature for four commercial pMDI products ; for these experiments, inhalers were in thermal equilibrium with ambient during testing. Data points are offset horizontally for visibility.

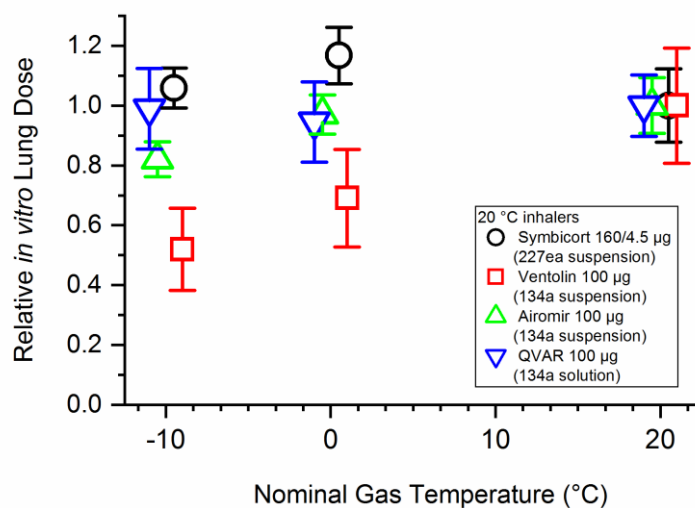


Figure A 5: Data of (Morin et al. 2014): *in vitro* lung dose (normalized by the mean at 20 °C) vs. gas temperature for four commercial pMDI products. In these experiments, inhalers were equilibrated at 20 °C and tested at varying ambient temperature. Data points are offset horizontally for visibility.

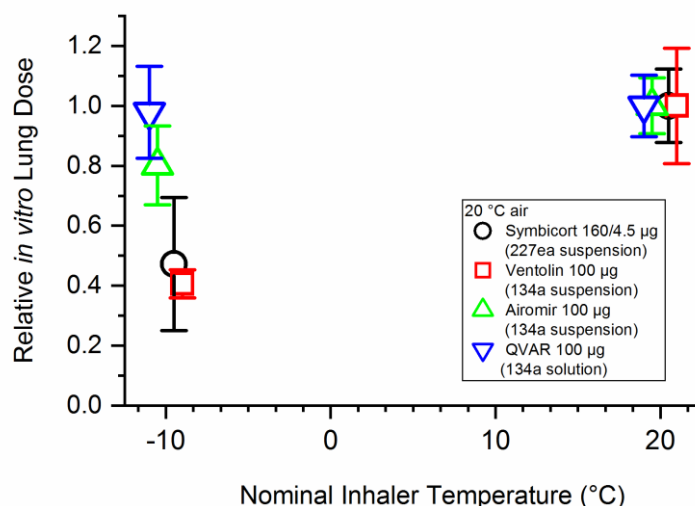


Figure A 6: Data of (Morin et al. 2014): *in vitro* lung dose (normalized by the mean at 20 °C) vs. inhaler temperature; here inhalers were equilibrated at the nominal temperature and tested at the ambient lab temperature of 20 °C. Data points are offset horizontally for visibility.

Deposition in the mouth-throat, both *in vitro* and *in vivo*, depends on the initial droplet diameter and spray momentum, the aerosol dynamics (which involve rapid size changes due to evaporation and condensation), the gas flow rate, and the geometry of the mouth-throat. The models employed in this work provide some insight into how ambient temperature and inhaler

temperature affect some of these factors. Droplet initial mass median diameter as computed using Equation A.17 is plotted against the temperature of the propellant in the metering chamber for HFA 134a and 227ea in the left panel of Figure A 7. The model predicts very substantial coarsening of the spray as inhaler temperature is reduced below 0 °C, particularly for HFA 227ea. This may partially explain the temperature dependent performance of the Symbicort inhaler, which employs p227ea: as seen in Figure A 4, Figure A 5, and Figure A 6, a decline in *in vitro* lung dose is only observed when the inhaler temperature is reduced; the *in vitro* lung dose is relatively unaffected by the ambient temperature. The differentiation between Ventolin, Airomir, and QVAR in Figure A 6 may be attributable to other factors (formulation composition, device geometry) which were not systematically varied in this study; this is an area for future work.

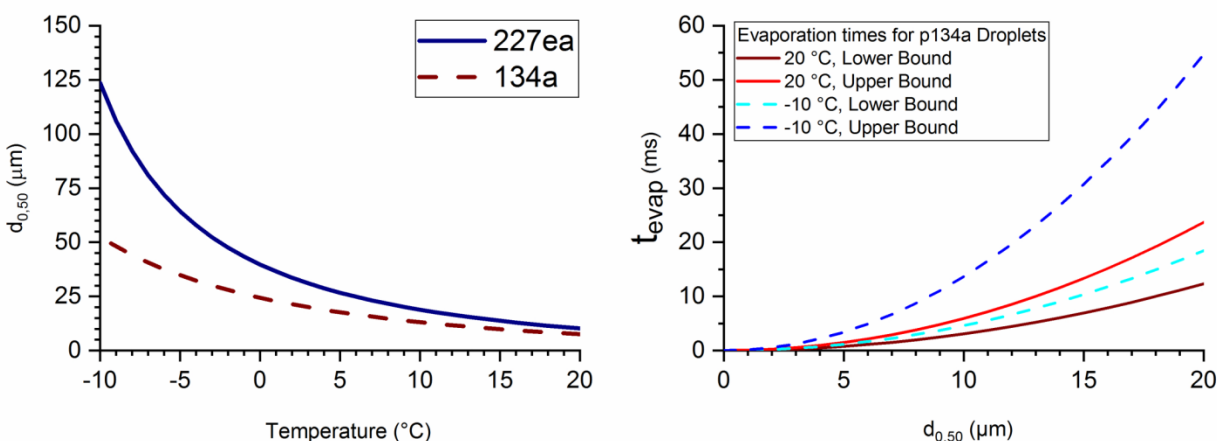


Figure A 7: Left panel—initial droplet mass median diameter (computed with Equation A.17) vs. propellant temperature for p134a and p227ea. Right panel—results from the quasistationary droplet evaporation model including Stefan flow assuming droplet evaporation at standard pressure: time required for droplet evaporation vs. the initial droplet diameter for p134a at -10 and 20 °C. “Lower bound” was calculated at nominal air temperature, while “upper bound” was calculated at an outlet condition assuming complete evaporation of propellant in an adiabatic process to provide an extremum case.

The quasistationary droplet evaporation model was used to assess the effect of ambient temperature on the evaporation rate of pure HFA 134a droplets; the results are presented in the right panel of Figure A 7, and indicate that droplets may take several times longer to evaporate at -10 °C than at 20 °C, which clearly has implications for the amount of deposition in the mouth-throat model. The differing response of *in vitro* lung dose to changes in ambient temperature

among the tested inhalers shown in Figure A 5 is likely related to the differences in formulation and delivery device.

A2.4. Conclusions

No significant effect of atmospheric pressure on *in vitro* lung dose was observed up to 4300 m elevation (~60 kPa atmospheric pressure). Increasing RH results in a small but significant reduction in *in vitro* lung dose for one inhaler type; others were unaffected. Both the ambient temperature and the inhaler temperature affect the *in vitro* lung dose; the effects are independent, and the strength varies across the tested pMDIs. This variation is likely attributable to differences in formulation or device variables. Simple mechanistic models provide qualitative insight into the problem, but further experimental and theoretical work is needed to fully understand what factors lead to robust performance at low temperatures or high humidity. Product developers and clinicians should be aware of these considerations to ensure that patients obtain consistent performance regardless of environmental conditions.

A3. Monodisperse spray drying calculations

A3.1. The dependence of the dry particle diameter on the operating parameters

For monodisperse breakup of a liquid jet with diameter d_j , the droplet volume V_d equals the volume expelled from the orifice during one pulse of the generator, or one complete wavelength λ :

$$V_d = \frac{\pi d_j^2}{4} \lambda . \quad (\text{A.18})$$

Using the formula for volume of a sphere and solving for droplet diameter d_d gives

$$d_d = \sqrt[3]{\frac{3\lambda d_j^2}{2}} . \quad (\text{A.19})$$

Monodisperse operation can only be achieved in a certain range of wavelengths; literature references give

$$\lambda_{\min} = \pi d_j \text{ (Rayleigh 1878)} \quad (\text{A.20})$$

and

$$\lambda_{\max} = 7d_j \text{ (Schneider and Hendricks 1964)}. \quad (\text{A.21})$$

Assuming the jet diameter is approximately equal to the orifice diameter, d_o , the limiting criteria of Equations (A.20) and (A.21) in combination with Equation (A.19) yield the inequality

$$1.7d_o \leq d_d \leq 2.2d_o . \quad (\text{A.22})$$

Assuming solid spherical particles of density ρ_p result from drying of a solution droplet with solute concentration c_s , dry particle diameter d_p is given by Equation (1.16):

$$d_p = \sqrt[3]{\frac{c_s}{\rho_p}} d_d . \quad (1.16)$$

Rearranging Equation (1.16) and substituting into Inequality (A.22) gives

$$1.7 \sqrt[3]{\frac{c_s}{\rho_p}} d_o \leq d_p \leq 2.2 \sqrt[3]{\frac{c_s}{\rho_p}} d_o , \quad (\text{A.23})$$

which provides approximate bounds on attainable dry particle size at monodisperse operation as a function of the chosen orifice diameter and solids content. The effects of orifice diameter and solution concentration on the dry particle diameter are explored graphically in Figure A 8; here $\rho_p = 1000 \text{ kg/m}^3$ and $d_d/d_o = 1.95$ were assumed.

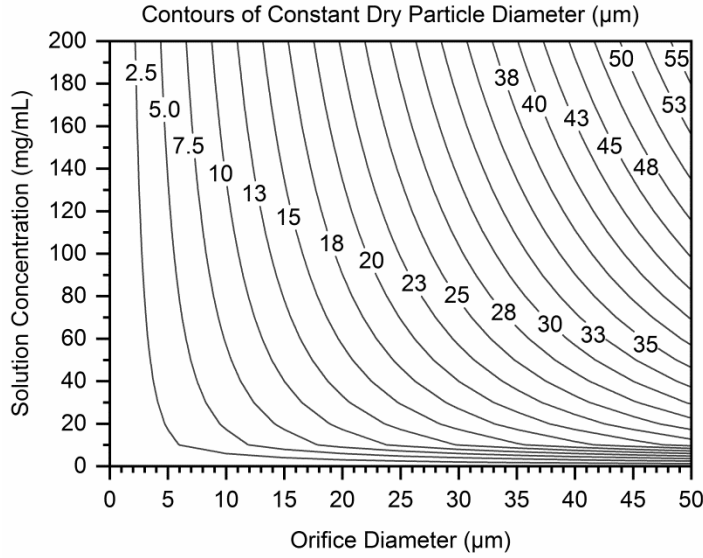


Figure A 8: Contour plot of dry particle size (μm) vs. orifice diameter and solution concentration for $\rho_p = 1000 \text{ kg/m}^3$ and $d_d/d_o = 1.95$.

A3.2. The dependence of the dry mass throughput on the operating parameters

For a cylindrical jet issuing from a circular orifice with diameter d_o and volume flow rate Q , and assuming $d_j \cong d_o$, the average jet velocity v_j is

$$v_j = \frac{4Q}{\pi d_o^2}. \quad (\text{A.24})$$

If the jet consists of a solution with concentration c_s and undergoes atomization and complete evaporation of solvent in a monodisperse spray drying process, the rate of solids production \dot{m} is

$$\dot{m} = c_s Q = \frac{\pi c_s d_o^2 v_j}{4}. \quad (\text{A.25})$$

Recalling the material presented in Section 4.2.3, monodisperse breakup can be achieved for operation in the Rayleigh breakup regime, which is characterized by

$$We_L = \frac{\rho_l v_j^2 d_o}{\sigma_{lg}} > 8 \quad (4.7)$$

and

$$We_G = \frac{\rho_g v_j^2 d_o}{\sigma_{lg}} < 0.4 \quad (4.8)$$

or

$$We_G < 1.2 + 3.41Oh^{0.9}, \text{ with } Oh = \frac{\mu_l}{\sqrt{\rho_l d_o \sigma_{lg}}}. \quad (4.9)$$

For purposes of estimating the maximum feasible solids throughput, we take Equation (4.9); then rearranging Equation (A.25), plugging in to Equation (4.9), and simplifying gives an expression for the maximal solids throughput:

$$\dot{m}_{\max} = \frac{\pi c_s}{4} \left[\frac{d_o^3 \sigma_{lg}}{\rho_g} (1.2 + 3.41Oh^{0.9}) \right]^{1/2}. \quad (A.26)$$

This relationship depends on the physical properties of the liquid and the gas, and is explored in Figure A 9 for jets of water (left panel) or the HFA propellant p134a (right panel). The maximal feasible throughput for fixed solution concentration and orifice diameter is substantially lower for p134a relative to water due to its lower surface tension.

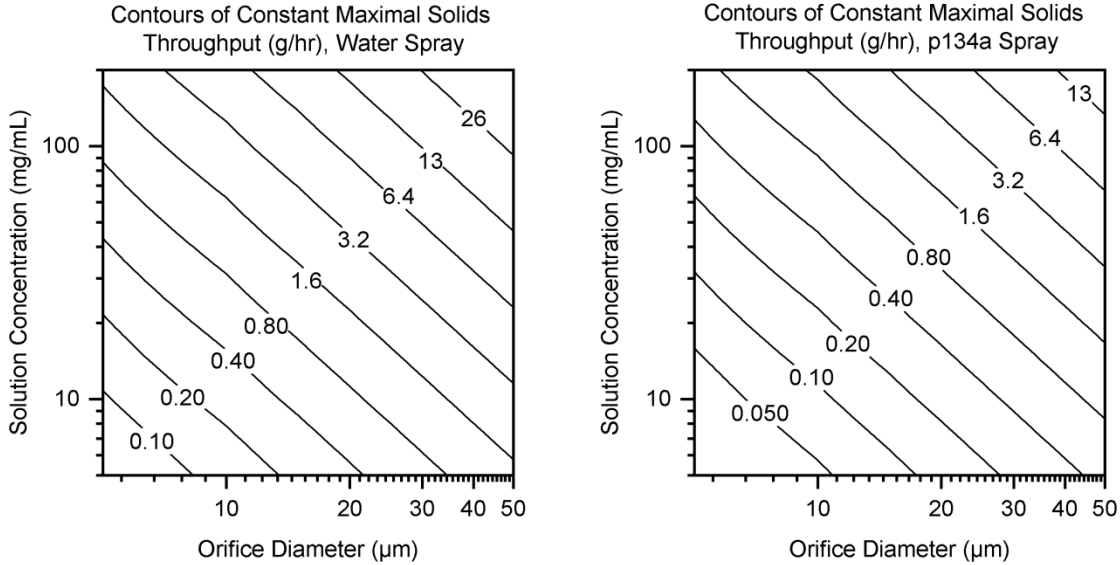


Figure A 9: Contour plots of maximal feasible solids throughput for monodisperse spray drying computed using Equation (A.26) for water (left panel) or p134a (right).

A3.3. Propellant jets and the Rayleigh breakup regime

For monodisperse atomization of propellants using the experimental setup presented in Section 4.5.2.1, the pressure upstream of the discharge orifice must remain above the saturation vapor pressure of the propellant to prevent flashing, and the breakup must occur in the Rayleigh regime. There is thus an upper limit on the orifice diameter with which monodisperse breakup can be achieved for a given propellant temperature and discharge pressure. For demonstration

purposes, the gas Weber number We_g is plotted against the pressure drop across the orifice, Δp_o , for p134a jets of 10 or 35 μm discharging into air at 101.3 kPa in Figure A 10. Taking Equation (4.9) as the transition Weber number We_t above which aerodynamic forces affect the breakup, for fixed orifice diameter there is a corresponding transition value of Δp_o above which monodisperse breakup is precluded. This transition value of Δp_o decreases as orifice diameter increases; for a sufficiently large orifice the Weber number constraint cannot be satisfied while maintaining the liquid upstream of the orifice in a saturated condition. This is an important consideration for experiments employing superheated liquid propellants in the monodisperse atomizer. In my own practice with p134a jets chilled to $\sim 0^\circ\text{C}$ at the injection point, monodisperse breakup was only achievable for orifice diameters of about 25 μm or smaller.

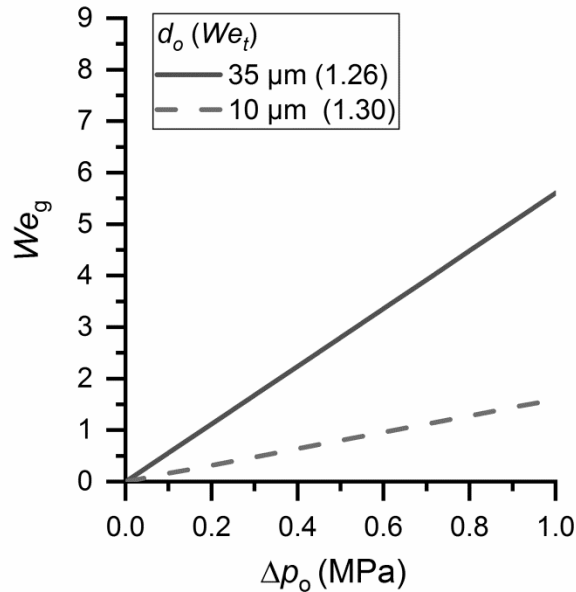


Figure A 10: Plot of gas Weber number vs. pressure drop across the orifice for 10 μm (dashed line, transition Weber number 1.30) or 35 μm (closed line, transition Weber number 1.26) liquid jets discharging into air at 101.3 kPa and 20°C . Propellant liquid properties were computed at 0°C .

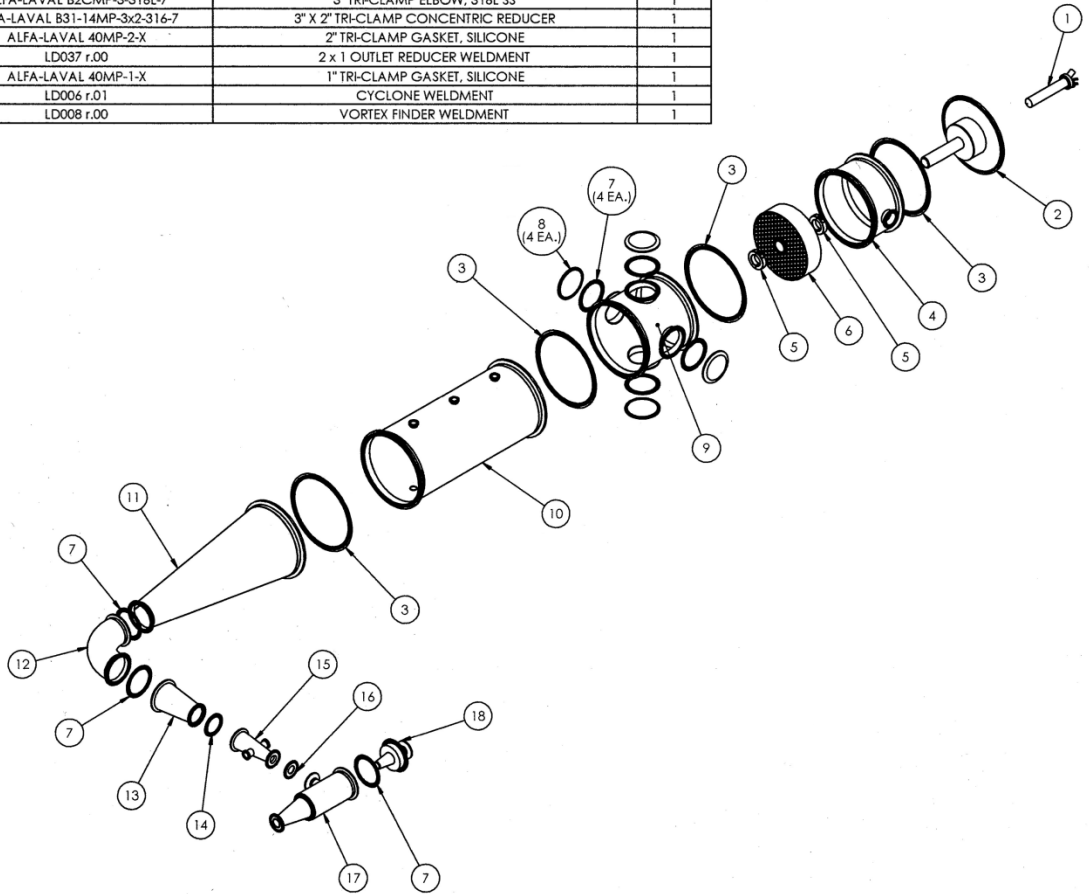
A4. Design documentation for modular laboratory scale research spray dryer and peripheral equipment

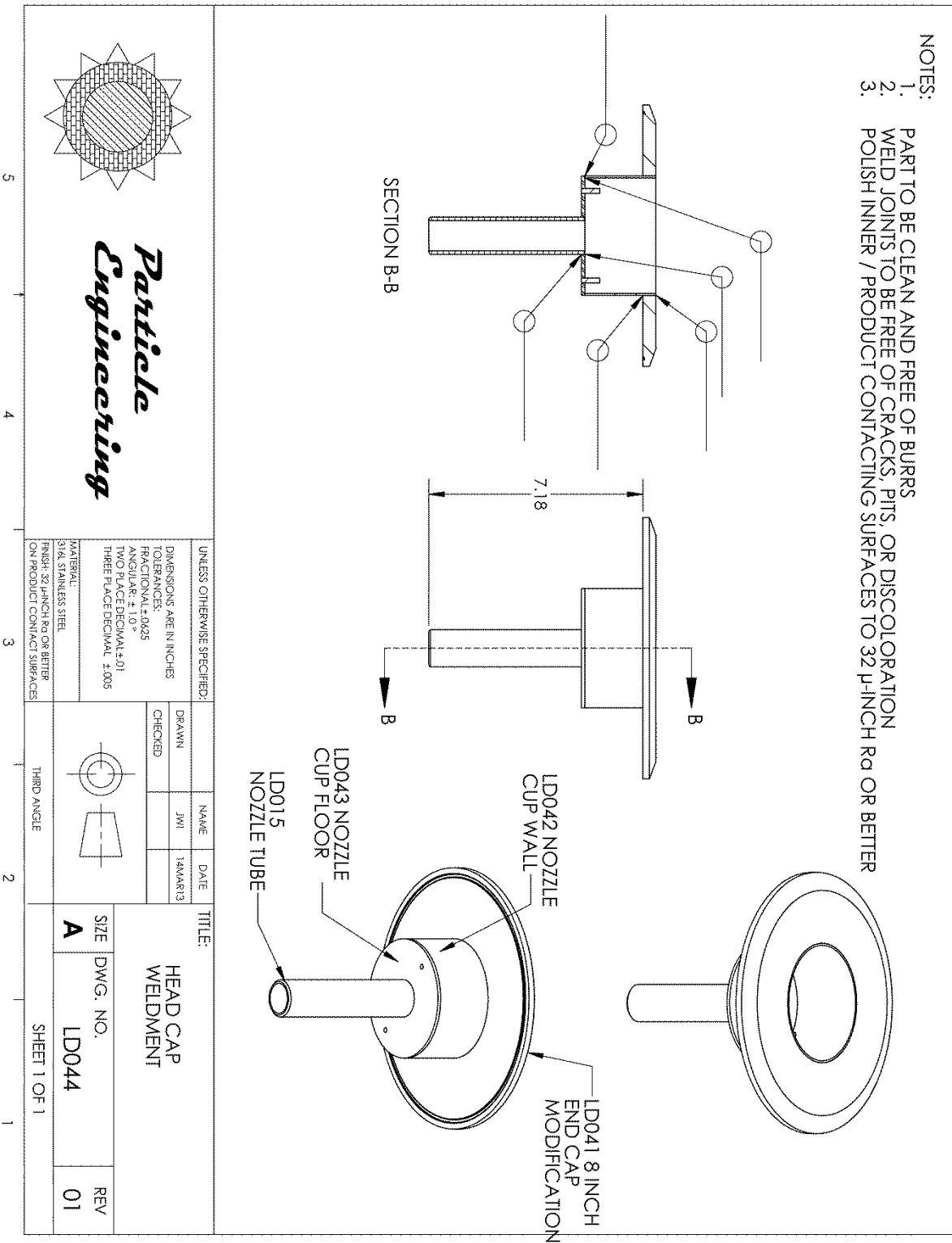
A4.1. Dryer hardware bill of materials

Vendor or Manufacturer	Part or Drawing #	Description	Qty
Custom	N/A	Atomizer	1
Custom	LD044 r.01 + LD062 r.00	Head cap weldment + modification	1
Alfa-Laval	40-MOF-8-X	8" tri-clamp gasket, silicone	4
Custom	LD019 r.01	Head weldment	1
McMaster-Carr	9421T210	Shaft collar, 1.25" OD	1
Custom	LD024 r.00	Straightener assembly	1
Alfa-Laval	40MP-3-X	3" tri-clamp gasket, silicone	7
Metaglas	Metaclamp 3S	3" sanitary sight glass	4
Custom	LD028 r.00	Sight glass weldment	1
Custom	LD011 r.00	Drying chamber spool weldment	2
Custom	LD014 r.01 + LD062 r.00	8 x 3 concentric reducer weldment, plus modification	1
Custom	LD061 r.00	TFA clamp	2
Alfa-Laval	B2CMP-3-316L-7	3" tri-clamp elbow, 316L SS	3
McMaster-Carr	50485K39	3" tri-clamp spool, 6" o' all lg., 316L SS	1
Alfa-Laval	B31-14MP-3x2-316-7	3 x 2 tri-clamp concentric reducer	1
Alfa-Laval	40MP-2-X	2" tri-clamp gasket, silicone	1
Custom	LD037 r.00	2 x 1 outlet reducer weldment	1
Alfa-Laval	40MP-1-X	1" tri-clamp gasket, silicone	4
Custom	LD031 r.01	ES precipitator adapter weldment	1
Büchi	N/A	B90 ESP gasket	1
Büchi	N/A	ESP assembly	1
McMaster-Carr	9396K32	AS568A-211 o-ring, silicone	1
Custom	LD033 r.00	ESP outlet elbow adapter weldment	1
Alfa-Laval	40MP-1-X	1" tri-clamp gasket, silicone	2
Custom	LD040 r.00	ESP outlet cross weldment	1
Solberg	PSL-UL850/1-200HC	Housing for HEPA filter element, for exhaust gas scrubbing	1
Solberg	UL850/1	Replacement HEPA element, for exhaust gas scrubbing	1

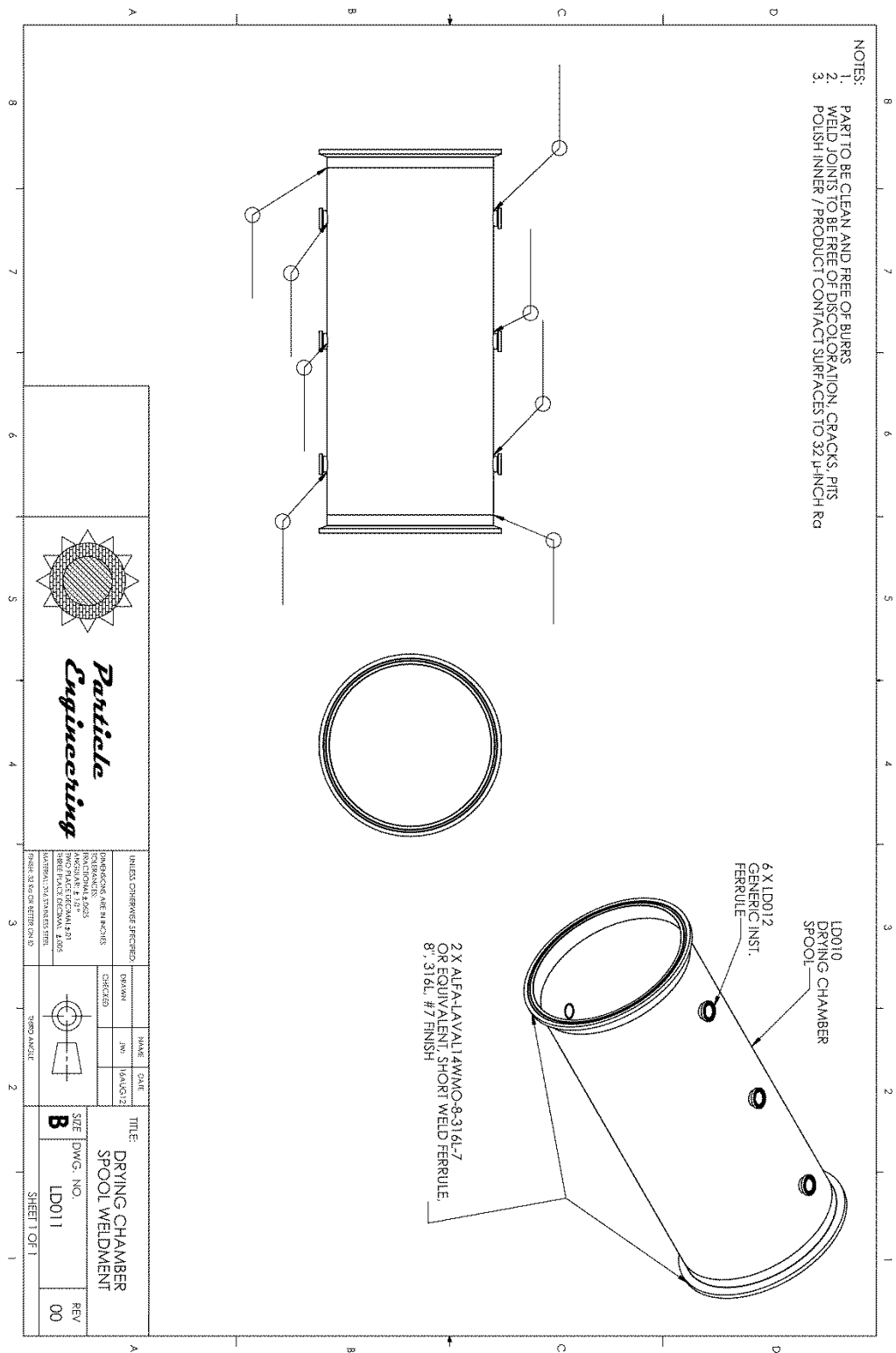
A4.2. Dryer hardware selected engineering drawings

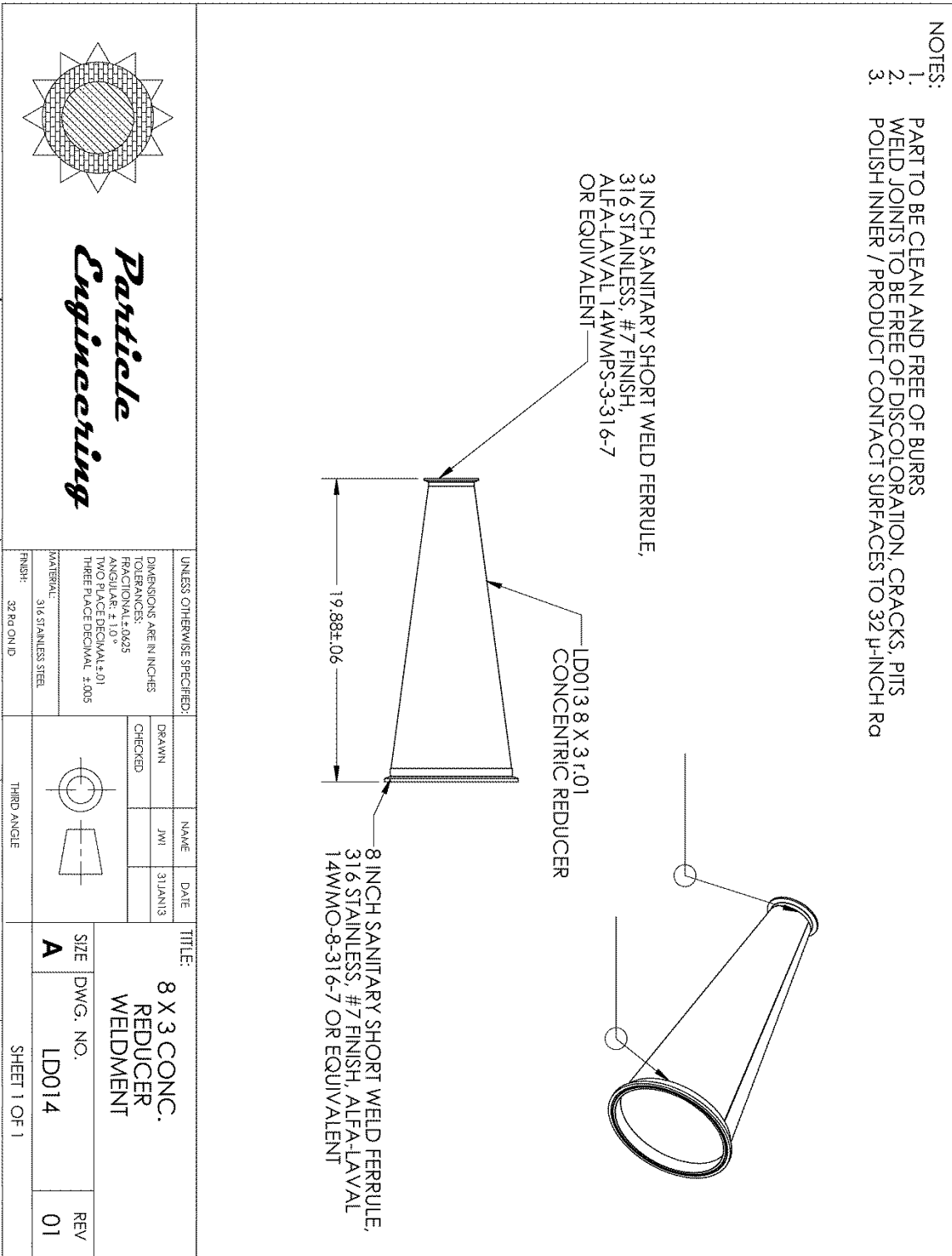
Item #	Part #	Description	Qty
1	N/A	ATOMIZER	1
2	LD044 r.00	HEAD CAP WELDMENT	1
3	ALFA-LAVAL 40-MOF-8-X	8" TRI-CLAMP GASKET, SILICONE	4
4	LD019 r.01	HEAD WELDMENT	1
5	MCMMASTER 9421T210	SHAFT COLLAR, 1.25" OD	1
6	LD024 r.00	STRAIGHTENER ASSEMBLY	1
7	ALFA-LAVAL 40MP-3-X	3" TRI-CLAMP GASKET, SILICONE	7
8	N/A	3" SANITARY SIGHT GLASS	4
9	LD028 r.00	SIGHT GLASS WELDMENT	1
10	LD011 r.00	DRYING CHAMBER SPOOL WELDMENT	2
11	LD014 r.01	8 X 3 CONCENTRIC REDUCER WELDMENT	1
12	ALFA-LAVAL B2CMP-3-316L-7	3" TRI-CLAMP ELBOW, 316L SS	1
13	ALFA-LAVAL B31-14MP-3x2-316-7	3" X 2" TRI-CLAMP CONCENTRIC REDUCER	1
14	ALFA-LAVAL 40MP-2-X	2" TRI-CLAMP GASKET, SILICONE	1
15	LD037 r.00	2 x 1 OUTLET REDUCER WELDMENT	1
16	ALFA-LAVAL 40MP-1-X	1" TRI-CLAMP GASKET, SILICONE	1
17	LD006 r.01	CYCLONE WELDMENT	1
18	LD008 r.00	VORTEX FINDER WELDMENT	1

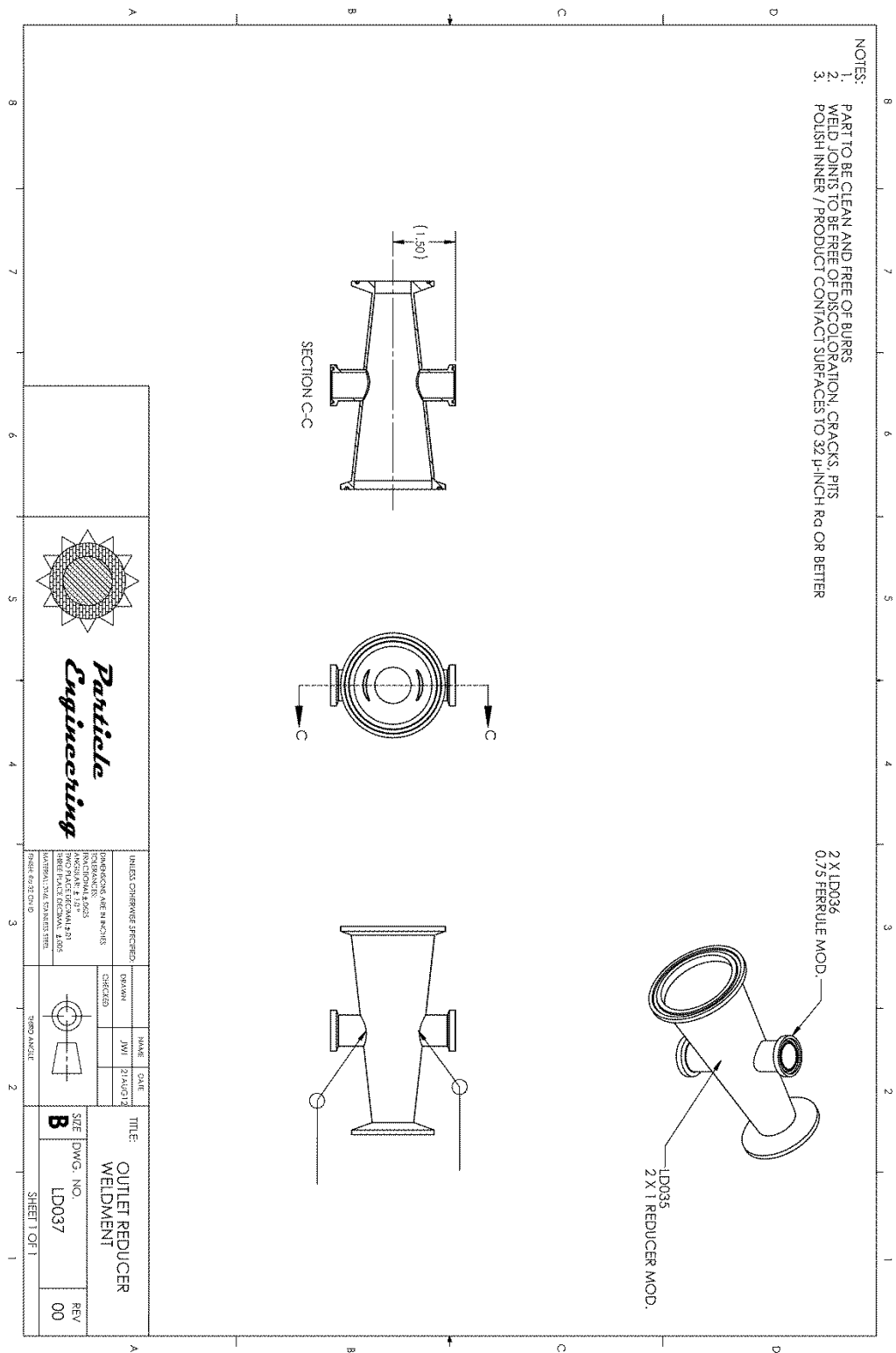




Particle Formation from Evaporating Microdroplets for Inhaled Drug Delivery







Particle Formation from Evaporating Microdroplets for Inhaled Drug Delivery

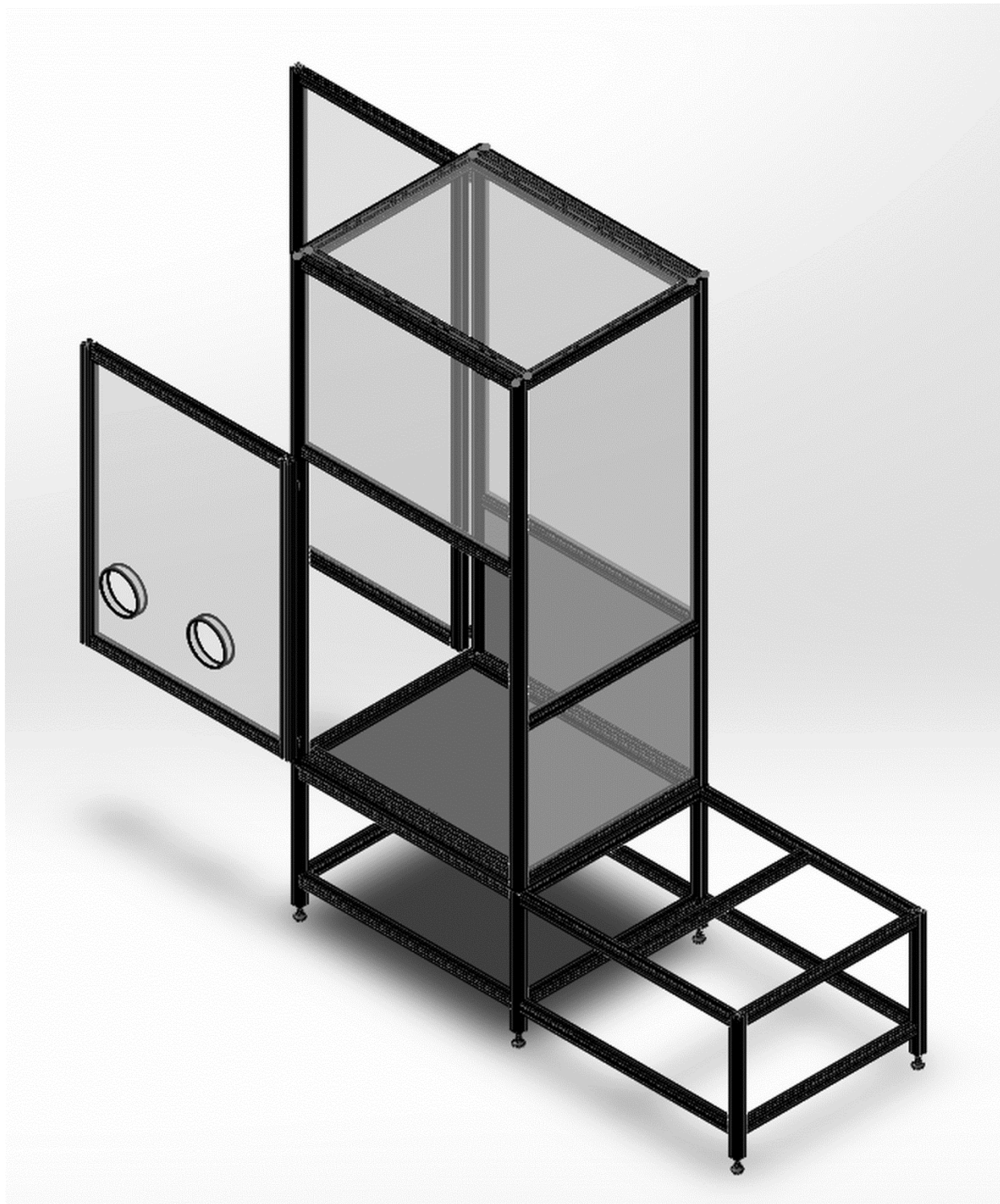
A4.3. Dryer enclosure bill of materials

Vendor / Manufacturer	Part / Drawing Number	Description	Qty
Bosch-Rexroth	8 981 992 027 / 635mm	45 x 45 Profile, 635 mm, M12 single end tapped	6
Bosch-Rexroth	8 981 992 026 / 900mm	45 x 45 Profile, 900 mm	13
Bosch-Rexroth	8 981 992 026 / 1100mm	45 x 45 Profile, 1100 mm	9
Bosch-Rexroth	3 842 352 061	M12 x 44 mm Leveling Foot	6
Bosch-Rexroth	8 981 992 026 / 2300mm	45 x 45 Profile, 2300 mm	4
Bosch-Rexroth	3 842 992 432/ 1100 mm	45 x 90 Profile, 1100 mm	4
Bosch-Rexroth	3 842 535 642	Clean room hinge, 45-series to 45-series	4
Bosch-Rexroth	3 842 524 986	Ball detent latch	2
Bosch-Rexroth	3 842 518 492	10mm door seal, 10,000mm long	2
Bosch-Rexroth	8 981 992 026 / 1000mm	45 x 45 Profile, 1000 mm	2
Bosch-Rexroth	8 981 992 026 / 2200mm	45 x 45 Profile, 2200 mm	4
Bosch-Rexroth	8 981 992 026 / 800mm	45 x 45 Profile, 800 mm	2
Bosch-Rexroth	8 981 992 026 /2210mm	45 x 45 Profile, 2210 mm	3
Bosch-Rexroth	8 981 992 026 /290mm	45 x 45 Profile, 290 mm	4
Bosch-Rexroth	8 981 992 026 /350mm	45 x 45 Profile, 350 mm	2
Bosch-Rexroth	8 981 992 028 /163mm	45 x 45 Profile, 163 mm, M12 tap on both ends	2
Bosch-Rexroth	3 842 502 684	45x45 multi-angle connector kit	2
Bosch-Rexroth	3 842 146 813	42 x 60 Sheet metal gusset	12
Bosch-Rexroth	3 842 523 561	45x45 gusset with fasteners	50
Bosch-Rexroth	3 842 535 572	10mm inside-to-outside gusset and set screws, pk of 10	4
Bosch-Rexroth	8 981 019 449	45-series rectangular joining plate	8
Bosch-Rexroth	3 842 527 185	10mm glazing strip, 10,000mm long	7
Custom	LD046 r.00	8 x 3 reducer bracket	1
Custom	LD047 r.00	Chamber bracket	2
Custom	LD048 r.00	Enclosure deck	1
Custom	LD050 r.00	Door panel A	1
Custom	LD051 r.01	Door panel B	1
Custom	LD052 r.00	Glove ring	2
Custom	LD053 r.00	Wall panel A	1
Custom	LD054 r.00	Wall panel B	1
Custom	LD055 r.00	Wall panel C	1
Custom	LD056 r.01	Wall panel D	1
Custom	LD058 r.00	Wall panel E	1

Particle Formation from Evaporating Microdroplets for Inhaled Drug Delivery

Vendor / Manufacturer	Part / Drawing Number	Description	Qty
Custom	LD059 r.00	Enclosure roof	1
Custom	LD049 r.00	Cyclone bracket	1

A4.4. Dryer enclosure assembly graphic



Particle Formation from Evaporating Microdroplets for Inhaled Drug Delivery

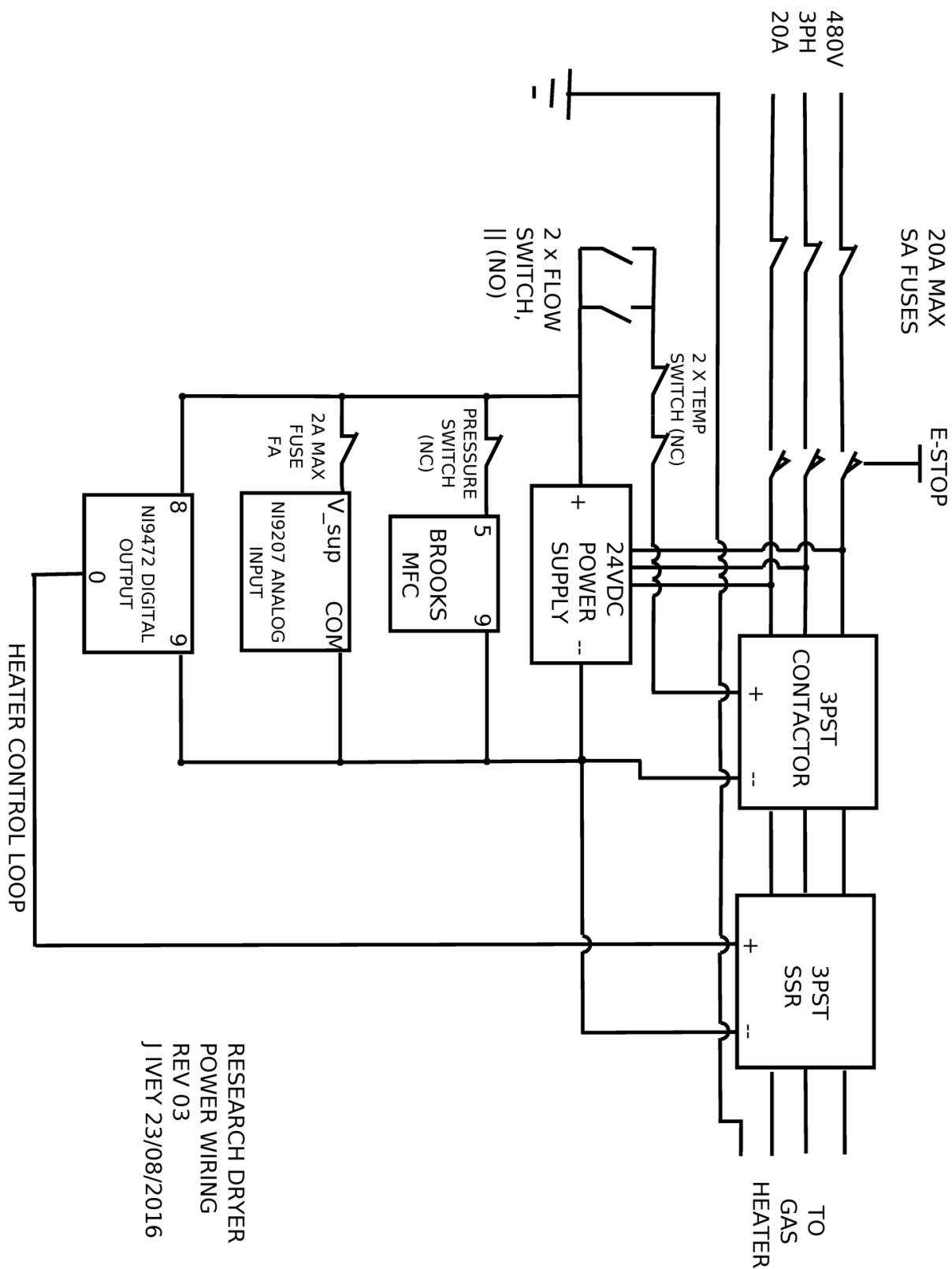
A4.5. Instruments and controls bill of materials

Vendor / Manufacturer	Part Number	Description	Qty
McMaster-Carr	6759K27	Panel power disconnect switch	1
McMaster-Carr	6113T16	3 position fuse block for panel power	1
McMaster-Carr	6323T19	Solid state relays for interlock and heater control circuits, 3PST-NO, 5-32V DC, 25 Amps @ 600V AC	2
McMaster-Carr	7009K51	24 VDC power supply for instrument power, Three Phase, 380-480V AC to 24V DC, 120W & 5A Output	1
McMaster-Carr	6113T12	2 position fuse block for NI9207 analog input	2
McMaster-Carr	75065K43	Panel enclosure, 18" x 18" x 8"	1
McMaster-Carr	7079K51	Temperature switch for heater outlet, Turns "on" to "Off", 3/8 NPT Male Threaded	1
McMaster-Carr	47515K71	Pressure switch, 5-30 PSI Setpoint	1
McMaster-Carr	91445K23	Flow switch for low drying gas flow range, Brass Body, 1/2 NPT Female	1
McMaster-Carr	2766K43	Flow switch for high drying gas flow range, 1/2 NPT Pipe Size	1
Brooks	SLA5853S2EAB3C2A1	Thermal gas mass flow controller for drying gas, 100-1000 SLPM	1
National Instruments	781156-01	cDAQ-9178 Compact DAQ chassis with USB comms for I/O	1
National Instruments	779473-01	NI9901 desktop mounting kit for cDAQ chassis	1
National Instruments	763000-01	Power cord for chassis	1
National Instruments	781068-01	NI9207 analog input module (8 ch current, 8 ch voltage) for instrumentation	1
National Instruments	781503-01	NI9923 37 pin D-sub connector kit for connecting instruments to analog input module	1
National Instruments	779001-01	NI9211 thermocouple-specific analog input module, 4 ch	2
National Instruments	779004-01	NI9472 8 ch, 24V sourcing digital output for inlet temperature control signal	1
National Instruments	779334-01	NI9265 analog output, 4-20 mA, for gas mass flow controller set point	1
National Instruments	779017-01	NI9932 connector kit w/ strain relief for wiring I/O modules	4
Omega Engineering	KMQSS-125G-3	Type K thermocouple probe with miniature connector, 3" o'all lg, for outlet temperature	2
Omega Engineering	KMQSS-125G-6	Type K thermocouple probe with miniature connector, 6" o'all lg, for inlet temperature	2
Omega Engineering	KMQSS-125G-9	Type K thermocouple probe with miniature connector, 9" o'all lg, for drying chamber temperature	2
Omega Engineering	EXPP-K-24-100	Type K thermocouple wire, spool, 100 ft.	1
Omega Engineering	SMPW-K-F	Type K mini thermocouple connector kit, female	8
Omega Engineering	PX319-015GI	Pressure transmitter, 4-20 mA, 0-15 psi, for dryer chamber pressure	1

Particle Formation from Evaporating Microdroplets for Inhaled Drug Delivery

Vendor / Manufacturer	Part Number	Description	Qty
Omega Engineering	PX419-001DWUI	Differential pressure transmitter, 4-20 mA, 0-1 psid, for laminar flow element delta P with monodisperse drying setup	1
Exergy	00256-03	Shell-and-tube heat exchanger, 316 stainless, for drying gas chilling	1

A4.6. Instruments and controls wiring diagrams



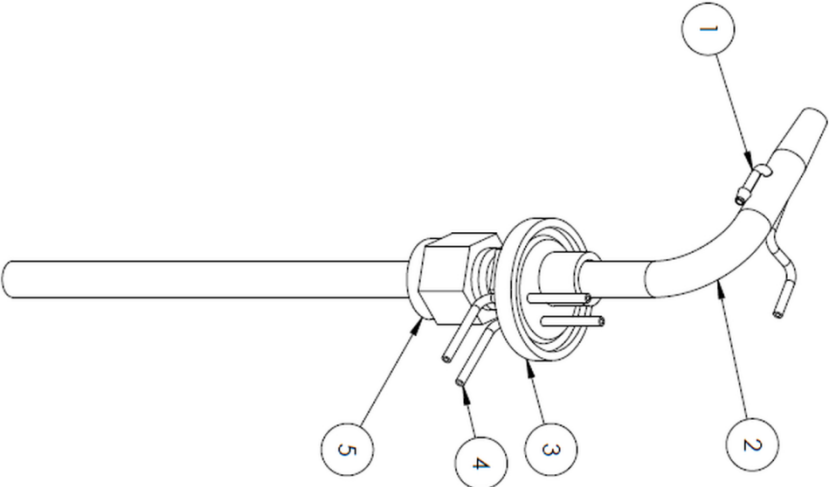
A4.7. Isokinetic sampling system bill of materials

Vendor / Manufacturer	Part / Drawing Number	Description	Qty
Custom	IKS01 r.00	Isokinetic sampler probe assembly	1
Custom	MC04 r.00	Top cap	1
Custom	MC02 r.00	Mixing cone upper	1
Custom	MC07 r.00	¼" tube 90 ° element	3
Custom	n/a	3d printed flow straightening element	1
Custom	MC03 r.00	Mixing cone lower	1
Custom	MC05 r.00	Bottom cap	1
Custom	MC07 r.00	¾" gas outlet	1
Pall	12144	HEPA capsule filter, 3/8" NPT connections	1
Dwyer Instruments	2300-0	Differential pressure gauge, ± 0.25" H ₂ O	1
TSI	4043	Gas mass flow meter, air, 0-300 SLPM	1
Swagelok	B-400-1-2	Straight connector, 1/8" NPT x ¼" tube, brass	2
Swagelok	B-400-2-6	90 ° elbow, 3/8" NPT x ¼" tube, brass	1
Swagelok	B-400-1-4	Straight connector, ¼" NPT x ¼" tube, brass	1
Swagelok	B-810-1-4	Straight connector, ¼" NPT x ½" tube, brass	1
Swagelok	B-200-1-2	Straight connector, 1/8" NPT x 1/8" tube, brass	2
Swagelok	NY-810-SET	Nylon front / back ferrule combo	1
Bosch-Rexroth	8 981 992 026 / 300mm	45 x 45 Profile, 300 mm	4
Bosch-Rexroth	8 981 992 026 / 200mm	45 x 45 Profile, 200 mm	2
Bosch-Rexroth	3 842 523 561	45x45 gusset with fasteners	6
McMaster-Carr	91339A150	3/8"-16 sealing hex nut	1
McMaster-Carr	97414A665	9/16" external retaining ring	2
McMaster-Carr	4322K675	2" sanitary spool, 8" o'all lg, 304 SS	1
McMaster-Carr	4520K45	2" sanitary gasket, silicone	2
McMaster-Carr	4322K153	2" sanitary clamp	2
McMaster-Carr	5463K447	Plastic barbed tube connector, 3/8" NPT x ¼" tube ID, pkg of 10	1
McMaster-Carr	7832K24	Needle valve, brass, 1/8" NPT, 1/8" orifice, Cv 0.22 full open	1
McMaster-Carr	8967K88	Copper tubing, ¼" OD, 1/8" ID, straight	3 ft.
McMaster-Carr	4114T23	Ball valve, brass, ¼" NPT	1
McMaster-Carr	4004K73	Dual-Scale Pressure & Vacuum Gauge with Steel Case, 2-1/2" Dial Diameter, 1/4 NPT Center Back Connection, 0 to 15 PSI	1
McMaster-Carr	44555K132	Brass barbed tube connector, ¼" NPT x ¼" ID	2
McMaster-Carr	4429K251	Brass tee, female, ¼" NPT	1
McMaster-Carr	5108K48	Abrasion-Resistant Polyurethane Tube for Air, 1/4" ID, 5/16" OD	25 ft
McMaster-Carr	5236K208	Silicone tubing, 1/16" ID	25 ft
McMaster-Carr	51135K73	Silicone tubing, 1/8" ID	10 ft
McMaster-Carr	563K47	Plastic Barbed Tube Fittings for Air & Water, Tight-Seal, Reducer, for 1/8" x 1/16" Tube ID, Pkg of 10	1

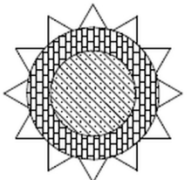
Particle Formation from Evaporating Microdroplets for Inhaled Drug Delivery

Vendor / Manufacturer	Part / Drawing Number	Description	Qty
McMaster-Carr	5393K43	Vacuum-Rated PVC Tubing for Food, Beverage, and Dairy, 1/2" ID, 3/4" OD	10 ft.
McMaster-Carr	5330K23	Noncontact Flow-Adjustment Valve, Nickel-Plated Brass, for 3/32" to 3/4" Tube OD	1

A4.8. Isokinetic sampling system selected engineering drawings



ITEM NO.	PartNo	DESCRIPTION
1	IKS05	Isokinetic Sampler - Pressure Tap A
2	IKS03	Isokinetic Sampler - Probe
3	N/A	14WMPs Cap 0.5 0.75in.
4	IKS06	Isokinetic Sampler - Pressure Tap B
5	SS-400-R-6BT	SS Swagelok Tube Fitting, 1/4 in. x 3/8 in. Reducer, Bored Through

		UNLESS OTHERWISE SPECIFIED:		DRAWN		NAME		DATE		TITLE:	
		DIMENSIONS ARE IN INCHES		CHECKED		LC		27JAN2016		Isokinetic Sampler ISO View	
TOLERANCES:		FRACTIONAL: ±.0025		THIRD ANGLE		SIZE		DWG. NO.		REV	
ANGULAR: ±.10°		TWO PLACE DECIMAL: ±.01		THIRD ANGLE		A		IKS01		00	
THREE PLACE DECIMAL: ±.005		MATERIAL: Various		FINISH: N/A		SHEET 1 OF 2				